Recovery and utilisation of waste heat from fuel cells powering fuel cell hybrid trains: the Birmingham New Street scenario

Marco Pignataro

A thesis submitted to

The University of Birmingham for the degree of

Doctor of Philosophy

School of Chemical Engineering
University of Birmingham
July 2023

ABSTRACT

This thesis presents a comprehensive energy analysis of a potential fuel cell hybrid (FCH) trains fleet operating in the Birmingham area, considering the current and future scenarios of the UK hydrogen economy. A well-to-wheel (WTW) approach was employed to evaluate fourteen different hydrogen pathways, with projections for 2030 and 2040. The study identifies the most efficient hydrogen production, transport, and storage methods, highlighting that Steam Methane Reforming (SMR) with Carbon Capture and Storage (CCS) offers higher efficiency than wind-powered electrolysis. Transporting hydrogen via 700 bar-tube trailers was found to be the most efficient method until an all-H2 network is established.

Although diesel trains currently have higher WTW efficiency, FCH trains demonstrate better fuel economy in kWh per km. Pathways involving mature technologies like natural gas reforming show lower standard deviations and less uncertainty in WTW efficiencies compared to those involving electrolysis. Green hydrogen pathways are expected to improve significantly from 2030 to 2040, with wind-powered electrolysis efficiency projected to increase from 52% to 58%.

The thesis also explores the potential of waste heat recovery from FCH trains. It estimates a daily waste heat potential of 114 MWh at Birmingham New Street (BNS) station, with only 3.9% required for cabin heating in winter. By 2040, TES systems could store and discharge significant amounts of heat, contributing to CO2 emissions savings (up to 10 ton per day) through integration with the Broad Street heating network. Design optimization could enhance energy discharge by 30% and reduce radiator surface area by 56% for trains running between Leicester and BNS.

These findings highlight FCH trains' potential for lower primary energy consumption compared to diesel trains, emphasizing the need for economic analysis and real-life driving profiles to fully assess the feasibility of hydrogen-fuelled trains. Future research should focus on integrating TES storage within train cabins, understanding train duty cycles and speed profiles, and evaluating the impact of Phase Change Material (PCM) weight on performance. Thermal integration of fuel cell modules and TES systems could be especially effective for trains using solid oxide fuel cells, enhancing energy efficiency and waste heat utilization.

Contents

List of Figures

List of Tables

1. Chapter One

Introduction

1.1 Background and motivation

In 2021, by releasing the Net Zero Strategy paper [1], the UK government officially sets itself the ambitious target to achieve net-zero greenhouse gas emissions by 2050. Transport is the largest contributor to UK domestic greenhouse gas (GHG) emissions, responsible for 27% in 2019 [2]. The decarbonisation of the transport sector is thus essential for the UK to meet its climate goals.

Rail has the lowest emissions intensity among passenger transport modes. According to a 2022 IEA study[1], rail emissions per passenger kilometre are approximately one-eighth of those generated by large cars and one-fifth of those of air travel, as Figure 1 shows. The smaller carbon footprint of rail is mainly attributed to its higher occupancy rates when compared to the other motorised urban transport modes.

[1] https://www.iea.org/energy-system/transport/rail

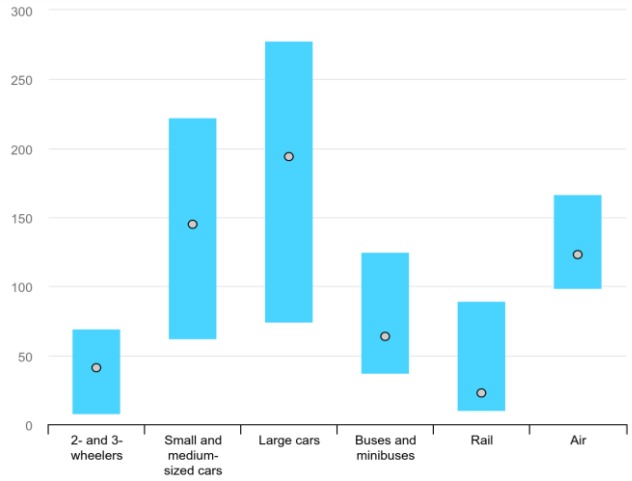

Figure 1 – Well-to-wheel GHG intensity of motorised passenger transport modes

Despite rail is already a green mode of transport, much remains to be done. Some of the key policies implemented by Department for Transport to reduce the emissions of railway sector are:

- electrification of rail lines.
- improved energy efficiency.
- shift to hydrogen and battery-powered trains, removing all the diesel trains from the rail network by 2040.

The UK government has shown a growing interest in hydrogen trains as part of its efforts to meet emissions targets. *Traction Decarbonisation Network Strategy*[2] and *Transport decarbonisation plan*[3] have in fact recently mentioned hydrogen energy as one of the most valid options to replace diesel trains travelling on unelectrified lines or to provide auxiliary power to conventional propulsion systems. Hydrogen fuel cell trains can then be either:

[2] https://www.networkrail.co.uk/wp-content/uploads/2020/09/Traction-Decarbonisation-Network-Strategy-Interim-Programme-Business-Case.pdf
[3] https://assets.publishing.service.gov.uk/government/uploads/system/uploads/attachment_data/file/1009448/decarbonising-transport-a-better-greener-britain.pdf

- an interim technology to realise carbon savings earlier in network areas where electrification cannot be delivered in time to meet Net Zero goals.
- a long-term solution to cut emissions on less intensively used routes or on lines too expensive to electrify.

The deployment of hydrogen fuel cell trains is crucial as it aligns with the broader plan of UK to develop a strong hydrogen economy and becoming a global leader in H_2 technologies. Moreover, hydrogen produced for use in trains can be sourced from renewable or low-carbon pathways, such as electrolysis powered by renewable energy. This creates an opportunity for cross-sectoral integration, where hydrogen for fuel cell trains can also be utilised for other applications, such as industry or heating, maximizing the efficiency and sustainability of the H_2 supply chain.

However, the adoption of hydrogen fuel cell trains faces several technical and economic barriers that need to be addressed for a widespread implementation. According to [3], the main obstacles for hydrogen fuel cell trains application are:

Technical

- limited knowledge in how to standardise and scale hybrid powertrain designs for trains.
- lack of a comprehensive network of refuelling infrastructures.
- absence of reliable and large-scale production paths of clean hydrogen from renewable or low-carbon sources.
- need for further technological advancements in order to improve fuel cell stack's durability and capacity of on-board hydrogen storages.

Economic

- High cost of H_2 production and its distribution. Hydrogen supply chain is then less economically viable than those of the traditional energy sources.
- High cost of fuel cell systems, hydrogen storage devices and refuelling stations.

Addressing these barriers is therefore fundamental to enhance the technical feasibility and economic attractiveness of hydrogen fuel cell trains, eventually accelerating their market penetration.

In this regard, waste heat recovery and effective thermal management strategies have been identified among the potential solutions to enhance the competitiveness of fuel cell vehicles. Although of low quality (~75°C), the large amount of heat generated by PEMFC fuel cells implemented on board may represent in fact a remarkable opportunity not just for the improvement of fuel cell trains efficiency and durability but also for all those stationary energy systems nearby railway lines in which this heat could be integrated.

In the context of hydrogen hybrid trains operating in the Birmingham area, capturing and using waste heat from fuel cells can offer substantial benefits. By integrating Phase Change Material (PCM)-based Thermal Energy Storage (TES) systems into the train layout, it is possible to store the waste heat generated during the train's journey. This stored heat can then be discharged when needed, supplying heat to local heating networks like the Broad Street one.

The motivation for this research lies then in demonstrating the feasibility and benefits of such an integrated thermal management approach. By optimizing the design of TES modules, assessing the amount of heat that can be stored and utilized, evaluating the potential reduction in CO2 emissions and radiator’s area through heat integration, this

research aims to suggest one possible opportunity to make fuel cell hybrid trains a more viable alternative to diesel ones.

1.2 Objectives of the thesis

This thesis has the following main objectives:

- To assess the full energy pathway efficiency of fuel cell trains within the emerging UK hydrogen economy and compare the values obtained with those characterising diesel trains technology.
- To demonstrate the feasibility of the proposed thermal integration between PCM based-TES and fuel cell hybrid trains by addressing issues like TES sizing and temperature level of the waste heat available from the fuel cell powertrain.
- To evaluate the Birmingham New Street waste heat potential by considering the timetable of the station.
- To quantify how much heat can be stored in the proposed TES systems and then discharged at the station, estimating the average round-trip efficiency.

1.3 Overview of the thesis

The thesis is organised as follows:

- Chapter 2: In the first part of the chapter, a literature review on the Well-to-Wheel approach and its application to hydrogen-fueled vehicles is presented. This is followed by a review on the importance of waste heat recovery and thermal storage integration to broaden fuel cell vehicles deployment.
- Chapter 3: a Well-to-Wheel analysis for the specific case of a fuel cell train running in the Birmingham area is conducted. Data from government reports and technical

documents of the main project currently shaping UK hydrogen strategy are used. WTW analysis is divided in two parts: in the WTT stage, hydrogen production, storage, transportation and dispensing steps are studied in order to evaluate the associated primary energy efficiency and energy consumption. In the second part, the WTT outcomes are combined with the fuel economy and powertrain efficiency of a prototype fuel cell hybrid train to obtain proper WTW indexes. Finally, a comparison based on the calculated WTW parameters between fuel cell train and diesel train is provided.

- Chapter 4: a waste heat recovery strategy based on thermal integration between fuel cell powertrain and PCM based TES is then proposed. As thermal storage modules are supposed to be installed on the train roof, issues such as TES sizing and positioning are addressed. Heat removed from fuel cell stacks is stored during train journey and discharged when train stops at BNS. By considering the current timetables of Birmingham New Street station and assuming to convert all its diesel trains into fuel cell hybrid vehicles, the waste heat potential of the station is estimated. A CFD model of the proposed TES system is developed in order to evaluate how much energy can be discharged daily. An optimisation study to maximise the discharged heat is performed. Finally, two examples of how waste heat discharged at the station can be efficiently used are analysed, highlighting the potential beneficial effects.

- Chapter 5: it summarises the main findings of the two core chapters of the thesis (i.e. Chapter 3 and Chapter 4), highlighting also the limits of the analyses conducted and suggesting specific questions or hypotheses for future studies.

2. Chapter two

Literature review on WTW analysis of hydrogen fuelled vehicles

2.1 Components of well-to-wheel analysis and their boundaries

Well-to-wheel analysis is a comprehensive methodology used to assess the energy, environmental and economic impacts of a fuel pathway, from its extraction or production to its utilization in the vehicle [4]. The main metrics used in well-to-wheel analyses are:

- Energy efficiency → kWh/km or kWh/passenger-km.
- Greenhouse gas emissions → grams of CO2 equivalent per km or passenger-km.
- Resource use → water consumption, land use, material inputs.
- Cost

By considering these metrics, policymakers and stakeholders can make informed decisions on transportation planning, infrastructure investment and regulatory frameworks.

The following literature review deals with the well-to-wheel analysis of hydrogen fuelled vehicles, focusing on the energy aspects associated with the entire life cycle of hydrogen production, distribution, storage and utilization in the railway sector.

The components of well-to-wheel analysis can be broadly categorized into two main stages:

Well-to-Tank (WTT) Analysis:

- Hydrogen production: this component evaluates the energy sources and pathways used to produce hydrogen for the fuel cells powering the trains. It considers different

production methods, such as steam methane reforming, electrolysis or renewable hydrogen production and assesses the energy efficiency of each pathway.

- Hydrogen storage: this step involves the estimation of both the energy required to store the hydrogen and energy losses occurred during storage and retrieval. Several storage methods are being researched and developed, such as compressed gas storage, liquid hydrogen storage, metal and chemical hydride storage, underground storage.
- Hydrogen transmission and distribution: the energy consumption related to the transportation and delivery of hydrogen from the production or storage facilities to the refuelling stations is here analysed. Hydrogen can be transported in gaseous form (by pipelines or high-pressure cylinders) or as cryogenic liquid in insulated tanker trucks or ships.
- Hydrogen dispensing: it focuses on the efficiency and energy requirements associated with hydrogen delivery from refuelling station's storage to the vehicle's fuel tank.

Tank-to-Wheel (TTW) Analysis:

- Vehicle operations: WTT analysis deals with the assessment of the drive system's overall efficiency, which can be also expressed in terms of energy required per km travelled per person. Below, fuel energy demands for the main passenger road transport modes are gathered in Table 1, where 100pkm stands for 100 passengers per kilometres. Data is retrieved from [5] and [6], considering an occupancy rate of 95%.

Mode	Fuel energy [kWh/100pkm]
Conventional car	13.9
Electric car	4.4
Conventional bus	6.6
Electric bus	2.2
Conventional train	8
Electric train	3.7

Table 1 – Fuel energy demand for the main passenger transport modes

2.2 WTT and TTW energy indexes

Most of the WTW studies, regardless of the fuel pathway and vehicle analysed, present their results in terms of primary energy consumption per km travelled or overall pathway's primary energy efficiency.

This WTW index can be broken down into WTT and TTW indexes:

WTT indexes

- $E_{WTT_s}\left[\frac{kWh_p}{kWh_f}\right]$: it is calculated by dividing the primary energy spent during the overall fuel pathway, from extraction/production to delivery to refuelling station, by the energy content of the fuel.
- $E_{WTT_t}\left[\frac{kWh_p}{kWh_f}\right]$: in contrast to E_{WTT_s}, it adds the fuel energy value to the WWT pathway energy consumption. In symbols,

$$E_{WTT_t} = E_{WTT_s} + 1 \quad (1)$$

- η_{TTW}: it is obtained by multiplying together the efficiencies of all the WTT steps

TTW indexes

- $FE_{vehicle}\left[\frac{L}{km}\right]$: it is expressed as litres of fuel consumed per km travelled
- η_{TTW}: it reflects the overall energy efficiency of the vehicle powertrain

2.3 Hydrogen Production Pathways

Hydrogen production pathways can be broadly classified into three main categories based on the primary energy source used and the method employed: fossil fuel-based pathways, renewable energy-based pathways and emerging pathways, such as solar thermochemical hydrogen production and LPG pyrolysis [7].

In 2021, more than 95% of the world hydrogen production was derived from fossil fuels: 47% from natural gas, 27% from coal and 22% from oil (as a by-product). The remaining 4% came from electrolysis[4].

2.3.1 Steam methane reforming

Steam methane reforming (SMR) is currently the most widely used method for hydrogen production [8]. The first step in SMR is the preparation of the feedstock. Natural gas, primarily composed of methane, is typically used. It is essential to ensure that the natural gas is free from impurities such as sulphur compounds, which can deactivate the catalyst.

The reforming reaction takes place in a reformer vessel. The natural gas is mixed with superheated steam and fed into the reformer. The steam and methane undergo a catalytic reaction in the presence of a suitable catalyst, often based on nickel, to produce hydrogen and carbon monoxide according to the following reaction:

$$CH_4 + H_2O \rightarrow CO + 3H_2 \quad (2)$$

[4] https://www.irena.org/Energy-Transition/Technology/Hydrogen#:~:text=As%20at%20the%20end%20of,around%204%25%20comes%20from%20electrolysis.

The reaction is endothermic, requiring high temperatures typically ranging from 700 to 900 degrees Celsius, and takes place at 25-35 atm [9].

The reformate gas leaving the reformer consists of hydrogen, carbon monoxide, steam, and small amounts of unreacted methane. To increase the hydrogen concentration and reduce the carbon monoxide content, the gas is passed through a shift conversion process. The most common method is the water-gas shift reaction, which converts carbon monoxide and steam into carbon dioxide and more hydrogen:

$$CO + H_2O \rightarrow CO_2 + H_2 \quad (3)$$

Finally, hydrogen is purified to obtain purities higher than 99.99% through various purification processes, such as pressure swing adsorption (PSA), membrane separation, or amine scrubbing [10]. As Eq. (3) shows, SMR process emits CO_2. Up to 12 tons of carbon dioxide can in fact be produced per ton of hydrogen obtained [11]. In order to mitigate the environmental impact of SMR, CCS technology is implemented. It captures the CO_2 from the flue gas or the syngas before it is released into the atmosphere. However, it requires additional energy for capturing, compressing, and transporting carbon dioxide. This additional energy demand can reduce the net energy available for hydrogen production, thereby impacting the efficiency of the overall SMR process. For instance, Longden et al. [12] calculate a drop of 4-9% of the overall efficiency for a 56-90% capture rate.

The reported energy efficiencies for SMR can vary depending on the specific conditions, catalysts and system configurations used in the studies. However, a range of 70-85% LHV efficiency is commonly cited in the literature. The table below summarises some of the studies reviewed, the claimed SMR process efficiencies and the energy penalties due to CCS.

Reference	Efficiency (%)	CCS	Energy drop (%)	Capture rate (%)
J. J. Hwang [9]	70.5	no	-	-
E. M. Washing and S. S. Pulugurtha [13]	71.4	no	-	-
Q. Wang et al. [14]	72	no	-	-
A. Martinez-Rodriguez and A. Abanades [15]	72	no	-	-
M. Younas et al. [16]	74 - 85	no	-	-
IEA[5]	76 (w/o CCS)	yes	7	95
T. Longden et al. [12]	78 (w/o CCS)	yes	4-9	56-90
S. Campanari et al. [17]	80	no	-	-

Table 2 – Reviewed literature on SMR efficiency

2.3.2 Coal gasification

Coal gasification is the second most used technology to produce hydrogen from fossil fuels. It converts coal into a synthetic gas mixture known as syngas, which contains mainly hydrogen, carbon monoxide and carbon dioxide.

Before the gasification process, coal undergoes preparation, which typically consists in crushing and sizing to achieve a suitable particle size for efficient gasification. Some impurities, such as sulphur and ash, may also be removed.

Coal gasification involves reacting coal with a controlled amount of oxygen or air at high temperatures in the presence of steam. The primary reactions that occur during coal gasification are:

$$C + H_2O \rightarrow CO + H_2 \quad (4)$$

[5] https://www.iea.org/data-and-statistics/charts/global-average-levelised-cost-of-hydrogen-production-by-energy-source-and-technology-2019-and-2050

$$C + CO_2 \rightarrow 2CO \quad (5)$$

The raw syngas produced goes through a series of cleanup processes, including filtration, desulfurization, and removal of impurities.

To further increase the hydrogen content and reduce the carbon monoxide levels, syngas is subjected to a shift conversion process, typically the water-gas shift reaction (Eq. (6)):

$$CO + H_2O \rightarrow CO_2 + H_2 \quad (6)$$

Through various separation methods (i.e. PSA or membrane separation), hydrogen is finally separated from syngas and purified. Despite being a proven and mature technology, coal gasification has the major drawback to be a huge source of carbon dioxide. CO_2 emissions ranging from 19.4 to 25.3 kg CO_2eq/kg H_2 have been reported by Burmistrz et al. [18]. As seen for SMR, CCS integration can significantly reduce the associated carbon emissions. The efficiency of coal gasification for hydrogen production can vary depending on several factors, including the specific gasification technology, the type and quality of coal used, the system configuration, and the inclusion of CCS technologies. Table 3 contains the main reviewed works on coal gasification, highlighting the process efficiency and the resulting energy drop if CCS is applied.

Reference	Efficiency (%)	CCS	Energy drop (%)	Capture rate (%)
A. Midilli et al. [19]	57	no	-	-
IEA[6]	60 (w/o CCS)	yes	2	90
C.-C. Cormos et al. [20]	60 (w/o CCS)	yes	1.8	93-97
N. V. Gnanapragasam et al. [21]	62	no	-	-

Table 3 – Main reviewed literature on coal gasification efficiency

[6] https://www.iea.org/data-and-statistics/charts/global-average-levelised-cost-of-hydrogen-production-by-energy-source-and-technology-2019-and-2050

2.3.3 Water electrolysis

Electrolysis of water is a well-established technique for hydrogen production. It involves passing an electric current through water, usually using an electrolyser, to split its molecules into hydrogen and oxygen. Electrolysis is a key technology in the production of green hydrogen as it enables the utilization of renewable energy sources to generate the necessary electrical energy.

The significant electrolyser types are proton exchange membrane (PEM) electrolyser, solid oxide (SO) electrolyser and alkaline (ALK) electrolyser [22]. While PEM and ALK electrolysers operate at relatively low temperatures (50-80°C), solid oxide electrolysers need high temperatures (between 650 and 1000°C) to work properly [23].

Alkaline electrolysis is the most mature and widely adopted technology among the three mentioned [24]. ALK electrolysers typically employ 30% wt KOH or 25% wt NaOH solutions as electrolyte. The two electrodes, immersed in the alkaline solution and separated by an asbestos/ZrO_2-based diaphragm, are usually made of nickel coated stainless steel. Alkaline electrolysis is characterised by relatively low manufacturing costs and high hydrogen throughput per hour (up to 1000 m^3/h), which makes it suitable for industrial applications [25]. The main disadvantages of these devices are the slow start-up, limited current densities and crossover of the gases [26].

In the 1960s, General Electric developed PEM electrolysers as a solution to address certain operational limitations encountered with alkaline electrolysers [23]. PEM electrolysis adopts a solid polymer membrane as electrolyte. The most commonly used membrane material is based on perfluorosulfonic acid [27], which allows for proton transport during the electrolysis process. Compared to ALK electrolysis, PEM electrolysers present faster response, higher

current densities, smaller footprint, better efficiencies and higher purities of the produced gases [28]. However, as they need noble metal catalysts and protective coatings for the electrodes, their production cost is significantly higher than that of ALK devices [29]. Besides, their operational lifetime is shorter.

Among the three technologies considered, solid oxide electrolysis is the newest and then the least developed one. However, thanks to the great advancements made over the last 15 years, the technology has transitioned from the research and development (R&D) stage to the demonstration and scale-up phase and now is near to commercialization [30]. In a typical solid oxide electrolysis cell (SOEC), the two electrodes are separated by a dense ceramic electrolyte capable of conducting oxide ions. The state-of-art materials are perovskites for the anode, ceramic metal composed of yttria-stabilized zirconia (YSZ) and nickel for the cathode and YSZ for the electrolyte [31]. The high operating temperatures, required to achieve a proper ionic conductivity, are responsible for the following advantages of SOECs over the other two electrolyser types: faster reaction kinetics and improved thermodynamics resulting in higher efficiencies and possibility of using cheap metals as catalysts; part of the energy for water decomposition can be provided through thermal energy, enabling the utilisation of waste heat [32]. At the same time, the high working temperatures lead to high degradation rates, so drastically reducing stack lifetime. Stability and durability are then the main challenges of solid oxide electrolysis [33].

Finally, costs and main technical characteristics of the three described water electrolysis technologies are gathered in Table 4 and Table 5, where the electrical efficiency $\eta_{el,system}$ is calculated as follows:

$$\eta_{el,system} = \frac{\dot{m}_{H_2} \cdot LHV_{H_2}}{P_{el_{stack+BoP}}} \quad (7)$$

where:

- $\dot{m}_{H_2}$: hydrogen mass flow rate produced [kg/s]
- LHV_{H_2}: hydrogen lower heat value [kWh/kg]
- $P_{el_{stack+BoP}}$: electric power in input for electrolyser and its BoP

Data are taken from [23], [34], [35] and [36].

Year	ALK	PEM	SO
2020	242-388 €/kW	384-1071 €/kW	700-1850 €/kW
2030	52-79 €/kW	63-243 €/kW	< 1000 €/kW

Table 4 - Present and future cost of ALK, PEM and SO electrolyser stacks

	ALK	PEM	SO
Operating temperature	65 – 85°C	40 – 80°C	700 – 900°C
Nominal current density	0.2 – 0.8 A/cm^2	1 – 2 A/cm^2	0.2 – 2 A/cm^2
Cell pressure	1 – 30 bar	30 – 80 bar	1 bar
Stack lifetime	60000 – 90000 h	30000 – 90000 h	10000 – 30000 h
H_2 purity	99.9%-99.9998%	99.9%-99.9999%	99.9%
Load range	10 – 105%	5 – 140%	25 – 110%
Electrical efficiency (LHV based)	50 – 78%	50 – 83%	74 – 81 %

Table 5 – State-of-the-art of ALK, PEM and SO electrolysers

2.4 Hydrogen storage

To unlock the full potential of hydrogen as energy carrier, it is crucial to develop efficient, reliable and cost-effective storage solutions.

One of the main benefit of hydrogen storage is its ability to provide a viable solution to address the intermittency of renewable energy sources[7] (RES). Surplus electricity from RES can indeed be converted into hydrogen via water electrolysis and stored for later use, allowing for a better integration of renewables into the energy system.

However, the variability and intermittent nature of RES pose challenges for electrolysers, as they struggle to adjust to sudden load changes and perform better at full or high loads [37]. Fluctuating power inputs into electrolysers alter not only voltage but also temperature, pressure and hydrogen purity, necessitating durability assurance for the entire system. The advancement of hydrogen production technologies optimised for intermittent renewable energy sources is then extremely important. Currently, alkaline water electrolysis faces significant catalyst degradation during start and stop operations due to reverse current. Proton exchange membrane water electrolysis, on the other hand, can operate under low power loads with fluctuating power but relies on costly precious metal catalysts. Solid oxide electrolysis cells (SOECs) exhibit resilience against power fluctuations at smaller scales but have to work below the thermo-neutral point [38].

Hydrogen storage can also play a vital role in balancing energy supply and demand in the electrical grid. By smoothing out fluctuations in electricity generation, it can contribute to grid stability in high renewable penetration scenarios, preventing the wastage of renewable energy resources [39].

The development of an efficient and cost-effective H_2 storage technology is an important driver for the deployment of hydrogen powered vehicles too. For instance, report 3 of the

[7] https://www.fchea.org/hydrogen-as-storage#:~:text=Hydrogen%20allows%20vast%20quantities%20of,electricity%20during%20peak%20production%20hours.

‘*Study on the use of fuel cells & hydrogen in the railway environment*’ [40] identifies the current on-board hydrogen storage technology as one of the main barrier preventing fuel cell trains from being deployed.

Finally, as end-users can be hundreds or thousands kilometres away from the H_2 production plants, storage is crucial in enabling the transportation of hydrogen in various forms, guaranteeing a reliable supply.

2.4.1 Hydrogen storage methods

Hydrogen storage can be classified into two main groups: physical-based and material-based [41]. The physical-based group comprises:

- compressed gas
- liquid hydrogen
- cold/cryo-compressed gas

On the other hand, material-based storage is divided into two sub-groups:

- chemical sorption/chemisorption
- physical sorption/physisorption

As the commercial implementation of material-based storage techniques is unlikely to occur in the near future [42], this review will focus only on the physical-based storage methods.

Compressed gas hydrogen storage (CGH_2)

Compressed gas hydrogen storage is the most established and widely used method for storing hydrogen in various applications, including fuel cell vehicles, industrial processes, and stationary power generation [43].

CGH_2 storage involves compressing gaseous hydrogen to high pressures and storing it in high-pressure tanks designed to handle the gas safely. Going from atmospheric to 700 bar (i.e. common operating pressure of hydrogen storage in fuel cell vehicles) reduces hydrogen gas volume by a factor of around 456 and then the volumetric energy density increases from $2.96 \cdot 10^{-3}$ kWh/L to 1.35 kWh/L. However, hydrogen compression is an energy-consuming process, requiring about 13-14% of the gas energy content to bring pressure from 1 to 700 bar.

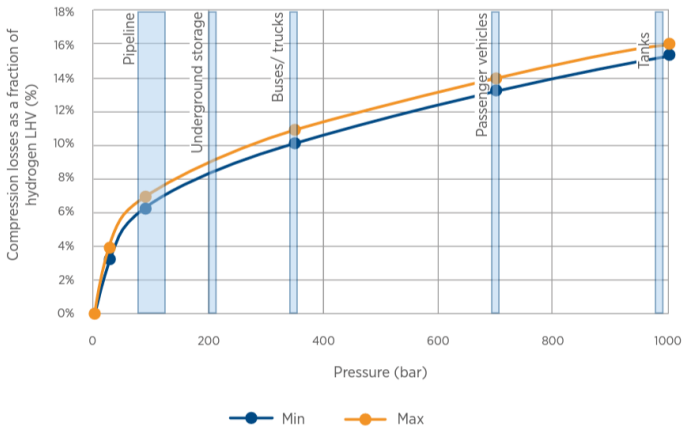

Figure 2 – Energy requirement for hydrogen compression [34]

There are four types of compressed gas storage containers, each designed to meet specific requirements and applications.

- Type I: they are made of steel or aluminium and typically used for low-pressure storage of hydrogen (up to 300 bar). They are the cheapest option but are relatively heavy and their gravimetric capacity does not exceed 1 wt% [44]
- Type II: Type II vessels are composite-wrapped pressure vessels made of a metal liner (usually aluminium) overwrapped with high-strength carbon fibers. Compared to Type I, they can withstand higher pressures, offer improved weight savings and can

achieve increased volumetric efficiency. They are one and half times more expensive than Type I [45]

- Type III: these are similar to Type II but have a thinner metal liner and more extensive carbon fiber overwrapping. They have been successfully used at 450 bar working pressures and provide a 25%–75% mass gain over Types I and II vessels [46]. At 350 bar Type III can attain gravimetric capacities close to 3.9 wt% but their cost is three times the one of Type I
- Type IV: Type IV vessels are fully composite pressure containers constructed entirely from high-strength carbon fibers and epoxy resin. According to Argonne National Laboratory data[8], Type IV has reached gravimetric densities of 4.2 wt% at 700 bar. These vessels can work even at 1000 bar [47] and currently represent the lightest option

For significant quantities of hydrogen or extended storage durations, the most cost-effective option is to store compressed hydrogen in sizable underground reservoirs located in suitable geological formations [48]. Underground storage sites can be classified into two main categories: conventional sites, which include salt caverns, aquifers, and depleted hydrocarbon reservoirs, and nonconventional sites, such as abandoned coal mines and lined hard rock caverns [49].

Liquid hydrogen storage (LH_2)

Liquid hydrogen storage is a method of storing hydrogen in its liquid state, achieved by cooling hydrogen gas to extremely low temperatures (i.e. 20 K) at which it undergoes the liquefaction process. This cryogenic storage approach allows for a significant increase in

[8] https://www.energy.gov/eere/fuelcells/physical-hydrogen-storage

energy density compared to storing hydrogen as a gas. At 20 K liquid hydrogen has in fact a density of 71 kg/m^3, equivalent to a volumetric energy density of about 2.4 kWh/L. Moreover, in its liquid form, hydrogen is non-corrosive [50], allowing for the use of stainless steel and aluminium alloy vessels with proper insulation layers. However, hydrogen liquefaction is a very energy-intensive process: producing 1 kg of liquid H_2 consumes up to 10 kWh of electricity, equivalent to 30% of the hydrogen energy content [51]. Besides, despite the best efforts to insulate and maintain extreme low temperatures in cryogenic storage tanks, some heat inevitably enters the system, causing a portion of the liquid hydrogen to evaporate. As tanks are not designed for high pressures, hydrogen gas has to be vented for safety reasons. This kind of losses, known as boil-off, ranges between 0.18 and 0.4% per day [52][53], significantly reducing the overall efficiency of liquid hydrogen storage.

Cryo-compressed hydrogen storage (CcH_2)

Cryo-compressed hydrogen storage is a promising method of storing hydrogen that combines elements of both cryogenic and compressed gas storage techniques. It aims to address the limitations of traditional gaseous and liquid hydrogen storage methods by offering a balance between energy density, safety, and efficiency.

CcH_2 concept consists of compressing hydrogen gas up to 250-350 bar [54], cooling it down until its temperature is close to the liquefaction one and finally storing it in proper insulated pressure vessels. At the end of the process, cryo-compressed hydrogen can achieve higher densities than LH_2 (i.e. 80 kg/m^3 vs. 71 kg/m^3) [55]. Furthermore, since no liquefaction occurs and cryo-compressed tanks can withstand higher pressures than cryogenic vessels before venting out, reduced energy consumption and boil-off losses are obtained [51][56].

2.5 Hydrogen transmission and distribution

Depending on the storage technique employed, two primary transportation pathways for hydrogen emerge:

- compressed gas hydrogen delivery
- liquid hydrogen delivery

In addition to the quantity to be transported, the appropriate delivery method is determined by many other factors such as distance and market characteristics, encompassing elements like target population, population density, refuelling station size [57].

2.5.1 Tube trailers

For distances not exceeding 300 km and for small quantities, hydrogen transportation via tube trailers is usually the most suitable option [23][58].

At loading bays, pressure vessels are first loaded with compressed hydrogen gas and then stacked on the trailer for trucking. Based on the vessel type adopted, the filling pressure ranges between 180 and 500 bar [59]. Type I cylinders are currently the most employed vessels for tube trailers[9]. In order to comply with weight restrictions (i.e. gross vehicle weight < 44 tons), a compressed hydrogen truck using type I tubes can carry no more than 270 kg of hydrogen at a pressure of 200 bar [60]. By replacing steel vessels with lighter options (i.e. Type III or Type IV), tube trailer's payload can increase up to 1000 kg of H_2 at 500 bar [61], as the weight is no longer the main limiting factor. However, many national road regulations still limit to 200 bar the maximum allowed pressure [62].

[9] https://www.energy.gov/eere/fuelcells/hydrogen-tube-trailers

An efficiency of 94% per 100 km for hydrogen transportation via tube trailers is reported in literature [63], where the 6% of energy lost includes hydrogen fugitive emissions and fuel for tube trailers.

2.5.2 Pipelines

Transport via pipeline networks is considered the best way to achieve a massive and continuous supply of hydrogen [59][62]. It is estimated that around 4500 km of hydrogen pipelines are currently in operation throughout the world, most of them serving big chemical and refinery plants. They have diameters between 25 and 30 cm, while their operating pressure is 10÷20 bar [64]. The main advantages linked to hydrogen transmission through pipelines are:

- best option in terms of cost per unit of delivered hydrogen for large-scale production scenarios [65]
- low operational costs and pipelines' lifetimes up to 80 years [23]
- as opposed to tube trailers, it does not cause road congestion

Some of the technological challenges that are slowing down the expansion of the hydrogen pipeline infrastructure are instead:

- high capital costs, even higher than those for natural gas networks construction, due to the need of bigger diameters and more powerful compressors to counterbalance lower mass density and volumetric energy density of hydrogen [66]
- embrittlement of the steel and welds of pipelines[10]

[10] https://www.energy.gov/eere/fuelcells/hydrogen-pipelines

- relatively high leakages from valves and seals due to the low molecular weight of hydrogen [67]

A potential solution to minimise infrastructure's capital costs consists in blending hydrogen into the existing natural gas network. If the blending ratio is less than 20%, modest modifications are needed [68].

Efficiencies higher than 99% can be attained if hydrogen is transported through pipelines [69].

2.5.3 Liquid hydrogen delivery

Despite the high energy consumption of liquefaction, trucking liquid hydrogen is cheaper than tube trailer option for amounts of hydrogen greater than 500 kg per day [70]. A liquid cryogenic trailer can in fact carry up to 4500 kg of LH_2[11], 16 times the payload of a tube trailer employing Type I cylinders and 4.5 times if Type III or IV vessels are instead used. However, liquid hydrogen delivery pathway suffers from boil-off losses, which can be significant. According to [68], up to 10% of the payload can be lost during the discharging of the trailer. Moreover, LH_2 delivery is viable only if the end-user owns a liquid storage.

2.6 Hydrogen dispensing

Hydrogen dispensing takes place at Hydrogen Refuelling Stations (HRSs), facilities designed to provide hydrogen to all the types of hydrogen-powered vehicles. HRS plays a crucial role in the hydrogen infrastructure, enabling the distribution and usage of hydrogen as a clean energy carrier for transportation purposes.

[11] https://www.cryolor.com/cryogenic-transport/liquid-hydrogen-transport

Based on hydrogen production location, hydrogen refuelling stations can be divided into on-site and off-site. While the latter receive hydrogen from an external production facility, either through pipelines or by trucks, the former have integrated hydrogen production capabilities. On-site HRSs offer greater independence and control over the hydrogen supply, flexibility in location and can easily integrate renewable energy sources for hydrogen production [71][72]. However, establishing on-site hydrogen production requires a higher initial investment compared to off-site stations (up to 1.5 times higher if water electrolysis is used for production [73]). On the other hand, off-site HRSs benefit from lower initial costs and leverage existing hydrogen infrastructure, but their carbon footprint depends on the source of the hydrogen supply.

It is possible to classify HRSs also according to the physical state in which hydrogen is delivered to the station. In the following lines, the different components and layouts characterising CGH_2 and LH_2 refuelling stations are briefly discussed.

2.6.1 CGH_2 refuelling station

The following four main modules can be usually found in the vast majority of CGH_2 refuelling stations: production or external supply, compression, storage and dispensing [74].

Depending on the adopted refuelling strategy, two different HRS layouts are possible:

- HRS with cascade refuelling process: the refuelling process is driven by the pressure gradient between the HRS's storage system and the vehicle's tank. No compressor is required.
- HRS using booster compressors: as hydrogen is stored at pressures lower than the vehicle's tank one, compressors are needed.

HRS with cascade refuelling

Once produced on-site or supplied to the station via pipelines or tube trailers, hydrogen is stored inside a bulk storage working at pressure typically ranging between 50 and 200 bar [75]. The station also includes a high-pressure storage, which is usually divided into multiple storage banks operating at different pressures. For the overflow filling to take place, the pressure level in the higher pressure bank of the storage has to be above that in the vehicle tank. Therefore, hydrogen is compressed to 900 [76] bar or 500 bar [77] depending on whether the station is designed for cars or heavy-duty vehicles, respectively. As the filling of the on-board tank involves the utilisation of sequentially higher-pressure hydrogen storage banks, this practice is called cascade refuelling.

Before entering the dispenser, hydrogen undergoes the last conditioning. To make sure that the operational limits set by the J2601-SAE 2016[12] (i.e. maximum H_2 temperature inside the vehicle tank < 85°C) are not violated for the entire duration of the refuelling, hydrogen has to be cooled down to -40°C. In fact, during the refuelling process, four main mechanisms causing the increase of hydrogen temperature within vehicle's tank occur: conversion of the incoming hydrogen flow's kinetic energy into internal energy, gas compression inside the tank, the heat flux from the surroundings and the negative Joule-Thomson effect due to the pressure drop across the fuel line. A pre-cooling unit is then installed in the HRS fuel line before the dispenser [78].

Mayer et al. [79] estimated, for different utilisation rates and ambient temperatures, the energy consumption of a station with trucked-in gaseous hydrogen and a 200 bar bulk storage. A value of 1.43 kWh of electricity per kg of hydrogen dispensed has been obtained

[12] https://www.sae.org/standards/content/j2601_201612/

for a large station having 100% utilisation rate and operating at -10°C of ambient temperature.

HRS using booster compressors

In this HRS concept, hydrogen from the supply source is compressed and stored in a medium-pressure storage system kept at pressures below the one in the vehicle. Booster compressors are then used to transfer hydrogen from the HRS storage to the vehicle's tank. They do not run continuously but only on-demand. A pre-cooling unit (PCU) and a dispenser complete the dispensing line.

2.6.2 LH_2 refuelling station

The core components of a LH2 refuelling station are the cryogenic storage, the high-pressure cryogenic pump, the evaporator, the high-pressure storage system and the dispenser.

Once delivered to the station via cryogenic tankers, liquid hydrogen is stored in highly insulated storage system working at nearly atmospheric pressure. In order to supply high pressure gaseous hydrogen to the vehicles, liquid hydrogen is first converted into a supercritical fluid and then processed by an ambient evaporator to meet the most suitable thermodynamic conditions for refuelling. If the cryogenic pump throughput is sufficiently high, a direct refuelling can be performed. Alternatively, a high-pressure storage system like the one seen in the CGH_2 station is integrated. As the upstream cryogenic hydrogen can be exploited for the precooling, a PCU is not necessary.

Thanks mainly to the cryogenically compression of the hydrogen, a LH_2 station can consume up to 85% less energy than a CGH_2 one [75].

2.7 Well-to-wheel analysis studies

Table 6 summarises the key WTW works reviewed, highlighting the geographical setting, vehicle type, year of publication and main results. These are expressed in terms of primary energy efficiency (%) or primary energy consumption per km travelled (kWh/km).

Reference	H_2 production method	H_2 transport method	Location	Vehicle	Year	Result
Correa et al. [80]	SMR	Pipeline	Argentina	FCEH[13] bus	2017	18%
Torchio and Santarelli [81]	On-site SMR	-	Europe	FCEH car	2010	0.44 kWh/km
Wang et al. [14]	SMR	Pipeline	China	FCH[14] light-duty	2020	0.69 kWh/km
Lu et al. [82]	SMR	Pipeline Tube trailers	China	Generic FCH[15] Vehicle	2022	26.4% 22.4%
Lombardi et al. [83]	SMR Electrolysis	Pipeline	Europe	44 ton-FC trucks	2020	6.0 kWh/km 6.7 kWh/km
Sheng et al. [84]	SMR	Not specified	Oceania	FCEH car	2021	0.7 kWh/km
Washing and Pulugurtha [13]	Distributed SMR	-	USA	FC train	2015	16.6-19.6%
Hoffrichter et al. [85]	SMR Electrolysis	Not specified	USA, UK	FC train	2012	25% 10%
Yazdanie et al. [86]	SMR Electrolysis	Not specified	Switzerland	Generic FC Vehicle	2016	0.63 kWh/km 1.5 kWh/km
Li et al. [87]	SMR	Pipeline	China	FCE Vehicle	2016	0.53 kWh/km

Table 6 – Key WTW studies reviewed

The literature review has highlighted the site-specific nature of WTW analysis and how it is deeply affected by the H_2 production and transport paths. In fact, each region is characterised by different infrastructure, with different degrees of development and then

[13] Fuel Cell Electric Hybrid
[14] Fuel Cell Hydrogen
[15] Fuel Cell Hybrid

different energy performance. The values of the WTW indexes must be then considered valid only for the geographical area in which the study is conducted.

Given the intention of the UK government to remove all diesel trains from the network by the end of 2040, the author of this thesis believes that a comprehensive energy analysis of fuel cell trains as a potential alternative could be beneficial for policymakers to develop effective strategies.

Therefore, a WTW approach is implemented to assess the full energy pathway efficiency of fuel cell trains within the emerging UK hydrogen economy.

Literature review on integration between TES and FECVs for waste heat recovery

In the second part of this literature review the importance of thermal energy storage and waste heat recovery in increasing fuel cell vehicles energy performance and their economic attractiveness is highlighted.

2.8 Fuel cell hybrid trains

In 2020, Network Rail published the *Traction Decarbonisation Network Strategy*[16], in which the strategic rationale for rail traction decarbonisation and the related work programme are presented. As Network Rail findings suggest, taking 2018 as baseline year, a 77.5% reduction in rail traction emissions must be achieved by 2050 to meet the net-zero UK legislative targets. A year later, in its *Transport decarbonisation plan*[17], the Department for

[16] https://www.networkrail.co.uk/wp-content/uploads/2020/09/Traction-Decarbonisation-Network-Strategy-Interim-Programme-Business-Case.pdf

[17] https://assets.publishing.service.gov.uk/government/uploads/system/uploads/attachment_data/file/1009448/decarbonising-transport-a-better-greener-britain.pdf

Transport (DfT) set the carbon reduction target for the Rail sector even higher, claiming its ambition to remove all the diesel trains from the network by 2040.

Both the above-mentioned documents have identified electrification as the main way to decarbonise rail sector. According to the *Office of Rail and Road annual statistical release*[18] for 2021-2022, while a diesel passenger train emits 1400 g of CO_2e per vehicle kilometre, an electric one releases just 358 gCO_2e/km. However, catenary electrification cannot be a commercially feasible solution for the whole network, especially for those lines characterised by low utilisation rates. In fact, as up to one million pounds may be needed to electrify each km of rail track [88], an high throughput of trains is essential to minimise the payback period and justify the investment. Therefore, alongside electrification, hydrogen propulsion has been considered by both Government and Network Rail as a valid option for the decarbonisation of the unelectrified tracks.

Fuel cell technology to exploit hydrogen energy and provide traction power has been tested successfully in rail transportation since 2001 [89]. In order to extend system lifetime and maximise the efficiency, abrupt changes in fuel cells' load profile should be avoided. The narrowing of the fuel cell operating power range is usually obtained by employing a hybrid powertrain [90]. It combines fuel cells as primary energy source of train traction system and auxiliaries with batteries. Their role is to compensate fuel cells' slow dynamic response during sudden accelerations and to store as much as possible of the vehicle's braking energy [91].

In 2018, Alstom Coradia iLint made its debut in Germany as the world's first commercial fuel cell hybrid passenger train. This two-cars train, built on the platform of Coradia Lint, is

[18] https://dataportal.orr.gov.uk/media/2112/rail-emissions-2021-22.pdf

equipped with two 200 kW Proton Exchange Membrane Fuel Cell (PEMFCs) packs (one for each car), two 111 kWh Li-ion battery units and as many hydrogen tanks, for a total storage capacity of 178 kg of H_2 at 350 bar [92]. While the hydrogen pressurised tanks and the fuel cell systems are mounted on the roof, battery packs are located on the underframe, as Figure 3 shows. Alstom has already sold 59 iLint trains across the Europe[19], which will gradually replace the existing vehicles in operation.

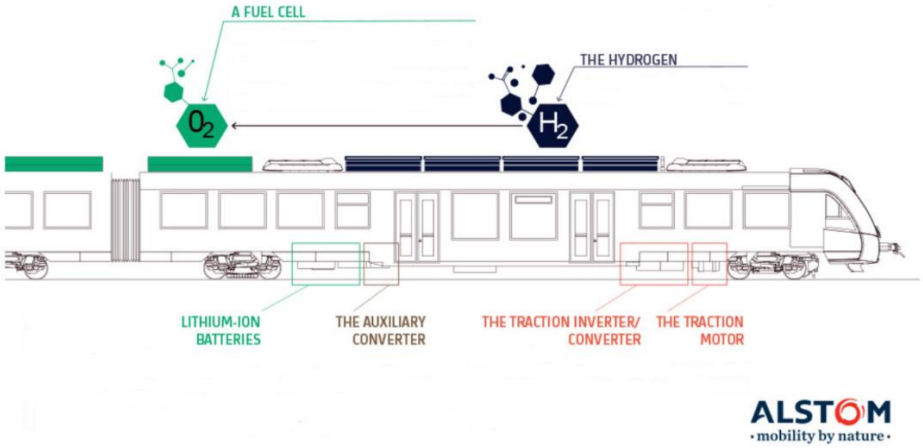

Figure 3 – Coradia iLint

Another important application of hydrogen fuel cell technology in railway is Mireo Plus H from Siemens Mobility. Developed on the Mireo platform, the hydrogen-powered counterpart integrates two 200 kW PEMFC modules with a 350 kWh lithium-ion battery pack. The energy management strategy is the same already seen for iLint, with batteries ready to assist fuel cells during high traction efforts. Siemens claims a maximum range of 600 km for the two-car unit and up to 1000 km for the three-car train[20]. Mireo Plus H will enter passenger service in Germany in 2024[21].

[19] https://www.alstom.com/world-leader-green-traction-solutions
[20] https://www.mobility.siemens.com/global/en/portfolio/rail/stories/mireo-plus-h-for-a-cleaner-emissions-free-operation.html
[21] https://press.siemens.com/global/en/pressrelease/maiden-trip-deutsche-bahn-and-siemens-test-hydrogen-train-and-mobile-hydrogen

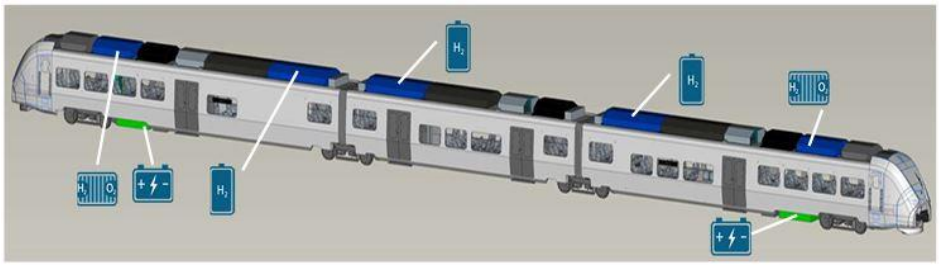

Figure 4 – Mireo Plus H

In 2020, Toyota Motor, Hitachi Ltd and East Japan Railway initialled a partnership with the aim of designing, developing and testing fuel cell hybrid railway vehicles. Based on the design of the EV-E301 series battery electric multiple unit, these innovative two-cars trains (HYBARI is the chosen nickname) are powered by four 60 kW PEMFC modules, which are assisted by two 120 kWh lithium-ion batteries[22]. In contrast to iLint and Mireo Plus H, HYBARI is equipped with hydrogen tanks working at 700 bar. About 1020 litres of gaseous H_2 can be stored on the train's roof, resulting in approximately 40 kg of hydrogen storage capacity. The stated maximum range is 140 km. Moreover, compared to the design adopted by Alstom and Siemens for theirs hybrid vehicles, HYBARI's fuel cell modules are installed on the underframe (see Figure 5). The test started on March 2022 and the first commercial application is expected to be ready by 2024[23].

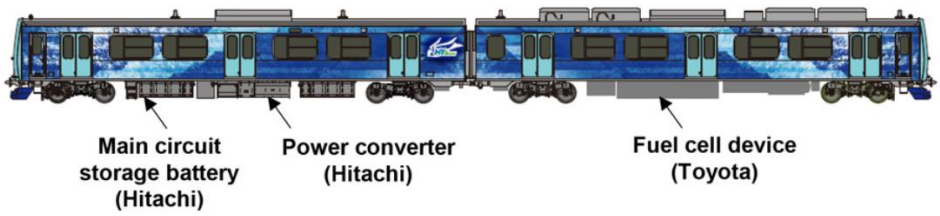

Figure 5 - HYBARI

[22] https://global.toyota/en/newsroom/corporate/33954855.html
[23] https://en.wikipedia.org/wiki/FV-E991_series

A further boost to the market penetration of the fuel cell hybrid trains may come from the possibility to convert the current in-service trains into hydrogen powertrain vehicles, instead of replacing them with newly built units. A successful example of the retrofit approach is represented by the UK's train HydroFLEX [93]. Additional efforts are however needed to improve the economic and technological feasibility of the retrofit option [94]. The EU project FCH2RAIL[24] is working in this direction. In particular, it aims to develop a modular, scalable and multi-purpose fuel cell hybrid powerpack suitable for retrofitting the existing electric and diesel trains [95]. The powerpack comprises fuel cell modules and their coolant system, hydrogen storage vessels, batteries, a HV DC/DC converter and an energy management system.

2.9 Main barriers to FCH trains deployment

Despite their high energy efficiency compared to conventional internal combustion engine vehicles [129], the market penetration of FCH trains is still very limited [96]. In addition to the inadequate deployment of hydrogen infrastructures [97], the other two main barriers to their broader applicability are fuel cells' durability and high capital costs of the vehicles, mainly due to the expensive materials used for fuel cell stack (e.g. platinum) [98].

Waste heat recovery and proper thermal management strategies have been included among those solutions potentially able to help fuel cell vehicles in their path towards competitiveness [99]. Both, in fact, have already proven to improve durability, system efficiency and cost [100].

[24] https://cordis.europa.eu/project/id/101006633

2.10 Basic principles of PEM fuel cell operation

In Figure 6 the schematic of a typical PEM fuel cell and its working principle are depicted.

A Proton Exchange Membrane Fuel Cell (PEMFC) operates by converting hydrogen and oxygen into water, producing electricity and heat in the process. The key components include the anode, cathode, proton exchange membrane (PEM), catalyst layers, gas diffusion layers (GDLs), and bipolar plates.

Hydrogen gas (H_2) is introduced at the anode, where a platinum catalyst splits it into protons (H^+) and electrons (e^-) according to Eq. (8). The protons pass through the PEM to reach the cathode, while the electrons travel through an external circuit, generating electricity.

$$Anode: \quad H_2 \rightarrow 2H^+ + 2e^- \tag{8}$$

At the cathode, the protons, electrons, and oxygen (O_2) from the air combine, forming water (H_2O). This reaction, represented by Eq. (9), is facilitated by another platinum catalyst.

$$Cathode: \quad \frac{1}{2}O_2 + 2H^+ + 2e^- \rightarrow H_2O \tag{9}$$

The bipolar plates distribute the gases evenly, conduct electrons, and provide structural support. They also contain channels for coolant to manage the heat produced during operation. The GDLs ensure even gas distribution and assist in water management.

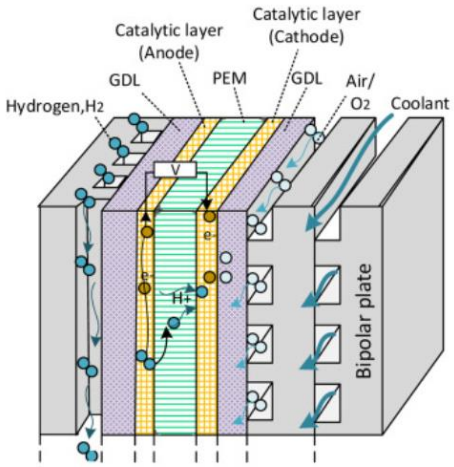

Figure 6 – Schematic of a PEM fuel cell with coolant channels passing through the bipolar plate [101]

2.11 Fuel cell heat generation

In fuel cells, part of the hydrogen energy in input is converted into heat. It is possible to identify three main thermal energy sources: entropic heat, irreversibilities and water condensation [102]. The entropic heat is a direct consequence of the second law of thermodynamic. It states that not all the change in enthalpy associated with the fuel cell's global reaction (i.e. $\Delta H_{reaction}(25°C, 100kPa) = \Delta H_{H_2O} - \Delta H_{H_2} - \frac{1}{2}\Delta H_{O_2} = -285.83\ \frac{kJ}{mol}$) can be converted into electricity, but only the corresponding Gibbs free energy gradient $\Delta G_{reaction}$ ($\Delta G_{reaction}(25°C, 100kPa) = -237.13 \frac{kJ}{mol}$). The quantity $(\Delta G - \Delta H)_{reaction}$ is released as thermal energy and is known as entropic heat. Irreversibilities occur as soon as a load starts to be applied. Typically, they are linked to the activation of the electrochemical reactions, mass transport mechanisms and flow of protons and electrons across the electrolyte and electrodes (e.g. ohmic loss) [103]. Water vapour condensation in the gas channels is another source of heat and is the result of low gas stoichiometry [104]. Figure 7 shows where the cell's main thermal energy sources are located.

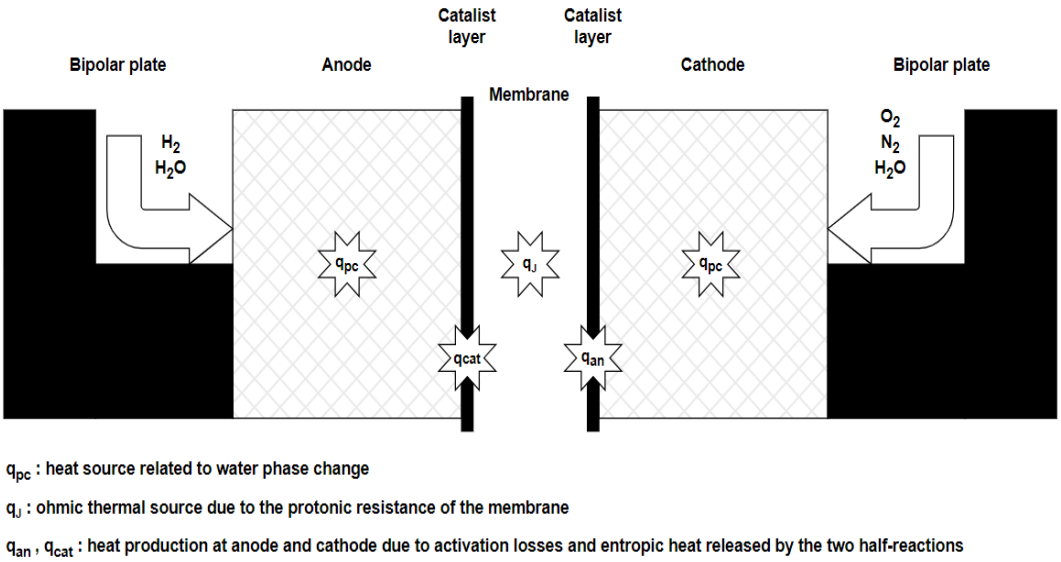

Figure 7 – Heat source distribution

The overall amount of heat produced by a fuel cell module per unit time can be assessed through the following equation [105]:

$$\dot{Q}_{module}(i) = N_{cell} \cdot \dot{W}_{cell}(i) \cdot \left(\frac{V_{cell,max}}{V_{cell}(i)} - 1\right) \quad (10)$$

where $\dot{Q}_{module}$ is expressed in W/cm^2, i is the cell's current density measured in A/cm^2, $\dot{W}_{cell}$ is the electric power generated by the fuel cell module, N_{cell} is the number of cells constituting the module, $V_{cell,max}$ is the ideal voltage for a 100% efficient fuel cell ($\Delta G_{reaction} = \Delta H_{reaction}$) and V_{cell} is the actual cell voltage. The typical trend of V_{cell} at different values of current density is showed below, along with in which part of the curve the three types of irreversibilities occur.

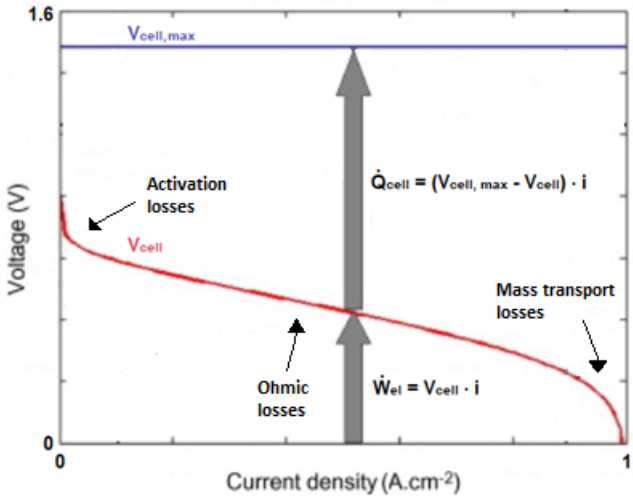

Figure 8 – Example of PEMFC polarisation curve

Based on the concept of fuel cell's electrical efficiency ($\eta_{el,cell}$), another way to assess $\dot{Q}_{module}$ is:

$$\dot{Q}_{module}(i) = \dot{W}_{module}(i) \cdot \left(\frac{1 - \eta_{el,cell}(i)}{\eta_{el,cell}(i)} \right) \tag{11}$$

where $\dot{W}_{module}$ and $\eta_{el,cell}$ can be calculated as:

$$\dot{W}_{module}(i) = \dot{W}_{cell}(i) \cdot N_{cell} \tag{12}$$

$$\eta_{el,cell}(i) = \frac{\dot{W}_{module}(i)}{\dot{W}_{module}(i) + \dot{Q}_{module}(i)} = \frac{V_{cell}(i)}{V_{cell,max}(i)} \tag{13}$$

As Eqs. (10) - (13) indicate, fuel cell electric performance and heat generation rate are strongly linked and vary with the desired current density, which in turn changes to match the time-dependent load power demand. Thus, the estimation of the total amount of heat produced is not straightforward as it requires the knowledge of both fuel cell's duty cycle (i.e. how the power output has to change over time to follow the load profile) and polarisation curve.

2.12 Thermal management

To work efficiently and safely, fuel cells need to operate within a certain range of temperatures. In particular, due to the intrinsic characteristics of the materials used, PEMFC operating temperature must be maintained between 60°C and 80°C. On the one hand, at lower temperatures water product is prone to exist in its liquid state, resulting in flooding of electrodes and sluggish kinetics. On the other hand, temperatures higher than 80°C would lead to severe dehydration of Nafion membrane, causing an unacceptable drop in its proton conductivity and so in cell performance and durability [106]. The removal of Q_{module} by means of a proper designed cooling system is then crucially important.

Table 7 summarises the most common cooling strategies for PEM fuel cells, highlighting their advantages and limitations.

Cooling technique	Description	Advantages	Limitations
Air cooling [107]	Air to dissipate heat from the stack, through fans or enhanced airflow designs	- Simple design - Lightweight - Low cost - Suitable for low power applications (100 W - 2 kW).	- Limited heat transfer capacity - Not suitable for high-power applications
Liquid cooling [108]	Water or other coolants circulated through channels or plates in the fuel cell stack	- High heat transfer efficiency - Suitable for high-power applications (>10 kW) - Precise temperature control.	- Complex design - Higher cost
Phase change cooling [100]	Phase change materials to absorb and release heat as they change state	- High heat absorption capacity - Passive operation - Eliminates need for pumps	- Limited to specific applications - Higher initial cost - Design complexity
Heat pipes [109]	Heat pipes to transfer heat through phase change and capillary action within a sealed pipe	- Efficient heat transfer - No moving parts - Can be integrated into compact designs	- Limited scalability - Potential reliability issues over time

Heat spreaders [108]	Materials with high thermal conductivity to spread heat across a larger surface area	- Simple design - Effective for low to moderate power applications - Low maintenance	- Limited cooling capacity - Not suitable for high-power applications - Potential for uneven heat distribution

Table 7 – Pros and cons of the main cooling strategies for PEMFC

Among the different heat management strategies [110][111], liquid cooling has been successfully applied in high-power PEMFC stacks (>10 kW), especially in automotive applications [112]. Despite significant efforts have been made in recent years to develop novel coolants with improved thermal properties (e.g. the Nusselt number and heat transfer coefficient were enhanced thanks to the use of nanofluids [113][114]), a mixture of deionised water and ethylene glycol is still the most popular option to remove excess heat from fuel cell based powertrains [115]. A typical liquid cooling system (Figure 9), besides the fuel cell stack, comprises a radiator, a coolant reservoir and a variable flow rate pump.

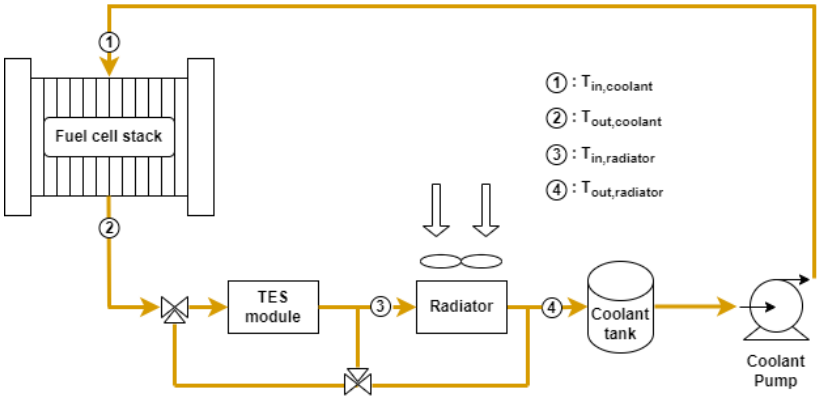

Figure 9 – Example of a PEM liquid cooling system

The chosen coolant, passing through dedicated cooling channels within the stack, absorbs the excess heat produced by the fuel cell module. The heated coolant leaves the fuel cell stack and is directed to a radiator, where heat is rejected into the environment. After releasing the heat, coolant is finally pumped back to the PEMFC module to start a new cycle.

2.13 Waste heat recovery strategies

Generally speaking, the main benefit associated with waste heat recovery from fuel cells is the improvement of the overall utilisation rate of hydrogen energy. The operating temperature of the fuel cell and then of the available waste heat plays a key role as it dictates which exploiting routes are technologically viable and which are not. Several heat recovery solutions have proven to be feasible for PEM fuel cells, ranging from self-servicing applications such as pre-heating of the reactants, to thermal integration into combined heat/cooling and power systems [116]. The coupling of the harvested heat with other conversion technologies or with the BoP of the fuel cell system itself allows to achieve higher energy conversion efficiencies. In fact, from the perspective of the integrated system, the heat recovered from fuel cells can no longer be treated as a mere by-product but rather incorporated into the calculation of their efficiency. Thus, by modifying Eq. (13), it follows that:

$$\eta_{fuel\ cell} = \frac{\dot{W}_{module} + \dot{Q}_{rec}}{\dot{W}_{module} + \dot{Q}_{module}} \tag{14}$$

where $\dot{Q}_{rec}$ is the thermal power captured from the cooling circuit and successfully integrated into another system.

Various waste heat recovery strategies have been successfully implemented also in fuel cell vehicles. Although of low quality (~75°C), the large amount of heat generated by PEMFC fuel cells implemented on board represents a remarkable opportunity for recovery. For instance, instead of being rejected into the environment via radiator, the heat retrieved from the coolant stream can be efficiently used on-board. Waste heat from PEMFC modules for electromobility has been effectively exploited for cabin space-heating [117], to power on-board thermoelectric generators [99] or as energy input to vehicle-integrated

thermochemical storages [118]. All the three above-mentioned heat recovery concepts have been shown to partially relieve fuel cells from the burden of auxiliaries. The resulting improved vehicle efficiency ultimately led to an increase of the driving range.

2.14 Contribution to research of this thesis

Another possible usage of the heat captured from the fuel cells' cooling system consists in storing it within proper on-board thermal energy storage devices (TES) with the aim of supplying it to different off-board thermal applications. If the vehicle under consideration is a fuel cell hybrid train, TES units are charged during the journey and then discharged at the stations, where it can be used in different ways.

The idea developed in this thesis is to store the waste heat produced by fuel cell powertrain into phase change material-based thermal energy storages. Phase change materials (PCMs) have been chosen for their large latent heat that allows them to retain and release between 5 and 100 times more energy than sensible heat devices with the same volume [119]. However, PCMs are also characterised by low thermal conductivity. The resulting poor heat transfer rate achieved during the charge/discharge processes is one of the main issues related to PCM-based TES deployment. In the framework of the present thesis, this may lead to charging and discharging times that do not match with train timetables and schedules. Additional details will be provided in the next sections. As regards the choice of the best suited PCM for PEMFC technology, paraffin waxes are selected. Their melting point lies indeed in the PEMFC operating temperature range. Moreover, they are relatively cheap, chemically stable, safe, harmless and present small volume variation during phase change and little thermal hysteresis [120]. The implementation in fuel cell hybrid trains of the heat recovery concept just described, the quantification of the heat that can be discharged at the

station and the potential benefits associated with its exploitation are the main topics of the present chapter. In fact, to the best of author's knowledge, the opportunity of a thermal integration between fuel cell hybrid trains and stationary energy systems nearby railway lines has not yet been investigated.

3. Chapter three

Well-to-wheel analysis of fuel cell hybrid train operating in the Birmingham area

3.1 Introduction

This chapter presents a well-to-wheel (WTW) analysis of a fuel cell hybrid train operating in the region of Birmingham, UK. The WTW analysis provides a comprehensive evaluation of the primary energy efficiency of the train through two crucial stages: the well-to-tank (WTT) and the tank-to-wheel (TTW) processes.

While the WTT stage focuses on the upstream processes that include hydrogen production, storage, distribution and dispensing, the TTW step examines the on-track operation of the fuel cell hybrid train.

For each WTW route analysed, the results will be presented both in terms of primary energy efficiency and primary energy consumed per km travelled.

To be site-specific, the analysis must consider the UK energy scenario, focusing on the future developments of its hydrogen economy. Before choosing which hydrogen supply pathways to include in the analysis, a brief overview of how UK plans to build a robust and efficient hydrogen sector is provided. The following analysis thus aims to be a proposal of how to supply, within the emerging UK hydrogen framework, hydrogen to the Birmingham area as efficiently as possible.

Birmingham New Street, like any other large train station, has in fact the potential to become a remarkable hydrogen hub in terms of quantity of hydrogen managed daily and can also

help stakeholders to better frame the hydrogen's role in the decarbonisation of transport sector.

3.2 UK hydrogen scenario

In August 2021, the Secretary of State for Business, Energy & Industrial Strategy presented to Parliament the *UK Hydrogen Strategy* [121], which has laid the foundation stone for the beginning of the hydrogen era in the UK. It contains the goals and the principles of UK hydrogen roadmap and clarifies the role of each stage of the hydrogen chain (production, storage, transmission, distribution and end use) in meeting the desired targets. Importing hydrogen is not an option for UK as it has no added benefits on national energy security.

UK government has identified "low-carbon hydrogen" as a key factor to achieve the Net Zero target by 2050 [1]. According to the *UK Low Carbon Hydrogen Standard* [122], hydrogen can be referred as low carbon if its GHG emissions intensity (E_T) is equal or below 20 gCO_2eq per MJ of produced hydrogen at lower heating value. E_T considers not only the GHG emissions directly associated with the H_2 production plant's operation, but also those related to extraction, refining and transportation of the raw fuel sources needed for H_2 generation. The greenhouse gases contributing to the above-mentioned emissions threshold are CO_2 , CH_4, N_2O, HFCs and SF6.

UK sets itself the very ambitious goal of achieving 10 GW of low carbon hydrogen production capacity by 2030. Among the different production pathways, hydrogen from water renewable electrolysis and steam reforming with carbon capture usage and storage (SR+CCUS) have been selected. In the early stages, offshore wind and natural gas will be the preferred energy sources for water electrolysis and SR+CCUS, respectively, but in the near future biomass and nuclear energy are expected to contribute to the H_2 production goal [123].

Nowadays, hydrocarbons steam reforming is by far the most mature technology for H_2 production. Over 90% of the industrial hydrogen production facilities use indeed this technology [124]. Not surprisingly, at least in the near-term, UK will rely mainly on the synergy SR-CCUS to produce large amounts of low carbon hydrogen. The availability of domestic large-scale production facilities for natural gas represents another factor in support of this choice. CCUS technology development is then essential in *UK Hydrogen Strategy* and will become a core component of the UK energy sector. Once captured, carbon dioxide can be used or stored. Depleted gas and oil fields in the North and Irish Sea are where UK aims to store permanently CO_2.

According to the *Energy White Paper* [125], UK will invest one billion pounds up to 2030 to support the CCUS establishment in four industrial clusters (two by 2025 and a further two by 2030). Here, the first H_2 production facilities are to be built, taking advantage of both CCUS infrastructures availability and industrial clusters' high hydrogen demand. Through a dedicated sequencing process ended on 19 October 2021[25], UK government announced HyNet and the East Coast Cluster as the two CCUS clusters that are suited to deployment in the mid-2020s. CCUS-enabled hydrogen from HyNet will be considered in our analysis, due to the greater proximity to Birmingham.

[25] https://www.gov.uk/government/publications/cluster-sequencing-for-carbon-capture-usage-and-storage-ccus-deployment-phase-1-expressions-of-interest

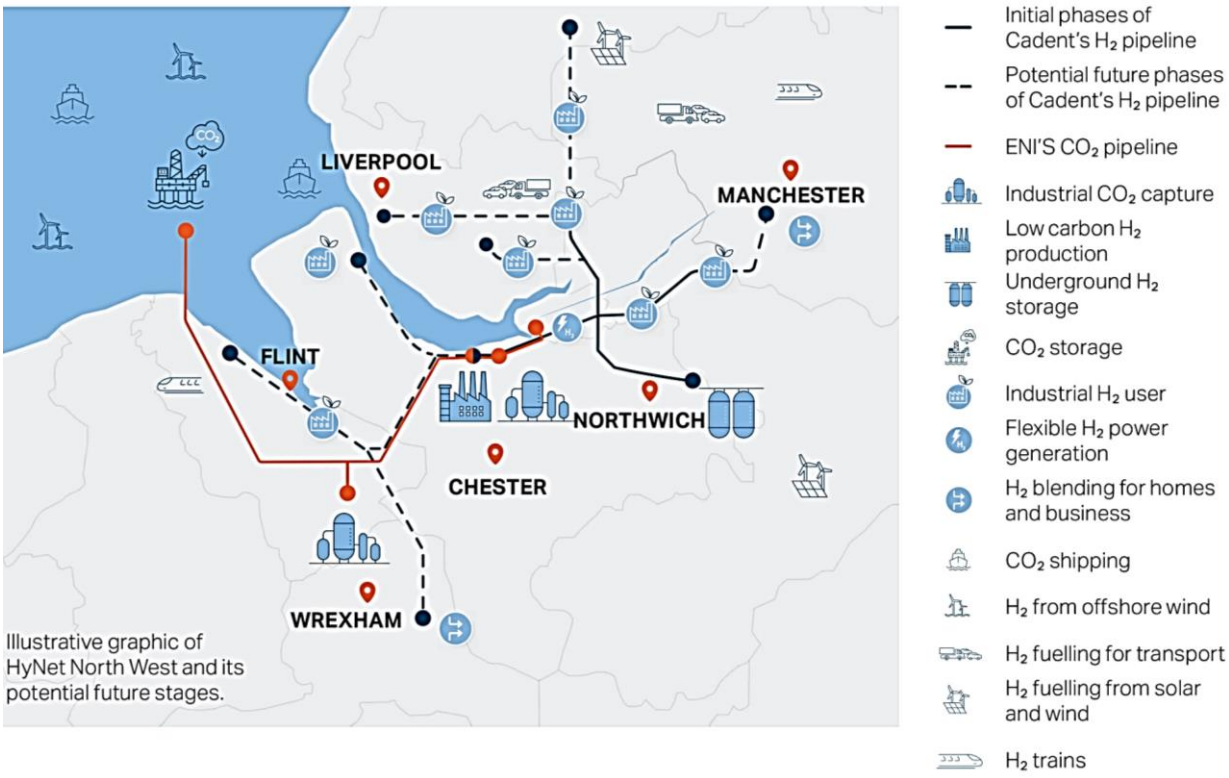

Figure 10 – HyNet Project map [126]

As mentioned, the other selected hydrogen production technology to meet net zero is water electrolysis. Alkaline and PEM electrolysers are ready for a full commercial deployment, but their typical size (< 1 MW) is today not sufficient to sustain a bulk scale hydrogen production. Despite that, water electrolysis technology will play a crucial role in *UK Hydrogen Strategy*, providing at least 5 GW of H_2 production capacity by 2030 [127]. The achievement of such an ambitious goal will necessarily require a scaling-up of electrolysers production capacity.

Electrolytic hydrogen is actually low carbon only if the electricity used to power electrolysers is produced from renewable sources. UK is characterised by a significant wind potential, making this country the current world's largest offshore wind market, with more than 10GW of installed capacity [128]. In the next 8 years, UK plans to increase this capacity up to 40 GW, investing around 160 million pounds. Electricity from offshore wind farms appears then to be the most suitable choice for green hydrogen bulk production. UK government included

a map in the *Hydrogen Investor Roadmap* [129] for keeping track of all the hydrogen projects across the UK. Its latest version, updated on 28 July 2022, counts 46 electrolytic projects of different scales. *Gigastack*[26] and *ERM Dolphyn*[27] are the two most relevant electrolytic hydrogen projects. Both projects aim to benefit of offshore wind turbines technology, but Dolphyn stands out for an innovative modular concept. It consists in a moored floating deck on which wind turbine, electrolyser, hydrogen storage and desalination unit are installed.

Another hydrogen's pros that UK intends to exploit is the possibility to store large quantities of energy over long period. Hydrogen storage ensures security of supply and offers a solution to the intermittence of renewable energy sources, speeding up RES penetration. Undersea and underground geological storage represents a great opportunity. UK can indeed claim more than 40 years of experience in hydrogen storing in Teesside's salt caverns. It has been estimated that UK has the potential to store millions of TJ of hydrogen in its salt formations [130]. Depleted offshore gas and oil fields have also been considered but some concerns on their suitability for hydrogen storage still remain.

Transmission and distribution to the centres of consumption is the next step in the hydrogen supply chain. The development of a dense nationwide hydrogen network by 2030 is what UK aims for. The amount of hydrogen transported by pipeline will gradually increase year by year, together with the growth in H_2 demand. In this regard, UK government decided to implement blending to support demand in the early stages of the strategy. Blending consists in injecting hydrogen into the existing natural gas network. Before using it, hydrogen must be separated from natural gas through the so-called deblending, which is a very energy-intensive process. If pressure swing adsorption is used, around 20 kWh/kg_{H2} are needed for

[26] https://gigastack.co.uk/
[27] https://ermdolphyn.erm.com/p/1

deblending 10% H_2 in CH_4 to obtain a hydrogen purity higher than 99% [131]. For this reason, blending is not seen as a long-term solution to meet zero net targets. At the same time, significant efforts are under way to investigate to which extent the repurposing of the existing gas grid is possible. Government, research and industry are in fact currently working together in joint projects with the aim of exploring the economic and technical feasibility of repurposing. Despite its potential benefits, repurposing may not be applied in all parts of the country or for all consumers [121]. New transmission pipelines could be then required. According to a report prepared by Element Energy Ltd [132], hydrogen networks will be characterised by either larger diameters, higher pressure drops or increased inlet pressures than those of gas grid. The reason behind these design choices is the need to counterbalance the lower hydrogen volumetric energy density. Delivery via pipeline is not however the only way to transport hydrogen to end-users. Especially before hydrogen network completion, large areas of the country may not be reached by pipelines. In such a case, UK relies on trucking for transportation. Hydrogen can be delivered in liquid or gaseous form. In the first case, a cryogenic liquid tanker truck is used. Generally, payload for this kind of vehicles is around 3500 kg of liquid H_2 [133]. As regards gaseous hydrogen, H_2 is instead transported via tube trailers at pressures between 200 – 300 bar [134]. Due to the low density (20.86 kg/m^3 at 20°C and 300 bar), each trailer can carry around 350 kg. Recently, thanks to newly built vessels made of composite material, trailer's payload has been increased up to 900 kg[28]. Despite the higher capacity of cryogenic tankers, the appeal of hydrogen transportation in liquid form is strongly limited by the high energy consumption for liquefaction.

[28] https://www.energy.gov/eere/fuelcells/hydrogen-tube-trailers

3.3 Well-to-tank stage

3.3.1 Analysed supply pathways

For practical reasons, WTT stage is split in two parts: the first covers hydrogen production, CO2 storage, H2 storage and transportation to the hydrogen refuelling station. Conversely, the second deals with the dispensing step and HRS layouts.

Once the UK's plan to develop its own hydrogen market in the next decades is known, the most likely supply pathways for the Birmingham area can be now assumed with a good level of accuracy. Thus, for each stage of the hydrogen supply chain, the options included in the analysis are:

- H_2 production:
  - Natural gas reforming coupled with carbon capture and storage
  - Wind powered water electrolysis
- H_2 storage:
  - Compression and injection of hydrogen into salt caverns
- CO_2 storage:
  - Compression and injection of carbon dioxide into depleted offshore gas fields
- H_2 transportation:
  - Pipelines network
  - Cryogenic liquid tankers
  - Tube trailers
- H_2 dispensing:
  - HRS with booster compressors
  - HRS with overflow filling

- LH_2 HRS

In addition to the first six supply routes depicted in Figure 11, a seventh one is examined: on-site hydrogen production by means of electrolysers. It is assumed that electrolysis is driven by grid electricity. Since no losses for hydrogen delivery are involved, on-site production paths are expected to be the most efficient ones. Energy efficiency is not however the only criterion in selecting the best hydrogen supply option for Birmingham. Environmental and economic considerations, such as costs and greenhouse gas emissions associated with each step of the analysis, are in fact equally important and should be included in the decision-making process.

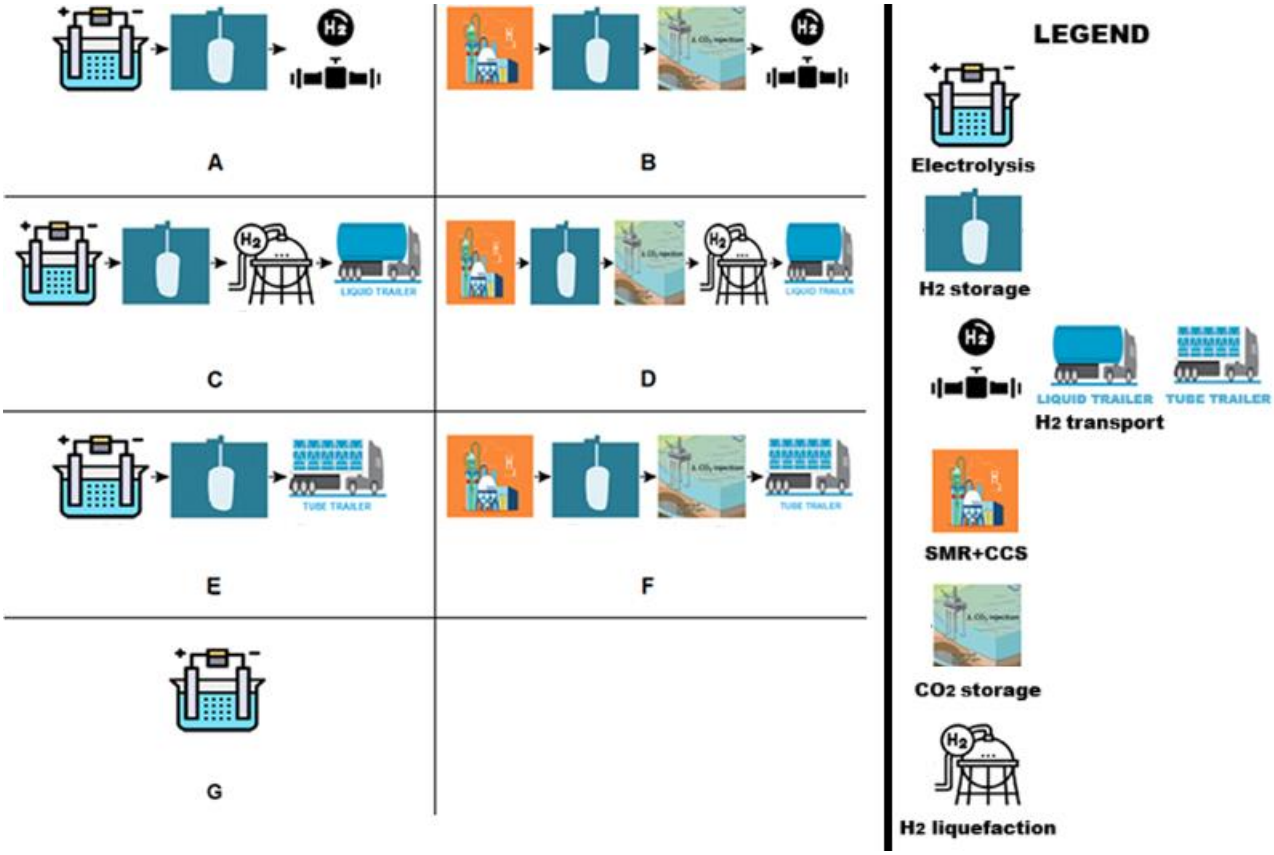

Figure 11 – Supply chains

The analysed WTT pathways, resulting from the combination of the considered seven supply options (Figure 11) and the three dispensing ones, are fourteen and are presented in Table 8 for the sake of clarity.

Pathway	Identification number
Electrolysis – H_2 storage – pipeline – HRS with booster compressors	1
Electrolysis – H_2 storage – pipeline – HRS using overflow filling	2
Electrolysis – H_2 storage – 300 bar-tube trailers – HRS with booster compressors	3
Electrolysis – H_2 storage – 300 bar-tube trailers – HRS using overflow filling	4
Electrolysis – H_2 storage – 700 bar-tube trailers – HRS using overflow filling	5
Electrolysis – H_2 storage – liquefaction – liquid tankers – LH_2 HRS	6
SMR – CO_2 storage – H_2 storage – pipeline – HRS with booster compressors	7
SMR – CO_2 storage – H_2 storage – pipeline – HRS using overflow filling	8
SMR – CO_2 storage – H_2 storage – 300 bar-tube trailers – HRS with booster compressors	9
SMR – CO_2 storage – H_2 storage – 300 bar-tube trailers – HRS using overflow filling	10
SMR – CO_2 storage – H_2 storage – 700 bar-tube trailers – HRS using overflow filling	11
SMR – CO_2 storage- H_2 storage – liquefaction – liquid tankers – LH_2 HRS	12
On-site electrolysis – HRS with booster compressors	13
On-site electrolysis – HRS using overflow filling	14

Table 8 – Analysed WTT routes

In the following sections, the energy efficiencies of the selected WTT pathways are assessed. They are calculated by multiplying the individual efficiencies of each step. Data and information needed for calculation, wherever possible, are taken from technical reports and feasibility studies of the main projects currently shaping UK hydrogen strategy. A database so built allows the analysis to be specific for UK scenario. When no or limited data is available, reasonable assumptions based on literature findings are made, explaining the reasons behind them. Greater detail on the data used to model each supply route will be provided further on.

3.3.2 New Street daily hydrogen demand

In this thesis, Birmingham New Street Station is the considered end user of the hydrogen supply chain. Every day enough hydrogen to cover the overall daily mileage of the train fleet has to be delivered to the station. The size of the fleet and the average fuel consumption of the trains dictate therefore the magnitude of the station's hydrogen demand.

In the *Transport decarbonisation plan*[29], the Department for Transport (DfT) announced its intention to remove all the diesel trains from UK network by the end of 2040. Currently, the four most relevant operators at BNS run approximately 243 diesel trains, totalling 735 carriages.

Company	# of 2-car trains	# of 3-car trains	# of 4-car trains	# of 5-car trains
Cross Country	7	22	38	20
London Northwestern Railway	3	0	0	0
West Midlands Railway	36	15	14	0
Transport for Wales	51	26	11	0
TOT	97	63	63	20

Table 9 – BNS main operators' diesel fleets

Since DfT has not provided a roadmap for diesel trains phase-out, it is assumed that the withdrawal rate of diesel carriages from the network will start slowly and then accelerate over time as technology becomes cheaper and more accessible. This behaviour can be described by a cubic polynomial law, whose general formula is:

$$N(t) = a \cdot (t - 2023)^3 + b \cdot (t - 2023)^2 + c \cdot (t - 2023) + d \qquad (15)$$

[29] https://assets.publishing.service.gov.uk/media/610d63ffe90e0706d92fa282/decarbonising-transport-a-better-greener-britain.pdf

where:

- $N(t)$ is the number of diesel cars remaining at time t
- N_0 is the initial number of diesel carriages (i.e. 735)
- a, b, c, d are the fitting coefficients

After adjusting Eq. (15) such that:

- $N(t = 2023) = 735$ → Number of diesel carriages starts at 735 in 2023
- $N(t = 2040) = 0$ → Number of diesel carriages is 0 in 2040
- $\frac{dN(t=2023)}{dt} = 0$ → No initial steep drop
- $\frac{d^2N(t=2023)}{dt^2} = 0$ → Smooth start

it follows that:

$$N(t) = -0.1496 \cdot (t - 2023)^3 + 735 \quad (16)$$

Table 10 shows how many diesel coaches have to be removed every year and replaced with as many hydrogen-powered ones.

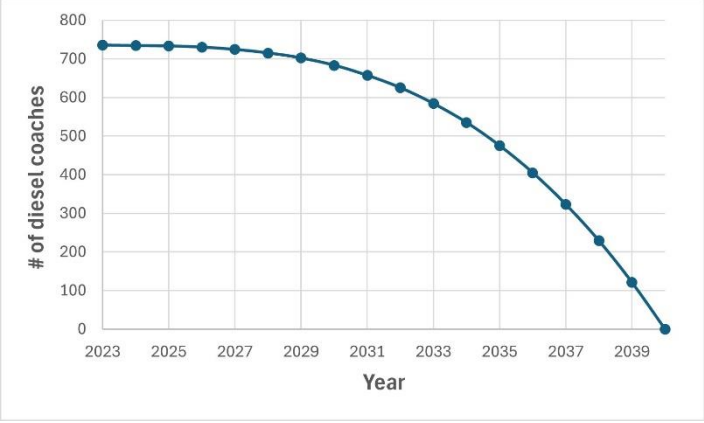

Figure 12 – Number of diesel carriages still in operation per year (Eq. 16)

Year	# of diesel coaches to replace
2024	1
2025	1
2026	3
2027	6
2028	9
2029	13
2030	19
2031	26
2032	32

Year	# of diesel coaches to replace
2033	41
2034	49
2035	60
2036	70
2037	82
2038	94
2039	108
2040	121

Table 10 – Number of diesel coaches to replace per year

Technical design of the train, size of the fuel cell powertrain, real-life driving profile, average seat load factor, number of coaches, typical daily mileage, topological characteristics of the routes, wind speed and direction are just some of the factors affecting the hydrogen consumption of the trains. An accurate estimation of the hydrogen usage can be achieved through field measurements or by means of proper models to simulate train performance in time-domain.

Given the impossibility of performing on board measurements and due to the lack of the required data for modelling, the hydrogen consumption levels for a typical fuel cell train are retrieved from literature. Report 1 of the '*Study on the use of fuel cells & hydrogen in the railway environment*' [89] is taken as a reference as it shares some important similarities with the present thesis. In particular, it estimates a hydrogen usage between 0.25 and 0.3 kg per km for a two-car Alstom Coradia iLint travelling under the following working conditions:

- Daily mileage of 800 km, with 8 stops per hour and a total operational time of 10 hours per day

- Flat topography of the route
- Average seat load factor of 50%

The above-mentioned consumption range is however valid only for the specific case of a half-loaded two-car train. To determine how much H_2 each train needs, whichever are its number of carriages and seat load factor, a simple Simulink model simulating the longitudinal dynamics of the train is used. It is based on the work of Spiryagin and his colleagues [135] and is built starting from the following equation:

$$m_{train}\frac{d}{dt}v(t) = F_{trac}(t) - F_a(t) - F_r(t) - F_g(t) \tag{17}$$

where:

- F_{trac} : traction force at the wheels
- F_a : aerodynamic friction
- F_r : rolling resistance
- F_g : gravitational force for non-horizontal roads

The aerodynamic friction, rolling resistance, and gravitational forces are calculated thus:

$$F_a = C \cdot v^2 \tag{18}$$

$$F_r = A + B \cdot v \tag{19}$$

$$F_g = m_{train} \cdot g \cdot \alpha \tag{20}$$

where A, B and C are the Davis equation's coefficients, v is the train velocity, m_{train} is the mass of the train, g is the gravitational acceleration and α is the track gradient. Below, the set of empirical expressions proposed by Armstrong and Swift [136] to determine the values of A, B and C is shown.

$$A = 6.4 \cdot m_{TC} + 8 \cdot m_{PC} \quad (21)$$

$$B = 0.18 \cdot m_{train} + 1 \cdot n_{TC} + 0.005 \cdot n_{PC} \cdot P \quad (22)$$

$$C = 0.6125 \cdot C_x \cdot S + 0.00197 \cdot d \cdot l + 0.0021 \cdot d \cdot I_g \cdot (n_{TC} + n_{PC} - 1) + 0.2061 \cdot C_x^B \cdot n_B \quad (23)$$

where:

- m_{TC}: total mass of trailer cars in tons
- m_{PC}: total mass of power cars in tons
- n_{TC}: number of trailer cars
- n_{PC}: number of power cars
- P: total power in kW
- C_x: head/tail drag coefficient
- S: car's cross-sectional area in m^2
- d: car's perimeter in m
- l: train length
- I_g: inter-vehicle gap in m
- C_x^B: bogie drag coefficient
- n_B: number of bogies

The resulting Simulink model is shown in Figure 13. It accepts in input the desired velocity profile (Figure 14), the train mass and the Davis equation's coefficients, printing out the distance covered by the train and the energy consumption. For the sake of simplicity, a horizontal track is considered and F_g can be neglected. Only the effects of aerodynamic friction and rolling resistance will be then taken into account.

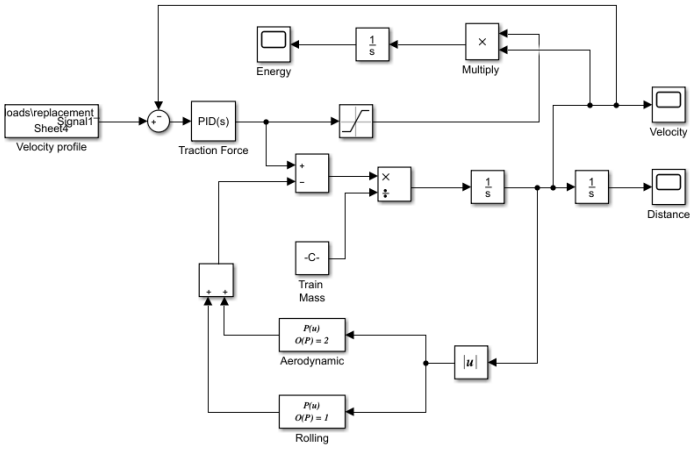

Figure 13 – Simulink model for longitudinal train dynamics and energy calculation

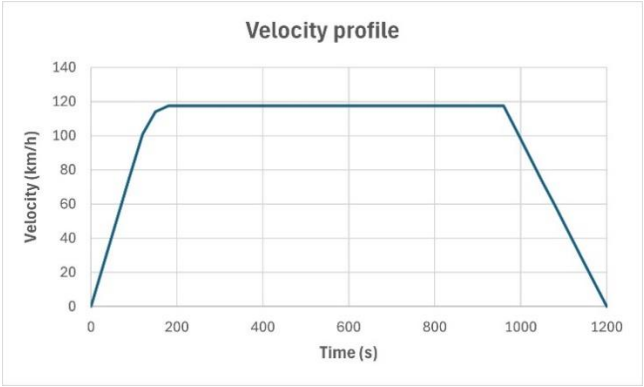

Figure 14 – Typical velocity profile between two consecutive stops

The relationship between fuel consumption, number of coaches and seat load factor is derived by considering how the traction force required by the train has to vary as vehicle mass increases (i.e. due to the addition of carriages and/or the increase of occupancy rate) so that train's velocity profile does not change. Therefore, it follows that:

$$E_{trac} = \int_0^t F_{trac}(t) \cdot v(t) dt$$

$$fuel_{n\_cars} = fuel_{two\_cars} \cdot \frac{E_{trac-n}}{E_{trac-two}}$$

where $fuel_{n\_cars}$ is the fuel consumption per km of a hybrid n-car train having an average seat load factor ranging from 0 and 150%, $fuel_{two\_cars}$ is the fuel usage per km of the half-loaded two-car Alstom Coradia iLint previously mentioned (i.e. 0.25-0.3 kg_{H2} per km), $E_{trac-two}$ is the energy needed by the half-loaded two-car iLint to travel an arbitrary distance d over the time frame t and E_{trac-n} is the energy required by the hybrid n-car train to cover the same distance d in the same amount of time t.

Figure 15 shows the effects of the number of coaches forming the train and seat load factor on train's fuel consumption. Tables 11 gather instead all the Davis coefficients implemented in the model, calculated using Eqs. (21) - (23).

seat load factor	coaches	A	B	C
0	2	856	23.26	2.091
0	3	1284	37.89	2.894
0	4	1712	54.52	3.697
0	5	2140	73.15	4.500
0	6	2568	93.78	5.303
0	7	2996	116.41	6.105

seat load factor	coaches	A	B	C
0.5	2	892	24.07	2.091
0.5	3	1338	39.11	2.894
0.5	4	1784	56.14	3.697
0.5	5	2230	75.18	4.500
0.5	6	2676	96.21	5.303
0.5	7	3122	119.25	6.105

seat load factor	coaches	A	B	C
1	2	928	24.88	2.091
1	3	1392	40.32	2.894
1	4	1856	57.76	3.697
1	5	2320	77.20	4.500
1	6	2784	98.64	5.303
1	7	3248	122.08	6.105

seat load factor	coaches	A	B	C
1.5	2	964	25.69	2.091
1.5	3	1446	41.54	2.894
1.5	4	1928	59.38	3.697
1.5	5	2410	79.23	4.500
1.5	6	2892	101.07	5.303
1.5	7	3374	124.92	6.105

Tables 11 – Davies equation's coefficients for different numbers of coaches and seat load factors

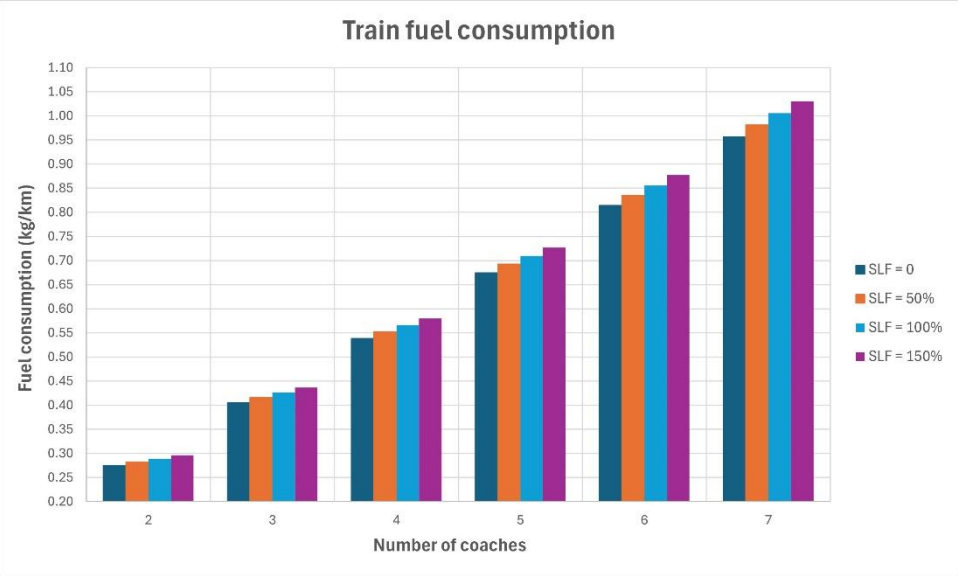

Figure 15 – Train fuel consumption for different numbers of coaches and seat load factors (SLF)

Once the relationship between train fuel usage, SLF and number of carriages is known, the other information needed to calculate Birmingham New Street's daily hydrogen demand are:

- train's average daily mileage
- average seat load factor

A typical daily seat load factor trend, retrieved from the National statistics on rail passenger numbers and crowding on weekdays[30], is displayed in Figure 16. According to the curve, the daily average SLF is equal to 87%. This value will be then used for calculations.

[30] https://www.gov.uk/government/statistics/rail-passenger-numbers-and-crowding-on-weekdays-in-major-cities-in-england-and-wales-2021/rail-passenger-numbers-and-crowding-on-weekdays-in-major-cities-in-england-and-wales-2021#rail-journey-distributions

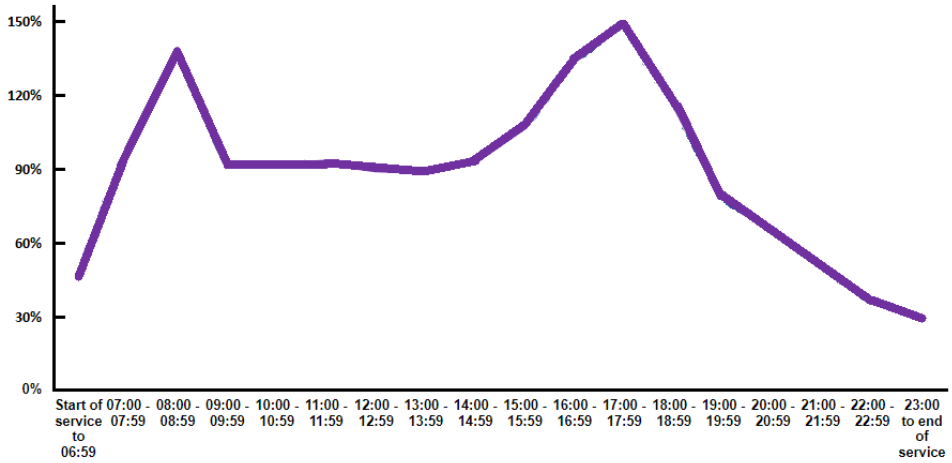

Figure 16 – Typical daily seat load factor

To estimate the train's average daily mileage, the timetables provided by the four companies operating at BNS have been examined. It is found that a Cross Country's train travels an average of 500 km per day, while a London Northwestern's one covers only 263 km/day. As regards West Midlands and Transport for Wales trains, their average daily mileages amount to 280 km and 440 km, respectively. Therefore, a train of the diesel fleet operating at BNS (see Table 9) covers, on average, 416 km every day. All the data for BNS daily hydrogen demand calculation are now known.

Based on Table 10 values, the table below shows how the station's daily hydrogen demand should change over the years to meet the 2040 target set by the DfT. Both a low and a high demand scenario are included.

Year	H_2 powered coaches	2-car H_2 trains	3-car H_2 trains	4-car H_2 trains	5-car H_2 trains	Low scenario (kg)	High scenario (kg)
2025	2	1	0	0	0	106	127
2030	52	6	5	5	1	2714	3257
2035	260	36	23	21	7	13585	16302

2040	735	97	63	63	20	38394	46073

Table 12 – Estimated BNS daily hydrogen demand over the years

Despite being a very rough estimate (an accurate calculation is beyond the scope of the thesis), the order of magnitude of the numbers in Table 12 suggests that BNS has the potential to play a major role in the next future as hydrogen hub. To give an idea, the 46 tons per day that would be required for the station in the 2040 would account for almost 2.1% of the HyNet's daily hydrogen production capacity.

3.3.3 WTT methodology

As stated before, the energy efficiency of each WTT chain examined is the result of the product between the efficiencies of all the steps involved,

$$\eta_{WTT\ path} = \prod_{i=1}^{n} \eta_i \tag{24}$$

where n is the number of the steps constituting the path and η stands for efficiency. The simplest definition of energy efficiency η_i (Eq. (25)) is the ratio between the energy content of the step's useful output ($E_{output,i}$) and the energy in input to produce it ($E_{input,i}$).

$$\eta_i = \frac{E_{output,i}}{E_{input,i}} = \frac{E_{output,i}}{E_{el} + E_{th}} \tag{25}$$

where E_{th} indicates the thermal energy or the LHV of the fuel in input, while E_{el} stands for electrical energy required by the process. This calculation approach makes no distinction between E_{th} and E_{el} in input, hence assuming 1 kWh_{el} equivalent to 1 kWh_{th}. Electricity, however, is not a primary energy sources and then the equivalence between heat and electrical energy is an oversimplification. Besides, as the energy processes involved in the analysis are different, the parameter η_i is not a fair index for comparison if calculated

according to Eq. (25). To fix this inaccuracy, anytime electricity or any other secondary sources is part of process inputs, a corresponding primary energy parameter is introduced. For the electrical energy, it can be calculated as follow:

$$PE_{el} = PE_{UK\ mix\ fuels} \cdot \frac{1}{\eta_{UK\ mix} \cdot \eta_{transm}} \tag{26}$$

where $\eta_{UK\ mix}$, η_{transm} and $PE_{UK\ mix\ fuels}$ are the efficiency of UK electricity generation mix, the transmission/distribution efficiency and the combined primary energy factor of all the fuels forming the electricity generation mix, respectively. $PE_{UK\ mix\ fuels}$ takes into account not only the energy content of raw fuels but also the energy consumed during the upstream activities (extraction, processing and delivery to the power plant) of each fuel type. Thus, its value depends on which primary energy sources are mainly exploited for electricity generation. In this analysis, two different cases are considered:

- UK energy mix as source. The corresponding $PE_{electricity}$ is 1.501 and is taken from *SAP 10 Technical Paper* [137]. This means that 1.501 units of primary energy are needed to generate and deliver 1 unit of electrical energy to consumers.
- Wind powered electricity, resulting in a $PE_{electricity}$ equal to 1. *JEC Well-to-Tank report v5* in fact assumes a 100% conversion efficiency for renewables as raw material is considered unlimited [138].

Eq. (25) is therefore modified to incorporate PE_{el} parameter. The equation for η_i estimation becomes:

$$\eta_i = \frac{E_{output,i}}{E_{el} + E_{th}} = \frac{E_{output,i}}{PE_{el} \cdot e_{el} + E_{th}} \tag{27}$$

where e_{el} is the amount of electricity needed for the i-th step.

In light of the above, WTT pathway's efficiency $\eta_{WTW\ path}$ holds an important information about primary energy consumption. In particular, its value tells us how many kWh of primary energy (kWh_P), both fossil and renewable, are expended per KWh of hydrogen dispensed to the train. In symbols:

$$E_{WTT_s} = \frac{1}{\eta_{WTT\ path}} - 1 \tag{28}$$

The WTT energy index can be also defined in order to include the energy value of the hydrogen itself. In symbols,

$$E_{WTT_t} = \frac{1}{\eta_{WTT\ path}} \tag{29}$$

It has been decided to present the final results in terms of E_{WTT_t}.

3.3.4 Analysis time horizon

In the next years, UK hydrogen sector will experience deep changes. The maturity level of the most innovative technologies is expected to rapidly increase, resulting in cost reductions and efficiency improvements. In such a fast-changing framework, two different scenarios are chosen: 2030 and 2040. The aim is to show how technological advancement may positively affect hydrogen pathways' efficiencies.

Focus on supply pathways

Before presenting the results, greater details on each stage of hydrogen supply route are now provided. As shown previously, two options for production and three for transmission have been included in the analysis. As regards carbon dioxide and hydrogen storage steps, only one option for each of them is evaluated. Assumptions, mathematical expressions and

calculation approaches are here introduced in order to make the analysis outcomes more transparent and reliable.

3.3.5 Well-to-tank stage main assumptions

Below, a table gathering the main assumptions for each of the stages of hydrogen supply route is provided.

Stages	Options	Main assumptions
H_2 production	NG reforming + carbon capture	1. Only NG from UK and its continental shelf 2. Low Carbon Hydrogen technology is used 3. H_2 and CO_2 streams leave the plant at 46 bar and 36 bar, respectively
	Wind powered water electrolysis	1. PEM electrolysers are chosen 2. Only offshore wind energy to power PEM 3. Wind farm 100% efficient 4. Cooling energy for intercoolers excluded (ideal heat sink assumed)
	On-site electrolysis	1. PEM electrolysers 2. Capacity factor: 0.9 3. City water reserves used 4. Grid electricity 5. Single-stage reciprocating compressor increases H_2 pressure from 30 bar to 46 bar
CO_2 storage	Injection into depleted offshore gas fields	1. Capture scenarios: 1 Mt/yr (2030), 3 Mt/yr (2040) 2. p_{field} < 37 bar: onshore and offshore networks operate in gas phase, p_{field} > 37 bar: offshore infrastructure works with liquid phase 3. Maximum operating pressure: 115 bar; PoA station outlet pressure: 126 bar
H_2 storage	Injection into salt caverns	1. Cavern pressure 80 bar (max), 30 bar (min) 2. Pipeline pressure: 46 bar 3. Multi-stage centrifugal compressors with intercooler, driven by electric motors
H_2 transportation	Compressed H_2 tube trailers	1. Trucks with Type I or Type IV cylinders 2. Green electricity used for compression 3. Compressors increase pressure to 300-700 bar 4. Reciprocating devices with intercooling 5. Fuel usage: 0.423 l/km
	Cryogenic liquid tankers	1. Energy for liquefaction: 10 kWh/kg H_2 2. Usable delivery capacity: 95% 3. Energy for transport to loading bay negligible 4. Fuel usage: 0.423 l/km

	Pipeline network	1. Blending ratio: 20% 2. Injection pressure: 46-70 bar 3. 20% blend powers centrifugal compressors 4. 10% H_2 not recoverable from blend
Hydrogen Refuelling Station	HRS with storage < 350 bar and booster compressors	1. Storage operating pressure: close to 350 bar 2. Minimum truck vessel operating pressure: 20 bar 3. Reciprocating compressors for unloading and refuelling 4. Constant flow rate and temperature (20°C) during discharge 5. Cooling towers for intercoolers 6. Electric motors drive compressors, grid energy used 7. Fuelling rate: 7.2 kg/min
	HRS with storage > 350 bar and overflow filling	1. H_2 storage subdivided into LP, MP and HP banks 2. Maximum banks operating pressure: 500 bar 3. Minimum banks operating pressure: 430 bar (HP), 329 bar (MP), 177 bar (LP) 4. Energy to fill the overcapacities not included in efficiency calculation
	HRS with LH_2 storage and cryogenic pumps	1. Dewar temperature and pressure: 20 K, 6 bar 2. Minimum pressure gradient for emptying the liquid trailers: 1 bar 3. Electric motors to drive cryopumps (grid electricity) 4. Cryo-pumps outlet pressure: 457 bar 5. Fuelling rate: 7.2 kg/min

Table 13 – Well-to-tank stage main assumptions

3.3.6 H_2 production – Natural gas reforming + carbon capture

In this section, the efficiency of the production step involving reforming and carbon capture is calculated using Eq. (30).

$$\eta_{prod,NGR+CC} = \eta_{NG} \cdot \eta_{plant+CC} \tag{30}$$

where η_{NG} is the efficiency related to the natural gas chain from field to reforming plant, while $\eta_{plant+CC}$ represents the efficiency of the plant coupled with carbon capture system. How η_{NG} and $\eta_{plant+CC}$ are evaluated will be explained in detail in the following lines.

In the next decades, natural gas reforming technology coupled with CCS will play a major role in producing large amounts of low carbon hydrogen. As anticipated in Section '*UK hydrogen scenario*', hydrogen from HyNet project is one of the two analysed off-site production options.

In November 2021, HyNet has been confirmed as CCUS Track-1 cluster by UK Government. HyNet project is located in the northwest of England and North Wales and has its heart at Stanlow Manufacturing Complex. Here, four hydrogen production units will be constructed by 2030. According to the project's timeline (see Table 14), the first unit will be operational by 2025 and will be able to produce 100 kNm^3/hour of hydrogen. Plant 2 will start operating by 2026, adding 200 kNm^3/hour to Stanlow's production capacity. The last two units will be turned on by 2028 and 2030 and together will produce 800 kNm^3/hour. After Plant 4 goes into operation, the overall production capacity will be equal to 1100 kNm^3 per hour [139]. Plants are equipped with CCS infrastructures, which will be capable to sequester and store up to 10 million tonnes of CO_2 per year by 2030.

Year	Operational Plants	Total production capacity (kNm^3/hour)
2025	1	100
2026	1 – 2	300
2028	1 – 2 – 3	700
2030	1 – 2 – 3 – 4	1100

Table 14 – Project timeline

For the sake of sustainability, only natural gas from UK and its continental shelf is used for HyNet hydrogen production. A recent study[31] by Oil and Gas Authority has in fact shown that UK domestic gas has one of the lowest carbon footprint among UK gas sources, second only to the gas imported by pipeline from Netherlands and Norway. Before being available for reforming, natural gas must be extracted, refined and transported to the conversion plant. All these upstream processes require energy and cannot be excluded from the calculations. An efficiency for natural gas supply is then introduced. It is defined as,

$$\eta_{NG} = \eta_{extract} \cdot \eta_{transm} \tag{31}$$

where:

- $\eta_{extract}$ is the efficiency related to gas extraction and processing. According to chapter 4 of the *Digest of UK Energy Statistics (DUKES)*[32], 42.82 TWh of gas have been consumed in 2021 for drilling, production and pumping operations. In the same year, gas gross production amounted to 363.99 TWh. The value of $\eta_{extract}$ is thus equal to (363.99-42.82)/363.99 = 0.882.
- η_{transm} accounts for the gas network transmission average efficiency. Its value, equal to 0.992, is also retrieved by chapter 4 of DUKES, by comparing gas output from the national transmission system with gas input into the same system. The mismatch between output and input is due to leakages and gas consumed by pipeline operators in pumping operations and on their own sites.

[31] https://www.nstauthority.co.uk/media/6522/emissions-intensity-comparison-of-ukcs-gas-production-and-imported-lng-and-pipelined-gas-v2.png
[32] https://www.gov.uk/government/statistics/natural-gas-chapter-4-digest-of-united-kingdom-energy-statistics-dukes

By calculating η_{NG} as described in Eq. (31), a value of 87.5% is obtained. Therefore, it follows that almost 1.143 units of primary energy have to be spent per each unit of gas entering the conversion plant.

HyNet deploys an advanced reforming process to generate hydrogen. It is developed by Johnson Matthey company and utilizes the so-called Low Carbon Hydrogen technology (LCH). By combining autothermal and gas heated reformers' technologies, a plant implementing LCH concept succeeds in achieving better efficiencies and higher carbon capture rates compared to those of a conventional SMR+CCS process. Data from "*Clean hydrogen. Hydrogen from natural gas through cost effective CO2 capture*" [140] demonstrate the superiority of LCH flowsheet: on hourly basis, a typical LCH unit (same size of Plant 1 – see Table 14) produces in fact 107.4 kNm^3 of hydrogen using 38.31 kNm^3 of natural gas, while a steam reformer needs 45.1 kNm^3 per hour for the same amount of H_2. The main characteristics of these two technologies are summarised in Table 15.

	LCH	**SMR**
NG in input (kNm^3/h)	38.31	45.1
H_2 production (kNm^3/h)	107.4	107.4
Efficiency (%)	80.6	73.3
CO_2 capture rate (%)	97	95

Table 15 – LCH and SMR main characteristics

The efficiency reported in Table 15 is on LHV basis and is calculated according to Eq. (32), by dividing the energy content of the produced hydrogen ($E_{H_2 out}$) by the one of the gas in input ($E_{th,NG}$). Due to how it is defined, this efficiency is just a measure of natural gas conversion effectiveness and does not represent then the actual performance of the plant.

$$\eta_{th,plant} = \frac{E_{H_2 out}}{E_{th,NG}} \tag{32}$$

In order to evaluate the overall efficiency $\eta_{plant+CC}$, Eq. (32) is modified to include in the calculation both electrical (E_{el}) and thermal energy (E_{th}) in input, as Eq. (33) shows.

$$\eta_{plant+CC} = \frac{E_{H_2 out}}{E_{el} \cdot PE_{el} + E_{th,NG} + E_{th,ext}} \tag{33}$$

Information on LCH electricity demand can be found in [126]. In HyNet project, it is assumed that hydrogen and carbon dioxide streams will leave the plant at 46 bar and 36 bar, respectively. The plant infrastructure, besides producing hydrogen, is therefore also responsible for H_2 and CO_2 compression up to delivery pressure. A unit generating 107.4 kNm^3 of hydrogen every hour requires in total 23 MW of electric power for its BoP, which correspond to 23 MWh of electrical energy consumed hourly. With regard to the plant thermal energy demand, no external heat sources are needed during nominal operations ($E_{th,ext}$ = 0) thanks to the optimal flowsheet thermal integration [139]. Prior to compression, hydrogen and carbon dioxide outlet streams are cooled to ambient temperature (20°C). The heat so recovered is supposed to fully meet LCH thermal energy demand. Plant overall efficiency can be finally calculated as all the involved terms are now known. By substituting their hourly values in Eq. (33), it follows that:

$$\eta_{plant+CC} = \frac{V_{H_2}[Nm^3] \cdot LHV_{H_2}\left[\frac{kWh}{Nm^3}\right]}{PE_{el} \cdot E_{el}[kWh] + V_{NG}[Nm^3] \cdot LHV_{NG}\left[\frac{kWh}{Nm^3}\right]} = \frac{107400 \cdot 2.78}{1.501 \cdot 23000 + 38310 \cdot 10.2} = 0.703 \tag{34}$$

where PE_{el} value is 1.501 as electricity from the grid is used.

The result above is around 8 percentage points less than the efficiency in Table 15. This reduction is caused by BoP energy consumption, carbon capture and compression of H_2 and CO_2. The choice of using “CC” and not “CCS” as subscript for η is not causal. The

additional energy related to CO_2 storage will be in fact assessed separately in a dedicated section.

As stated at the beginning of the section, the ultimate goal is the estimation of the global efficiency for the production option here analysed, that is natural gas reforming associated with carbon capture. For the sake of clarity, Eq. (30) is reintroduced below.

$$\eta_{prod,NGR+CC} = \eta_{NG} \cdot \eta_{plant+CC} = 0.875 \cdot 0.7 = 0.61 \tag{35}$$

From the result of Eq. (35), it is possible to infer that about additional 0.64 kWh of primary energy are spent for each kWh of low carbon H_2 leaving plant boundaries.

Figure 17 and Figure 18 provide a quick visual summary of the section. LCH plant is then where most of the losses occurs, around 66% of the total.

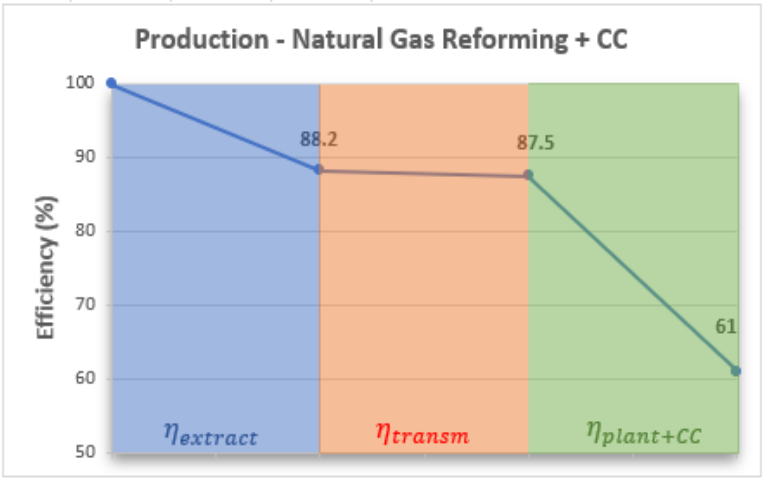

Figure 17 – Overall primary energy efficiency of SMR+CC

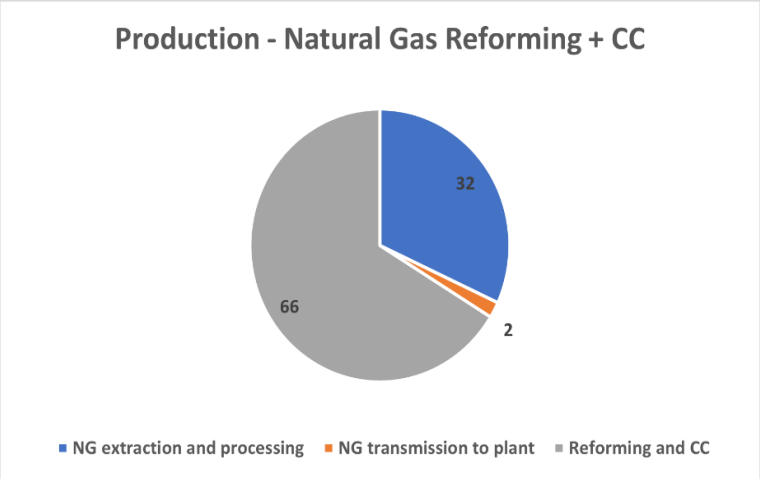

Figure 18 – Percentage incidence of each process on production energy loss

3.3.7 H_2 production – Wind powered water electrolysis

As mentioned in '*UK hydrogen scenario*' section, 46 electrolytic projects of different scales are currently under development in UK. Among these, Trafford Green project has been selected as the reference bulk supply solution for green hydrogen. Its proximity to HyNet is the main reason behind the choice. Selecting Trafford Green allows indeed to compare the electrolytic hydrogen pathways (options A, C and E in Figure 11) and the ones involving reforming and carbon capture under almost the same conditions for hydrogen transport. In doing so, the aim is to highlight even more the impact of production method on the overall hydrogen pathway efficiency. Unlike Gigastack and Dolphyn cases, for which detailed reports have been produced by stakeholders, technical data on Trafford Green project is unfortunately scarce. The only available information can be found on the project website[33]. The project will be developed at Trafford Low Carbon Energy Park, in Carrington. Starting from a hydrogen production plant of 20 MW, the ultimate goal is to reach 200 MW of installed capacity. Electricity from solar and wind energy is planned to power electrolysis. Since no

[33] https://www.traffordgreenhydrogen.co.uk/theproject

other data is provided, proper assumptions will be made in order to estimate the production efficiency.

Only hydrogen generated by using offshore wind energy is covered by the scope of the present section. So, no solar energy is supposed to contribute to hydrogen production at Trafford. From Figure 19, the closest offshore wind farms to Trafford Energy Park are Burbo Bank, Burbo Bank Extension, North Hoyle, Gwynt y Mor and Rhyl Flats.

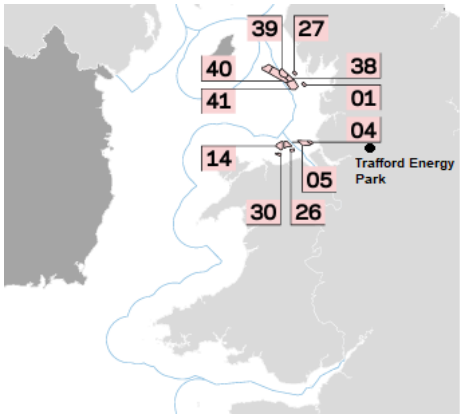

		Capacity MW
01	Barrow	90
04	Burbo Bank	90
05	Burbo Bank Extension	259
14	Gwynt y Môr	576
26	North Hoyle	60
27	Ormonde	150
30	Rhyl Flats	90
38	Walney 1	184
39	Walney 2	184
40	Walney Extension	659
41	West of Duddon Sands	389

Figure 19 – Offshore wind farms in the Irish Sea [141]

Burbo Bank Extension is chosen as is the most recently built and the most productive wind farm of the five. While its life capacity factor (defined as the ratio between average power and rated peak capacity) is approximately 40%[34], the same parameter for the other four is less than 35%. The wind farm is formed by 32 turbine units, for a total installed capacity of 259 MW. A 24.3 km long undersea cable[35] connects the offshore substation of the farm to the shore. Electrical energy is then brought to the onshore substation at Bodelwyddan by a 10.4 km long onshore cable.

[34] https://energynumbers.info/uk-offshore-wind-capacity-factors
[35] https://www.diamondtransmissionpartners.com/our-projects/burbo-bank-extension-ofto#:~:text=The%20OFTO%20is%20a%20258MW,which%20comes%20ashore%20near%20Bodelwyddan.

Among the water electrolysis technologies, PEM electrolysers are chosen in agreement with the predictions of '*UK Hydrogen Strategy*'. PEM technology is in fact expected to play a major role in the UK hydrogen framework. For the sake of sustainability, it is assumed that PEM electrolyser operates at the same capacity factor of the wind farm. This ensures that only green electricity powers the electrolysis process. PEM electrolyser device is placed in close proximity to the onshore substation at Bodelwyddan with the aim of minimising transmission loss. In the early phase of Trafford Green project, 20 MW will be installed. In order to determine the corresponding maximum hydrogen production capacity in terms of tonnes per year (m_{H_2PEM}) , the following formula is implemented:

$$m_{H_2PEM} = \frac{P_{el} \cdot cf \cdot 8760}{e_{H_2PEM}} = \frac{20[MW] \cdot 0.4 \cdot 8760[h]}{62\left[\frac{MWh}{ton}\right]} = 1130\ tons \qquad (36)$$

where P_{el} is the PEM nominal power, cf is the average annual capacity factor of the wind farm and e_{H_2PEM} is the energy required by the electrolyser to generate 1 ton of H_2. In one of the last report on green hydrogen by IRENA [34], the PEM stack efficiency for the state-of-the-art ranges between 50 – 70% on LHV basis. If BoP energy demand is included, the efficiency drops, varying between 40% and 66%. An average value of 0.53 for system efficiency is considered, equivalent to 62 MWh_{el} to produce 1 ton of hydrogen. PEM electrolysis currently operates between 50 and 80°C, at operating pressures not exceeding 30 bar. However, significant improvements are expected in the next 25 years. The same report sets indeed as target for 2050 an energy consumption of 45 MWh_{el} per ton of hydrogen produced and a H_2 outlet pressure above 70 bar. By comparing the result of Eq. (36) with the train fleet's hydrogen consumption, it can be noted that the initial size of 20 MW planned for the electrolyser is not sufficient. The installed capacity at Trafford Energy Park is nevertheless going to increase up to 200 MW, as mentioned before. It is thus

assumed that PEM size in 2030 will be sufficient to cover the train station's highest hydrogen demand (i.e. 3.26 tons from Table 12), that is when analysis time horizon starts. Rearranging Eq. (36), the minimum power needed to meet the daily 3.26 tons-scenario defined in the '*New Street daily hydrogen demand*' section is:

$$P_{el} = \frac{m_{H_2PEM} \cdot e_{H_2PEM}}{cf \cdot 8760} = \frac{(3.26\,[ton] \cdot 365) \cdot 62\left[\frac{MWh}{ton}\right]}{0.4 \cdot 8760[h]} = 21.1\,MW \quad (37)$$

In addition to electricity, water is the other main input for an electrolyser. For each mole of hydrogen produced, one mole of water has to be supplied. Ideally, water consumption is therefore 9 kg_{H_2O}/kg_{H_2}. Before electrolysis, water must satisfy strict purity requirements and then undergoes demineralisation and purification. During such processes, some water is lost. According to [34], 18 – 24 kg of H_2O may be necessary for each kg_{H_2}. Freshwater availability as well as the impact of water usage on the local ecosystem are issues to be taken into account, especially in a context where hydrogen production from water electrolysis is becoming increasingly important. As the electrolyser is located in a coastal area (less than 10 km from the shore) and in order to not affect the accessibility to freshwater, seawater is supposed to be utilised. Reverse osmosis is the option chosen for desalinisation due to its better energetics and lower footprint compared to competing technologies [142]. About 0.003 MWh_{el} per ton of H_2O are required to desalinate seawater [143]. If an average water consumption of 21 kg_{H_2O}/kg_{H_2} applies, additional 0.063 MWh_{el} of electrical energy must be spent per ton of hydrogen produced.

Before leaving the plant, hydrogen is cooled down to ambient temperature. The obtained heat is used to partially preheat water stream in inlet. The rest of the system's thermal energy demand is assumed to be covered by electrical heaters, whose energy input is already included in the 62 MWh_{el} per ton_{H_2} mentioned before.

The mathematical relation to calculate the efficiency of H_2 generation by PEM electrolysis is outlined below:

$$\eta_{prod,PEM} = \frac{\frac{m_{H_2PEM}}{365} \cdot LHV_{H_2}}{\frac{m_{H_2PEM} + m_{H_2fug}}{365} \cdot \left(e_{H_2PEM} \cdot \frac{1}{\eta_{transm}} + e_{des}\right) + E_{H_2compr} + E_{H_2O-pump}} \quad (38)$$

where m_{H_2PEM} is the H_2 production in ton per year (net of any mass losses), m_{H_2fug} represents the yearly hydrogen leakage during production phase, η_{transm} is the efficiency associated to the transmission of electricity from wind farm to onshore substation, e_{des} (0.063 MWh_{el}/ton_{H_2}) is the energy supplied every day to the desalinisation plant per ton of seawater and $E_{H_2O-pump}$ is the pumping energy in terms of kWh per day to bring water to PEM electrolyser. The role of E_{H_2compr} will be clarified in the next lines. The efficiency $\eta_{prod,PEM}$ will be determined for two different values of m_{H_2PEM}, corresponding to the minimum (2.7 tons/day) and the maximum (3.3 tons/day) train station's hydrogen demand in 2030. It is important to highlight that no parameter characterising the windfarm performance can be found in Eq. (38). This is consistent with the approach taken by *JEC Well-to-Tank report v5* [138], in which the wind energy source is deemed to be unlimited and the wind farm 100% efficient. A different approach is followed in [144], where the windfarm efficiency is equal to capacity factor. In the present analysis, capacity factor has no effect on production efficiency. It is involved instead in the definition of the levelized cost of hydrogen, as it strongly affects the size of the electrolyser. As all the used electricity comes from the wind farm, no PE factor is needed in Eq. (38).

Hydrogen crossover and leakage during H_2 purification process are two of the three main mass loss mechanisms contributing to m_{H_2fug}. The third one is the mass lost through

compressors' seals during compression. An average leakage of 1.38% of the total hydrogen produced is predicted by [145]. The annual H_2 loss is equal to:

$$m_{H_2fug} = \frac{\%m_{H_2fug}}{1 - \%m_{H_2fug}} \cdot m_{H_2PEM} \quad (39)$$

where $\%m_{H_2fug}$ is 0.0138.

High-voltage cross-linked polyethylene AC cables[36] connect the offshore substation to the onshore one at Bodelwyddan. Both [146] and [147] estimate an approximately 2% power loss for a 35 km long HVAC export system design. The value of η_{transm} is then set at 0.98.

As concerns the E_{H_2compr} parameter, it accounts for the daily energy to compress the quantity $\frac{m_{H_2PEM}+m_{H_2fug}}{365}$ from the electrolysis operating pressure to 46 bar. The quantity E_{H_2compr} is hence added to Eq. (38) so the efficiency for the two analysed production pathways (LCH plants and PEM electrolyser) is assessed under the same outlet conditions (20°C and 46 bar). The evaluation of E_{H_2compr} is based on Eq. (40).

$$E_{H_2compr} = {}^{1}/_{\eta_{el,motor}} \cdot W_{compr} \cdot time\ (h) \cdot PE_{el} \quad (40)$$

where W_{compr} is the power absorbed by compressors, PE_{el} has been defined in Eq. (26), time(h) is the time unit and $\eta_{el,motor}$ represents the efficiency of the electric motor. According to HDSAM model developed by Argonne National Laboratory, a proper value for $\eta_{el,motor}$ is 0.94.

In turn, the parameter W_{compr} can be calculated through the following formula:

$$W_{compr} = \frac{\dot{m}}{\eta_{mass}} \cdot Z \cdot R \cdot n_{stages} \cdot T \cdot \frac{k}{k-1} \cdot \left[\beta^{\left(\frac{k-1}{k \cdot n_{stages}}\right)} - 1\right] \cdot {}^{1}/_{\eta_{is}} \cdot {}^{1}/_{\eta_{mec}} \quad (41)$$

[36] https://www.nkt.com/references/burbo-bank-uk

where:

- $\dot{m}$ is the mass flow rate
- Z is the compressibility factor
- R is the gas constant
- n_{stages} is the number of compressor's stages
- T is the inlet temperature
- k is the ratio between c_p/c_v
- β is the overall pressure ratio (= p_{outlet}/p_{inlet})
- η_{is} is the compressor isentropic efficiency
- η_{mec} is the compressor mechanical efficiency
- η_{mass} is the compressor mass efficiency (= m_{outlet}/m_{inlet})

The choice of which values to use for η_{is}, η_{mec}, η_{mass} and n_{stages} depends on size and type of compressor. Given the high flow rates to process and the relatively low pressure ratio requested (46/30 = 1.53), centrifugal compressor type is selected. According to a report by Siemens Energy USA [148], the maximum pressure ratio for hydrogen centrifugal compressors is 1.45. A two-stage compression with intercooling at 20°C and driven by electric motor is hence implemented. As stated in '*Methodology*', the PE factor for green electricity is 1. From now on, unless otherwise specified, cooling energy for intercoolers will be always excluded from compressor's energy demand. It is supposed, in fact, that a body of water approaching an ideal heat sink (i.e. infinite heat capacity) and with a temperature always lower than 20°C is available. No chiller facility is thus needed. The chosen values for isentropic, mass and mechanical efficiencies are 0.8 [149], 0.99 and 0.95, respectively.

A pipeline, following the same route of the onshore cable to Bodelwyddan substation, is supposed to be purposely built to bring water to PEM plant. Seawater is extracted from Irish Sea and desalinised before being pumped into a 10 km long pipe. The calculation of $E_{H_2O-pump}$ is performed by means of Eq. (42).

$$E_{H_2O-pump} = \frac{m_{H_2O_{liq}}}{\rho_{H_2O_{liq}}} \cdot \Delta p \cdot {}^{1}/_{\eta_{pump}} \cdot {}^{1}/_{\eta_{el}} \cdot PE_{el} \quad (42)$$

where $m_{H_2O_{liq}}$ is the water mass pumped daily towards the desalinisation plant, $\rho_{H_2O_{liq}}$ is the water density at 293.15 K and 1 atm (≈ 1000 kg/m^3), η_{pump} is the pump efficiency (≈ 0.75) and η_{el} is the efficiency of the electric motor driving the pump. No relevant changes in pipe elevation occur. The pressure gradient Δp appearing in the formula is therefore equal to the pressure drops across the pipeline. A simple model consisting in a 'PIPE' block is built in Aspen Plus to evaluate Δp. Length, diameter, roughness of pipeline and mass flow rate are the needed inputs for the model. The table below summarises the values adopted.

Scenario	Length (km)	Diameter (mm)	Roughness (mm)	H_2O flow rate (kg/s)
2.7 tons/day	10	80 [150]	0.045[37]	0.66
3.3 tons/day				0.79

Table 16 – Aspen Plus model inputs

The Δp in output is however just a roughly estimation of pressure drops as only frictional losses through Darcy model are accounted by 'PIPE' block.

[37] https://www.worldironsteel.com/news/the-surface-roughness-of-gas-pipeline-44836901.html

The results of Eq. (38) for the two considered hydrogen demand scenarios (2.7 and 3.26 tons per day) are summarised in Table 17, together with the values of all the parameters involved in the calculations.

m_{H_2PEM} (ton/y)	m_{H_2fug} (ton/y)	e_{H_2PEM} (MWh/ton)	e_{des} (MWh/ton)	E_{H_2compr} (MWh/day)	$E_{H_2O-pump}$ (MWh/day)	$\eta_{prod,PEM}$
993	13.9	62	0.063	0.59	0.006	0.517
1190	16.7	62	0.063	0.71	0.007	0.517

Table 17 – Inputs and outcomes of Eq. (38)

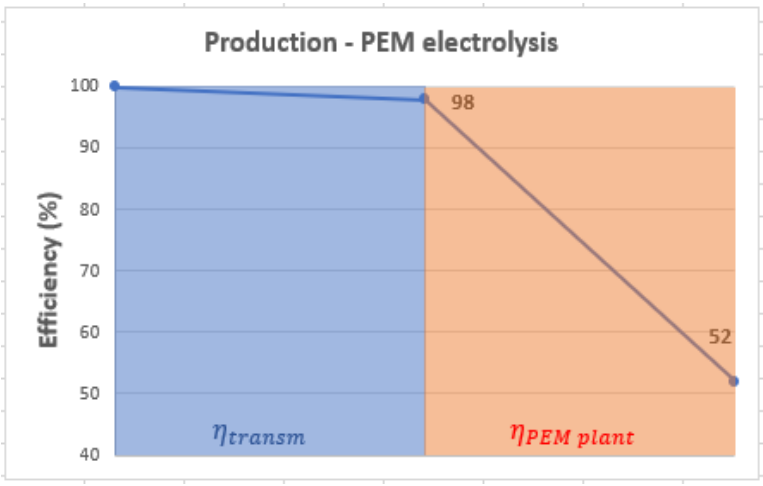

Figure 20 – Overall primary energy efficiency of PEM electrolysis production

The section's results are displayed in Figure 20 and Figure 21. In the pie chart below, it is possible to see how energy losses in the PEM electrolysis plant are mainly due to electrolyser and its BoP, while the contributions of H_2 leakages, water desalinisation and pumping and hydrogen compression to 46 bar are almost negligible.

Based on the overall efficiency of PEM electrolysis production step shown in Figure 20 (i.e. ≈ 52%), around 0.92 kWh of renewable primary energy are expended per kWh of hydrogen produced.

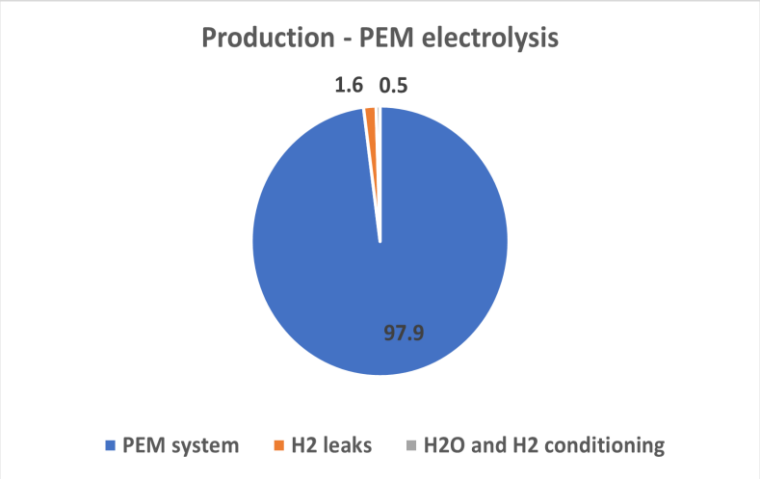

Figure 21 – Relative contribution to energy losses in PEM plant

3.3.8 Carbon dioxide storage efficiency

Compression and injection of CO_2 into depleted offshore gas fields is the only chosen option for carbon dioxide storage. Once again, actual data from HyNet reports [151] [152] [153] will form the framework for calculations.

The definition of energy efficiency given in '*Methodology*' section and the related equation Eq. (25) to calculate it are unsuitable for CO_2 storage process. It is, in fact, not possible to define an energy content for carbon dioxide as it is not a fuel. So, a different strategy is pursued. It consists in modifying Eq. (34) to also include the energy for CO_2 storage. By comparing the result of Eq. (43) with that of Eq. (34), the impact of carbon storage on hydrogen supply pathways can be evaluated (see Eq. (44))

$$\eta_{plant+CCS} = \frac{\dot{m}_{H_2} \cdot LHV_{H_2}}{PE_{el} \cdot E_{el} + \dot{m}_{NG} \cdot LHV_{NG} + E_{CO_2\,path}} \tag{43}$$

$$\eta_{CO_2 storage} = \frac{\eta_{plant+CCS}}{\eta_{plant+CC}} \tag{44}$$

where $E_{CO_2\,path}$ is the overall energy needed per hour for the CO_2 storage process.

The main stages of CCS process are now described, framing them within HyNet context. HyNet CCS feasibility studies consider four mass flow rate scenarios (Low, Baseline, Mid and High) for CCS system. They are characterised by increasing values of CO_2 stored per year (Table 18) and by different operating strategies.

Scenario	Flow rate in 2030 ($MtCO_2$/yr)	Flow rate in 2040 ($MtCO_2$/yr)
Low	0.3	1.2
Baseline	1	3
Mid	1	5.9
High	1	10

Table 18 – Mass flow rate scenarios [153]

In this analysis, the calculation of CO_2 storage efficiency is based on baseline scenario and only the baseline case is thus discussed below.

CO_2 capture

The first step of CCS process is carbon capture. All the capture sources operate at the same fixed pressure. Stanlow refinery, Protos, Ince fertiliser plant and hydrogen production units at Stanlow manufacturing complex are the industrial facilities included in baseline scenario. By 2029, up to 3 $MtCO_2$ per year, equivalent to 105.7 kg/s for a 90% CCS system availability [153], are expected to be captured from plants' air emissions and injected into a low-pressure collector network. It operates at the same working pressure of the capture plants. About 1 $MtCO_2$ per year can be captured from each LCH hydrogen production unit. The contribution of the hydrogen production activity to the total CO_2 captured is highlighted in Table 19.

Scenario	LCH contribution	Total
2030	1 Mt/yr	1 Mt/yr
2040	2.4 Mt/yr	3 Mt/yr

Table 19 – Relative contribution of LCH units to CO_2 capture

CO_2 transport

CCS system network transports the captured carbon dioxide from plants to Douglas platform, in Liverpool Bay Area, where it is stored into gas fields. The network can be divided in two parts, offshore and onshore. The onshore section comprises capture plants, low-pressure collector, pipelines to Point of Ayr (PoA) terminal and the terminal itself. Offshore section's boundaries range instead from Point of Ayr terminal to Liverpool Bay platforms and wells. In order to minimise costs and delay major investments, part of the existing facilities (platforms, wells and pipelines) used for natural gas will be re-purposed for CO_2. It has been also decided to avoid multiphase flow inside pipelines [152]. Since onshore and offshore infrastructures are both designed for single-phase operations, the simultaneous presence of more than one phase could in fact compromise their integrity.

It is possible to identify two different periods in HyNet CCS project lifetime, characterised by as many operating strategies. In the early stages, both onshore and offshore networks will operate in gas phase. A compressor station at each capture plant and another one at Point of Ayr are installed to ensure that CO_2 pressure at platforms is higher than that of the reservoir.

The turning point will occur when pressure inside the field will reach 37 bar. Above this threshold, CO_2 storage can indeed continue only if offshore system is modified to allow liquid phase flow. Not only offshore pipelines, but also Point of Ayr compressor station needs to be upgraded. Figure 22 shows that the trigger point for transition to liquid phase flow is at

37 bar (red-dotted line) for a flowrate of 1 $MtCO_2$, which is the design flowrate for the 2030 scenario.

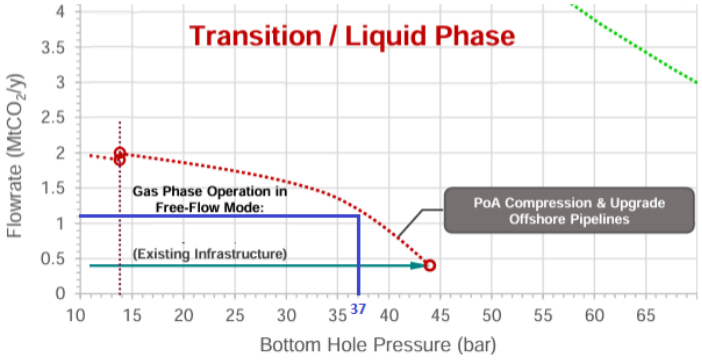

Figure 22 – System constraints map for HyNet CCS project [152]

It will be then resized according to the following consideration: as the highest maximum operating pressure among fields is 115 bar, injection will be feasible in any case only if CO_2 pressure at platform is at least equal to this value. Since an additional pressure gradient is required to overcome the pressure loss across pipelines to fields, an outlet pressure of 126 bar is set for PoA compressor station. Onshore infrastructures remain instead unchanged as they keep processing CO_2 in gas phase.

Figure 23 and Figure 24 display the pathways just described, highlighting the system pressures involved during the two stages of HyNet CCS project. While transport of carbon dioxide in gas phase across the entire network is the option considered for the short-term, offshore system handling liquid CO_2 is instead the most likely scenario from 2030 onwards.

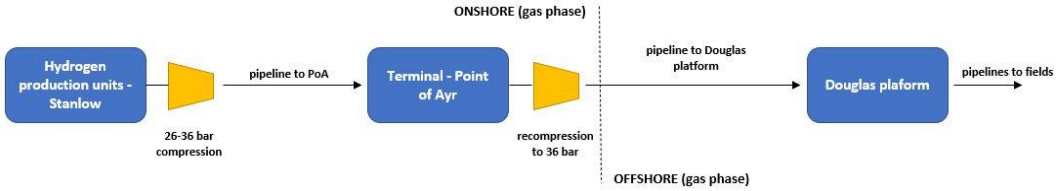

Figure 23 – CO_2 path 1 to fields during 1st stage of HyNet lifetime (scenario 2030)

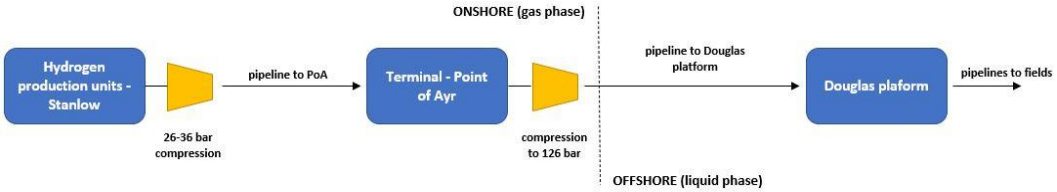

Figure 24 – CO_2 path 2 to fields during 2nd stage of HyNet lifetime (scenario 2040)

Inlet pressure at Point of Ayr terminal could not be found in technical reports and so has to be assessed. Its value depends on the magnitude of pressure drops across Stanlow – PoA pipeline.

Stanlow – PoA pipeline is made of steel and is formed by two sections: the first one, connecting Stanlow complex to Connah's Quay power station, is 33 km long and has an outside diameter of 914 mm; the second section has an outside diameter of 610 mm and travels for 27 km before arriving to Point of Ayr. Two 'PIPE' Aspen Plus blocks are used to assess pressure drops. As no significant changes in the elevation of the pipe are supposed to exist, the variation of the potential energy is negligible. For a more accurate evaluation of the pressure drops, the actual pipeline path should be considered as well as losses through valves, bend pipes and other local components. Length, diameter, roughness of pipeline and mass flow rate are the needed parameters. The table below gathers the inputs required and the model's outputs.

Scenario	Section	Length	Diameter	Roughness	Total mass flow rate	Mass flow rate from LCH units	Pressure drops
2030	1	33 km	914 mm	0.045[38] mm	35.2 kg/s	35.2 kg/s (4 units)	0.1 bar
	2	27 km	610 mm				0.45 bar
2040	1	33 km	914 mm	0.045 mm	105.7 kg/s	84.56 kg/s (4 units)	0.6 bar
	2	27 km	610 mm				4.2 bar

Table 20 – Inputs for 'PIPE' Aspen blocks and obtained pressure drops

[38] https://www.worldironsteel.com/news/the-surface-roughness-of-gas-pipeline-44836901.html

As a consequence, inlet pressure to PoA compressor station is 35.45 bar during the first stage of HyNet CCS project and 31.2 bar after transition to liquid phase flow. Pressure ratio at PoA is now known for both the CO2 paths and then compression work can be finally calculated. Two 'COMPR' blocks simulating pressure boost at Stanlow and PoA are added to Aspen Plus model. When 'isentropic' is specified as compressor type, 'COMPR' block implements the mathematical relation in Eq. (41) for power calculation. Integrally geared centrifugal compressors are assumed to be employed for CO_2 as their application range[39] matches Stanlow and PoA's requirements. The reference values for isentropic efficiency (80%) and single stage maximum pressure ratio (2.5) are taken from [154]. A mechanical efficiency equal to 95% is adopted [155]. As regards compressor mass efficiency, HDSAM model[40] considers a compressor mass efficiency of 99% based on industry experience. To reduce compression work, intercoolers between stages are added. The temperature after each stage cooling is set to 20°C, which is the maximum allowable value in the pipelines due to environmental constraints [153]. Once again, compression is electric driven. In particular, since both Stanlow and PoA are close to the shore, only green electricity from wind farms (i.e. PE_{el} = 1) is supposed to be used. $E_{CO_{2,}compr}$ is then expressed in terms of primary energy to generate the required electricity for compression, as explained in '*Methodology*' section. The formula used for $E_{CO_{2,}compr}$ calculation is:

$$E_{CO_2 compr} = {}^{1}/_{\eta_{el,motor}} \cdot W_{compr} \cdot \alpha_{LCH} \cdot time\ (h) \cdot PE_{el} \qquad (45)$$

where PE_{el} has been defined in Eq. (26), time(h) is the time unit (1 hour), $\eta_{el,motor}$ represents the efficiency of the electric motor, set to 0.94, and α_{LCH} is the contribution of one LCH unit

[39] https://www.siemens-energy.com/global/en/offerings/industrial-applications/compression/co2-compression.html
[40] https://hdsam.es.anl.gov/index.php?content=hdsam

to the total CO_2 mass flow rate. α_{LCH} is equal to 1 for the 2030 scenario and 0.8 for the 2040 one.

Table 21 shows the main parameters, the power output (W_{compr} from Aspen Plus model) and the hourly compression energy $E_{CO_2 compr}$ related to Stanlow and PoA stations.

Station	p_{inlet} (bar)	p_{outlet} (bar)	n_{stages}	β_{tot}	W_{compr} (kW)	$E_{CO_2 compr}$ (MWh)
Stanlow	26	37	1	1.385	1218	1.17
PoA (1st stage)	35.45	37	1	1.016	40.7	0.04
PoA (2nd stage)	31.2	126	2	4.04	13730.7	4.4

Table 21 – Hourly primary energy demand at Stanlow and PoA stations for compression

Energy for CO_2 transport is estimated for both the CO_2 pathways presented above (Figure 23 and Figure 24). During the first stage of HyNet CCS project lifetime, about 1.21 MWh will be spent every hour to move CO_2 from Stanlow complex to platforms. Throughout the second stage, hourly energy consumption will increase to 5.57 MWh due to a higher pressure ratio and mass flow rate characterising PoA terminal.

Table 22 summarises the energy requirements for the two CO_2 operational stages.

Scenario	Operational strategy	$E_{CO_2\ compr}$
2030	Gas - gas	1.21 MWh
2040	Gas - liquid	5.57 MWh

Table 22 – CO_2 paths energy requirements

<u>CO_2 injection and storage</u>

The storage sites for CO_2 are located in Liverpool Bay Area. The offshore gas fields of Lennox, Hamilton Main and Hamilton North have been selected. They will be depleted by 2024 and can potentially store a total of 228 $MtCO_2$ in liquid form [151].

To ensure a safe and permanent storage, CO_2 injection will be stopped as soon as reservoir pressure reaches its initial value at the start of gas extraction. In this way, even at full capacity, operations will be conducted below the fracture pressure of the rocks. Reservoir pressure at the start of CO_2 injection, maximum operating pressure and full capacity are presented for each field in Table 23.

Field	**Pressure at the start of CO_2 injection (bar)** [152]	**Maximum operating pressure (bar)** [153]	**Full capacity ($MtCO_2$ in liquid phase)** [151]
Lennox	10	115	80
Hamilton Main	5.5	97	125
Hamilton North	13.8	106	23

Table 23 – Fields operating features

Injection process is driven by the pressure gradient existing between wellhead and bottom hole location. Point of Ayr compression facility is hence designed so that pressure at the wellheads, after the drop due to friction across pipelines to platforms, is still higher than field's one. No additional energy beyond that already provided by PoA compressor station is considered for injection and so $E_{CO_2 path}$ is equal to $E_{CO_2 compr}$. Pressure ratio at PoA terminal (β_{PoA}) needs therefore to be adjusted over time to overcome the increase in reservoirs pressure. In the absence of an injection profile, the β_{PoA} values in Table 21 correspond to the most energy-intensive circumstances for each stage of the HyNet lifespan. The rationale behind this conservative approach is to assess the biggest impact of CO_2 storage on hydrogen supply pathway efficiency.

Finally, the efficiency for the overall CO_2 storage process can be calculated. As mentioned at the beginning of the section, Eq. (43) and Eq. (44) are used. Below, the outcomes of the calculations are shown:

Scenario	E_{CO_2path}	$\eta_{CO_2storage}$	$\eta_{plant+CCS}$
2030	1.21 MWh	0.997	0.7
2040	5.57 MWh	0.985	0.692

Table 24 – CO_2 storage efficiencies

Thus, for both the scenarios, the effect of CO_2 storage path on LCH energy efficiency is almost negligible.

3.3.9 Hydrogen storage efficiency

The HySecure project [156] is here taken as a reference for the hydrogen storage step. It is part of HyNet context and aims to develop a large-scale bulk hydrogen storage in the Cheshire salt basin. The exact location is on the Stublach Site of the Holford Brinefield. Over two years of construction will be necessary to create the planned cavern. A process known as solution mining is used to form the cavern by dissolving the natural salt below the surface. Water is injected underground through a well previously drilled, determining the formation of the brine. An additional well is dug to dispose the brine. After the completion of the mining, a free volume between 300000 m^3 and 350000 m^3 will be available. The amount of hydrogen that can be stored depends on the cavern operating pressure range. A maximum pressure of 80 bar and a minimum one equal to 30 bar are set for the cavern. Operating within this range protects the integrity of the geological structure. The quantity of hydrogen corresponding to the minimum operating pressure is the so-called ‘cushion gas’. At the end of cavern’s life, it will be recovered and then it does not affect cavern round-trip efficiency. ‘Working gas’ represents instead the operable mass and equals 1100 tonnes of hydrogen (36.3 GWh on LHV basis). Stublach Site storage will be in operation by 2026 and will pave the way for the creation of several other caverns. In reference to HyNet timeline, the working storage capacity will reach in fact a value of 1.3 TWh within a few years.

As in the case of CO_2, hydrogen injection is performed by establishing a pressure gradient between the surface and the cavern. Hydrogen compressors are thus included among surface facilities. The energy for storing hydrogen results from the chosen injection-withdrawal profile. Approximately 40 tonnes of H_2 are expected to be compressed every day in HySecure project. Under the assumption that all the hydrogen involved in cavern operations comes from HyNet LCH units, it follows that around 20% of the H_2 produced at Stanlow complex in 2025 is planned to be stored at Stublach site. Despite HyNet's production and storage capacities may not increase at the same rate, the ratio hydrogen stored/hydrogen produced is supposed to remain constant at 20% throughout the analysis time horizon.

Hydrogen will be delivered to Stublach by pipeline. In the early stages of the project, when H_2 flow is still relatively low (40 tonnes/day), an existing ethylene pipe will be used for hydrogen transport. It currently works with natural gas, so it will be repurposed. After work completion, it will run for 30 km and will be characterised by a diameter of 20 cm. Pipeline operating pressure will be 46 bar.

In order to meet the increase in demand for hydrogen storage capacity, a new pipeline connecting Stanlow to Stublach will be available in the near future. This pipeline, together with three other sections, will be part of the upcoming HyNet hydrogen network. It will operate at 46 bar, same pressure of the H_2 exiting LCH units, and will deliver hydrogen to industrial customers, power generators and storage sites. The figure below shows an overview of the potential routes for the four 'legs' of the network.

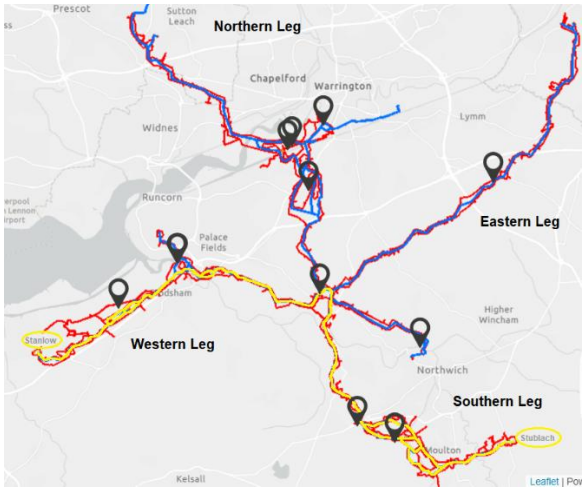

Figure 25 – Hydrogen network[41]

Starting from Stanlow, hydrogen will need first to travel across western leg and then across southern leg before reaching Stublach, for a total of approximately 35 km. The path just described is highlighted in yellow and will be characterised, in its final version, by pipelines up to 107 cm in diameter. If an upper limit of 15 m/s is set for flow velocity [157], a maximum of 4312 tonnes of hydrogen per day can run safely inside pipelines. Cadent Gas Limited company will develop the network. Additional information can be found on the project's dedicated website[42].

The mathematical expression to estimate the efficiency of H_2 storage at Stublach has the following form:

$$\eta_{H_2 storage} = \frac{(m_{H_2 stored} - m_{H_2 fug}) \cdot LHV_{H_2}}{m_{H_2 stored} \cdot LHV_{H_2} + E_{H_2 compr}} \tag{46}$$

[41] https://feedback.hynethydrogenpipeline.co.uk/
[42] https://www.hynethydrogenpipeline.co.uk/the-project/knowledge-hub/

where $m_{H_2 stored}$ is the mass of hydrogen injected daily into the cavern, $E_{H_2 compr}$ is the energy required per day for hydrogen compression before injection and $m_{H_2 fug}$ accounts for the daily H_2 lost due to unintentional releases.

$E_{H_2 compr}$ is determined using Eq. (40) and Eq. (41). Pressure ratio at Stublach needs to be calculated. With regards to inlet pressure, it depends on the pressure drop's extent across the pipeline connecting Stanlow complex to the storage site. Table 25 contains both the parameters entered as inputs to 'PIPE' Aspen block to simulate Stanlow – Stublach section and the model's results. Once again, only the option for the short-term (i.e. 2030 scenario) is here analysed, postponing to a specific section any considerations on how hydrogen network may affect future storage efficiency.

Length (km)	Diameter (cm)	Roughness (mm)	Mass flow (tonnes/day)	Pressure at Stanlow (bar)	Pressure drops (bar)	Inlet pressure (bar)
30	20	0.03 [158]	40	46	5.5	40.5

Table 25 – Inputs to 'PIPE' Aspen block

The outlet pressure at Stublach compressor station cycles between the minimum and the maximum working pressure of the cavern. The conservative approach already seen for CO_2 is applied again for H_2 storage. The resulting pressure ratio is therefore constantly fixed at 80/40.5 (≈ 2). Multi-stage centrifugal compressors with intercooler and driven by electrical motors are assumed to be used. This time, as the distance between Stublach and the shore is not negligible, the required electricity for compression is drawn from the grid (PE_{el} = 1.501). The choice of centrifugal technology, based on the typical application range charts showed in [159], aims to minimise the number of compressor units needed. As already said in '*H2 production – Wind powered water electrolysis*', the maximum pressure ratio for hydrogen centrifugal compressors is 1.45 and hence two stages are necessary. Since

HySecure report [156] supposes a temperature of 20°C to evaluate how much hydrogen can be stored inside the cavern, the same temperature is set for pipelines and intercooling process. The chosen values for isentropic, mass, electric and mechanical efficiencies are 0.8 [149], 0.99, 0.94 and 0.95, respectively. Table 26 summarises the main parameters and the daily energy consumption at Stublach to store hydrogen.

Station	P_{inlet} (bar)	n_{stages}	β_{tot}	E_{H_2compr} (MWh)
Stublach	40.5	2	2	21

Table 26 – Stublach daily energy consumption

The parameter m_{H_2fug} measures H_2 fugitive emissions during the storage process. Hydrogen is lost along the transport route from Stanlow to storage site and due to cavern leakages. As regards hydrogen transport, a study by Frazer-Nash Consultancy [145] estimates an average leakage rate of 0.25% in mass terms from pipelines. Starting from the statistics provided by the National Transmission System, the study derives hydrogen losses by multiplying gas leakages by the ratio between densities of H_2 and natural gas. The same study also predicts a fugitive rate of 0.04% per year for salt cavern, because of salt permeability and surface facilities operations.

Hydrogen storage efficiency is now calculated. By substituting the proper daily values in Eq. (46), it follows that:

$$\eta_{H_2storage} = \frac{(40[ton] - 0.0029 \cdot 40[ton]) \cdot 33.3\left[\frac{MWh}{ton}\right]}{40[ton] \cdot 33.3\left[\frac{MWh}{ton}\right] + 21[MWh]} = 0.98 \qquad (47)$$

Hydrogen storage is then an efficient process and consumes only around 1.02 kWh of primary energy per kWh of hydrogen stored. H_2 storage primary energy efficiency is slightly

lower than that of CO_2 storage due to the use of electricity from the grid and the higher specific compression work per kg_{H2}.

As regards the incidence of compression and fugitive emissions on H_2 storage's energy losses, the latter account for only the 0.3%.

3.3.10 H_2 transportation – compressed hydrogen tube trailers

Hydrogen delivery by trucks is expected to dominate the UK market until a national hydrogen network is developed. One of the three analysed options for H_2 transport from production centre to consumers is represented by tube trailers. Hydrogen is compressed to 200 bar or even higher pressures[43] into metallic or composite storage tanks, which are stacked and then loaded onto a trailer hauled by a truck. Metallic (Type I) vessel, typically made of steel, is the cheapest and most mature technology but can store only approximately 1 - 2 wt% hydrogen at 200 – 300 bar [160]. For instance, an empty 12 meters long vessel from Tenaris[44] weighs 3057 kg and can contain about 52 kg of hydrogen at 300 bar in 2.495 m^3. Therefore, in order to not exceed the load capacity limit, a 40 tons-truck (with a maximum payload of 25000 kg) utilising Type I vessels at 300 bar can carry around 416 kg of H_2. All-composite storage tanks (Type IV) are the lightest among pressure vessels. They can withstand pressures up to 700 bar, achieving gravimetric storage densities close to 5.7 wt% [161]. A 40 tons-tube trailer using Type IV cylinders would thus have a capacity of 1400 kg. However, the high cost of composite materials is slowing down Type IV market penetration. Moreover, safety issues related to the higher operating pressure have still to be addressed. The different effects on transport efficiency of Type I and Type IV storage technologies have been included in the analysis.

[43] https://www.energy.gov/eere/fuelcells/hydrogen-tube-trailers
[44] https://www.tenaris.com/media/opcpmpll/seamless-pressure-vessels-for-gas-transportation-alta-10-2017.pdf

The amount of hydrogen to deliver via trucks to Birmingham depends on H_2 train fleet's demand. In the '*New Street daily hydrogen demand*' section, the daily hydrogen consumption at BNS has been roughly assessed. In the impossibility to determine the actual hydrogen usage of trains, as it would require the knowledge of the real-life driving profile for the selected routes, a range of values has been considered. For the 2030 scenario, station's daily hydrogen consumption varies between 2.7 and 3.3 tonnes (Table 12) but only the boundary values will be taken into account. Below, the equation for hydrogen transport efficiency is introduced.

$$\eta_{H_2 transp-gas\ trucks} = \frac{m_{H_2 out} \cdot LHV_{H_2}}{m_{H_2 in} \cdot LHV_{H_2} + E_{H_2 compr} + n_{trucks} \cdot E_{truck}} \quad (48)$$

where $m_{H_2 in}$ is the mass of hydrogen loaded daily into tube trailers, $m_{H_2 out}$ is the mass discharged per day at train station (2.7 or 3.3 tons), $E_{H_2 compr}$ is energy needed each day to compress $m_{H_2 in}$ up to the operating pressure of storage tanks, n_{trucks} is the number of trucks to transport hydrogen and E_{truck} is the energy in the form of fuel that each trailer consumes for a roundtrip.

One trip per day is assumed for hydrogen delivery. Under this assumption, n_{trucks} is equal to the ratio between $m_{H_2 out}$ and tube trailer's capacity, which in turn depends on the chosen vessel technology (Type I or Type IV). Before proceeding with n_{trucks} calculation, $m_{H_2 in}$ must be determined. The quantity of hydrogen loaded into trucks ($m_{H_2 in}$) differs from that discharged at the station ($m_{H_2 out}$) because of two factors. The first one is linked to the fugitive emissions associated with hydrogen delivery and filling truck processes. A report by Element Energy [162] estimates at 1.5% the total mass lost due to transport. The second factor is related to the fact that tube trailer's usable capacity is always lower than 100%. The values mentioned above for the trucks carrying Type I or Type IV cylinders (i.e. 416 kg and

1400 kg) imply in fact a complete discharge of the trailer once the unloading process at the station has ended. However, in line with HDSAM model, tanks can never be completely emptied. If a minimum tube pressure (p_{min}) of 20 bar is hypothesized, the undischarged hydrogen mass per truck is:

$$m_{H_2 undisch} = \frac{p_{min} \cdot \frac{m_{H_2 trailer}}{\rho_{H_2}}}{R_{H_2} \cdot T \cdot Z_{H_2}} = \frac{2000[kPa] \cdot \frac{416[kg]}{20.86\left[\frac{kg}{m^3}\right]}}{4.157\left[\frac{kPa \cdot m^3}{kg \cdot K}\right] \cdot 293.15[K] \cdot 1.013} = 32[kg] \quad (49)$$

$$m_{H_2 undisch} = \frac{p_{min} \cdot \frac{m_{H_2 trailer}}{\rho_{H_2}}}{R_{H_2} \cdot T \cdot Z_{H_2}} = \frac{2000[kPa] \cdot \frac{1400[kg]}{38.73\left[\frac{kg}{m^3}\right]}}{4.157\left[\frac{kPa \cdot m^3}{kg \cdot K}\right] \cdot 293.15[K] \cdot 1.013} = 58.5[kg] \quad (50)$$

where $m_{H_2 trailer}$ is the maximum capacity of the trailer, ρ_{H_2} is the hydrogen density at vessel's operating pressure and Z_{H_2} is the hydrogen compressibility factor at p_{min}. From Eq. (49) and Eq. (50), the usable capacities for a 40 tons-truck are then 384 kg or 1341.5 kg, if Type I or Type IV cylinders are used, respectively. After including in the calculation the impact of the losses and of the actual tube trailer's capacities, it follows that:

$$n_{trucks} = \frac{m_{H_2 out}}{m_{H_2 trailer} - m_{H_2 undisch}} = \frac{m_{H_2 out}}{m_{H_2 cap}} \quad (51)$$

$$m_{H_2 in} = \frac{m_{H_2 out} + n_{trucks} \cdot m_{H_2 undisch}}{1 - \%m_{H_2 fug}} \quad (52)$$

where $m_{H_2 cap}$ is the usable capacity of the truck.

$m_{H_2 out}$ (kg)	$m_{H_2 cap}$ (kg)	$m_{H_2 in}$ (kg)	n_{trucks}
2700	384 (Type I)	3001	8
2700	1341 (Type IV)	2919	3
3300	384	3675	10
3300	1341	3528	3

Table 27 – number of required trucks per day

It is already possible to draw the first conclusions by analysing the outcomes for n_{trucks} in Table 27. The only feasible options seem to be the transport of 2.92 or 3.5 tonnes through 3 tube trailers carrying Type IV vessels. Managing such a large number of trucks on the road makes the other two scenarios impossible to implement from a logistic and economic point of view, even doubling the trips per day. Despite the foregoing, all four options will be analysed in terms of energy efficiency, neglecting any possible economic considerations as beyond thesis' scope.

Truck loading is performed by means of compressors and is supposed to takes place at Stanlow. As seen in '*Production step efficiency – Natural gas reforming + carbon capture*' section, hydrogen flow exiting from LCH plant is at 46 bar. $E_{H_2 compr}$ is obtained once again by applying Eq. (40). Green electricity from wind farms is utilised for compression. Truck loading compressors must increase inlet pressure to at least 300 bar or up to 700 bar depending on which Type of storage tanks is employed. Given the high discharge pressures required, the choice of which type of compressors to install falls on reciprocating devices with intercooling. Compared to centrifugal technology, they can achieve pressure ratios of 2:1 [148], so allowing to reduce the number of stages needed. The suction temperature of hydrogen at the beginning of each stage is set to 20°C. Again, the assumption of no chiller facility for intercoolers is applied. As concerns η_{mass}, η_{mec} and η_{el}, the same values already mentioned in '*Hydrogen storage efficiency*' section are used. The isentropic efficiency has instead a lower value (i.e. 75%), as the compressor is characterised by a smaller scale compared to the ones installed at Stublach for hydrogen storage. For the sake of clarity, the efficiencies are listed below.

- $\eta_{mass} = 0.99$
- $\eta_{is} = 0.75$

- η_{mec} = 0.95
- η_{el} = 0.94

Table 28 gathers the main parameters involved in the calculation and the obtained results for E_{H_2compr}.

Vessel type	m_{H_2in} (kg)	β_{tot}	n_{stages}	E_{H_2compr} (MWh)
I	3000	6.5	3	3.3
IV	2919	15.2	4	4.9
I	3675	6.5	3	4.0
IV	3528	15.2	4	6.0

Table 28 – Energy needed each day for truck loading

The only left unknown parameter of Eq. (48) is E_{truck}. As stated before, it consists in the fuel energy consumed by each tube trailer to cover the round-trip distance of 293 km between Stanlow and Birmingham New Street Station. Vehicle's fuel usage is retrieved from '*Government conversion factors for greenhouse gas*'[45] publication. For a diesel articulated lorry with a gross weight > 33 tonnes, the document assumes fuel consumptions of 0.423 and 0.26 litres per km for fully laden and unladen conditions, respectively. Since hydrogen is just a small fraction of the carried mass load, 0.423 l/km is the considered fuel usage also for the return trip. E_{trucks} is hence equal to:

$$E_{trucks} = 0.423\left[\frac{l}{km}\right] \cdot 293[km] \cdot 10\left[\frac{kWh}{l}\right] = 1.24[MWh] \quad (53)$$

where 10 kWh/l is the LHV of diesel.

Finally, efficiency of hydrogen transport is assessed through Eq. (48). Calculation's outcomes are presented in Table 29.

[45] https://www.gov.uk/government/collections/government-conversion-factors-for-company-reporting

m_{H2out} (kg)	Vessel type	$\eta_{H2transp}$
2700	I	0.795
2700	IV	0.849
3300	I	0.792
3300	IV	0.864

Table 29 – Results for H_2 transport efficiency through tube trailers

As expected, in addition to reduce road congestion, trucking of hydrogen through Type IV vessels is more efficient than using Type I steel cylinders. There are no significative differences between 8.6 and 10.3 scenario in terms of efficiency.

Figure 26 shows that energy to fuel the trucks is the most energy-intensive element of transport process if Type I vessels are used. On the other hand, if Type IV cylinders are adopted, energy for compression becomes the main contributor.

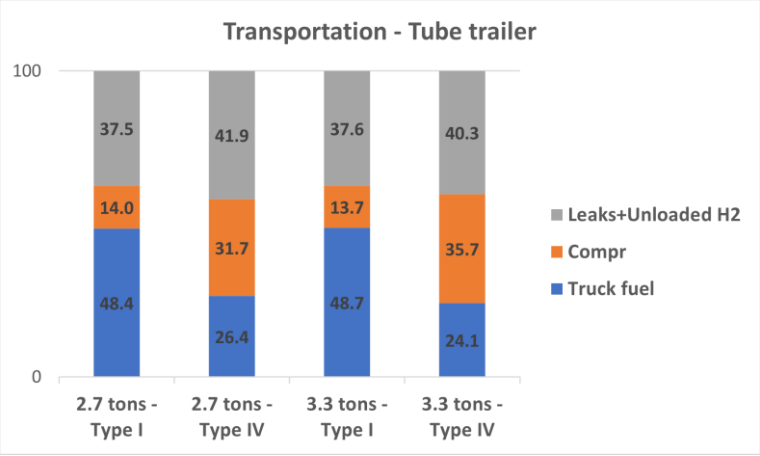

Figure 26 – Percentage incidence of each element on CGH_2 transport losses

3.3.11 H_2 transportation – cryogenic liquid tankers

Liquid hydrogen stored in thermally insulated vessels is a viable solution to overcome the issue of low gravimetric and volumetric storage densities characterising pressurized tanks. According to [163], liquid hydrogen's volumetric density is 80% higher than gaseous H_2 at 700 bar. Hydrogen liquefaction is, however, an energy-intensive process as temperatures

below 20 K are required to turn hydrogen into liquid under atmospheric pressure. Large-scale plants are usually based on Claude cycle [164]. It is a self-refrigeration process (part of the liquid H_2 yield is recirculated) consisting mainly in three stages: compression, cooling and Joule-Thompson expansion. The state-of-the-art specific energy consumption (E_{H_2liq}) for industrial plants is approximately 10 kWh/kg$_{H2}$ but system optimization is expected to reduce this value to 6 – 8 kWh/kg$_{H2}$ in the near future [163]. A liquefaction facility is supposed to be constructed at Stanlow, where liquid tankers filling is also carried out. Liquid hydrogen trailers from *Cryogenic Industrial Solutions (CIS)* company are taken as a reference. CIS claims that the vehicle[46] can carry 4451 kg of liquid hydrogen in about 67.4 m^3 at ambient pressure.

The equation for estimating liquid hydrogen transport efficiency (Eq. (54)) is obtained from Eq. (48) by replacing E_{H_2compr} with the daily pumping energy to load each truck (E_{H_2pump}) and by adding to denominator the energy for liquefaction (E_{H_2liq}).

$$\eta_{H_2 transp-liq\ trucks} = \frac{m_{H_2out} \cdot LHV_{H_2}}{m_{H_2in} \cdot LHV_{H_2} + E_{H_2pump} + n_{trucks} \cdot E_{truck} + E_{H_2liq}} \quad (54)$$

As already outlined for tube trailers, a mismatch between m_{H_2out} and m_{H_2in} exists. For the specific case of liquid trailers, a usable delivery capacity of 95% is assumed in accordance with HDSAM model. A small part of the hydrogen mass (223 kg per truck) is in fact needed in the return trip to keep the tank cold and so is not unloaded. Losses due to boil-off (0.4% per day [162]) from cryogenic trucks increase, albeit slightly, the gap between m_{H_2out} and m_{H_2in}. Table 30 shows the results for n_{trucks} and m_{H_2in} derived by adapting Eq. (51) and Eq. (52) for the liquid hydrogen scenario.

[46] https://www.cryoindsolutions.com/hydrogen

m_{H_2out} (kg)	m_{H_2cap} (kg)	m_{H_2in} (kg)	n_{trucks}
2700	4228	2935	1
3300	4228	3537	1

Table 30 – Daily n_{trucks} and m_{H2in} for H_2 transport through liquid trailers

As regards E_{H_2pump}, trailers are located in the proximity of the liquefaction plant so the energy to bring LH_2 from liquefaction plant to loading bay can be neglected. A short pipeline is supposed to be used. E_{H_2pump} is calculated by means of the following formula:

$$E_{H_2pump} = \frac{m_{H_2in}}{\rho_{H_2liq}} \cdot \Delta p \cdot {}^{1}/_{\eta_{pump}} \cdot {}^{1}/_{\eta_{el}} \cdot PE_{el} \quad (55)$$

where ρ_{H_2liq} is the hydrogen density at 20 K and 1 atm (≈ 71 kg/m^3), η_{pump} is the pump efficiency, η_{el} is the efficiency of the electric motor driving the pump and Δp is a minimum pressure gradient of 100 kPa (i.e. 1 bar) to ensure hydrogen loading into trucks.

Now that all the parameters are determined, the efficiency of hydrogen transport via cryogenic liquid tankers can be evaluated. The findings of Eq. (54) for the two values of hydrogen demand are displayed in Table 31.

m_{H2out} (kg)	$\eta_{H2transp}$
2700	0.714
3300	0.723

Table 31 – Results for liquid H_2 transport efficiency

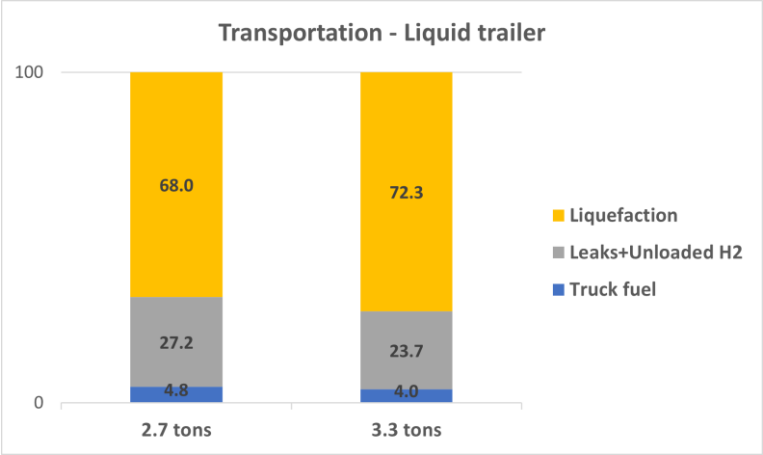

Figure 27 – Relative contribution of each element on LH_2 transport energy consumption

As Figure 27 displays, liquefaction is the most energy consuming element and deeply affects LH_2 transport efficiency. The energy $E_{H_2 pump}$ is negligible.

3.3.12 H_2 transportation – pipelines networks

Hydrogen via pipelines is the last analysed option for the delivery step. As seen in the previous two sections, transporting H_2 on the road can be unfeasible in terms of logistics (tube trailers) or highly energy consuming (liquid tankers). A fundamental role in the transition towards a dense hydrogen network will be played by blending. UK government relies on it to stimulate hydrogen demand growth in the first stages of its Strategy. Blending into the existing gas grid thus represents the most cost-effective solution in the short term to boost hydrogen market. However, as mentioned in '*UK hydrogen scenario*' section, blending will be abandoned in favour of all-H_2 grids due to its high energy consumption. In the following lines, how blending affects transport efficiency is investigated. The scenario involving networks carrying only hydrogen will be addressed in the last part of the section, where a longer-term framework is analysed.

In line with [162], a 20% blending ratio is selected. Under this condition, approximately $1.85 \cdot 10^{10}$ Nm^3 of hydrogen and $7.4 \cdot 10^{10}$ Nm^3 of natural gas are expected to flow every year

through the pipelines if the same overall throughput of energy (808 TWh/year[47]) is maintained. The equation on which transport efficiency by pipelines is based is shown below.

$$\eta_{H_2 transp-pipes} = \frac{m_{H_2 out} \cdot LHV_{H_2}}{m_{H_2 in} \cdot \left(E_{debl} + LHV_{H_2}\right) + E_{H_2 blend} + E_{H_2 compr}} \quad (56)$$

where $E_{H_2 blend}$ is the energy spent every day for transporting only the mass $m_{H_2 in}$ across the network, $E_{H_2 compr}$ is the daily energy demand to boost $m_{H_2 in}$ pressure from 46 bar to 70 bar for injection in the National Transmission System and E_{debl} is the energy for deblending expressed in kWh/kg$_{H_2}$.

The daily amount of hydrogen at the outlet of the grid and ready to be used at Birmingham New Street Station ($m_{H_2 out}$) for our purposes ranges from 2.7 to 3.3 tonnes, between the minimum and the maximum train fleet's demand per day.

Because of the leakages from the gas transmission system, $m_{H_2 in}$ must be increased. Frazer-Nash Consultancy [145] claims that around 0.25% of the hydrogen transported through the gas network is lost. Besides, about 10% of the hydrogen cannot be recovered from blend. On a daily basis, the hydrogen at the inlet of the pipeline network ($m_{H_2 in}$) is therefore equal to:

$$m_{H_2 in} = \frac{m_{H_2 out}}{\left(1 - \%m_{H_2 fug} - \%m_{H_2 debl}\right)} \quad (57)$$

This results in:

$m_{H_2 out}$ (kg)	$m_{H_2 in}$ (kg)
2700	3008
3300	3677

[47] https://www.gov.uk/government/statistics/natural-gas-chapter-4-digest-of-united-kingdom-energy-statistics-dukes

Table 32 – Daily m_{H2in} and m_{H2out}

As concerns $E_{H_2 blend}$, it is inferred from the energy consumption associated with gas grid management. DUKES publication on natural gas[48] states that around 3.7 TWh have been consumed in 2021 by pipeline operators for pumping and on their own sites. Blending changes the energy requirements of the gas network. In fact, because of the lower volumetric energy density of hydrogen, flow rates need to be 16% higher to maintain the same overall energy output if a 20% blending ratio is applied. Energy for compression is then expected to increase by a factor of 1.16. However, the change of the physical properties due to hydrogen injection may result in a deviation from this value. In order to quantify the total effect of blending on transmission system's energy demand, a proper Aspen Plus flowsheet is built. Two simulations are launched: while in the first one 1 Nm^3 per second of natural gas is processed, in the second one the flow rate is brought to 1.16 Nm^3/s and the material stream entering the block is changed into a mixture with 20% of hydrogen blend. All the other settings (pressure ratio, inlet pressure and temperature, compressor efficiency) remain unchanged. Model outcomes show that energy for compression is 1.165 times higher when blending is implemented. The energy needed to compress all the hydrogen in the mixture ($E_{grid\ blend\ H_2}$) is determined by using Eq. (58) and Eq. (59).

$$v_{NG(grid\ NG)} = \frac{E_{output\ grid}}{LHV_{NG}\left[\frac{kWh}{Nm^3}\right]} \qquad v_{NG(grid\ blend)} = 0.8 \cdot \frac{E_{output\ grid}}{0.8 \cdot LHV_{NG}\left[\frac{kWh}{Nm^3}\right] + 0.2 \cdot LHV_{H_2}\left[\frac{kWh}{Nm^3}\right]} \quad (58)$$

$$E_{grid\ blend\ H_2} = 1.165 \cdot E_{grid\ NG} - \frac{E_{grid\ NG}}{v_{NG(grid\ NG)}} \cdot v_{NG(grid\ blend)} \quad (59)$$

[48] https://www.gov.uk/government/statistics/natural-gas-chapter-4-digest-of-united-kingdom-energy-statistics-dukes

where $E_{output\ grid}$ is 808 TWh per year, $E_{grid\ NG}$ is the energy per year for pumping operations (3.7 TWh), $v_{NG(grid\ NG)}$ is the Nm^3 of natural gas transported every year in the all-NG grid scenario and $v_{NG(grid\ blend)}$ corresponds to the normal cubic meters of natural gas running yearly across the pipelines when blending is applied. While the minuend of Eq. (59) represents the transmission system's energy requirements after hydrogen injection, the subtrahend measures the contribution of the natural gas in the mixture to the overall energy demand. Finally, the equation to evaluate $E_{H_2 blend}$ is introduced:

$$E_{H_2 blend} = \frac{E_{grid\ blend\ H_2}}{365} \cdot \frac{m_{H_2 in}}{m_{H_2 grid}} \tag{60}$$

where $m_{H_2 grid}$ is the total quantity of hydrogen flowing daily across the grid. As said before, at the same overall throughput of energy (808 TWh per year), approximately $1.85 \cdot 10^{10}$ Nm^3 of hydrogen are expected to run every year through the pipelines if a 20% blending ratio is applied. Considering the H_2 density equal to 0.089 kg/m^3 at normal conditions, $m_{H_2 grid}$ is 4500 tons. Grid compressors are assumed to be driven by a turbine powered by the H_2-NG mixture. Consistently with the approach set out for electrical compressors (Eq.(40)), a PE factor for the blend must be assessed. Hydrogen is indeed a secondary energy source and here is used in combination with NG to provide work to compressors, just like electricity in the previous sections. Based on the PE generic definition given in [137], the PE factor for the blend can be calculated as follows:

$$b = \frac{0.2 \cdot LHV_{H_2}\left[\frac{kWh}{Nm^3}\right]}{0.8 \cdot LHV_{NG}\left[\frac{kWh}{Nm^3}\right] + 0.2 \cdot LHV_{H_2}\left[\frac{kWh}{Nm^3}\right]} \tag{61}$$

$$PE_{blend-CCS\ H_2} = 1 + b \cdot \frac{1}{\eta_{plant+CCS}} \qquad PE_{blend-PEM\ H_2} = 1 + b \cdot \frac{1}{\eta_{prod,PEM}} \tag{62}$$

where ρ_{NG} and ρ_{H_2} are the NG and H_2 densities at normal conditions, $PE_{blend-CCS\,H_2}$ is the blend's PE factor if CCS-based hydrogen is used and $PE_{blend-PEM\,H_2}$ if hydrogen is instead produced via PEM electrolysis. The result of Eq. (62) includes, in fact, the primary energy spent both in hydrogen production process and in all the activities that precede the H_2 injection into the pipelines. Eq. (60) is then modified to incorporate the effect of PE factor. It becomes:

$$E_{H_2 blend} = \frac{PE_{blend} \cdot E_{grid\ blend\ H_2}}{365} \cdot \frac{m_{H_2 in}}{m_{H_2 grid}} \tag{63}$$

Before being usable as high purity hydrogen, H_2 must be separated from natural gas by means of a deblending process. Separation is achieved thanks to the synergy between pressure swing adsorption technology and proper selective membranes. Energy is required and not all the hydrogen can be recovered from the blend. According to [162], 3.7 kWh per kg of hydrogen have to be spent for deblending (E_{debl}).

$E_{H_2 compr}$ is essential to increase the pressure of the hydrogen stream leaving LCH plants up to the working conditions of the National Transmission System. Depending on the zone, NTS operating pressure can be as high as 95 bar [165]. Figure 28 shows that the pipelines around Stublach can operate at a maximum pressure of 70 bar. Therefore, prior to injection into the grid, compressors must be able to develop a pressure ratio of 70/46 ≈ 1.52.

Figure 28 – UK grid map[49]

Centrifugal compressors are usually the preferred choice for pipeline applications[50]. As already mentioned, they are characterised by a maximum pressure ratio of 1.45 per stage and so a two-stage machine is necessary. Eq. (40) and Eq. (41) are used to estimate $E_{H_2 compr}$. The 20% hydrogen blend is supposed to power these compressors and so Eq. (40) has to be modified to also account for the impact of PE_{blend}. The new equation is:

$$E_{H_2 compr} = {}^{1}/_{\eta_{engine}} \cdot W_{compr} \cdot 24\ (h) \cdot PE_{blend} \tag{64}$$

where η_{engine} is the efficiency of the gas turbine driving compressor. The value for η_{engine} is 0.39 and is taken from the technical datasheet[51] of a Mitsubishi turbine.

For the sake of clarity, all the parameters involved in Eq. (56) and the corresponding outcomes are gathered in Table 33.

[49] https://www.nationalgrid.com/gas-transmission/document/133611/download
[50] https://www.energy.gov/eere/fuelcells/gaseous-hydrogen-compression
[51] https://power.mhi.com/products/gasturbines/technology/mechanical-drive-applications

m_{H_2out} (ton)	m_{H_2in} (ton)	E_{debl} (MWh/ton)	E_{H_2blend} (MWh/day)	E_{H_2compr} (MWh/day)	$\eta_{H_2transp-pipes}$
2.7	3.0	3.7	1.61	0.21	0.795
3.3	3.67	3.7	1.97	0.26	0.795

Table 33 – Eq. (56) inputs and outcome

Based on the $\eta_{H_2transp-pipes}$ values obtained, delivering hydrogen via pipelines is as efficient as transporting it through tube trailers but the first do not cause road congestion.

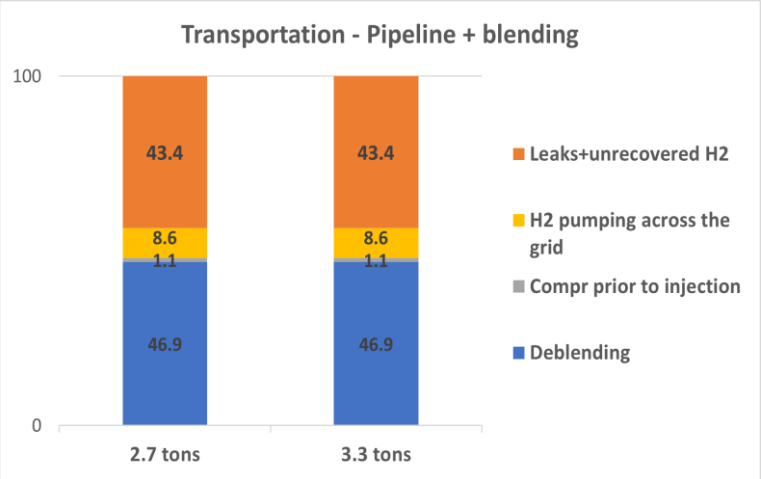

Figure 29 – Percentage incidence on transport losses of each element

After switching to an all-H_2 grid, much higher transport efficiencies are expected to be achieved. Starting from Eq. (56), the formula to calculate the efficiency in the all-H2 grid scenario is:

$$\eta_{H_2transp-pipes} = \frac{m_{H_2out} \cdot LHV_{H_2}}{m_{H_2in} \cdot LHV_{H_2} + E_{H_2\,grid} + E_{H_2compr}} \tag{65}$$

where

$$m_{H_2in} = \frac{m_{H_2out}}{\left(1 - \%m_{H_2fug}\right)} \tag{66}$$

$$m_{H_2grid} = \frac{E_{output\ grid}}{LHV_{H_2}} \cdot \frac{1}{365} \tag{67}$$

$$E_{H_2\,grid} = PE_{H_2} \cdot \frac{E_{grid\,NG}}{365} \cdot \frac{LHV_{NG}}{LHV_{H_2}} \cdot \frac{m_{H_2in}}{m_{H_2grid}} \quad (68)$$

$$E_{H_2compr} = {}^{1}/_{\eta_{engine}} \cdot W_{compr} \cdot 24\ (h) \cdot PE_{H_2} \quad (69)$$

m_{H_2out} (ton)	m_{H_2in} (ton)	E_{H_2grid} (MWh/day)	E_{H_2compr} (MWh/day)	$\eta_{H_2transp-pipes}$
2.7	2.71	2.35	2.45	0.947
3.3	3.31	2.87	2.98	0.947

Table 34 – Eq. (65) inputs and output

Table 34 proves that an all-H_2 grid scenario allows to transport hydrogen more efficiently. Besides, as Figure 30 shows, compression from 46 to 70 bar required for hydrogen injection into the grid (i.e. E_{H_2compr}) becomes the most affecting element.

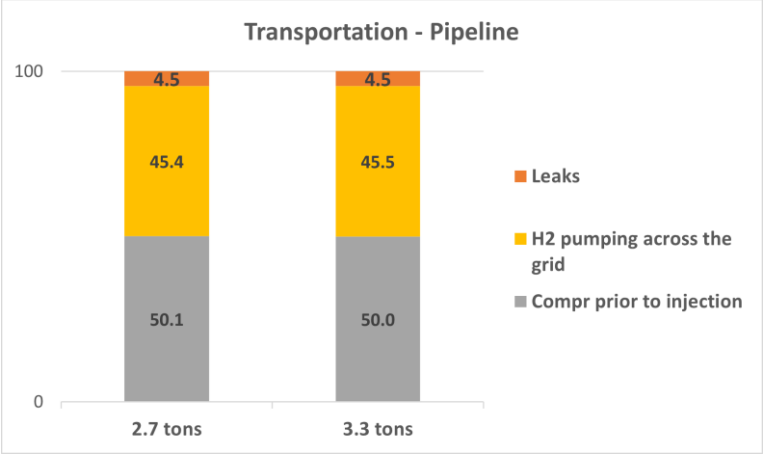

Figure 30 – Relative contribution on energy losses

3.3.13 H_2 production – on-site electrolysis

The third and last H_2 production option consists in generating hydrogen directly at the refuelling station where it is later dispensed to the trains. The selected technology to produce hydrogen is electrolysis by means of PEM electrolysers. The reasons behind the choice have already been discussed in the '*H_2 production – Wind powered water electrolysis*'

section. Before calculating the efficiency of production, the size of PEM plant is defined. The design criterion is to install as many kW_{el} of electrolysers as needed to meet the hydrogen demand of the fleet. Rearranging Eq. (36), it follows that:

$$P_{el} = \frac{m_{H_2PEM} \cdot e_{H_2PEM}}{cf \cdot 24} \tag{70}$$

where P_{el} is the desired size, m_{H_2PEM} is 2.7 tons or 3.3 tons per day, cf is the capacity factor of PEM plant and e_{H_2PEM} is the electrical energy to produce one ton of hydrogen (i.e. 62 MWh/ton). As the electrolysers are driven by grid electricity, they can be run almost continuously. A capacity factor of 0.9 is so chosen, much higher than that assumed for the PEM plant seen in the '*H_2 production – Wind powered water electrolysis*' section. The outcomes of Eq. (70) for the two analysed demand scenarios can be found in Table 35.

Scenario	Size (MW)
3.3 tons/day	9.5
2.7 tons/day	7.8

Table 35 – PEM plant sizes for the on-site electrolysis option

Another major difference between the on-site electrolysis option and the wind powered electrolysis case is where water is withdrawn. To not affect the freshwater availability, the latter employs seawater as raw material. Thus, the construction of a desalinisation plant near the onshore substation serving the wind farm has been envisaged. Seawater is treated by reverse osmosis and thereby pumped to the PEM plant. The same does not apply for the on-site electrolysis. In fact, given the remarkable distance of Birmingham from the coast, the utilisation of desalinated seawater is not a viable solution and water is taken from the water network. Although this results in a lower energy consumption, the effect on city's water reserves might be so remarkable to make the plant not feasible.

The equation for evaluating the on-site electrolysis production efficiency is obtained from Eq. (38) by setting $E_{H_2O-pump}$ and e_{des} equal to zero, where the first term is the energy that would be spent daily to pump seawater from the withdrawal point to the desalinisation facility, while the second is the electricity demand to desalinate one kg of water. Moreover, since PEM electrolysers are not powered by green electricity only but by the grid, the primary energy factor PE related to the UK energy mix is considered. So, Eq. (38) becomes:

$$\eta_{prod,on-site\ PEM} = \frac{m_{H_2PEM} \cdot LHV_{H_2}}{\left(m_{H_2PEM} + m_{H_2fug}\right) \cdot \left(LHV_{H_2} + PE_{grid} \cdot e_{H_2PEM} \cdot \frac{1}{\eta_{transm}}\right) + E_{H_2compr}} \quad (71)$$

In a 2019 report by the National Grid ESO [166], the electrical energy losses over the transmission network amount to 1.7% of the electricity transferred. The parameter η_{transm} is then set to 0.983. As concerns m_{H_2fug}, the same value seen in the '*H_2 production – Wind powered water electrolysis*' section is here utilised too. Finally, E_{H_2compr} is once again estimated through Eq. (40) and Eq. (41). A single stage reciprocating compressor is sufficient to increase hydrogen pressure from 30 bar to 46 bar. At the end of compression, H_2 is cooled down to room temperature (i.e. 20°C).

The efficiency of the on-site electrolysis production option for both the hydrogen demand scenarios are presented in Table 36. It also contains the values of all the parameters embodied in Eq. (71).

m_{H_2PEM} (ton/day)	m_{H_2fug} (kg/day)	e_{H_2PEM} (MWh/ton)	η_{transm}	PE_{grid}	E_{H_2compr} (MWh/day)	$\eta_{prod,on-site\ PEM}$
3.3	46	62	0.983	1.501	1.07	0.345
2.7	37	62	0.983	1.501	0.88	0.345

Table 36 – Main parameters and results for the on-site electrolysis production scenario

The efficiencies in Table 36 are around 34% lower than those of the off-site PEM electrolysis plant. The reduction is due to the use of grid electricity instead of green energy from wind farms.

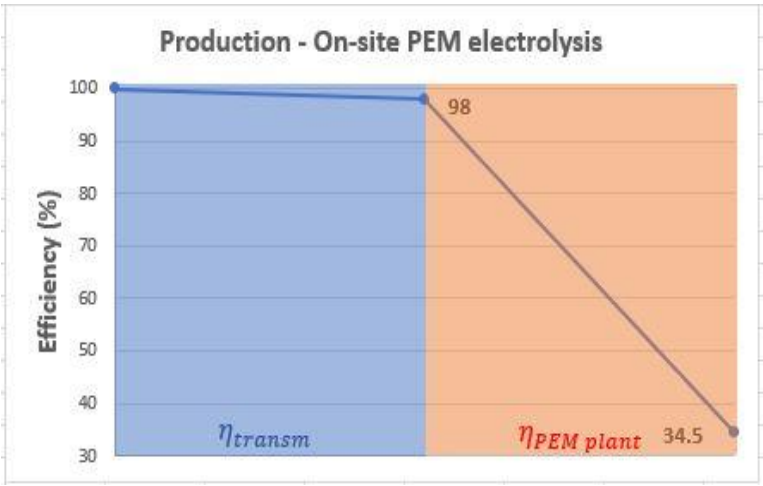

Figure 31 – Primary energy efficiency of on-site electrolysis plant

3.3.14 Hydrogen Refuelling Station

The second part of the WTT analysis is focused on the Hydrogen Refuelling Station (HRS) energy efficiency calculation.

The technical features characterising the infrastructure of the refuelling station depend both on in which state hydrogen is delivered and on dispensing pressure. Unlike cars, where hydrogen is stored at 700 bar, weight and volume constraints for trains are less strict and a dispensing pressure of 350 bar is hence adopted. The reasons behind this choice are manifold, such as less energy for hydrogen compression and the opportunity to deploy less complex components for the refuelling station. Moreover, hydrogen precooling to -40°C before dispensing is no longer required.

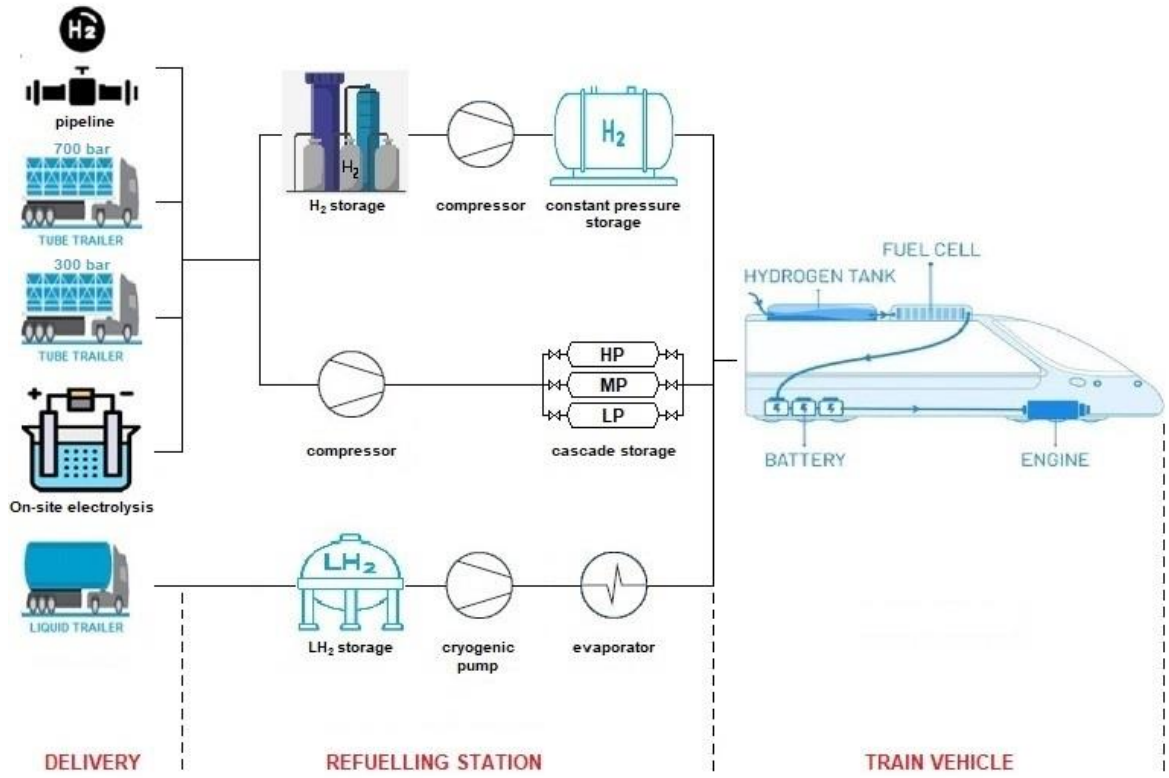

Figure 32 – HRS dispensing options

As Figure 32 shows, three different HRS concepts have been selected for the analysis. To make use of the delivery pressure level and avoid inefficiencies, the operating pressure chosen for the gaseous storage module at the HRS is never lower than that of hydrogen delivery. As a consequence, the HRS layout equipped with booster compressors is not taken into account when 700 bar-tube trailer is the delivery choice.

In one of the supporting documents developed for the *NewBusFuel Project* [167], the most important HRS concepts are described. Each of them is formed by four main modules: delivery or production, compression, storage and dispensing. H_2 can be supplied to the HRS in gaseous or liquid form. If hydrogen is transported as a gas, it can be delivered via pipelines or by means of tube trailers. On the contrary, once liquefied, the only analysed supply option for hydrogen is the on-road transportation through cryogenic liquid tankers. In addition to

the off-site hydrogen routes just mentioned, an on-site solution using PEM electrolyser for production is also examined. The form of the delivered hydrogen also dictates the technologies employed for compression and storage. Liquid H_2 is transferred from liquid tankers to a dedicated highly insulated storage working at nearly atmospheric pressure. When refuelling is needed, cryogenic pumps move hydrogen towards the dispenser unit. Before dispensing, H_2 is processed by an appropriate evaporator to meet the most suitable thermodynamic conditions for refuelling.

As regards gaseous hydrogen, two different ways of handling it are possible, resulting in as many HRS layouts. If H_2 is stored above the pressure level at which the train's tank operates (i.e. 350 bar), the existing pressure gradient between the releasing and the receiving storage vessels can be exploited to drive the refuelling process. The hydrogen storage of the station is often subdivided into a certain number of storage banks operating at different pressure levels. Such a concept is known as cascade storage. However, it should be noted that hydrogen can overflow only as long as a pressure difference between the involved tanks persists. Therefore, a complete fill-up of the vehicles can be carried out without the need of compressors only if storage overcapacities are installed at the HRS. If the choice is instead to store hydrogen below 350 bar, booster compressors are used during the refuelling to transfer H_2 from the storage to the trains' tanks. In this case, minimum overcapacities have to be implemented as compressors can draw almost the entire quantity of hydrogen from the storage.

The last module constituting an HRS is the dispensing unit. It represents the interface between the trains and the station. In addition to the dispenser, the fuel line also includes a breakaway, hoses, nozzles, pipes and valves. The Society of Automotive Engineers (SAE) has standardised the refuelling process. Depending on the mass flow through the fuel line

(i.e. refuelling speed), it differentiates between slow (up to 1.8 kg/min), normal (up to 3.6 kg/min) and fast fuelling (up to 7.2 kg/min). SAE identifies a fundamental safety-related objective too. In particular, hydrogen temperature and pressure inside the vehicle tank must not exceed the operational limits, which are 85°C and 437.5 bar. Pre-cooling of hydrogen before it reaches the dispenser may be necessary to remain within the safe range, especially when fast refuelling is desired. The main mechanisms causing the increase of hydrogen temperature in the train's tank during the refuelling are listed hereafter: the conversion of the incoming hydrogen flow's kinetic energy into internal energy, the gas compression inside the tank, the heat flux from the surroundings and the negative Joule-Thomson effect due to the pressure drop across the fuel line [168].

It is assumed that the refuelling operations for the entire fleet are conducted overnight, within a time window of 5 hours. Trains are filled in parallel and a fuelling rate of 7.2 kg/min is adopted. According to the HDRSAM model by the Argonne National Laboratory[52], given the pressure ramp rate resulting from the desired fuelling speed, the maximum dispensing temperature to prevent tank overheating is set at 5°C. If hydrogen in the storage is deemed to be in equilibrium with ambient temperature (i.e. 20°C), the pre-cooling unit must be sized to cool down the H_2 flow by 15 degrees.

The HRS is supposed to be built as close as possible to the train station. New Street Station lies in the heart of Birmingham urban area and thus space constraint becomes a critical issue when designing the HRS, especially if gaseous H_2 is to be handled. So, whilst the refuelling station with booster compressors has the minimum amount of storage overcapacities, the HRS exploiting overflow filling mechanism takes advantage of the higher

[52] https://hdsam.es.anl.gov/index.php?content=hdrsam

pressures to store hydrogen. The estimation of the space occupied by the refuelling station layouts involves several elements and therefore requires a more thorough evaluation, which is beyond the scope of the thesis. The energy efficiencies of the three selected designs are now determined.

HRS with storage working below 350 bar and booster compressors

As Figure 32 evidences, the HRS concept considered in the present section can be supplied with all the gaseous H_2 delivery paths included in the analysis, with the exception of the 700 bar-tube trailers option. The choice of the operating pressure for the hydrogen storage plays a central role in the HRS design. In order to minimise the footprint of the storage module, H_2 is stored at a pressure as close as possible to the upper boundary of 350 bar. For the sake of simplicity, the chosen value (i.e. 300 bar) corresponds to the highest pressure among those characterising the three compatible delivery pathways.

The efficiency of the refuelling station is calculated on the basis of the following equation:

$$\eta_{HRS_{<350\,bar}} = \frac{m_{H_2 disp} \cdot LHV_{H_2}}{m_{H_2 delivered} \cdot LHV_{H_2} + E_{unload-store} + E_{disp} + E_{cool}} \quad (72)$$

where $m_{H_2 disp}$ is the daily amount of hydrogen entering trains' tanks, $m_{H_2 delivered}$ is the hydrogen mass arriving on a daily basis at the HRS, $E_{unload-store}$ is the energy consumed each day by compressors to store H_2 at the HRS, E_{disp} is the daily energy needed to dispense hydrogen and E_{cool} is the energy required every day by the pre-cooling unit.

As stated in '*H_2 transportation – compressed hydrogen tube trailers*' section, not all the carried hydrogen can be discharged at the HRS. The effect of the incomplete unloading has been already assessed and included in the calculation of the H_2 transport efficiency. In fact, despite the discharging takes place within the HRS boundary, the usable capacity is an

intrinsic property of the trailers and thus addressed as such. The magnitude of the hydrogen mass unloaded already takes into account the above-mentioned effect.

The first term of Eq. (72) to specify is $m_{H_2 disp}$. Because of the fugitive emissions connected to each process undergone by H_2, not all the hydrogen supplied to the HRS reaches the vehicle's tank. The relation between $m_{H_2 disp}$ and $m_{H_2 delivered}$ is expressed by the equation below.

$$m_{H_2 disp} = m_{H_2 delivered} - m_{H_2 fug,HRS} = m_{H_2 disp} - \left(m_{H_2 fug,stor} + m_{H_2 fug,compr}\right) \quad (73)$$

According to the study coordinated by Frazer-Nash Consultancy on fugitive hydrogen emissions [145], the two main contributions to $m_{H_2 fug,HRS}$ are the leakages from the pressurised vessels forming the HRS storage system ($m_{H_2 fug,stor}$) and those through compressors' seals ($m_{H_2 fug,compr}$). An average emission rate of 0.18% per day from compressed gas tanks is assumed by [145]. Approximately 9.7 kg (2.7 tons scenario) and 11.9 kg (3.3 tons scenario) of hydrogen are then lost daily if the HRS storage is sized to have an autonomy of 2 days. As regards leakages during compression, they are quantified by means of the compressor mass efficiency η_{mass}. Since η_{mass} is 0.99, it means that 1% of the H_2 processed by compressors permeates through seals every day, so being lost in the environment. The overall daily fugitive emission characterising the HRS and the amount of hydrogen entering each day the trains' tanks are reported in Table 37.

Scenario	$m_{H_2 fug,stor}$	$m_{H_2 fug,compr}$	$m_{H_2 fug,HRS}$	$m_{H_2 disp}$
2.7 tons/day	9.7 kg/day	27.3 kg/day	37 kg/day	2663 kg/day
3.3 tons/day	11.9 kg/day	33.3 kg/day	45.2 kg/day	3255 kg/day

Table 37 – Fugitive emissions from HRS

The evaluation of $E_{unload-store}$ is based on Eq. (40). The power absorbed by compressors (W_{compr}) is once again computed with the help of the Aspen block 'COMPR'. The first step implies the determination of the compressors' pressure ratio β (p_{outlet}/p_{inlet}). The outlet pressure matches that of hydrogen storage, which has been set to 300 bar. As regards inlet pressure, it differs depending on how hydrogen is delivered to the HRS. The table below summarises the inlet and outlet pressure values for the three supply paths.

Path	p_{inlet} (bar)	p_{outlet} (bar)
pipeline	70	300
300 bar-tube trailer	?	300
on-site electrolysis	30	300

Table 38 – Inlet and outlet pressures of unloading compressors

While for pipeline and on-site electrolysis routes the suction pressure seen by compressors is constant, the same cannot be said for the 300 bar-tube trailer option. During the unloading, the pressure in the truck vessel gradually decreases until it reaches the minimum value of 20 bar (see p_{min} in the '*H_2 transportation – compressed hydrogen tube trailers*' section). More and more energy is therefore necessary to draw and transfer hydrogen from the trailers to the storage as the unloading goes on. To estimate how hydrogen pressure inside the tube trailer (p_{truck}) varies throughout the discharging, Eq. (74) is used.

$$p_{truck}(t) = \frac{m_{H_2 truck}(t) \cdot Z_{H_2}(p_{truck}) \cdot R_{H_2} \cdot T(t)}{V_{truck}} \quad (74)$$

where $m_{H_2 truck}(t)$ is the mass in kg of H_2 in each 300 bar-tube trailer at time t and V_{truck} is the volume in m^3 of the truck tank. It is assumed that the discharge flow rate and the temperature of the hydrogen in the trucks remain constant and respectively equal to the compressor's throughput and 20°C for all the duration of the unloading. These assumptions allow both to eliminate the dependence on time of the temperature and to know how much

hydrogen is in the trailer at any time t. The compressibility factor Z_{H_2} is, in turn, a linear function of p_{truck}. The dependence of Z_{H_2} upon p_{truck} is retrieved from NIST data[53] and can be expressed as follows:

$$Z_{H_2}(p_{truck}) = 6.928 \cdot 10^{-4} \cdot p_{truck}(t) + 9.974 \cdot 10^{-1} \quad (75)$$

where p_{truck} is measured in bar. By substituting Eq. (75) into Eq. (74) and rearranging the resulting equation, p_{truck} becomes equal to:

$$p_{truck}(t) = \frac{9.974 \cdot 10^{-1} \cdot m_{H_2 truck}(t) \cdot R_{H_2} \cdot T}{100 \cdot V_{truck} - 6.928 \cdot 10^{-4} \cdot m_{H_2 truck}(t) \cdot R_{H_2} \cdot T)} \quad (76)$$

where R_{H_2} is in kJ/kg/K and V_{truck} in m^3.

Figure 33 shows graphically the trend of p_{truck} as it approaches p_{min} and how pressure ratio has to change during the unloading.

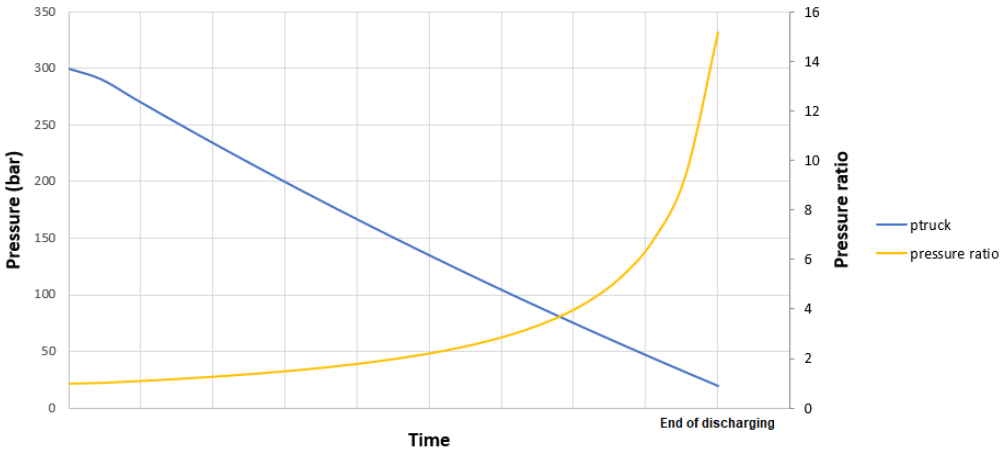

Figure 33 – p_{truck} and β variations with time – 300 bar trailer

Now that inlet and outlet pressures of unloading compressors are known for all the three pathways, another crucial factor to consider is the compressors' daily running time. A technical document [169] from Linde Group sets the time needed to unload each truck and

[53] https://webbook.nist.gov/chemistry/fluid/'

fill the HRS storage at approximately 2 hours. Supposing to implement a parallel discharging scheme where half of the tube trailer fleet is unloaded simultaneously, the total discharging time will be 4 hours, both for the 2.7 and 3.3 tons scenarios. For the pipeline and on-site electrolysis paths, the assumption is that storage compressors are in operation outside the refuelling time window, so for 19 hours per day. Reciprocating compressors are installed at HRS, that is the same hypothesis made by the HDRSAM model. As previously stated, this type of compressors can achieve pressure ratios of 2:1 for a single stage. An intercooler between each stage cools the hydrogen gas, bringing it back to the original feed temperature (T_{truck} = 20°C). Due to the urban location of the HRS, a natural body of water as ideal heat sink for intercoolers is no longer a reasonable assumption. A viable solution is represented by cooling towers. To cool down the water, they make use of power driven fans to force or draw air through the tower. Eq. (40) is hence modified as follows to include cooling towers' energy requirements:

$$E_{unload-store} = \left({}^{1}/_{\eta_{el,motor}} \cdot W_{compr} \cdot time(h) + E_{towers}\right) \cdot PE_{el} \quad (77)$$

where E_{towers} is the energy consumed by the cooling tower fan motors and time(h) is the daily running time of compressors. The relationship between E_{towers} and the amount of heat that cooling towers need to dissipate is derived from an actual datasheet by Vistech company[54]. According to it, about 6.5 Wh of electrical energy are required for each kWh of heat. Therefore, E_{towers} can be calculated as:

$$E_{towers} = \sum_{i=1}^{n_{stages}} Q_{int,i} \cdot time(h) \cdot 6.5 \cdot 10^{-3} \quad (78)$$

where $Q_{int,i}$ is the size in kW of the intercooler associated with the i-th stage

[54] https://www.vistechcooling.co.uk/product/ewk-moducell/

As concerns η_{mass}, η_{mec} and η_{is}, the same values already chosen for the '*H2 transportation – compressed hydrogen tube trailers*' section are selected. Electric motors are employed as prime movers to drive the compressors. The required electric energy is taken from the grid and thus the corresponding primary energy factor PE_{el} has to be considered. Its value for the UK energy mix is 1.501. For clarity, Table 39 and Table 40 are introduced. While the first gathers all the main parameters involved in the $E_{unload-store}$ calculation, the second displays the results for the three delivery routes, both for 2.7 and 3.3 tons scenarios.

Path	β_{tot}	n_{stages}	η_{is}	η_{mec}	η_{el}	η_{mass}
pipeline	4.3	2	0.70	0.95	0.94	0.99
300 bar-tube trailer	1 – 15	4	0.75 – 0.65[55]	0.95	0.94	0.99
on-site electrolysis	10	4	0.67	0.95	0.94	0.99

Table 39 – Main parameters to calculate $E_{unload-store}$

Scenario	Path	$E_{unload-store}$ (MWh/day)
2.7 tons/day	pipeline	3.73
	300 bar-tube trailer	2.72
	on-site electrolysis	5.94
3.3 tons/day	pipeline	4.56
	300 bar-tube trailer	3.33
	on-site electrolysis	7.24

Table 40 – Results for $E_{unload-store}$

The estimation of E_{disp} is performed following the same pattern just seen for $E_{unload-store}$. Storing hydrogen below the operating pressure of the train's tank necessitates booster compressors to refuel the fleet. They are operational only during the refuelling, working then

[55] A range of values for efficiency is considered. This is because of the decrease in compressor's performance as the pressure ratio increases (source: Polytropic Efficiency - an overview | ScienceDirect Topics)

5 hours per day. Their task is to move hydrogen from the storage to the vehicle's tank and, in doing so, they must increase H_2 pressure up to the target for refuelling. Taking as reference the HDRSAM model, booster compressor discharge pressure (i.e. p_{outlet}) is set at 457 bar. This value is given by summing a further 20 bar gradient to the maximum allowable pressure inside the train's hydrogen vessel. The evaluation of p_{inlet} is instead more challenging. In fact, for all the three paths, the suction pressure of the compressors corresponds to that inside the storage ($p_{storage}$), which decreases as H_2 is drawn out for the refuelling process. In order to obtain for $p_{storage}$ a mathematical relation like the one derived for p_{truck} (Eq.(76)), the storage has to be first sized. In particular, it is dimensioned so that the HRS can have an autonomy of 2 days. This means that the storage capacity must be large enough to contain 5.4 or 6.6 tons of hydrogen gas, depending on the analysed scenario. As the H_2 density at 300 bar and 20°C is 20.86 kg/m^3, the needed total volume $V_{storage}$ is 113 m^3 or 138 m^3. By replacing V_{truck} with $V_{storage}$ in Eq. (76), the trend over time of $p_{storage}$ is derived. Figure 34 shows the variations of $p_{storage}$ and β during the refuelling time. Since the criterion behind the storage sizing (i.e. 2 days of autonomy) is the same for both the 2.7 and 3.3 demand scenarios, just two curves, one for $p_{storage}$ and one for β, are presented.

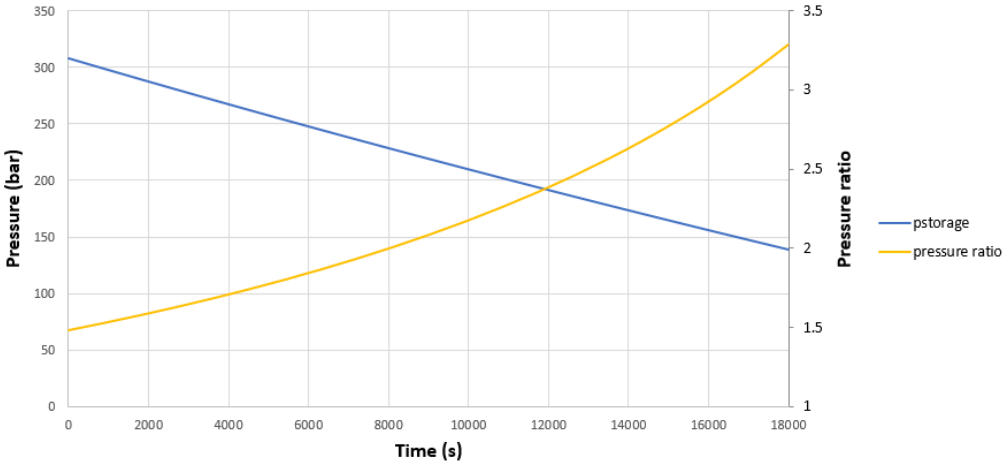

Figure 34 – $p_{storage}$ and β trends over refuelling time

The compressors for refuelling are of the same type of those used to fill the HRS storage system and so share the same operating parameters. Table 41 contains all the most important quantities to calculate E_{disp} and also presents the results achieved.

Scenario	β_{tot}	n_{stages}	η_{is}	η_{mec}	η_{el}	η_{mass}	PE_{el}	E_{disp} (MWh/day)
2.7 tons	1.48 - 3.29	2	0.75 – 0.70	0.95	0.94	0.99	1.501	1.98
3.3 tons	1.48 - 3.29	2	0.75 – 0.70	0.95	0.94	0.99	1.501	2.45

Table 41 – Elements for E_{disp} evaluation

E_{cool} is indispensable to ensure that the hydrogen in the train tank does not exceed, for the entire duration of the refuelling, the safety limits for temperature and pressure dictated by SAE. As mentioned in the last part of the '*Hydrogen Refuelling Station*' section, HDRSAM model prescribes to precool the H_2 flow to 5°C when the vehicle service pressure is 350 bar and the fuelling rate is 7.2 kg/min. The working principle of the precooling unit (PU) is based on a refrigeration cycle. A minimum temperature difference of 10 degrees between the hot and cold fluids is chosen as design criterion. Hence, if the hot heat reservoir is the outdoor environment, the gas refrigerant's temperature must be (20+10) = 30°C at the condenser

and (5-10) = -5°C at the evaporator. The upper limit for the coefficient of performance (COP) is function of only heat reservoirs' temperatures, as Eq. (79) proves.

$$COP_{id} = \frac{T_C}{T_H - T_C} = \frac{268.15}{303.15 - 268.15} = 7.66 \tag{79}$$

where T_C and T_H are the cold and hot heat reservoir temperatures measured in K, respectively. The maximum COP operating between 30°C and -5°C is thus 7.66. However, due to all the irreversibilities related to the precooling unit's components, the actual COP is much lower than the ideal one. A single stage vapour compression cycle between the same T_H and T_C is implemented in Aspen Plus with the aim of estimating the actual performance of the precooling unit. The flowsheet (see Figure 35) consists of four blocks: an evaporator, a condenser, an expansion valve and a compressor.

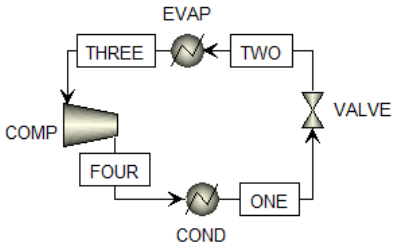

Figure 35 – Refrigeration cycle in Aspen Plus

R32 is supposed to be the refrigerant flowing in the cycle. The two working pressure levels of the system are retrieved from [170]: while the evaporator works at 6 bar, the condenser operates at 25 bar. The ratio between the heat absorbed by the evaporator (Q_C) and the electric power provided to compressor ($W_{compr,PU}$) is the actual COP of the unit. In symbols, it follows that:

$$COP_{act} = \frac{Q_C}{W_{compr,PU}} = \frac{m_{H_2 disp} \cdot c_{p_{H_2}} \cdot \left(T_{in,PU} - T_{out,PU}\right)}{W_{compr,PU}} \tag{80}$$

where $m_{H_2 disp}$ has been introduced in Eq. (72), $T_{in,PU}$ (20°C) and $T_{out,PU}$ (5°C) are the inlet and outlet temperature of hydrogen at the PU. Based on the definition given before, E_{cool} corresponds to the product between the running time of the PU's compressor (5 hours) and the $W_{compr,PU}$ appearing in Eq. (80), which is one of the outcomes of the refrigeration cycle modelled in Aspen. PU compressor is powered by grid electricity.

E_{cool} values for both the demand scenarios are summarised in Table 42.

Scenario	COP_{act}	E_{cool} (MWh/day)
2.7 tons/day	3.47	0.095
3.3 tons/day	3.47	0.112

Table 42 – E_{cool} values

The global efficiency of the HRS concept here analysed can be finally determined as all the parameters in Eq. (72) are now known.

In conclusion, a table gathering the values of $\eta_{HRS<350\ bar}$ for the three delivery pathways and for both the demand scenarios is shown.

Scenario	Path	$\eta_{HRS<350\ bar}$
3.3 tons/day	pipeline	0.926
	300 bar-tube trailer	0.936
	on-site electrolysis	0.906
2.7 tons/day	pipeline	0.926
	300 bar-tube trailer	0.936
	on-site electrolysis	0.906

Table 43 – $HRS_{<350}$ efficiency

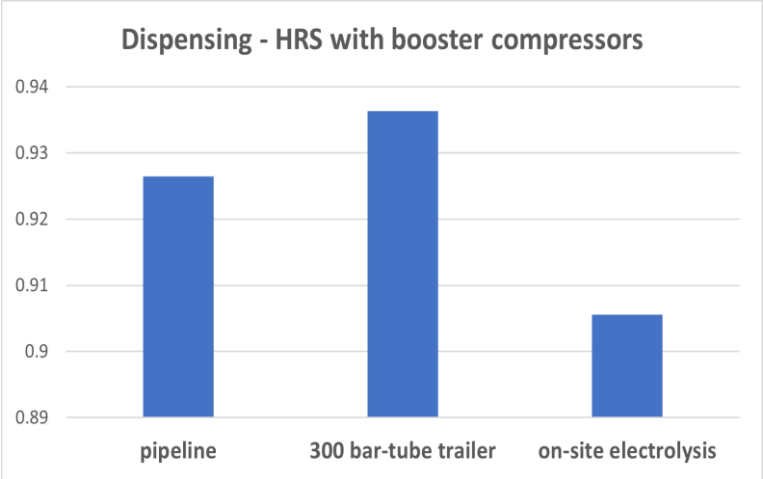

Figure 36 - HRS<350 primary energy efficiency for the three delivery pathways analysed

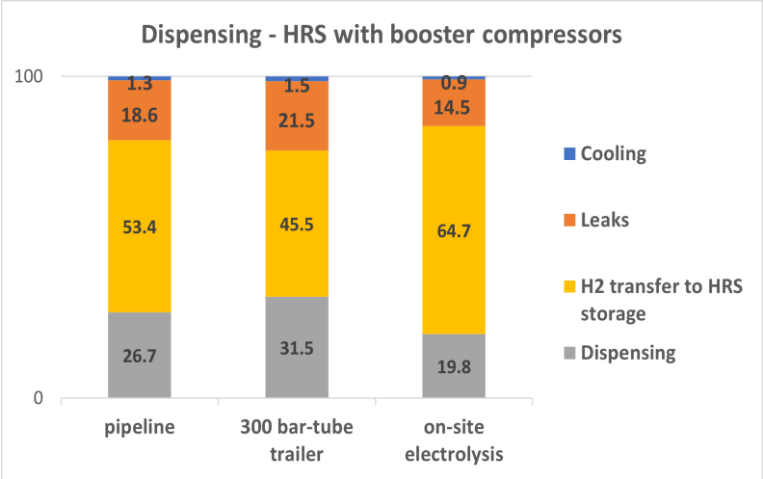

Figure 37 – Percentage incidence of each element on energy losses at HRS for the three delivery pathways analysed

According to Figure 37, the most impacting factor on efficiency is the transfer of H_2 to the HRS storage. Therefore, delivering high pressure hydrogen via tube trailers turns out to be the most efficient option for an HRS station with booster compressor.

Figure 36 and Figure 37 do not differentiate between 2.7 tons and 3.3 tons scenarios as there are no significant differences.

HRS with storage working above 350 bar and overflow filling

Unlike the previous HRS concept, this one is compatible with all the four gaseous supply routes. Storing the H_2 above the target pressure for refuelling makes the usage of compressors to transfer hydrogen from the storage to the train's fuel tanks unnecessary. The only driving force is in fact the pressure difference existing between the releasing and the receiving vessels. For a better implementation of the overflow filling procedure, the hydrogen storage is subdivided into multiple banks operating at three different pressure levels (low LP, medium MP and high HP), forming a cascade storage system. However, as highlighted in the 'Hydrogen Refuelling Station' section, adopting overflow filling as refuelling strategy requires the installation of certain storage overcapacities. The choice of the most suitable storage pressure to enable overflow filling is so the result of two competing priorities, the minimisation of overcapacities and the reduction of the HRS energy requirements. Both the HDRSAM model and the work done by Guerra et al. [77] set such pressure at 500 bar for trains and heavy-duty vehicles. The same value is selected here as maximum working pressure for all the three storage banks, regardless of the delivery option. The HDRSAM model suggests also what should be the minimum pressure in each bank. The full characterisation of the cascade storage system in terms of operating pressures is provided in Table 44. Trains are refuelled first from the LP storage. Once the pressure inside the vehicle's tank reaches 177 bar, the MP storage bank takes over, continuing the refuelling process. The switch to the HP bank is the last step and occurs at 329 bar.

Type	p_{max} (bar)	p_{min} (bar)
HP	500	430
MP	500	329
LP	500	177

Table 44 – Cascade storage's operating range

Table 44 also shows that some hydrogen must remain in the vessels to keep the pressure within the specified operational limits. The addition of overcapacities to the HRS facility is hence essential to meet the fleet's hydrogen demand.

The equation for the estimation of the HRS energy efficiency (Eq. (81)) does not differ greatly from Eq. (72). The only difference is that E_{disp} is equal to 0 for overflow filling.

$$\eta_{HRS_{>350\ bar}} = \frac{m_{H_2 disp} \cdot LHV_{H_2}}{m_{H_2 delivered} \cdot LHV_{H_2} + E_{unload-store} + E_{cool}} \quad (81)$$

The additional energy needed to transport and store hydrogen into the overcapacities is not included in the efficiency. In contrast with the energy processes considered by Eq. (81), which take place on a daily basis, overcapacities are filled just once at the beginning of the HRS life and thus the corresponding effect on $\eta_{HRS_{>350\ bar}}$ is deemed as negligible.

The quantity $E_{unload-store}$ is assessed in the same way as explained in the previous section. The parameters involved in the calculation of $E_{unload-store}$ are introduced with the help of Table 45. Because of the higher working pressure chosen for the HRS storage (i.e. $p_{storage}$ = 500 bar), the pressure ratio β and the number of compression stages n_{stages} are higher than those in Table 39.

Path	β_{tot}	n_{stages}	η_{is}	η_{mec}	η_{el}	η_{mass}
pipeline	7.2	3	0.68	0.95	0.94	0.99
300 bar-tube trailer	1.7 – 25	5	0.75 – 0.62	0.95	0.94	0.99
on-site electrolysis	16.7	4	0.65	0.95	0.94	0.99
700 bar-tube trailer	?	?	0.75	0.95	0.94	0.99

Table 45 – Necessary parameters for $E_{unload-store}$ determination

In order to complete Table 45, β_{tot} and n_{stages} for the 700 bar-tube trailer supply pathway must be evaluated. Figure 38 displays how p_{truck} changes as the unloading goes on and is obtained by adapting Eq. (76) to the 700 bar-tube trailer case.

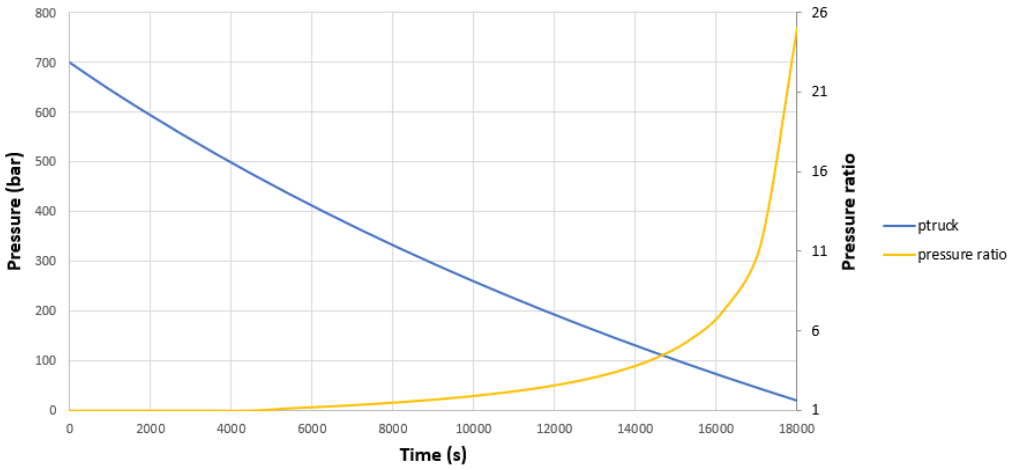

Figure 38 – p_{truck} and β trends over refuelling time – 700 bar trailer

Thanks to the high pressure at which H_2 is stored inside the 700 bar trailers, for about the first 5000 seconds the discharging progresses without any compressors, exploiting only the difference between p_{truck} and $p_{storage}$. The obtained results for $E_{unload-store}$ are reported in Table 46.

Scenario	Path	$E_{unload-store}$ (MWh/day)
2.7 tons/day	pipeline	5.26
	300 bar-tube trailer	4.39
	on-site electrolysis	7.46
	700 bar-tube trailer	3.29
3.3 tons/day	pipeline	6.43
	300 bar-tube trailer	5.36
	on-site electrolysis	9.12
	700 bar-tube trailer	4.02

Table 46 - Results for $E_{unload-store}$

As Eq. (73) proves, the value of $m_{H_2 disp}$ is linked to the extent of the fugitive emissions $m_{H_2 fug,HRS}$. More hydrogen is stored and dispensed, the larger is the amount of leakages from the HRS facility. Two different sources of H_2 loss have been identified: compressors and pressurised vessels. Every day, approximately 1% of $m_{H_2 delivered}$ is lost during compression. As concerns instead the emissions from the storage system, they depend on the sizes of the three pressure banks and of the related overcapacities. The sizing of the cascade storage is therefore necessary. It essentially consists in determining how much hydrogen each pressure bank has to supply to the train's tank, also making sure that the pressure limits indicated in Table 44 are not violated. For the sake of simplicity, the calculations for the cascade sizing are carried out considering a single apparent big tank containing all the H_2 required by the fleet (i.e. $_{H_2 capacity,fleet}$). So, the useable storage capacity of the entire fleet must be large enough to hold 2.7 tons or 3.3 tons of H_2, that are the daily fleet's demands ($m_{H_2 demand}$) for the two studied scenarios. The total volume $V_{H_2 capacity,fleet}$ is conservatively calculated taking into account 358.15 K (i.e. 85°C) and 437.5 bar as the operating conditions for the trains' tanks. Rearranging Eq. (76), it follows that:

$$V_{H_2 capacity,fleet} = m_{H_2 demand} \cdot R_{H_2} \cdot T \cdot \left(6.928 \cdot 10^{-6} + \frac{9.974 \cdot 10^{-1}}{100 \cdot p_{tank,max}} \right) \quad (82)$$

The outcomes of Eq. (82) are 120 m^3 and 147 m^3, respectively for the 2.7 tons and the 3.3 tons scenario. As described previously, the LP bank refuels the train until the pressure in the vehicles' vessels reaches 177 bar. At such pressure, the corresponding mass of hydrogen inside the apparent fleet's fuel tank is:

$$m_{LP\rightarrow H_2 fleet} = \frac{100 \cdot V_{H_2 capacity,fleet} \cdot p_{min,LP}}{R_{H_2} \cdot\cdot \left(9.974 \cdot 10^{-1} + 6.928 \cdot 10^{-4} \cdot p_{min,LP}\right)} \quad (83)$$

Eq. (83) provides then the mass of H_2 that has to come daily from the LP bank. However, to keep the pressure within the operational range, the low-pressure cascade vessel must be able to store more hydrogen than $m_{LP\rightarrow H_2 fleet}$. In other words, the LP bank is sized so that its pressure, after the discharge of a quantity of H_2 equal to $m_{LP\rightarrow H_2 fleet}$, amounts to 177 bar. In view of this, the equation behind the design of the LP cascade tank is:

$$\frac{100 \cdot V_{LP\ bank} \cdot p_{max,LP}}{R_{H_2} \cdot T_{amb} \cdot \left(b + a \cdot p_{max,LP}\right)} - \frac{100 \cdot V_{LP\ bank} \cdot p_{min,LP}}{R_{H_2} \cdot T_{amb} \cdot \left(b + a \cdot p_{min,LP}\right)} = m_{LP\rightarrow H_2 fleet} \quad (84)$$

where a is $6.928 \cdot 10^{-4}$, b is $9.974 \cdot 10^{-1}$, $p_{max,LP}$ is 500 bar, $p_{min,LP}$ is 177 bar and $V_{LP\ bank}$ is the only unknown term of the equation. The temperature of hydrogen in the cascade system is assumed to be the same of the ambient and so T in Eq. (84) is 293.15 K. Once $V_{LP\ bank}$ is known, the LP bank capacity in terms of kg can be finally evaluated by means of Eq. (85).

$$m_{H_2 capacity,LP} = \frac{100 \cdot V_{LP\ bank} \cdot p_{max,LP}}{R_{H_2} \cdot T_{amb} \cdot \left(b + a \cdot p_{max,LP}\right)} \quad (85)$$

The next step is the sizing of the MP bank. The kilograms of hydrogen moved every day from MP vessel to the trains result from Eq. (86).

$$m_{MP\rightarrow H_2 fleet} = \frac{100 \cdot V_{H_2 capacity,fleet} \cdot p_{min,MP}}{R_{H_2} \cdot T \cdot \left(b + a \cdot p_{min,MP}\right)} - \frac{100 \cdot V_{H_2 capacity,fleet} \cdot p_{min,LP}}{R_{H_2} \cdot T \cdot \left(b + a \cdot p_{min,LP}\right)} \quad (86)$$

Thanks to the two equations below, the volume of the MP tank ($V_{MP\ bank}$) and the mass of hydrogen stored in it at the beginning of the refuelling ($m_{H_2 capaciy,MP}$) are estimated.

$$\frac{100 \cdot V_{MP\ bank} \cdot p_{max,MP}}{R_{H_2} \cdot T_{amb} \cdot \left(b + a \cdot p_{max,MP}\right)} - \frac{100 \cdot V_{MP\ bank} \cdot p_{min,MP}}{R_{H_2} \cdot T_{amb} \cdot \left(b + a \cdot p_{min,MP}\right)} = m_{MP\rightarrow H_2 fleet} \quad (87)$$

$$m_{H_2 capacity,MP} = \frac{100 \cdot V_{MP\ bank} \cdot p_{max,MP}}{R_{H_2} \cdot T_{amb} \cdot (b + a \cdot p_{max,MP})} \quad (88)$$

The HP bank completes the refuelling process, supplying the missing portion of hydrogen to meet the fleet's demand. The equations needed for its design are introduced below.

$$m_{HP \rightarrow H_2 fleet} = m_{H_2 demand} - m_{LP \rightarrow H_2 fleet} - m_{MP \rightarrow H_2 fleet} \quad (89)$$

$$\frac{100 \cdot V_{HP\ bank} \cdot p_{max,HP}}{R_{H_2} \cdot T_{amb} \cdot (b + a \cdot p_{max,HP})} - \frac{100 \cdot V_{HP\ bank} \cdot p_{min,HP}}{R_{H_2} \cdot T_{amb} \cdot (b + a \cdot p_{min,HP})} = m_{HP \rightarrow H_2 fleet} \quad (90)$$

$$m_{H_2 capacity,HP} = \frac{100 \cdot V_{HP\ bank} \cdot p_{max,HP}}{R_{H_2} \cdot T_{amb} \cdot (b + a \cdot p_{max,HP})} \quad (91)$$

In the interest of clarity, all the findings related to the sizing of the cascade dispensing system are summarised in Table 47.

Scenario	Bank type	$m_{LP,MP,HP \rightarrow H_2 fleet}$ (kg)	V_{bank} (m^3)	$m_{H_2 capacity,bank}$ (kg)
3.3 tons/day	HP	667	202.5	6182
	MP	1083	127.5	3892
	LP	1550	88.3	2695
2.7 tons/day	HP	540	164	5007
	MP	887	104.3	3184
	LP	1273	72.5	2214

Table 47 – Cascade features

Now that the capacities of the three pressure banks are known, the associated hydrogen leakages can be assessed.

Scenario	$m_{H_2 fug,stor}$	$m_{H_2 fug,compr}$	$m_{H_2 fug,HRS}$	$m_{H_2 disp}$
2.7 tons/day	17.7 kg/day	27.3 kg/day	45.1	2609.9
3.3 tons/day	21.6 kg/day	33.4 kg/day	55.1	3189.9

Table 48 – Fugitive emissions

As regards the energy E_{cool} to precool the H_2 before dispensing, the values that can be found in Table 42 are also valid here.

Having defined all the necessary parameters, the efficiency of the HRS ($\eta_{HRS_{>350\ bar}}$) is finally determined. The results of Eq. (81) for the two demand scenarios and for the four delivery pathways are gathered in Table 49.

Scenario	Path	$\eta_{HRS_{>350\ bar}}$
3.3 tons/day	pipeline	0.912
	300 bar-tube trailer	0.921
	on-site electrolysis	0.892
	700 bar-tube trailer	0.932
2.7 tons/day	pipeline	0.912
	300 bar-tube trailer	0.921
	on-site electrolysis	0.892
	700 bar-tube trailer	0.932

Table 49 – HRS $_{>350}$ efficiency

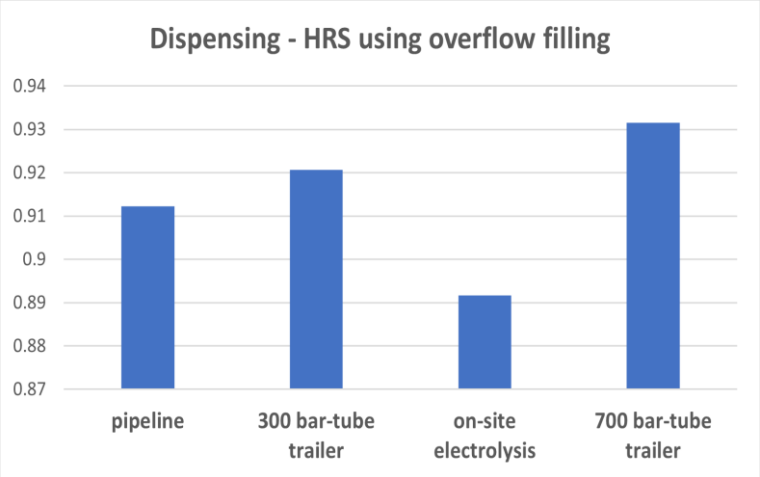

Figure 39 – HRS$_{>350}$ primary energy efficiency for the delivery pathways analysed

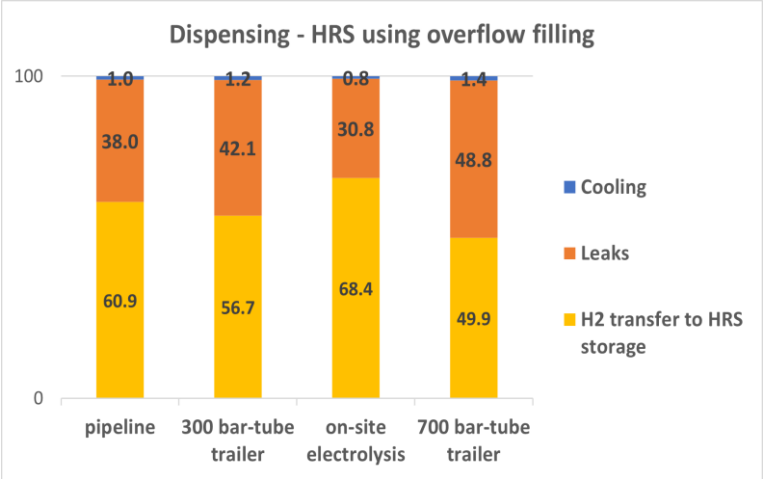

Figure 40 – Relative importance of each element on HRS efficiency loss

Transferring hydrogen to the HRS storage is confirmed as the most primary energy-intensive process. On-site electrolysis is the worst option in terms of primary energy consumption, while 700 bar-tube trailer is the most convenient one.

Figure 39 and Figure 40 do not differentiate between 2.7 tons and 3.3 tons scenarios as there are no significant differences.

HRS with LH_2 storage and cryogenic pumps

The only way to supply hydrogen to an HRS with LH_2 storage and cryogenic pumps is through liquid tankers. In fact, H_2 liquefaction at the refuelling station is not considered as a viable option since it would significantly increase the complexity and the energy use of the HRS. The equation for the calculation of the HRS energy efficiency is shown below:

$$\eta_{HRS_{LH_2}} = \frac{m_{H_2 disp} \cdot LHV_{H_2}}{m_{LH_2 delivered} \cdot LHV_{H_2} + E_{unload-store} + E_{disp} + E_{evap}} \quad (92)$$

where $E_{unload-store}$ is the energy per day to transfer the LH_2 from liquid tankers to the storage of the HRS, E_{disp} is the daily energy consumption of the cryogenic pumps employed

for dispensing and E_{evap} is the thermal energy absorbed every day by $m_{LH_2 disp}$ at the evaporator to reach the thermodynamic conditions set for refuelling.

For the same reasons given in the '*HRS with storage working below 350 bar and booster compressors*' section, the effect of the liquid tanker's usable capacity has been already included in the $\eta_{H_2 transp-liq\ trucks}$ (see Eq. (54)) and thus is excluded from the definition of the HRS efficiency.

The unloading and the storing of the liquid hydrogen inside highly insulated vessels is performed via cryogenic pumps. According to [169], 20 K and 6 bar are the temperature and the pressure established within the Dewar at the HRS holding the LH_2. The same document suggests a minimum pressure gradient of 1 bar to drive the emptying of the liquid trailers. Cryo-pumps are then asked to raise the pressure up to at least 7 bar. As the liquid tankers contain LH_2 at nearly atmospheric pressure, the pressure jump Δp_{pump} is $6 \cdot 10^2$ kPa. The energy $E_{unload-store}$ is obtained by solving the following equation:

$$E_{unload-store} = \frac{m_{LH_2 delivered}}{\rho_{H_2 liq}} \cdot \Delta p_{pump} \cdot {}^{1}/_{\eta_{pump}} \cdot {}^{1}/_{\eta_{el}} \cdot PE_{el} \qquad (93)$$

where $\rho_{H_2 liq}$ is the hydrogen density at 20 K and $m_{LH_2 delivered}$ is 2.7 or 3.3 tons per day. The prime movers of the cryogenic pumps are electric motors. From the HDRSAM model, theirs electric efficiency η_{el} is 0.88, while 0.75 and 1.501 are respectively the values for η_{pump} and PE_{el}. The results of Eq. (93) for the two demand scenarios are displayed in Table 50.

Scenario	Path	$E_{unload-store}$ (MWh/day)
3.3 tons/day	Liquid tankers	0.018
2.7 tons/day		0.014

Table 50 - $E_{unload-store}$ values

The refuelling strategy adopted by the station concept analysed here is analogous to that of the HRS using booster compressors. The refuelling time window is 5 hours long and the fuelling rate is 7.2 kg/min, as for the other two HRS concepts. Because of the liquid form and the temperature of the hydrogen processed, compressors are replaced by cryo-pumps. They draw LH_2 at 6 bar from the liquid storage and bring the pressure to 457 bar, that is the same level set for the HRS utilising booster compressors. Eq. (93) is used also to find the magnitude of E_{disp}. Despite being characterised by the same values of η_{el} and η_{pump}, the cryogenic pumps involved in the refuelling have to provide a much higher pressure increase, equivalent to $4.5 \cdot 10^4$ kPa. The results for E_{disp} can be seen in Table 51.

Scenario	Path	E_{disp} (MWh/day)
3.3 tons/day	Liquid tankers	1.33
2.7 tons/day		1.09

Table 51 – Energy E_{disp}

The state-of-art of hydrogen storage in transport sector is represented by pressurised tanks in which H_2 is stored in gaseous form. Although the first prototypes of cryogenic LH_2 vessels date back to 50 years ago, no vehicle equipped with LH_2 storage systems is currently available on the market [171]. An air forced evaporator is therefore added before dispensers so that hydrogen temperature can become compliant with the refuelling protocol. Since active fans are supposed to support the heating process, ambient air is the only exploited heat source. As a consequence, E_{evap} coincides with the fans' electricity requirements. The power absorbed by the fans depends on the mass flow rate to be supplied, which is in turn chosen on the basis of the desired vaporizer's heat duty. Hydrogen enters the evaporator in liquid state at -253.15°C and 457 bar, exchanges heat almost isobarically (negligible pressure drops) with air and finally flows out at 5°C. The vaporizer must be able to convert

and condition, within the 5 hours long refuelling time window, 2700 kg or 3300 kg per day of LH_2. The resulting heat duty, evaluated with Aspen Plus, is hence approximately 665 kW or 813 kW. A relationship between the evaporator heat duty and the electric power absorbed by the motors driving the fans is retrieved from [172]. For each kW of vaporizer's heat duty, about 0.028 kW of forced-air fan motor are required. The corresponding installed capacities are then 18.6 kW and 22.7 kW for the 2.7 tons and the 3.3 tons demand scenarios, respectively. Fans' daily electricity requirements are presented in Table 52. The values below are obtained under the assumption that the motors are in operation only during the refuelling time window.

Scenario	Path	E_{evap} (kWh)
3.3 tons/day	Liquid tankers	0.18
2.7 tons/day		0.15

Table 52 - E_{evap}

The assessment of the fugitive emissions from the HRS ($m_{H_2 fug,HRS}$) is crucial to determine how much hydrogen is actually dispensed at the refuelling station. As [162] states, two main sources of hydrogen losses can be identified in a HRS treating LH_2: storage boil-off and emissions related to the usage of cryo-pumps. As regards the former, every day around 0.7% of the LH_2 stored at the station evaporates and cannot be recovered. If a LH_2 storage with an autonomy of two days is implemented at the HRS, the associated leakages are 38 kg/day for the 2.7 tons scenario and 46 kg/day for the 3.3 tons scenario. The second type of losses, instead, are mainly due to the warming up experienced by the cryo-pumps during their idle periods and equate to the 1.1% of the liquid hydrogen dispensed daily. A summary of the fugitive emissions is given in Table 53.

Scenario	$m_{H_2fug,boil-off}$	$m_{H_2fug,cryo-pump}$	$m_{H_2fug,HRS}$	m_{H_2disp}
3.3 tons/day	46 kg/day	36 kg/day	82 kg/day	3218 kg/day
2.7 tons/day	38 kg/day	30 kg/day	68 kg/day	2632 kg/day

Table 53 – Fugitive emissions and dispensed H_2 for the LH_2 HRS

All the terms included in Eq. (92) are now known and thus the efficiency $\eta_{HRS_{LH_2}}$ of the refuelling station can be finally estimated. Table 54 shows the efficiency values calculated for the two demand scenarios.

Scenario	$\eta_{HRS_{LH_2}}$
3.3 tons/day	0.96
2.7 tons/day	0.96

Table 54 - LH_2 HRS efficiency results

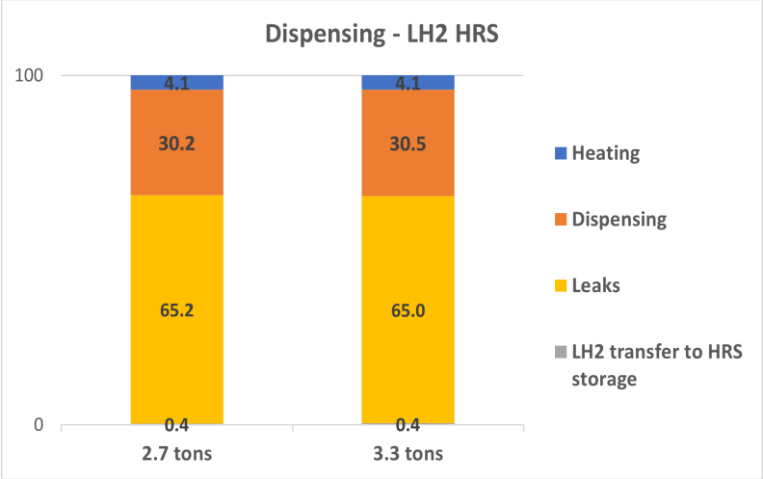

Figure 41 – Percentage incidence of each element on energy loss at LH_2 HRS

Thanks to the lower energy requirements for LH_2 pumping compared to gaseous hydrogen compression, LH_2 HRS has the highest primary energy efficiency among the three HRS concept evaluated.

Hydrogen fugitive emissions strongly affects the primary energy efficiency of LH_2 refuelling station and then represent a serious issue to address when a LH_2 storage is designed.

3.4 Tank-to-wheels stage

The tank-to-wheels analysis (TTW) is the second pillar of a well-to-wheel study. The TTW stage covers train operation activities and mainly consists in the evaluation of the vehicle energy performance, which can be expressed either in terms of energy required per km travelled or overall powertrain efficiency.

The vehicle taken into account is a two-car fuel cell hybrid regional train. It combines PEM fuel cell technology as main power source with Li-ion batteries to better manage rapid changes in load. Vehicle powertrain efficiency and fuel consumption are retrieved through literature research and data analysis.

As seen in *'New Street daily hydrogen demand'* section, a first approximation value for the fuel economy (i.e. L/km) of a typical two-car fuel cell hybrid train is obtained from [89]. Afterwards, the impact of number of carriages and seat load factor on train's fuel consumption has been assessed. The results are displayed in Figure 15.

As regards vehicle operation efficiency, it is determined by including typical power battery performance (i.e. 80% [173]) into the efficiency chain provided in [13]. The final mean value obtained is 43%.

Propulsion system devices	LHV efficiency
Fuel cell stacks	60 – 71%
Electric motors	92%
Batteries	80%
Transmission	95%
Motor auxiliaries	99%
Traction auxiliaries	94%
Vehicle	**39 – 46%**

Table 55 – Fuel cell hybrid train's efficiency chain

3.5 Well-to-wheel indexes

Two different indexes are used to present WTW analysis outcomes:

$$\eta_{WTW\ path} = \eta_{WTT\ path} \cdot \eta_{FCH\ train} \quad (94)$$

$$E_{WTW} = E_{WTT_t} \cdot FE_{FCH\ train} \cdot LHV_{H_2} \quad (95)$$

where $\eta_{FCH\ train}$ is equal to 0.43 and $FE_{FCH\ train}$ is 0.28 kg_{H2} per km travelled for a two-car train characterised by the daily average seat load factor (i.e. 87%).

3.6 Results and discussion

3.6.1 Well-To-Tank (WTT) stage – 2030 scenario

By combining the six supply routes displayed in Figure 11 with the three dispensing options analysed and on-site electrolysis solution, fourteen WTT pathways are obtained.

Pathway	Identification number
Electrolysis – H_2 storage – pipeline – HRS with booster compressors	1
Electrolysis – H_2 storage – pipeline – HRS using overflow filling	2
Electrolysis – H_2 storage – 300 bar-tube trailers – HRS with booster compressors	3
Electrolysis – H_2 storage – 300 bar-tube trailers – HRS using overflow filling	4
Electrolysis – H_2 storage – 700 bar-tube trailers – HRS using overflow filling	5
Electrolysis – H_2 storage – liquefaction – liquid tankers – LH_2 HRS	6
SMR – CO_2 storage – H_2 storage – pipeline – HRS with booster compressors	7
SMR – CO_2 storage – H_2 storage – pipeline – HRS using overflow filling	8
SMR – CO_2 storage – H_2 storage – 300 bar-tube trailers – HRS with booster compressors	9
SMR – CO_2 storage – H_2 storage – 300 bar-tube trailers – HRS using overflow filling	10
SMR – CO_2 storage – H_2 storage – 700 bar-tube trailers – HRS using overflow filling	11
SMR – CO_2 storage- H_2 storage – liquefaction – liquid tankers – LH_2 HRS	12
On-site electrolysis – HRS with booster compressors	13
On-site electrolysis – HRS using overflow filling	14

Figure 42 – Analysed WTT pathways

Figure 43 and Figure 44 summarise the main results of WTT stage. The worst pathways are those including on-site electrolysis. Despite no transportation losses occur, routes 13 and 14 are significantly disadvantaged by the utilisation of electricity from the grid, whose PE_{el} is 1.501. The best path is instead the one that combines the best production technology in terms of efficiency, SMR+CCS, with the most efficient way of transport, 700 bar-tube trailer. Figure 43 also highlights that the green hydrogen routes (paths 1 – 6) are inferior in terms of $\eta_{WTT\ path}$ than the blue hydrogen[56] ones (paths 7 – 12). The reason is the higher primary energy efficiency of SMR+CCS production technology compared to PEM electrolysis.

Figure 44 shows that production is the most-energy consuming step, followed by transport. Dispensing and H_2 storage have a minor effect on efficiency reduction, especially the latter.

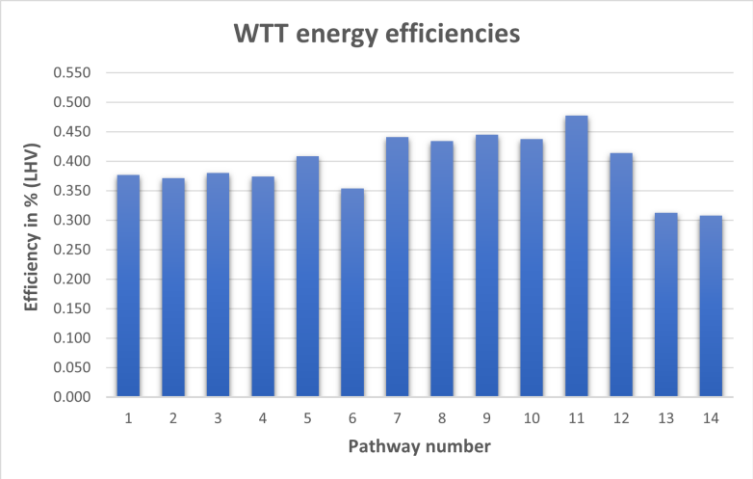

Figure 43 – WTT energy efficiencies of the analysed routes

[56] https://www.nationalgrid.com/stories/energy-explained/hydrogen-colour-spectrum

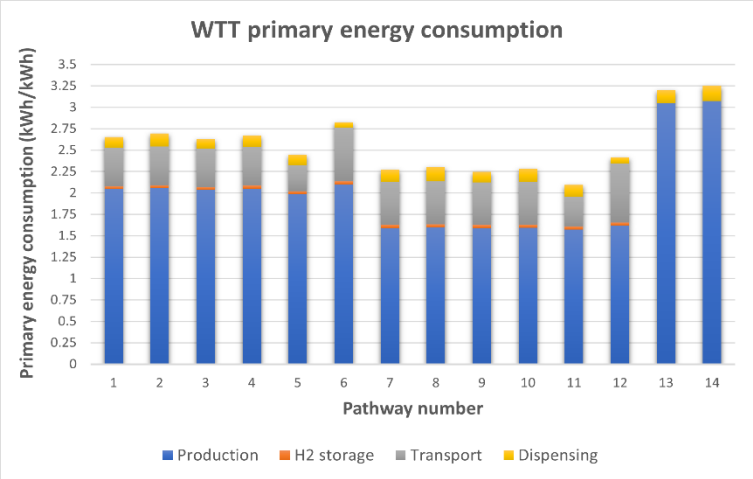

Figure 44 – WTT energy consumption of the analysed paths

3.6.2 Well-To-Tank (WTT) stage – 2040 scenario

WTT energy efficiency and primary energy consumption for the same fourteen routes are now evaluated in the context of the 2040 scenario.

The main differences between the two scenarios are gathered in Table 56.

Parameter	2030	2040
e_{H_2PEM}	62 MWh/ton	55 MWh/ton
$\eta_{CO_2storage}$	0.997	0.985
$\eta_{H_2transp-pipes}$	0.795	0.947
E_{H_2liq}	10 MWh/ton	7 MWh/ton
$PE_{electricity}$	1.501	1.2
H_2 demand	2.7 – 3.3 ton	38 – 46 ton

Table 56 – Changes between 2030 and 2040 scenario

- e_{H_2PEM}: the specific energy consumption of PEM electrolysis is expected to decrease in the near future [23]
- $\eta_{CO_2storage}$: energy spent to store a unit mass of CO_2 is going to increase in the second stage of HyNet CCS project lifetime, when injection of liquid carbon dioxide will be adopted

- $\eta_{H_2 transp-pipes}$: as discussed, blending is not considered a long-term option for hydrogen transport. An all-H_2 network is what UK aims to achieve.
- $E_{H_2 liq}$: according to Ghafri et al. [163], a reduction from 10 MWh to 6 – 8 to liquify a ton of H_2 is expected in the next years
- $PE_{electricity}$: thanks to the increase in renewable penetration to meet net zero targets, PE of UK electricity is going to decrease. Based on energy and emissions projections for the period 2021-2040[57] provided by the Department of Business, Energy, and Industrial Strategy (BEIS), an average $PE_{electricity}$ of 1.2 has been calculated for 2040.

The main findings of the WTT analysis for the 2040 scenario are given below.

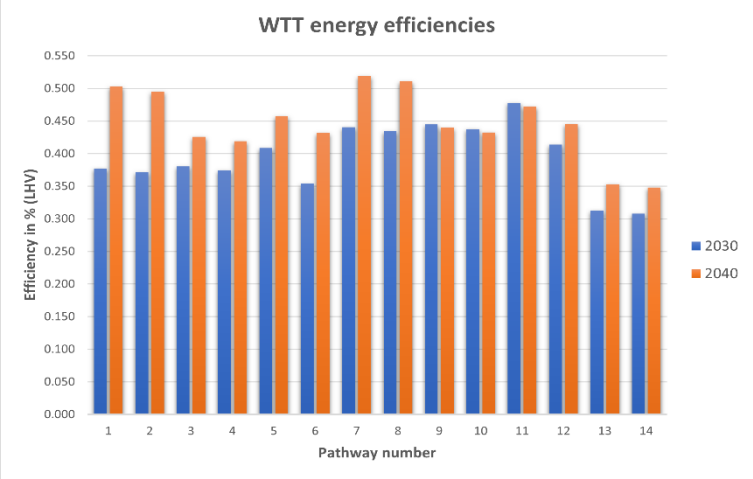

Figure 45 – Comparison between 2040 and 2030 in terms of WTT efficiency

[57] https://assets.publishing.service.gov.uk/media/634e5f75e90e0731a8008927/updated-energy-and-emissions-projections-2021-2040.pdf

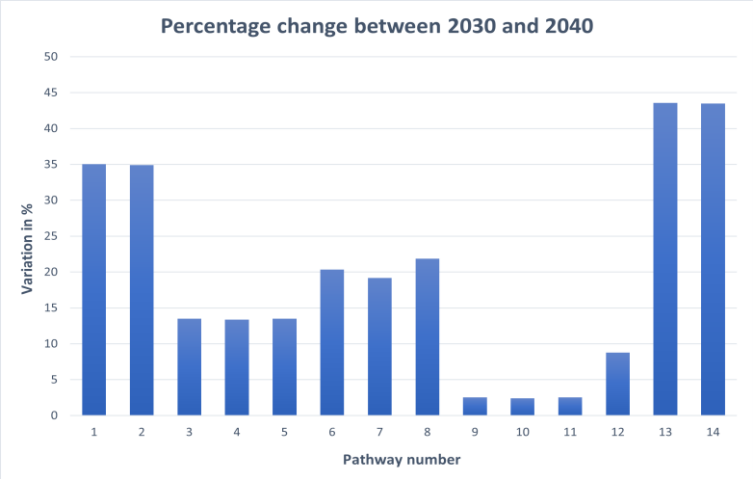

Figure 46 – WTT efficiency percentage change between 2030 and 2040

As shown in Figure 45, the improvement in electrolysis efficiency and $PE_{electricity}$ bridges distances between green hydrogen and blue hydrogen pathways. In fact, while in 2030 the top 3 most efficient WTT paths were of the blue hydrogen type, in 2040 one green route manages to reach the podium. Furthermore, it is interesting to note that in 2040 pathways including liquefaction may offer efficiencies in line with those related to gaseous hydrogen.

As Figure 46 proves, all the WTT efficiencies are expected to be higher in 2040. While the green paths' efficiencies (i.e. from 1 to 6) are characterised by an average percentage growth of 22%, those of blue ones increase by an average of 10%. The highest percentage rise is experienced by the on-site electrolysis routes (i.e. number 13 and 14), mainly thanks to the reduction of $PE_{electricity}$.

3.6.3 Well-To-Wheel (WTW) analysis – scenario 2030 and 2040

The most efficient WTT routes, listed in Table 57, are now combined with $\eta_{WTW\ path}$ and $FE_{FCH\ train}$ to obtain the WTW indexes.

Scenario	Pathway	Number
2030	SMR – CO_2 storage – H_2 storage – pipeline – HRS with booster compressors	7
	SMR – CO_2 storage – H_2 storage – 300 bar-tube trailers – HRS with booster compressors	9
	SMR – CO_2 storage – H_2 storage – 700 bar-tube trailers – HRS using overflow filling	11
2040	Electrolysis – H_2 storage – pipeline – HRS with booster compressors	1
	SMR – CO_2 storage – H_2 storage – pipeline – HRS with booster compressors	7
	SMR – CO_2 storage – H_2 storage – pipeline – HRS using overflow filling	8

Table 57 – Pathways considered for the WTW analysis

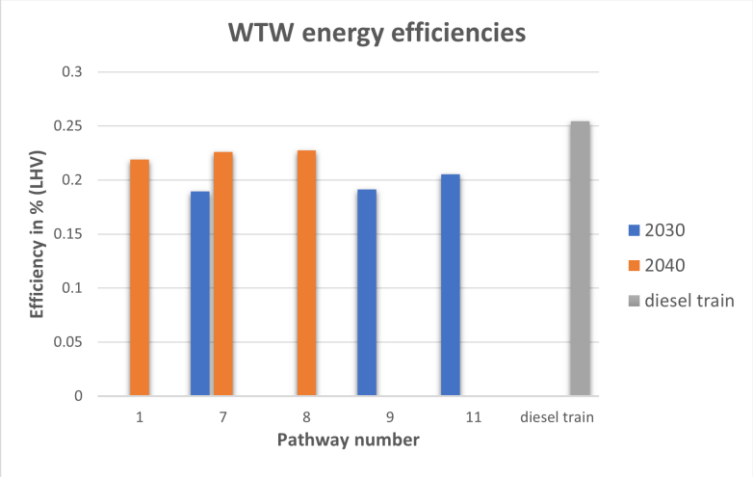

Figure 47 – WTT energy efficiencies for the WTT routes examined

In Figure 47 a comparison between the WTW efficiencies of the two studied scenarios is made. The WTW efficiency of a typical diesel train is also included in the figure as a benchmark. The value of $\eta_{WTW\ pth}$ for the diesel train is estimated as follows:

$$\eta_{WTW\ path_{diesel\ train}} = \eta_{WTT\ path_{diesel}} \cdot \eta_{diesel\ train} \quad (96)$$

where:

- $\eta_{WTT\ path_{diesel}}$ is equal to 0.847. It is calculated as the inverse of the PE_{diesel}, which is taken from [137]
- $\eta_{diesel\ train}$ is 0.3 and is retrieved from [85]

Diesel train achieves better WTW performance thanks to the high value of $\eta_{WTT\ path_{diesel}}$. Looking at the 2030 scenario, diesel train presents a WTW efficiency 24% higher than that of the fuel cell train supplied by the most efficient WTT pathway. This gap decreases for the 2040 scenario, when the $\eta_{WTW\ path}$ of diesel train is just 10% higher than path 8's WTW efficiency.

Another way to present the WTW outcomes is through the E_{WTW} index.

As Eq. (95) shows, diesel train's fuel consumption is needed. The value of $FE_{diesel\ train}$ is retrieved from literature. Kapetanovic et al. [174] estimated in 1.96 litres per km the fuel economy of a two-car diesel multiple unit regional train connecting Leeuwarden to Groningen. The selected route is 54 km long, has a flat topography and 8 stops between the first and last station. Since this working conditions do not differ much from the ones considered for fuel cell train, the choice of [174] as reference seems appropriate.

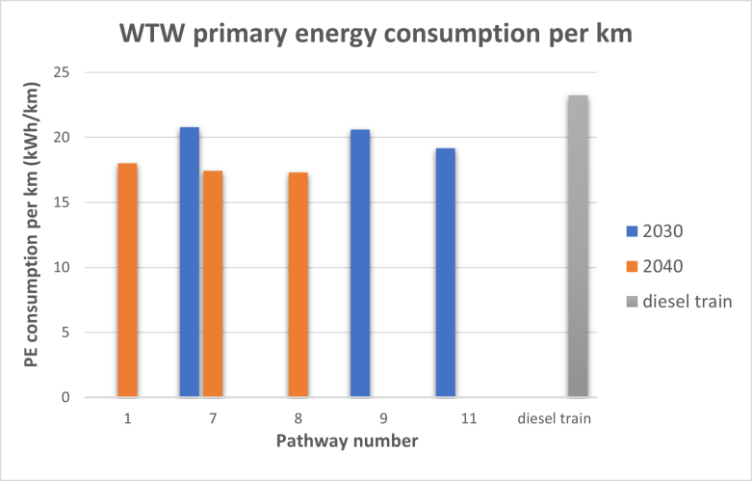

Figure 48 – Comparison between fuel cell and diesel train's WTW energy consumption

Figure 48 reveals that fuel cell hybrid train becomes a better option than diesel train if the comparison is based on E_{WTW}. The reason is the higher fuel consumption per km of diesel train, which suffers from the inefficiency of its powertrain.

3.7 Sensitivity analysis

In this section, a sensitivity analysis to identify which parameters have the most significant impact on the WTW results is performed. The selected key parameters include electrolysis specific energy consumption and grid electricity's primary energy factor.

To perform the sensitivity analysis, each parameter is varied by ±10% while keeping the other ones constant. Their impact on each $\eta_{WTW\ path}$ is then assessed.

In Table 58, parameters' baseline values and their variations are showed.

Parameter	Baseline	Upper value	Lower value
e_{H_2PEM}	62	68.2	55.8
$PE_{electricity}$	1.501	1.651	1.351

Table 58 – Parameters and baseline values for sensitivity analysis

Figure 49 illustrates the impact of electrolysis energy consumption on various pathways. Specifically, it shows the percentage change in WTW efficiency when the energy consumption for electrolysis is increased by 10% (blue bars) and decreased by 10% (orange bars). Paths 7-12 do not include electrolysis and then no values are showed for them. The results suggest an almost linear relationship between electrolysis energy demand and WTT efficiencies.

Figure 50 displays instead the percentage change in pathway WTW performance when the PE factor for grid electricity is increased by 10% (blue bars) and decreased by 10% (orange bars). Pathways 13 and 14 are highly sensitive to changes in the grid electricity PE factor as they exploit grid electricity to power electrolysis. When the PE factor is increased by 10%, the WTW efficiencies decreases by approximately 9.83% and 9.78%, respectively. Conversely, when the PE factor is decreased by 10%, their WTW performance improves by

11.95% and 11.91%, respectively. The other pathways show minimal sensitivity to changes in the grid electricity PE factor, with percentage changes generally within ±0.65%. The reason is that PE factor is involved only in the calculation of dispensing efficiencies.

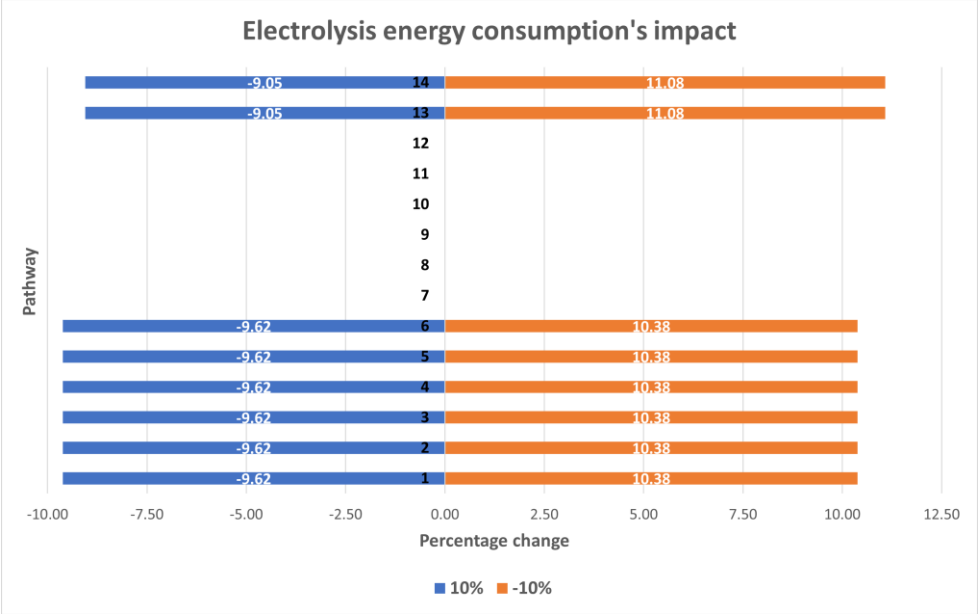

Figure 49 – Impact of electrolysis energy consumption's variation by ±10% on WTW efficiencies

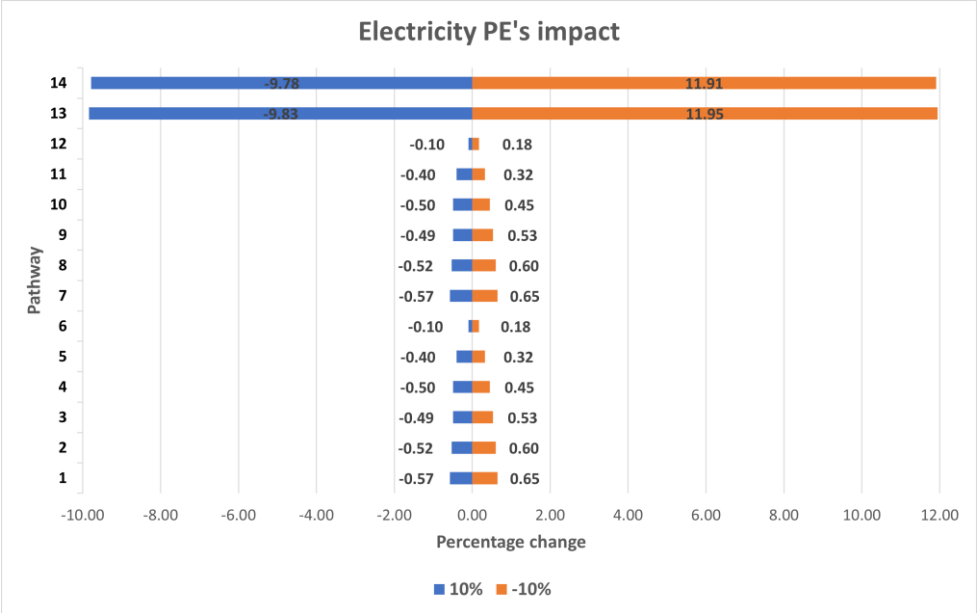

Figure 50 – Impact of grid electricity PE's variation by ±10% on WTW efficiencies

3.8 Uncertainty analysis

Following the sensitivity analysis, an uncertainty study is now conducted. The goal is to quantify the overall variability in WTW efficiencies due to the inherent uncertainties in the two key parameters selected (i.e. grid electricity's primary energy factor and electrolysis energy demand).

Table 59 outlines the parameters, variability ranges, and calculated standard deviations for the key parameters included in the uncertainty analysis, for both the scenarios. While the row 'Baseline' gathers the parameters' values adopted in the previous paragraphs, the last column of the table shows the calculated mean value and the relative standard deviation σ.

Since the standard deviations for the two key parameters are not available, various references, including those used for the baseline values, have been selected. The range of values in these references have been then used to estimate the standard deviations. For the sake of clarity, the calculation of $\sigma_{e_{H_2PEM}}$ for 2030 scenario is now illustrated. The first step is the calculation of the mean, as shown below:

$$Mean_{e_{H_2PEM}} = \frac{50 + 71 + 53 + 67 + 50 + 78}{6} = 61.5 \quad (97)$$

The next step consists in calculating the squared differences from the mean and sum them. The obtained value (i.e. 729.5) is divided by the number of values minus one to get the variance, which is:

$$Variance_{e_{H_2PEM}} = \frac{2 \cdot (50 - 61.5)^2 + (71 - 61.5)^2 + (53 - 61.5)^2 + (67 - 61.5)^2 + (78 - 61.5)^2}{5} = 145.9$$

Finally, the standard deviation is found by taking the square root of the variance. The result is σ equals to 12.1.

The same process is followed to estimate the σ for $PE_{electricity}$.

Scenario	Parameter	Baseline	Variability range	Reference	Calculated mean value ± σ
2030	e_{H_2PEM}	62 MWh/ton	50÷71 MWh/ton	David et al. [24]	61.5 ± 12.1
			53÷67 MWh/ton	IEA [23]	
			50÷78 MWh/ton	IRENA [34]	
	$PE_{electricity}$	1.50	1.40	EPP – Annex J[58], scenario FFP Exten High	1.46 ± 0.04
			1.42	EPP – Annex J, scenario FFP High	
			1.45	EPP – Annex J, scenario reference	
			1.48	EPP – Annex J, scenario FFP Low	
			1.50	SAP 10 [137]	
2040	e_{H_2PEM}	55 MWh/ton	49÷65 MWh/ton	David et al. [24]	57.2 ± 9.9
			48÷63 MWh/ton	IEA [23]	
			46÷72 MWh/ton	IRENA [34]	
	$PE_{electricity}$	1.2	1.13	EPP – Annex J, scenario FFP Exten High	1.2 ± 0.076
			1.17	EPP – Annex J, scenario FFP High	
			1.18	EPP – Annex J, scenario reference	
			1.33	EPP – Annex J, scenario FFP Low	

Table 59 – Parameters, variability ranges and calculated standard deviations for uncertainty analysis

Once the σ for both the key parameters and scenarios are known, a Monte Carlo approach is used to assess the impact of the uncertainties and understand how they propagate through the model. This method involves generating a large number (e.g. 10000) of random samples for each parameter based on normal probability distributions and calculating the WTW efficiency for each path multiple times to generate a distribution of possible outcomes.

The outcomes of the uncertainty study for scenario 2030 are presented in Table 60, Figure 51 and Figure 52. While the latter shows, as an example, the probability density function of WTW efficiencies for path 1 (i.e. WTW efficiency = 0.169 ± 0.038), Table 60 and Figure 51 provide mean WTW efficiency's values and standard deviations for all the pathways. Error

[58] https://www.gov.uk/government/publications/energy-and-emissions-projections-2021-to-2040

bars representing one standard deviation are clearly visible in Figure 51. Pathways 7 to 12 have low standard deviations because they do not involve electrolysis and their WTW efficiencies are minimally affected by grid electricity's PE factor (see Figure 50).

Pathway	σ	Mean WTW efficiency	5th Percentile	95th Percentile
1	0.0383	0.1694	0.1215	0.2397
2	0.0377	0.1668	0.1197	0.2360
3	0.0386	0.1707	0.1225	0.2416
4	0.0379	0.1679	0.1204	0.2375
5	0.0414	0.1833	0.1314	0.2594
6	0.0359	0.1588	0.1139	0.2246
7	$3.1 \cdot 10^{-4}$	0.1899	0.1894	0.1905
8	$2.8 \cdot 10^{-4}$	0.1870	0.1866	0.1875
9	$2.6 \cdot 10^{-4}$	0.1914	0.1910	0.1919
10	$2.4 \cdot 10^{-4}$	0.1882	0.1878	0.1886
11	$2.0 \cdot 10^{-4}$	0.2055	0.2052	0.2058
12	$6.4 \cdot 10^{-4}$	0.1781	0.1780	0.1782
13	0.0332	0.1458	0.1043	0.2065
14	0.0327	0.1435	0.1027	0.2033

Table 60 – Uncertainty analysis outcomes for 2030 scenario

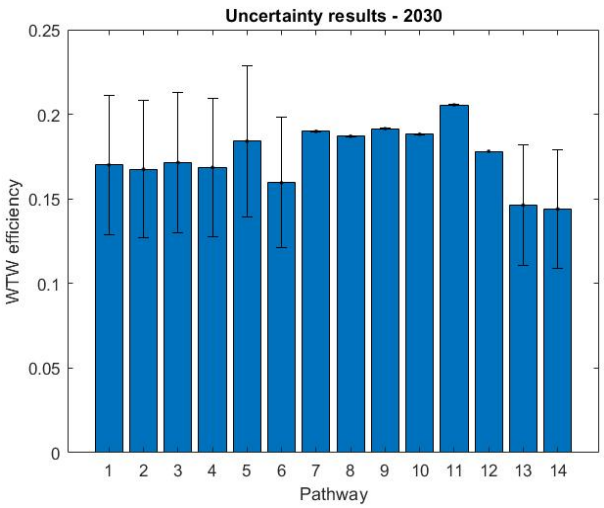

Figure 51 – Histogram of mean WTW efficiencies with error bars (scenario 2030)

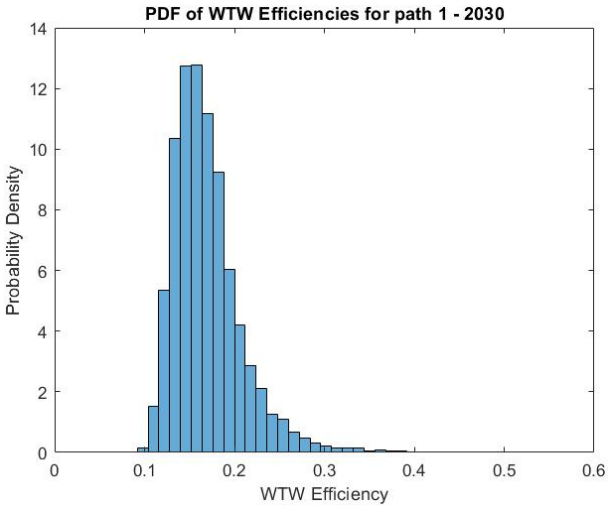

Figure 52 – Probability density function for path 1 (scenario 2030)

In a similar fashion, the results for the 2040 uncertainty analysis are given below.

Pathway	σ	Mean WTW efficiency	5th Percentile	95th Percentile
1	0.0411	0.2174	0.1645	0.2923
2	0.0404	0.2139	0.1619	0.2876
3	0.0348	0.1842	0.1394	0.2477
4	0.0342	0.181	0.137	0.2435
5	0.0374	0.198	0.1498	0.2663
6	0.0344	0.1817	0.1375	0.2444
7	$7 \cdot 10^{-4}$	0.2312	0.2301	0.2324
8	$6 \cdot 10^{-4}$	0.2275	0.2264	0.2285
9	$5 \cdot 10^{-4}$	0.196	0.1951	0.1968
10	$5 \cdot 10^{-4}$	0.1926	0.1918	0.1933
11	$4 \cdot 10^{-4}$	0.2106	0.21	0.2112
12	$1 \cdot 10^{-4}$	0.1933	0.1931	0.1935
13	0.0385	0.1924	0.1421	0.2626
14	0.0379	0.1893	0.1398	0.2584

Table 61 – Uncertainty analysis outcomes for 2040 scenario

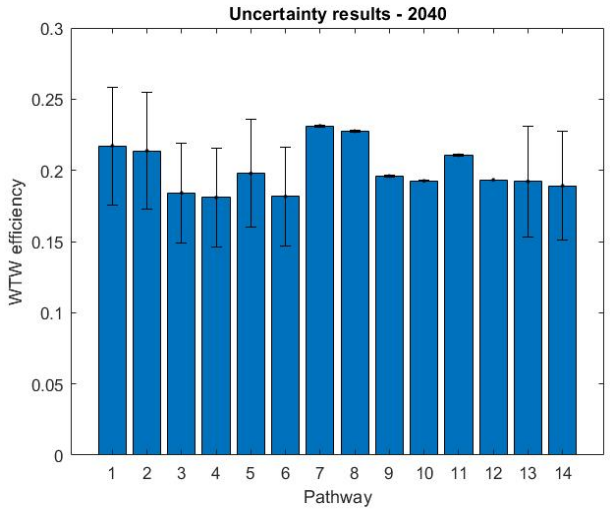

Figure 53 – Histogram of mean WTW efficiencies with error bars (scenario 2040)

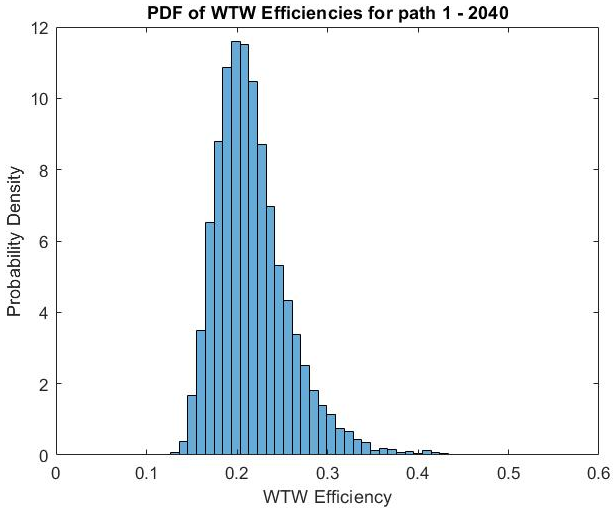

Figure 54 – Probability density function for path 1 (scenario 2040)

By comparing the results for scenario 2030 with those related to scenario 2040, it emerges that the average standard deviation for the fourteen routes is about 0.021 for both the scenarios. The slight variations in WTW efficiencies for paths from 7 to 12 are a sign of how little the uncertainty in grid electricity's PE factor affects the outcomes, given that the PE

factor is the only source of uncertainty acting for these routes. In other words, the reason for the low standard deviation in blue hydrogen pathways (i.e. 7 to 12) is that they use more mature technologies, like natural gas reforming, leading to less uncertainty in WTW efficiencies.

4. Chapter four

Waste heat from fuel cell hybrid trains: the Birmingham New Street station scenario

4.1 Fuel cell heat generation

In a fuel cell hybrid vehicle, as previously said, hybridisation of the powertrain allows fuel cells to constantly provide just the average power demand, as power fluctuations are covered by batteries. Even at train stops, fuel cells keep running to recharge the batteries. The assumption of a constant electric power output for the fuel cells is then a very close approximation to their actual duty cycle and makes the determination of $\dot{Q}_{module}$ much easier. In fact, in order to generate a constant $\dot{W}_{module}$, fuel cell module must work at the same current density throughout the duration of the journey. According to Eqs. (10) - (13), this implies that $\dot{Q}_{module}$ is a constant quantity too, as all the parameters involved in its calculation are uniquely determined by a single value of current density. As regards the magnitude of the output ($\dot{W}_{module}$), a distinction between retrofitted and newly built commercial units needs to be made. While the fuel cell powerpack of the former is appositely designed for the specific route through which the train runs, the fuel cells mounted on the latter are sized to meet the typical technical and non-technical requirements (e.g. acceleration, speed, drive profile, passenger capacity) of a certain train segment (e.g. regional passenger trains). It follows that the fuel cell powerpack of some commercial units operating on less energy-demanding tracks may turn out to be oversized and therefore a significative part of the installed capacity of each module may not be exploited. Conversely,

in retrofitted vehicles, fuel cell modules' output can be considered much closer to the overall installed power as the result of the "customised" design approach. As Eq. (11) shows, $\eta_{el,cell}$ can replace cell voltage in the calculation of heat generation rate. It is clear from Eq. (13) that the electrical efficiency of the fuel cells depends both on their polarisation curves and working current density value. Because of the lack of information on technical specifications and actual working conditions of the fuel cell modules implemented on the trains, $\eta_{el,cell}$ is not known. A reasonable assumption is hence needed. Ballard claims a peak efficiency of 0.6 for its fuel cell power module designed for heavy duty motive[59]. In this thesis a fuel cell electric efficiency equal to 0.5 is supposed, which is also consistent with the values often encountered in literature [102] [175] [176]. It is also assumed that efficiency is constant during the journey, as direct consequence of the constant electric power output. In fact, if $\dot{W}_{module}$ in Eq. (13) is constant, then $\dot{Q}_{module}$ is uniquely determined by the polarisation curve (Figure 8), resulting in a constant fuel cell efficiency. Therefore, based on what has been said so far, the total amount of heat released by a fuel cell module during the train journey (Q_{module}) is then roughly equivalent to the electrical energy produced in the same time span. Since the electric power does not change with time, Q_{module} is simply the product between $\dot{W}_{module}$ and $t_{journey}$ (Eq. (98)).

$$Q_{module} = \int_0^t \dot{Q}_{module}\ dt = \int_0^t \dot{W}_{module}\ dt = \dot{W}_{module} \cdot t_{journey} \tag{98}$$

[59] https://www.ballard.com/docs/default-source/spec-sheets/fcmove-xd.pdf?sfvrsn=6510de80_9

4.2 Cooling system

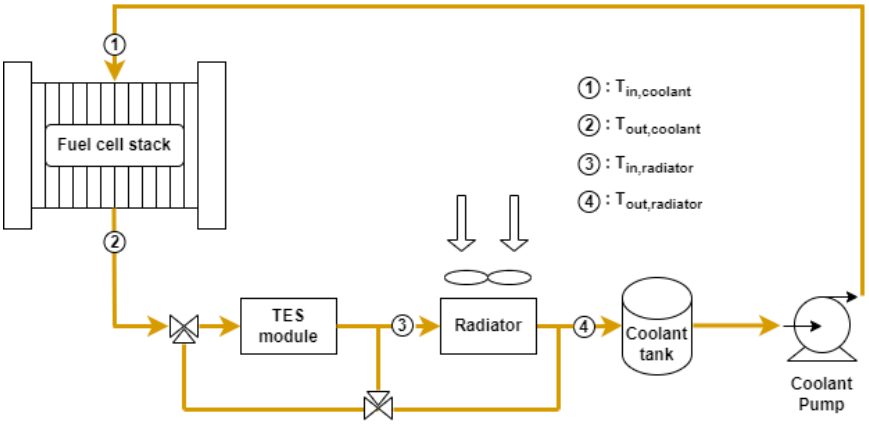

Figure 55 – PEMFC module's coolant circuit

The amount of heat removed per unit time by coolant can be expressed as:

$$\dot{Q}_{coolant} = \dot{m}_{coolant} \cdot c_{p_{coolant}} \cdot \Delta T_{coolant} \tag{99}$$

where $\dot{m}_{coolant}$ is the coolant mass flow rate, $c_{p_{coolant}}$ is the specific heat capacity of the coolant and $\Delta T_{coolant}$ is the coolant temperature difference between the inlet ($T_{in,coolant}$) and the outlet ($T_{out,coolant}$) of the module. The dynamic behaviour of the PEMFC module temperature is governed by the following differential equation:

$$\left(c_p \cdot m\right)_{module} \cdot \frac{dT_{module}}{dt} = 0.95 \cdot \dot{Q}_{module} - \dot{Q}_{coolant} - \dot{Q}_{amb} \tag{100}$$

where $\left(c_p \cdot m\right)_{module}$ is the heat capacity of the module, $\dot{Q}_{amb}$ is the thermal power exchanged by the module with the ambient and 0.95 is the factor introduced to take into account that almost 5% of the produced heat is actually lost through the anode and cathode exhausts [177]. Since the module is thermally insulated, $\dot{Q}_{amb}$ can be regarded as negligible in comparison with $\dot{Q}_{coolant}$. As Eq. (100) shows, in order to maintain stable the operating temperature of the fuel cells and avoid sudden overshoots, $\dot{Q}_{coolant}$ shall match $\dot{Q}_{module}$ at any time. This is achieved by varying the speed of circulating pump, while ensuring that

$\Delta T_{coolant} \leq \Delta T_{coolant,max}$. Many studies, such as [104] [178] [179], set $\Delta T_{coolant} = \Delta T_{coolant,max} = 5\ K$ and so the same assumption is also applied here. As concerns instead the values of $T_{out,coolant}$ and $T_{in,coolant}$, the Ballard's FCmove power module for heavy duty motive is again taken as a reference. According to the datasheet[60], the radiator coolant outlet temperature ($T_{out,radiator}$) is 70°C at nominal conditions. If $T_{out,radiator}$ is supposed to coincide with $T_{in,coolant}$, the coolant temperature at the exit of the module will be hence equal to $T_{out,coolant} = 70 + \Delta T_{coolant} = 75°C$.

As mentioned in the '*Fuel cell heat generation*' section, the heat generation rate $\dot{Q}_{module}$ can be considered constant in a fuel cell hybrid train, resulting in pump continuously working at the same speed and so in $\dot{m}_{coolant}$ unchanged over time. Therefore, rearranging Eq. (99), the coolant mass flow rate through a fuel cell module is constantly equal to:

$$\dot{m}_{coolant} = \frac{0.95 \cdot \dot{W}_{module}}{c_{p_{coolant}} \cdot \Delta T_{module} (= 5\ K)} \tag{101}$$

4.3 Birmingham New Street waste heat potential

As stated in the '*Fuel cell hybrid trains*' section, the Department for Transport (DfT) hopes to remove all the diesel trains from UK network by 2040. Currently, the most relevant train operators at New Street station are Avanti West Coast (AWC), Cross Country (CC), London Northwestern Railway (LNR), West Midlands Railway (WMR) and Transport for Wales[61] (TfW). These companies operate a total of 485 trains: 243 diesel, 200 electric and 42 bi-mode, for a total of 2072 carriages.

[60] https://www.ballard.com/fuel-cell-solutions/fuel-cell-power-products/motive-modules
[61] https://www.networkrail.co.uk/communities/passengers/our-stations/birmingham-new-street/

Company	N of diesel trains	N of electric trains	N of bi-mode trains	Total trains	Total carriages	Diesel carriages	Class of diesel train
AWC	0	66	13	79	709	0	
CC	87	0	0	87	332	332	170, 220, 221
LNR	3	95	0	98	413	6	230
WMR	65	39	0	104	290	173	196, 170, 172
TfW	88	0	29	117	328	224	197, 231
Total	**243**	**200**	**42**	**485**	**2072**	**735**	

Table 62 – Train operators' fleets

In order to meet the decarbonisation target set by DfT, it is supposed that all the trains equipped with diesel engines are going to be retrofitted with fuel cell hybrid powertrains. However, of the 243 diesel vehicles, only those running on lines in which Birmingham New Street station is one of the two terminus are taken into account for the estimation of the station's waste heat potential (i.e. the maximum amount of heat that trains can discharged every day). Conversely, all the lines having New Street station as intermediate call are excluded from the calculation, as well as the trains serving them. The reason behind this choice is linked to the short time usually available at intermediate stops for heat discharging. In fact, while at terminus a train stops for a time that can be of the order of tens of minutes before starting a new journey, it instead waits for a very short time (1÷2 minutes) if the station is just an intermediate call.

After having selected the routes satisfying the criterion just described, New Street station's daily waste heat potential is determined as follows:

$$Q_{BNS\,potential} = \sum_{routes} 0.95 \cdot n_{disch} \cdot \dot{W}_{module} \cdot n_{car} \cdot t_{1way/2way} \tag{102}$$

where the factor 0.95 has been introduced in Eq. (100), n_{disch} is how often a day the trains operating on the considered route stop at Birmingham New Street station, $\dot{W}_{module}$ is the

electric power output of the fuel cell hybrid powertrain characterising the trains running on the i-th route, n_{car} is the number of coaches forming the trains, $t_{1way/2way}$ is the time required for a one-way or a two-way journey.

As no information on n_{car} is available for the selected routes, an average value for each train operator is defined. Cross Country operates a total of 332 carriages, which are arranged in 87 trains. Thus, one of their train is formed, on average, by 3.8 cars. West Midlands Railway manages instead 173 diesel units, arranged in 65 trains. The average train length is 2.7 coaches.

The parameters n_{disch} and $t_{1way/2way}$ for each of the selected routes are obtained from the related timetables and gathered in Table 63.

Operator	Route	n_{disch}	n_{car}	t_{1way} (hr)	t_{2way} (hr)
Cross Country	Leicester - BNS	17	3.8	0.93	1.86
	Nottingham - BNS	16	3.8	1.25	2.50
	Stansted - BNS	11	3.8	3.27	6.54
	Cambridge - BNS	5	3.8	2.70	5.40
	Derby - BNS	4	3.8	0.60	1.20
West Midlands Railway	Shrewsbury - BNS	17	2.7	1.20	2.40
	Worcester - BNS	2	2.7	0.75	1.50
	Hereford - BNS	12	2.7	1.53	3.06
	G. Malvern - BNS	3	2.7	1	2

Table 63 – n_{disch}, n_{car} and $t_{1way/2way}$ for the chosen routes

To clarify how n_{disch} and $t_{1way/2way}$ are retrieved, the case of the '*Hereford – BNS*' route is now provided as example (Table 64). The first step is the determination of the minimum number of vehicles (row A). The four different colours identify the four trains needed to meet the timetable of the route (rows B and C). Row D shows that t_{1way} has to be considered for

the first two discharging events of the day as trains 2 ad 3 have been on the rail just for a one way trip. However, not all the stops at BNS involve a discharging, as the 'NO disch' in the row E suggests. In fact, every time a train stops at BNS for less than 15 mins, it is supposed there is not enough time to set up and complete a discharging process. So, for instance, train 2 arriving at New Street Station at 8:39 cannot unload the heat as it has to depart again just after 11 minutes (i.e. 8.50). Finally, '12' in row F represents the number of possible discharges per day. According to Eq. (102), the contribution of the Hereford-BNS route to BNS waste heat potential can be written as:

$$Q_{Her-BNS} = 0.95 \cdot 2 \cdot \dot{W}_{module} \cdot 2.7 \cdot t_{1way} + 0.95 \cdot 10 \cdot \dot{W}_{module} \cdot 2.7 \cdot t_{2way} \qquad (103)$$

A	train 1	train 2	train 3	train 4													
B	Birm - Here	6.59 - 8.29	8.00 - 9.32	8.50 - 10.14	9.50 - 11.16	10.50 - 12.15	11.50 - 13.15	12.50 - 14.15	13.50 - 15.14	14.50 - 16.12	15.50 - 17.13	16.50 - 18.17	17.20 - 18.46	18.20 - 19.42	19.20 - 21.01	21.00 - 22.34	
C	Here - Birm	7.10 - 8.39	7.32 - 9.09	8.37 - 10.08	9.39 - 11.09	10.39 - 12.08	11.39 - 13.10	12.39 - 14.09	13.41 - 15.09	14.39 - 16.10	15.39 - 17.10	16.39 - 18.09	17.39 - 19.10	18.48 - 20.19	19.51 - 21.20	20.58 - 22.36	21.28 - 22.52
D		t 1 way	t 1 way	t 2 way	t 2 way	t 2 way	t 2 way	t 2 way	t 2 way	t 2 way	t 2 way	t 2 way	t 2 way	t 2 way	t 2 way	t 2 way	t 2 way
E		NO disch	disch	disch	disch	disch	disch	disch	disch	disch	NO disch	NO disch	NO disch	disch	disch	disch	disch
F	12																

Table 64 – Hereford-BNS case

In a retrofitted fuel cell hybrid train, as discussed in the '*Fuel cell heat generation*' section, the powertrain module is sized to meet the specific average power demand of the journey at issue. In particular, for a given track, the benchmark for the proper design of fuel cell hybrid vehicles is usually derived from the duty-cycle and speed profile of the trains that are going to undergo retrofitting [180]. The magnitude of $\dot{W}_{module}$ hence depends both on route and train's characteristics. Due to the lack of such data, the work by S. Kent [181] is used as a basis for the evaluation of $\dot{W}_{module}$. In his study, Kent aims to develop a fuel cell hybrid powertrain for retrofitting the two-cars Class 156 diesel trains serving the Norwich-Sheringham regional line. He finds that 150 kW per carriage is the minimum required fuel cell module output, increased to 200 kW to make use of the commercially available FC module sizes. Despite the outcomes of Kent's study are specific to Class 156 and Norwich-

Sheringham line, it has been decided to assume an installed capacity of 200 kW per carriage and an actual power output of 150 kW per carriage for all the trains, regardless of the route and class of trains. The reasons why this assumption seems reasonable are explained in the following lines. In fact, even if belonging to different classes, both Class 156 and the diesel trains considered in this thesis fall within the regional passenger train segment. Thus, they are all designed to address the same technical and non-technical requirements. Moreover, if it is supposed that the higher energy demand of some tracks can be met by increasing only the size of the battery pack, then the fuel cell module output can be considered to be the same for all the selected lines. In summary, in the light of the above, $\dot{W}_{module}$ is assumed to be always equal to 150 kW per carriage, regardless of the train model, route at issue and number of cars forming the train.

The New Street station's waste heat potential can be now estimated by means of Eq. (102). The table below highlights the contribution of each route to the total amount of heat ideally available at the station at the end of the day.

Route	Q_{route} (MWh)
Leicester - BNS	16.17
Nottingham - BNS	20.31
Stansted - BNS	30.29
Cambridge - BNS	13.16
Derby - BNS	2.60
Shrewsbury - BNS	15.70
Worcester - BNS	0.87
Hereford - BNS	13.57
G. Malvern - BNS	1.54
BNS TOT	**114.21**

Table 65 – Contribution of each analysed route to the daily BNS waste heat potential

The value of $Q_{NS\,potential}$ shown in Table 65 corresponds therefore to the heat that would be available at the station if all the thermal energy generated by fuel cells is first stored in the on-board TES and then discharged with a 100% efficiency. Because of the limited space for TES on the train and the impossibility to achieve a 100% round-trip efficiency, only a fraction of the $Q_{NS\,potential}$ can be discharged at the station. The actual heat quantity available at New Street station will be assessed later on in the thesis.

4.4 Energy demand for train cabin heating

Besides the space restrictions for TES implementation and a round-trip efficiency certainly lower than 1, another factor that affects $Q_{NS\,potential}$ is the thermal energy demand for cabin heating. In fact, it is supposed that part of the heat removed from the fuel cell powertrain by the coolant is used to maintain cabin air temperature within a comfortable range.

The average energy demand per unit time for cabin heating is assessed by means of a dynamic thermal lumped model of a typical train carriage. The model is developed in the Simulink environment and its mathematical formulation can be summarised as:

$$C_{in}\frac{dT_{in}}{dt} = \dot{Q}_{env} + \dot{Q}_{windows} + \dot{Q}_{vent} + \dot{Q}_{people} + \dot{Q}_{lights} + \dot{Q}_{heater} \tag{104}$$

where C_{in} is the thermal capacitance of the cabin air and train body (i.e. $C_{in} = m_{air} \cdot c_{p_{air}} + m_{train} \cdot c_{p_{train}}$), T_{in} is cabin air temperature, $\dot{Q}_{env}$ and $\dot{Q}_{windows}$ are the heat losses through the coach envelope and windows, $\dot{Q}_{vent}$ is the heat load to comply with the ventilation requirements, $\dot{Q}_{people}$ is the thermal energy per unit time gained due to the metabolic activities of human bodies, $\dot{Q}_{lights}$ is the heat from the lighting system and $\dot{Q}_{heater}$ is the heat per unit time that heater transfers to cabin air to keep indoor temperature constant.

Using an electric circuit analogy, $\dot{Q}_{env}$ and $\dot{Q}_{windows}$ can be described as:

$$\dot{Q}_{env} = \frac{A_{roof}(T_{out} - T_{in})}{R_{roof}} + \frac{A_{walls}(T_{out} - T_{in})}{R_{wall}} + \frac{A_{floor}(T_{out} - T_{in})}{R_{floor}} \quad (105)$$

$$\dot{Q}_{windows} = \frac{A_{windows}(T_{out} - T_{in})}{R_{windows}} \quad (106)$$

where A is the surface, T_{out} is the outdoor temperature and R is the thermal resistance calculated as the reciprocal of the overall heat transfer coefficient U [W m^{-2} K^{-1}]. Typical U-values for train envelopes and windows are found in [182] and are displayed in Table 66.

Component	U-value (W m^{-2} K^{-1})	R-value (m^2 K W^{-1})
Roof	0.87	1.15
Wall	0.87	1.15
Floor	1.8	0.56
Windows	1.3	0.77

Table 66 – U-values and R-values for coach components

U-values take into account both the conduction and convection heat transfer mechanisms. The formula to calculate the overall heat transfer coefficient is provided in Eq. (107).

$$\frac{1}{U} = \frac{1}{h_i} + \sum_{k=1}^{n} \frac{L_k}{k_k} + \frac{1}{h_e} \quad (107)$$

where h_i is the convective heat transfer coefficient on the inner surfaces, L_k is the thickness of layer k, k_k is the thermal conductivity of layer k, n is the number of the layers and h_e is the convective heat transfer coefficient on the outer surfaces. Contrary to what the reader might expect, h_e has a minor impact when it comes to calculate the surfaces' thermal resistances for a fast moving train. For instance, if the same correlation used by Barone et al. [183] is adopted to determine h_e (i.e. $h_e = 3.5 \cdot v^{0.66} + 9$), a value of 38 W m^{-2} K^{-1} is obtained for an average velocity of 90 km/h. This means that the contribution to the thermal resistance is 0.026 m^2 K W^{-1}, less than 5% for all the R-values reported in Table 66.

Taking the coach of the Class 172 diesel train as a reference, whose surface areas A_{roof}, A_{floor}, $A_{windows}$ and A_{walls} have been estimated from drawings, it follows that:

Figure 56 – Class 172 carriage

Component	A (m^2)
Roof	54
Walls	67
Floor	54
Windows	38

Table 67 – Components' surface areas

To ensure an acceptable air quality for passengers, a minimum flow of fresh air has to be guaranteed. The heat gain due to ventilation can be determined through the following equation [184]:

$$\dot{Q}_{vent} = n_{people} \cdot \dot{m}_{vent} \cdot (h_{out} - h_{in}) \quad (108)$$

where n_{people} is the number of people inside the cabin, $\dot{m}_{vent}$ is the ventilation mass flow rate prescribed by ASHRAE Standard 62[62] (i.e. 25 m^3 per hour per person), h_{out} is the ambient air enthalpy and h_{in} is the enthalpy of cabin air. The variation of n_{people} over the day is assumed to follow the same trend of the distribution of rail journeys into and out of regional major cities[63].

[62] https://www.ashrae.org/technical-resources/bookstore/standards-62-1-62-2#:~:text=ANSI%2FASHRAE%20Standards%2062.1%20and,adverse%20health%20effects%20for%20occupants.
[63] https://www.gov.uk/government/statistics/rail-passenger-numbers-and-crowding-on-weekdays-in-major-cities-in-england-and-wales-2021/rail-passenger-numbers-and-crowding-on-weekdays-in-major-cities-in-england-and-wales-2021

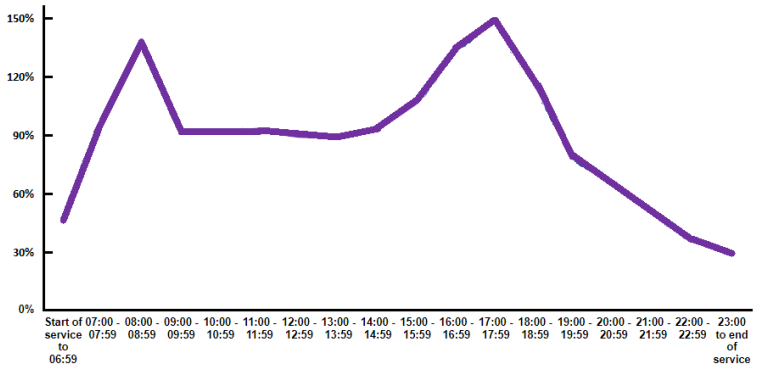

Figure 57 – Occupancy profile[58]

The heat emitted by human bodies $\dot{Q}_{people}$ is taken from [185] and amounts to 116 W per passenger. Thus,

$$\dot{Q}_{people} = 116 \cdot n_{people} \tag{109}$$

As regards $\dot{Q}_{lights}$, LED lights are considered. In compliance with EN 13272, the seating areas shall have an average illuminance greater than or equal to 300 lx[64]. The correlation for the calculation of $\dot{Q}_{lights}$ is the same used in [186] and has the following form:

$$\dot{Q}_{lights} = A_{floor} \cdot E_{il} \cdot \frac{1}{\eta_{lum}} \cdot H_e \tag{110}$$

where E_{il} is the required illuminance (300 lx), η_{lum} is the LED luminous efficacy (up to 150 lx m^2 W^{-1} [187]) and H_e is the LED heat emission coefficient (0.08 W/W).

Once all the terms of Eq. (104) have been defined, Simulink simulation can be launched. The main output of the model is $\dot{Q}_{heater}$, which is varied by the program so that T_{in} falls within the desired thermal comfort range (i.e. 19.5 – 20.5 °C). The heating system essentially consists of inlet and outlet dampers, an air blower and a heating coil. The only manipulated

[64] https://www.transport.nsw.gov.au/industry/asset-standards-authority/find-a-standard/interior-and-exterior-lighting-for-passenger-0

variable to control the magnitude of $\dot{Q}_{heater}$ is the air flow rate injected into the cabin, which in turn affects the amount of coolant that has to flow inside the heating coil. A PID controller is then implemented in the model to simulate the control strategy. The heating system operates between 6 am and 12 am, matching the train working day. The simulation covers 365 days, from 1st January to 31st December. To account for hourly temperature variations throughout the year, a weather file for Birmingham is downloaded from the EnergyPlus database[65] and implemented into the model.

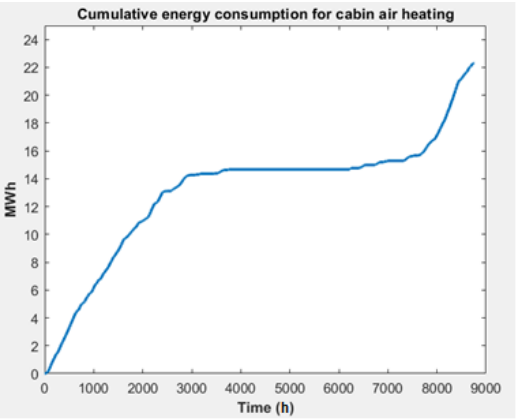

Figure 58 – Cumulative yearly energy consumption for cabin air heating (one cabin)

According to the model outcome, about 22.3 MWh of heat per carriage are consumed yearly for cabin air heating. Table 68 shows the average hourly energy consumption for cabin heating by season.

Season	Hourly energy consumption (kWh)
Winter	5.44
Spring	1.76
Summer	0.04
Autumn	2.99

Table 68 – Average hourly energy usage per carriage in summer, winter, autumn and spring

[65] https://energyplus.net/weather

For the sake of validation, the developed model is applied to the same case studied by Barone et al. in [183]. Figure 59 shows the hourly thermal loads variation during a sample winter day for a MDVC railway coach running in the surrounding area of Naples. A good agreement between the two models is achieved, except for the time ranging from 9 am to 14 pm. This discrepancy is due to the effect of the incident solar radiation onto the coach body. In fact, given the many factors involved in the calculation of solar heat gains (e.g. weather conditions, data, time, specific location, travel direction), it has been decided to not include them in the Simulink model, adopting then a conservative approach.

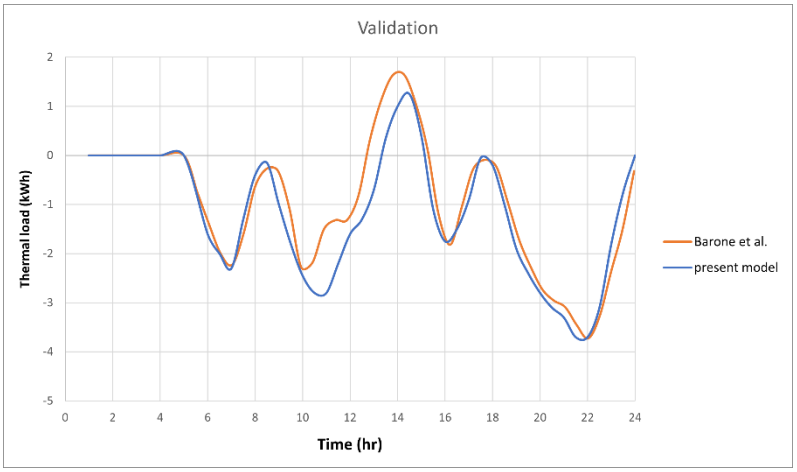

Figure 59 – Simulink model validation

The BNS daily waste heat potential can be now recalculated taking also into account the energy for cabin air heating. Starting from Eq. (102), the new formula becomes:

$$Q_{BNS\ potential_{rec}} = Q_{BNS\ potential} - \sum_{routes} E_{heating} \cdot n_{disch} \cdot n_{car} \cdot t_{1way/2way} \qquad (111)$$

where $E_{heating}$ is taken from Table 68.

By comparing Table 69 with Table 65, it emerges that only 3.9% of the BNS daily waste heat potential is spent for cabin heating during winter.

Route	Q_{route} winter (MWh)	Q_{route} spring (MWh)	Q_{route} summer (MWh)	Q_{route} autumn (MWh)
Leicester - BNS	15.55	15.97	16.17	15.83
Nottingham - BNS	19.53	20.06	20.30	19.88
Stansted - BNS	29.12	29.91	30.28	29.65
Cambridge - BNS	12.64	12.99	13.16	12.87
Derby - BNS	2.50	2.57	2.60	2.55
Shrewsbury - BNS	15.10	15.51	15.70	15.37
Worcester - BNS	0.83	0.86	0.87	0.85
Hereford - BNS	13.05	13.40	13.57	13.28
G. Malvern - BNS	1.48	1.52	1.54	1.51
BNS TOT	**109.80**	**112.78**	**114.18**	**111.79**

Table 69 – BNS daily waste heat potential considering the energy for cabin heating

4.5 TES positioning

The magnitude of the waste heat from fuel cell module storable in a train carriage depends on the space availability for the installation of TES devices. In the present work, thermal energy storages are supposed to be mounted on the train roof. Additional space for TES positioning may be available inside the train cabin but, due to internal layout complexity, only the roof option has been analysed.

The free room on the roof for TES implementation depends in turn on which design choices are taken to perform the retrofit process. Converting diesel trains into hybrid fuel cell ones implies the replacement of those components no longer needed with the new equipment required (i.e. fuel cell module, battery pack, hydrogen storage tanks, electric motors). In the '*Fuel cell hybrid trains*' section, the design concepts of Coradia iLint (Figure 3), Mireo Plus H (Figure 4) and HYBARI (Figure 5) have been introduced. While in the first two the roof is almost completely occupied by fuel cells and hydrogen pressurised vessels, in HYBARI the

roof accommodates the H_2 storages only. A concept design that offers even more space on the roof than HYBARI is the one proposed by S. Kent in [181]. He claims that all the equipment required to transform the Class 156 diesel train into a fuel cell hybrid one can be fitted on the underframe of each carriage, including nine vessels containing 69 kg of hydrogen at 350 bar (see Figure 60). According to Kent's calculations, 69 kg of H_2 per carriage are enough for the retrofitted two-car train to achieve a daily operating range of 800 km, which is the average daily mileage of a typical regional train [89]. TES positioning will be then based on the concept illustrated in Figure 60, as it allows to maximise the heat storable on the vehicle's roof.

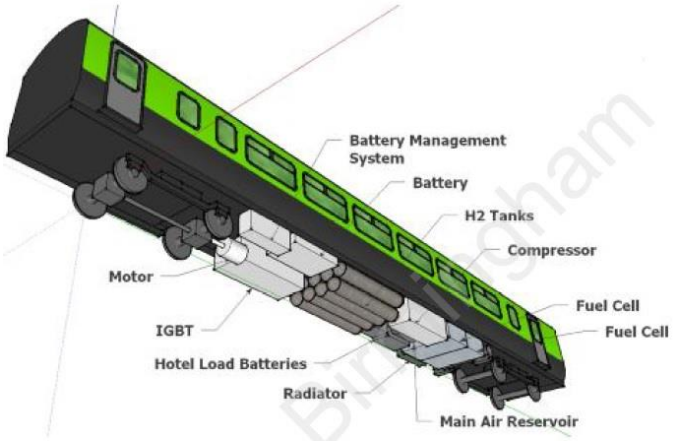

Figure 60 – Train carriage after the retrofitting [181]

The curved shape of the train roof is the major problem linked to the installation of TES. A possible solution to this issue is to follow the same design approach adopted by Eversholt Rail in the refurbishment of the Class 321 Renatus fleet[66]. In order to implement some of the planned upgrades, Eversholt Rail team removed the curved roof (Figure 61 and Figure

[66] https://eversholtrail.co.uk/fleet/321-renatus/

62) and inserted a metallic shelf (Figure 63 and Figure 64). Such a structure can also be suitable to accommodate TES systems.

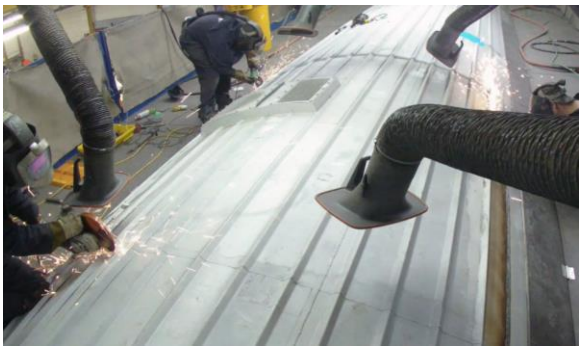

Figure 61 – Beginning of roof removal

Figure 62 – End of roof removal

Figure 63 – Shelf installation

Figure 64 – Final result

In the case of roof integration, the volume for TES is determined by carriage length, width and gauge limitations. Despite being part of different classes, all the trains involved in the routes selected are characterised by similar dimensions. So, for the sake of simplicity, a carriage with average sizes is considered from now on.

H_{car}	L_{car}	W_{car}
3.8 m	23.5 m	2.7 m

Table 70 – Carriage with average dimensions

As regards gauge restrictions, the maximum dimensions permitted in UK railway sector are displayed in Figure 65.

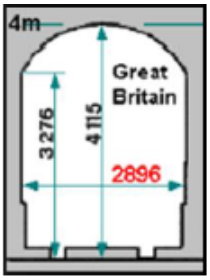

Figure 65 – UK gauge

By taking into account both carriage dimensions and gauge constraints, the space available on the roof for TES amounts to 28.5 m^3 per carriage. Figure 66 displays a 3D representation of train carriage, where the volume intended for TES is highlighted in yellow. The 3D model is built in '*Design Modeler*' software.

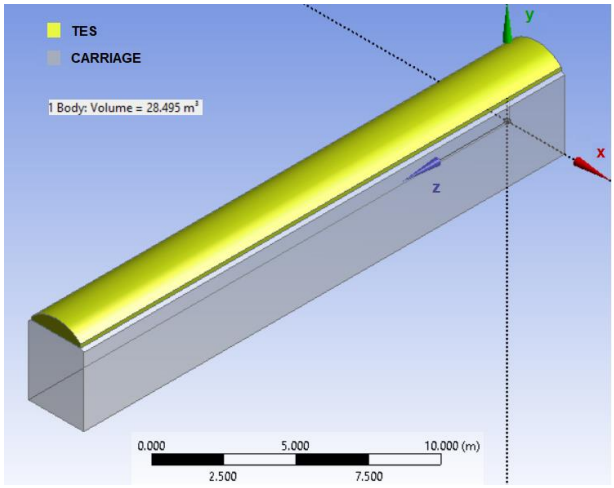

Figure 66 – 3D image of carriage and TES

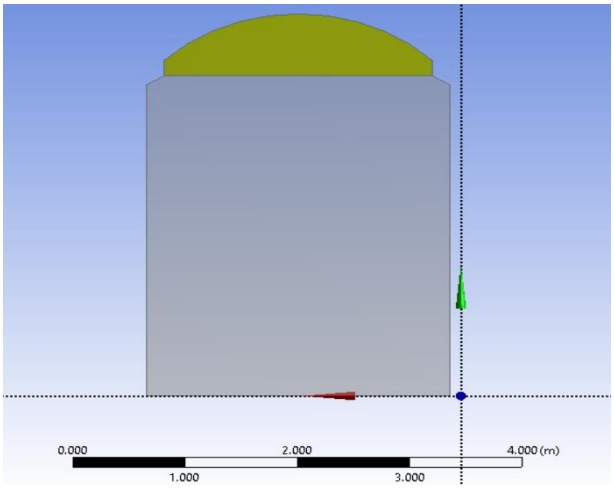

Figure 67 – Front view of carriage and TES

4.6 TES system sizing

The most common designs for PCM based-TES are shell-and-tube and stacked flat slabs. The latter is preferred for the purposes of this thesis, due to its high surface to volume ratio and ease of construction [188]. Because of the difference in shape between the geometry

chosen for TES (i.e. rectangular parallelepiped) and the gauge, the volume actually occupied by TES will be inevitably lower than 28.5 m^3/carriage.

Since trains are usually more than 3.5 m high, TES height needs to be carefully sized to not violate gauge limitations. By comparing UK gauge with the value of height in Table 70, it follows that TES cannot measure more than $(4.115 - 3.8) = 0.315\ m$ in height.

Nevertheless, after the removal of the roof, the shelf is positioned at a lower level (see Figure 64) and so the maximum vertical size of TES system can actually be increased. Given the impossibility to accurately establish how much the height decreases, an approximate calculation is performed.

Figure 68 depicts a carriage of the Class 172 diesel train.

Figure 68 – Class 172 drawing[67]

Under the assumption that the figure above is a scale drawing and knowing that the Class 172 is 3.77 m high, it has been inferred that the roof structure is attached to the carriage body at roughly 3.35 m from the ground. As the shelf does not sit directly on the edges of the train body but on some brackets (circled in blue in Figure 64), thus TES maximum height can be estimated as:

$$h_{max,TES} = H_{gauge} - H_{shelf} = H_{gauge} - \left(H_{roof} + h_{brackets}\right) = 4.115 - (3.35 + h_{brackets}) \quad (112)$$

[67] https://it.wikipedia.org/wiki/File:Class_172_LO_Diagram.PNG

where H stands for height measured from the ground, while $h_{brackets}$ is the vertical space lost due to brackets. Assuming $h_{brackets}$ equal to 0.10 m, H_{shelf} is 3.45 m and $h_{max,TES}$ is around 0.65 m.

However, a TES having a rectangular cross-section of dimensions $H_{max,TES}$ x W_{car} does not respect UK gauge restrictions, as Figure 69 proves.

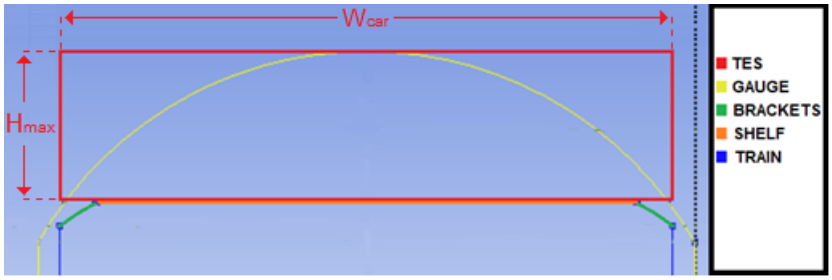

Figure 69 – TES of dimensions $H_{max,TES}$ x W_{car}

A thermal storage system with different dimensions is therefore designed. The new values of width and height are obtained as outputs of a purposely written MATLAB script. It finds, implementing the nonlinear programming solver '*fmincon*', the maximum of the constrained nonlinear multivariable function f(x_1,x_2). In symbols,

$$\underbrace{min}_{x}\ [-f(x)]\ such\ that \begin{cases} lb \leq x \leq ub \\ A \cdot x \leq b \\ A_{eq} \cdot x = b_{eq} \end{cases} \tag{113}$$

where x is the vector $x = [x_1, x_2]$, $A \cdot x \leq b$ and $A_{eq} \cdot x = b_{eq}$ express the linear inequalities and equalities to which $f(x)$ is subjected, lb and ub are the lower and upper bounds of the vector x and $min\ [-f(x)]$ is equivalent to $max\ [f(x)]$. As neither equalities nor inequalities exist, then A, b, A_{eq} and b_{eq} are not defined. The function to maximise is the rectangular cross-sectional area of the TES and is calculated as:

$$f(x_1, x_2, y_2) = (x_2 - x_1) \cdot (y_2 - H_{shelf}) \tag{114}$$

where y_2 is the y-component of point F, while x_2 and x_1 are the x-components of points E and D, respectively (see Figure 70). To make sure to comply gauge limits and at the same time to maximise TES cross-section, point F must be on the arc ABC. In other words, for a given x_2, the corresponding y_2 has to be retrieved from the equation of the circle passing through the points A,B and C, whose coordinates are known. After getting the circle's equation, which is of the form $[(x_2 - x_O)^2 + (y_2 - y_O)^2 = r^2]$, y_2 can be written as:

$$y_2 = y_O + \sqrt{r^2 - (x_2 - x_O)^2} \tag{115}$$

where x_O and y_O are the coordinates of the circle's centre O and r is the radius. By substituting Eq. (115) in Eq. (114), it follows that:

$$f(x_1, x_2) = (x_2 - x_1) \cdot \left(y_O + \sqrt{r^2 - (x_2 - x_O)^2} - H_{shelf}\right) \tag{116}$$

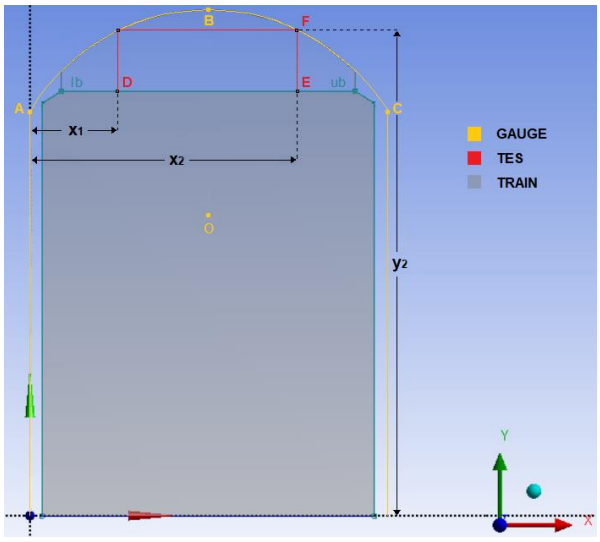

Figure 70 – TES of dimensions ($x_2 - x_1$) x ($y_2 - H_{shelf}$)

The outputs of the MATLAB script are the x-coordinates of the points D and E (i.e. x_1 and x_2) that allow to maximise the function $f(x_1, x_2)$. Figure 71 shows how TES cross-sectional area varies at each solver's iteration, until it reaches its maximum at the fifth one for x_1 =

0.635 m and x_2 = 2.26 m. Once x_1 and x_2 are known, the corresponding y-coordinate of point F can be derived from Eq. (115).

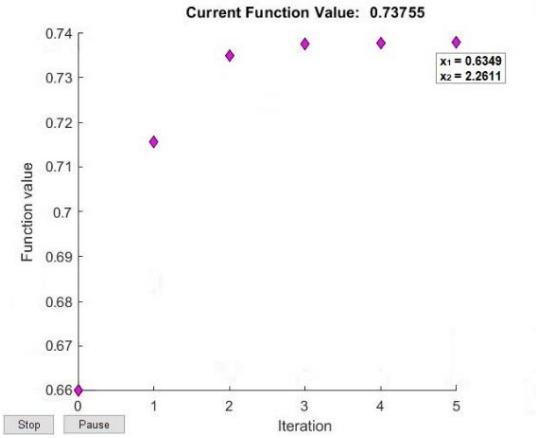

Figure 71 – f(x_1,x_2) value at each solver's iteration

Thus, the new values of TES width (W_{TES}) and height (h_{TES}) are equal to:

- $W_{TES} = x_2 - x_1 = 1.625$ m
- $h_{TES} = y_2 - H_{shelf} \approx 0.45$ m

The product between W_{TES}, h_{TES} and L_{car} (see Table 70) provides the space actually occupied by TES. It amounts to approximately 17.2 m^3 per carriage, about 60% of the maximum volume available.

In order to achieve a better utilisation of the available space, a different shape for TES system is developed. Again, both Design Modeler and MATLAB are used to solve the optimisation problem. The new geometry is presented in Figure 72. The same programming solver '*fmincon*' is implemented in the MATLAB script. The only difference is the mathematical relation assessing the TES cross-sectional area, which has now the following form:

$$f(x_1, x_2, y_1, y_2) = 2 \cdot \left[(x_2 - x_1) \cdot \left(y_1 - H_{shelf}\right) + (x_m - x_2) \cdot \left(y_2 - H_{shelf}\right)\right] \quad (117)$$

where the factor 2 refers to the symmetry of TES with respect to point M, while the meaning of x_1, x_2, y_1, y_2 and x_m can be inferred from Figure 72.

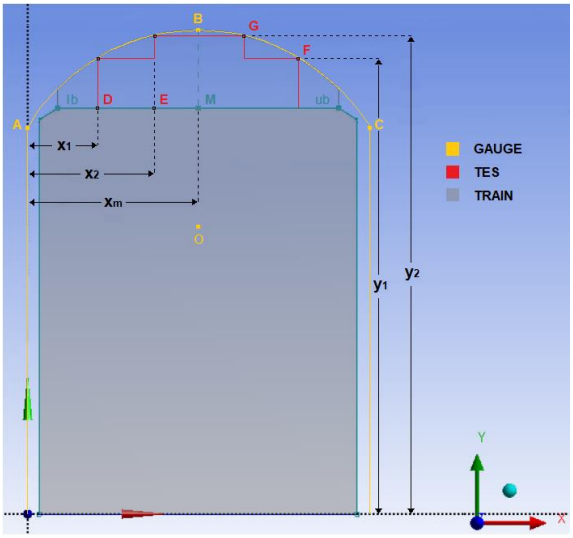

Figure 72 – New design for TES system

As points F and G belong to the arc ABC, Eq. (117) can be reformulated in terms of x_1 and x_2 only. In doing so, the function f becomes:

$$f(x_1,x_2) = 2 \cdot \left[(x_2 - x_1) \cdot \left(y_O + \sqrt{r^2 - (x_1 - x_O)^2} - H_{shelf}\right) + (x_m - x_2) \cdot \left(y_O + \sqrt{r^2 - (x_2 - x_O)^2} - H_{shelf}\right)\right] \quad (118)$$

The values of x_1 and x_2 able to maximise $f(x_1,x_2)$ are 0.43 m and 0.845 m, respectively. TES cross-sectional area, thanks to the new shape, is about 26% larger than before. The volume actually occupied by TES is now equal to 21.3 m^3 per carriage, around 74.7% of the maximum available space. Below, the upward trend of the objective function $f(x_1,x_2)$ throughout the optimisation process is shown.

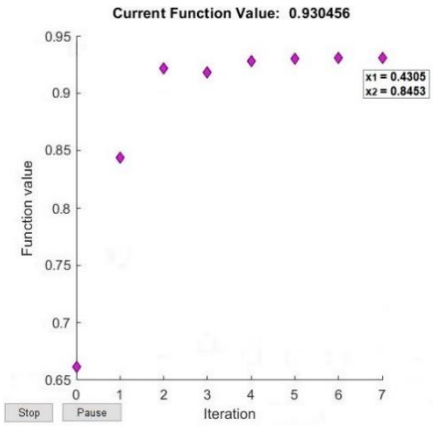

Figure 73 – $f(x_1,x_2)$ value at each solver's iteration

TES system, regardless of the shape chosen, is not installed on the carriage roof as a single block but is usually made up of several interconnected modules. If the geometry displayed in Figure 72 is adopted, it is assumed that TES system consists of the repetition of two parallelepiped-shaped modules having different sizes and arranged in four different lines (see Figure 74). The dimensions of the modules' cross-sections are indicated in Table 71.

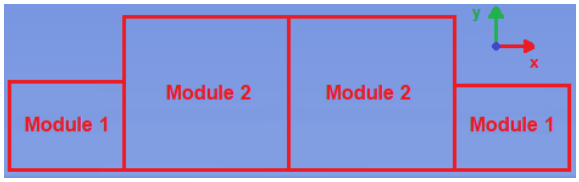

Figure 74 – TES module arrangement

	Module 1	Module 2
Width (m)	x_2-x_1 ≈ 0.415	(x_m-x_2) ≈ 0.6
Height (m)	y_1-H_{shelf} ≈ 0.315	y_2-H_{shelf} ≈ 0.545

Table 71 – TES modules dimensions

A last important issue when designing a TES system is the minimisation of the heat losses to the surroundings. The selection of the proper insulation material and the determination of the required insulation layer thickness are then crucial and are now addressed. Instead of wrapping each module with an insulating layer, the entire TES system is supposed to be

enclosed inside a shell of the same shape. The shell is made of stainless steel and is internally coated with polyurethane-polyisocyanurate (PUR-PIR), foam, a commonly used material for TES thermal insulation [189].

4.7 CFD analysis of TES modules: physical problem description

As mentioned in the '*Birmingham New Street waste heat potential*' section, the quantity of waste heat produced by fuel cells that can be discharged at the station depends on the overall energy storage capacity of TES system and on its round-trip efficiency. To characterise TES in terms of dynamic thermal performance, a CFD model investigating transient heat transfer between PCM slabs and water as HTF during charging and discharging processes is built in ANSYS Fluent environment. Fluent solves the partial differential equations governing thermo-fluid dynamics in the forms of algebraic relations by using the finite volume approach (FVM). In the FVM, the computational domain is first divided into several control volumes by a grid. After the domain discretisation, the values of the physical variables are calculated and stored at the volumes' centroids.

TES performance evaluation is first carried out for a default design. Afterwards, a series of parameters such as PCM slab and plate thickness, Reynolds number, channel cross-sectional area and total serpentine length are varied to obtain the optimal TES performance.

The first step of CFD analysis is the modelling of TES geometry with the CAD software ANSYS DesignModeler. The analysed PCM-based TES module is the result of several flat PCM slabs stacked one on top of the other forming a layered structure (Figure 75). Between each pair of PCM slabs, a metallic plate with the same x-z cross-sectional area of the slabs is placed. Besides, a serpentine rectangular-section channel is drilled into every metallic plate, allowing the passage of the water. The whole sandwich assembly of plates and slabs

is in turn housed inside a metallic casing. Stand-alone containers for PCM are then not needed as it is contained between the plates and the casing walls.

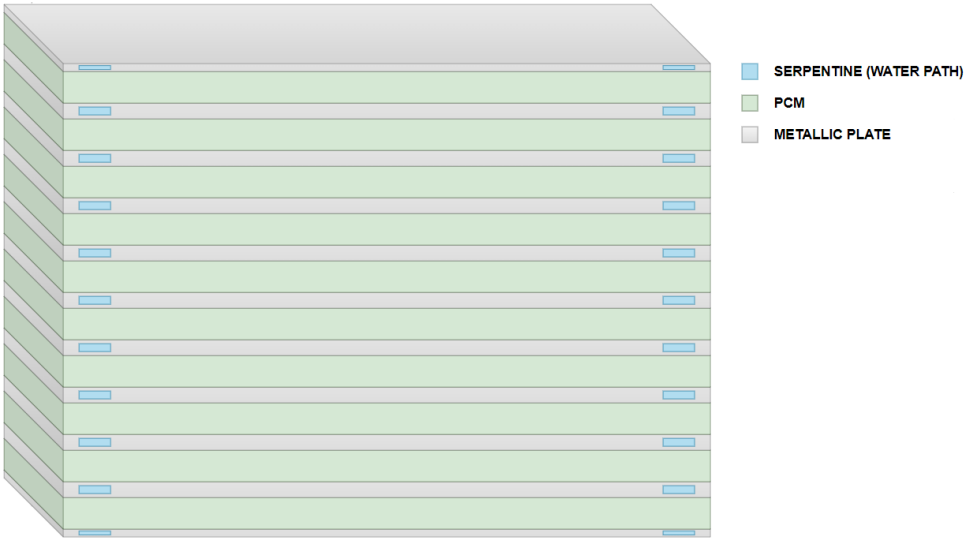

Figure 75 – Simplified drawing of TES module's layered structure (Module 1)

The default designs for TES modules 1 and 2 present a square section, with the depth supposed equal to the width. The dimensions (WxDxH) of the PCM slab are 0.41x0.41x0.02m in module 1 and 0.595x0.595x0.02m in module 2. The metallic plate is instead 0.41 m in width, 0.41 m in depth and 0.01 m in height in module 1, while its sizes are 0.595x0.595x0.1m in module 2. Finally, the rectangular section of the serpentine channel is 0.02x0.006m in module 1 and 0.029x0.006m in module 2. The number of turns, equal to 8, is the same in both the modules. The main dimensions of the two modules are summarised in Table 72. As at the top and bottom of the modules only half of the plate is placed, the number of PCM slabs is equal to that of the plates.

Module	PCM slab dimensions (WxDxH)	Plate dimensions (WxDxH)	Number of PCM slabs	Number of plates	Module dimensions (WxDxH)
1	0.41x0.41x0.02m	0.41x0.41x0.01m	10	10	0.41x0.41x0.3m
2	0.595x0.595x0.02m	0.595x0.595x0.01m	17	17	0.595x0.595x0.53m

Table 72 – Dimensions of TES default designs

During charging, a fraction of the hot water flow rate coming out from PEMFC powertrain is diverted from the cooling circuit before it reaches the radiator and pumped towards the TES system. Here, water flow is equally distributed among the TES modules. Each of them is equipped with an inlet manifold, which splits the flow among all the channels. Once the water is inside the modules, it transfers heat through convection to the boundary layer of PCM slab. Since the average temperature of the water flowing inside TES modules is higher than paraffin melting point, a melting front between HTF and PCM starts forming. Heat is transferred within PCM domain by means of conduction and natural convection, whose relative contributions vary as the melting goes on. In fact, while at the beginning of the melting process heat transfer is dominated by conduction as PCM is mostly in solid state, in the later stages of melting natural convection can play a fundamental role. Finally, the water flows exiting the channels are rejoined at the module's outlet manifold and fed back to the powertrain cooling circuit.

In the discharging phase, cold water from the station is injected within the TES system loop through a hose and then divided equally among all the TES modules. Water absorbs heat from the PCM slabs, increasing its temperature and causing the onset of the paraffin solidification. As opposed to melting, natural convection has a minor effect on discharging. Thus, solidification process is dominated by heat conduction [190].

Given the layered structure of TES modules, not the whole physical geometry has to be simulated but just the smallest unit representing all the phenomena occurring inside the storage. Due to the natural convection effect, the temperature distribution inside the PCM is not symmetrical along the thickness direction and so the entire PCM slab has to be simulated. So, for the analysed case, the computational domain includes one PCM slab and two half metallic plates. One half is positioned above the PCM slab and the other half below, as shown in Figure 76.

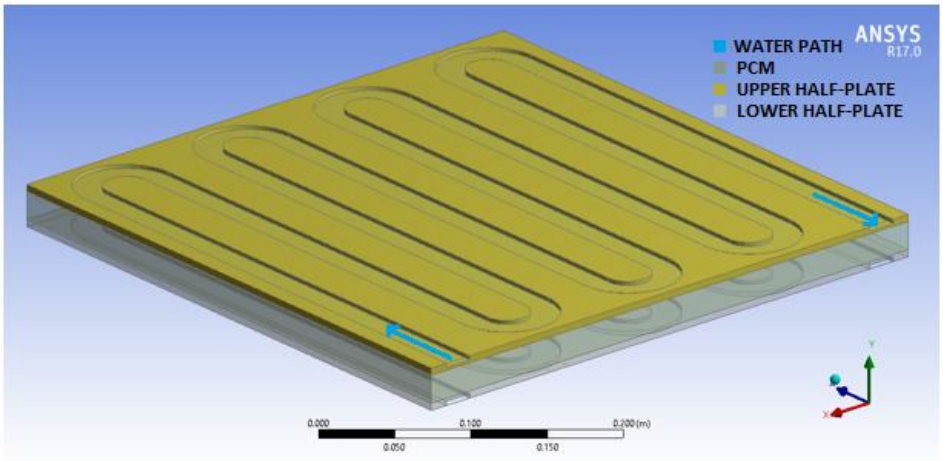

Figure 76 – Computational domain

The PCM material chosen for the TES default design is paraffin RT64HC from Rubitherm Technologies. Its thermo-physical properties are listed in Table 73. Plates and outer casing are made of aluminium and stainless steel, respectively.

Heat conductivity (W/m/K)	Specific heat capacity (kJ/kg/K)	Melting area (°C)	Latent heat (kJ/kg)	Thermal expansion coefficient (1/K)	Density (kg/m^3)	Dynamic viscosity (Pa·s)
0.2 (both phases)	2 (both phases)	60 - 67	220	$8.72 \cdot 10^{-4}$	880 (20°C) 780 (80°C)	0.0198 (20°C) 0.0053 (80°C)

Table 73 – RT64HC thermo-physical properties[68]

[68] https://www.rubitherm.eu/en/productcategory/organische-pcm-rt

4.8 CFD analysis of TES modules: numerical model

ANSYS Fluent solidification and melting model is used to solve the transient heat transfer problem in the PCM. The numerical procedure implemented in Fluent software to model phase change is based on the enthalpy-porosity method by Voller [191]. It associates with each volume of the domain a parameter β_L called liquid fraction, which measures the fraction of the control volume occupied by the liquid phase. The liquid fraction ranges between 0 and 1 and its value can be expressed as:

$$\beta_L = \begin{cases} 0 & if \quad T < T_{sol} \\ \dfrac{T - T_{sol}}{T_{liq} - T_{sol}} & if \quad T_{sol} \leq T \leq T_{liq} \\ 1 & if \quad T > T_{liq} \end{cases} \tag{119}$$

where T_{sol} is the highest temperature at which all the PCM content is still in solid state and T_{liq} is the lowest temperature value at which the whole PCM mass is in liquid form. The quantity β_L is calculated at every time step as a result of enthalpy balance at cell level. In particular, the method developed by Voller makes use of the liquid fraction parameter to evaluate the mass enthalpy of the material according to the equation below:

$$h = h_{ref} + \int_{T_{ref}=25°C}^{T} c_p dT + \beta_L L \tag{120}$$

where the sum of the first two terms is the sensible enthalpy and the product of β_L and the heat of fusion L represents the latent heat content.

For phase change problems, the partial differential equation arising from the energy conservation law can be written in terms of enthalpy H[69] .

[69] https://www.afs.enea.it/project/neptunius/docs/fluent/html/th/node353.htm

$$\frac{\partial}{\partial t}(\rho h) + \nabla \cdot (\rho \vec{u} h) = \nabla \cdot (k \nabla T) + S \quad (121)$$

where h is defined as indicated in Eq. (120), ρ is the density of the PCM, $\vec{u}$ is the velocity vector, k is the PCM thermal conductivity, T is the temperature and S is the source term. Fluent finds the temperature T in each cell of the domain by means of an iterative process involving Eq. (119), Eq. (120) and Eq. (121). The liquid fraction β_L is also introduced in the momentum source term to account for the gradual reduction of velocities in the PCM region during the solidification process. The source term is derived from the Darcy law for flows through porous media and takes the following form:

$$S = \frac{(1-\beta_L)^2}{\left({\beta_L}^3 + \epsilon\right)} A_{mush} \vec{u} \quad (122)$$

where ϵ, equal to 0.001, is included just to avoid division by zero and A_{mush} is an arbitrary model constant. Its value, typically set between 10^4 – 10^7 [192], is a measure of how rapidly the velocity approaches zero when PCM solidifies. A_{mush} is also found to affect melting process: the larger is this model constant, the higher is the melting rate [193].

To simplify calculations, the numerical model for the default case is developed under the following assumptions, valid for both charging and discharging:

- PCM is isotropic and homogeneous
- Except for density and dynamic viscosity, all the other thermo-physical properties of the PCM, both for liquid and solid phase, are constant and do not depend on temperature
- The impact of natural convection flows during phase change process is taken into account through Boussinesq approximation. While in the energy and continuity

equations it assumes constant density, in the momentum equation ρ is instead supposed to vary as:

$$\rho = \rho_{op}\left[1 - \beta\left(T - T_{op}\right)\right] \quad (123)$$

where ρ_{op} is the operating density, β is the thermal expansion coefficient and T_{op} is the operating temperature. As suggested in [193], T_{op} and ρ_{op} are the density of the liquid PCM and the melting temperature $\left(\frac{T_{sol}+T_{liq}}{2}\right)$, respectively.

- The variation with temperature of the PCM dynamic viscosity is retrieved from [194] and depicted in Figure 77

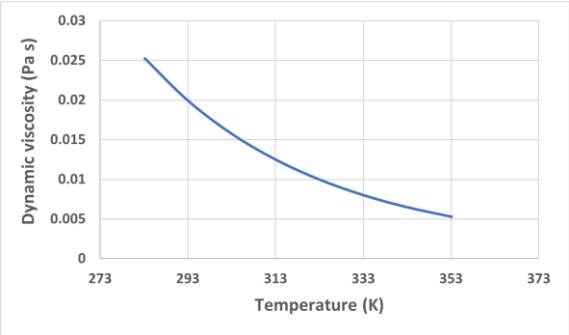

Figure 77 – PCM dynamic viscosity with temperature

- The volume change due to phase transition is neglected
- Liquid PCM flow and water flow are unsteady, laminar and incompressible
- Water properties are temperature independent
- The wall thickness of the metalling casing is not simulated
- As casing walls are well insulated, heat loss to ambient can be ignored

4.9 CFD analysis of TES modules: initial and boundary conditions

The last step before launching the set of simulations that will determine TES performance is the definition of initial and boundary conditions.

To proceed with simulations, Fluent requires in fact that the user assigns, to each cell of the computational domain, an initial guess for the solution variables. As concerns charging, it is necessary to distinguish between the first TES charging of the train's working day and a charging occurring just after a discharging process. For the first charging of the day, the initial temperature is set to 15°C in all the cells of the three subdomains (i.e. PCM, plate and HTF). Additionally, all velocity components are initialised to zero in the whole domain. For the other type of charging considered, the initial temperature and velocity distributions across the domain are set equal to the ones obtained at the end of the discharging stage. The only exception is the velocity in the HTF subdomain, which is changed to zero. On the other hand, at the beginning of every discharging process the domain is initialised with temperature and velocity values from the last time step of charging simulation. A zero value for the three velocity components is patched into the entire water subdomain.

The boundary conditions for the CFD model are defined for all the outer surfaces of the computational domain. So, the two surfaces of the metallic plates parallel to the XZ plane and not in contact with the PCM are of the type '*Symmetry*', while the inlet and outlet regions for water are respectively set as '*Mass flow inlet*' and '*Outflow*'. The '*Wall*' condition with heat flux equal to zero (i.e. adiabatic) is applied to the rest of the outer surfaces. Moreover, if the CAD models of the TES modules are properly drawn, Fluent automatically applies to the surfaces between subdomains a boundary condition such that the continuity of heat flux and temperature is ensured. The boundary conditions are almost the same for charging and discharging. The only difference is that inlet for charging becomes outlet for discharging and vice versa.

The set-up of the '*Mass flow inlet*' boundary condition type requires two inputs from the user: temperature and mass flow rate. During charging, water is supplied to the TES system at

approximately 75°C, which is equal to the PEMFC powertrain working temperature. The inlet temperature of the water used to recover the heat from TES modules is instead supposed to be 25°C. Such a value is not casual. The choice is indeed consistent with the return temperatures of those systems in which the heat stored could be integrated (e.g. low-temperature heating systems, such as radiant floor, to satisfy station heating demand).

The inlet mass flow rate value for the default case is chosen so that the flow pattern inside the TES channels is laminar. Turbulent flow is not advisable as would cause a steep increase of the pressure drops. The increased energy requirements for pumping would result in a decrease of fuel cell powertrain performance. The validity of assuming a laminar flow regime within the channels of the TES depends not so much on the flow pattern in the fuel cell stack's cooling channels, but rather on the Reynolds number characterizing the new branch of the cooling circuit purposely created for transferring heat to the TES modules. The TES system can therefore be designed to operate at lower flow rates than those in the main cooling circuit. The technical feasibility of regulating the flow through the TES system supports the laminar flow assumption, regardless the main cooling circuit's flow regime.

The reference parameter for this calculation is the Reynolds number, whose definition is provided in Eq. (124):

$$Re = \frac{\rho_w \cdot u_w \cdot D_H}{\mu_w} < 2000 \qquad (124)$$

where the subscript w refers to water, ρ_w is the density, u_w is the inlet velocity, μ_w is the dynamic viscosity and D_H is the hydraulic diameter of the rectangular cross-section channel. Rewriting D_H in terms of cross-sectional area A_c and wetted perimeter P_c of the channel, Reynolds number becomes:

$$Re = \frac{\rho_w \cdot u_w \cdot 4 \cdot A_c}{\mu_w \cdot P_c} = \frac{4 \cdot \dot{m}_w}{\mu_w \cdot P_c} < 2000 \quad (125)$$

and then

$$\dot{m}_w < 1000 \cdot \mu_w \cdot (W_c + H_c) \quad (126)$$

with W_c and H_c standing for channel's width and height, respectively. Thus, for the default case, the inlet mass flow rate is held constant at $\dot{m}_w$ throughout the entire duration of both charging and discharging stages. For the sake of clarity, the inlet conditions for modules 1 and 2 are gathered and showed in Table 74. The mass flow rate values are to be intended for the single channel.

Module	$T_{w,in,ch}$ (°C)	μ_w (mPa s)	Reynolds number	$\dot{m}_{w,ch}$ (kg/s)	$T_{w,in,disch}$	μ_w	Reynolds number	$\dot{m}_{w,disch}$
1	75	0.4044	1800	$9.46 \cdot 10^{-3}$	25	0.65	1800	$1.52 \cdot 10^{-2}$
2				$1.274 \cdot 10^{-2}$				$2.05 \cdot 10^{-2}$

Table 74 – Charging and discharging inlet conditions for the single channel (modules 1 and 2)

4.10 CFD analysis of TES modules: definition of TES performance

The maximum time available for the charging process ($t_{ch,max}$) is dictated by the train timetable and route length. In particular, $t_{ch,max}$ corresponds to the return journey time of the route at issue. A TES module takes a time equal to t_{ch} to be fully charged, that is when all the PCM inside is in liquid phase ($\beta_L = 1$). If $t_{ch} \leq t_{ch,max}$, a complete charging process can be achieved.

The total energy stored in a TES module during a complete charging process (i.e. $T_{PCM} \geq T_{liq}$, no solid phase exists in the entire PCM domain) can be specified as:

$$E_{ch} = m_{PCM} \cdot \left[c_{p_s} \cdot (T_{sol} - T_0)_{PCM} + L + c_{p_l} \cdot \left(T_{end} - T_{liq}\right)_{PCM} \right] \quad (127)$$

where m_{PCM} is the total PCM mass inside a TES module (i.e. 28 kg for module 1 and 100 kg for module 2), c_{p_s} and c_{p_l} are the specific heat capacities of solid and liquid phase, T_0 and T_{end} are the average temperatures of the PCM mass at the beginning and at the end of the charging. Conversely, in the event of incomplete charging (i.e. $T_{sol} \leq T_{PCM} \leq T_{liq}$, PCM domain only partially melted), E_{ch} is estimated as:

$$E_{ch} = m_{PCM} \cdot \left[c_{p_s} \cdot (T_{sol} - T_0)_{PCM} + \beta_L \cdot L\right] \quad (128)$$

Once the train arrives at the station, the heat stored in the TES system can be finally discharged. Like charging, the maximum time available for the discharging ($t_{disch,max}$) is route and timetables dependent as it coincides with the timespan the train waits at terminus (i.e. New Street station) before leaving again in the reserve direction. To simplify the analysis of the default case, a $t_{disch,max}$ of 15 minutes is assumed for all the considered routes and for every discharging event of the day. In order to set a lower bound for the quality of the heat retrieved from trains, a discharging cut-off temperature $T_{cut-off}$ of 40°C is selected. If $t_{cut-off}$ is the time after which the water temperature at the exit of TES reaches 40°C, it follows that:

$$E_{disch} = n_{ch} \cdot c_{p_w} \cdot \int_{t_{start}}^{t_{cut-off}} \dot{m}_{w,disch}(t) \cdot \left(T_{w,out}(t) - T_{w,in,disch}\right) \cdot dt \qquad if\ t_{cut-off} \leq t_{disch,max} \quad (129)$$

$$E_{disch} = n_{ch} \cdot c_{p_w} \cdot \int_{t_{start}}^{t_{disch,max}} \dot{m}_{w,disch}(t) \cdot \left(T_{w,out}(t) - T_{w,in,disch}\right) \cdot dt \qquad if\ t_{cut-off} > t_{disch,max} \quad (130)$$

where E_{disch} is the thermal energy discharged at the station by a TES module, n_{ch} is the number of channels (10 for module 1 and 17 for module 2), $\dot{m}_{w,out,disch}$ is the mass flow rate measured at each channel's outlet, t_{start} is the time the water takes to reach the end of the serpentine channel and $T_{w,out}(t)$ describes how water temperature at the channel outlet

varies throughout the discharging time. The trend over time of the outlet mass flow rate $\dot{m}_{w,disch}$ is therefore:

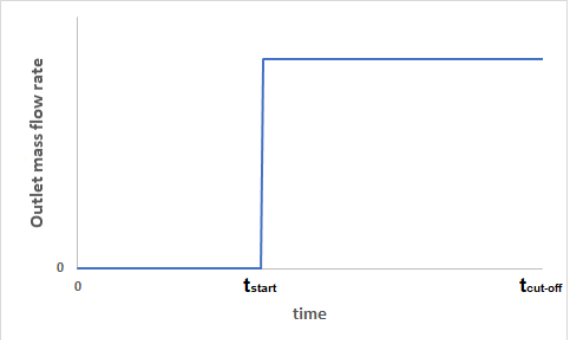

Figure 78 – Outlet mass flow rate trend over time

where t_{start} is in turn calculated as:

$$t_{start} = \frac{l_{channel}}{v_w} = \frac{l_{channel} \cdot W_c \cdot H_c \cdot \rho_w}{\dot{m}_{w,disch}} \tag{131}$$

Having defined both E_{disch} and E_{ch}, it is now possible to evaluate TES round-trip performance as:

$$\eta_{round-trip} = \frac{E_{disch}}{E_{ch}} \tag{132}$$

4.11 CFD analysis of TES modules: grid and time step independence check

The grid for the computational domain discretisation is generated by using the FLUENT meshing package. Polyhedral elements are preferred over the more conventional tetrahedral and hexahedral cells as they can lead to a more accurate solution with a lower cell count [195].

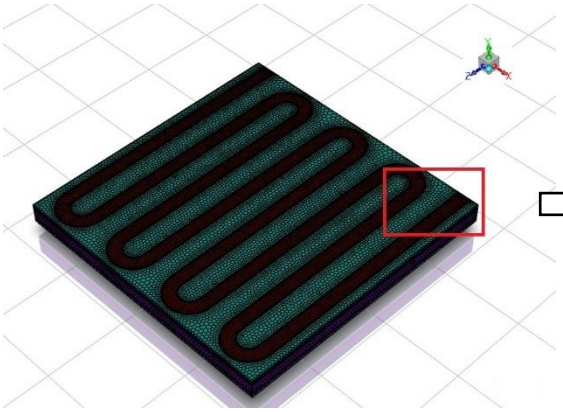

Figure 79 – TES module mesh

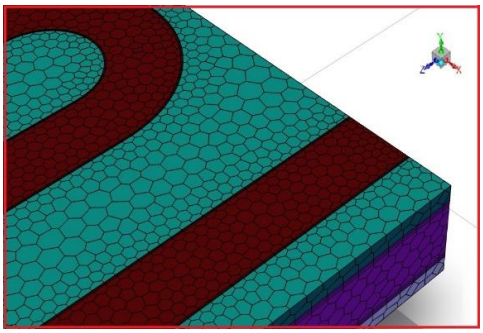

Figure 80 – Detail of polyhedral elements

Furthermore, to improve the accuracy of the solution, two thin boundary layers of prismatic elements are added on channel-plate and plate-PCM interfaces. As suggested in [196], the total thickness of the two prism layers is set to one fourth of that of the channel.

The monitored parameter to check the independence of the model results from grid and timestep size is the water outlet temperature from module 1 during discharging. As Figure 81 proves, the discrepancy between the three curves is minimal and the grid with 297525 cells is then adopted in this study to reduce computational time.

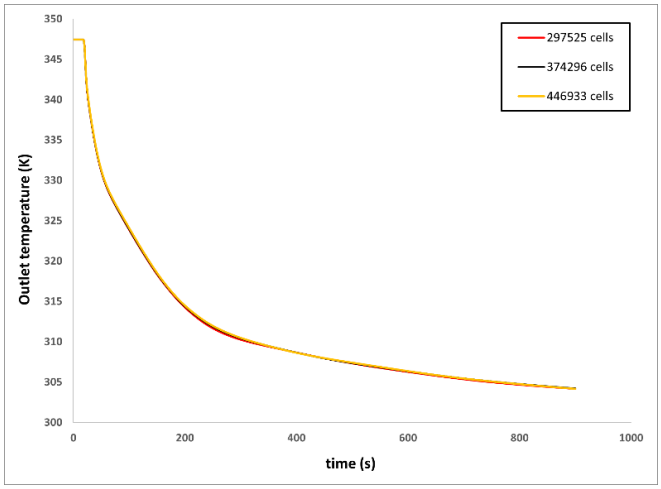

Figure 81 – Mesh size independence test

The generated mesh has a minimum orthogonal quality of 0.3. According to ANSYS mesh quality recommendations, any grid having a minimum orthogonal quality higher than 0.15 is acceptable (see Figure 82).

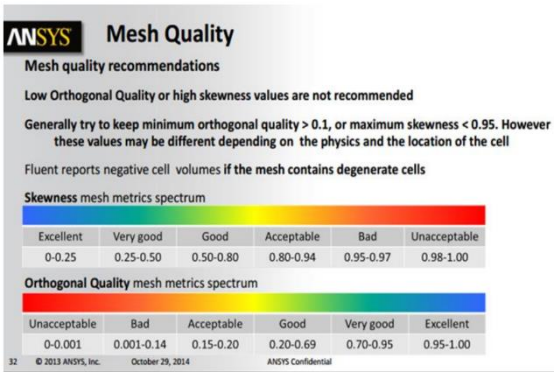

Figure 82 – Mesh quality recommendations [197]

The result of the time step size independence check is shown in Figure 83. The time step equal to 0.25 s is chosen as it minimises the computational burden without significantly affecting the accuracy of the outcome.

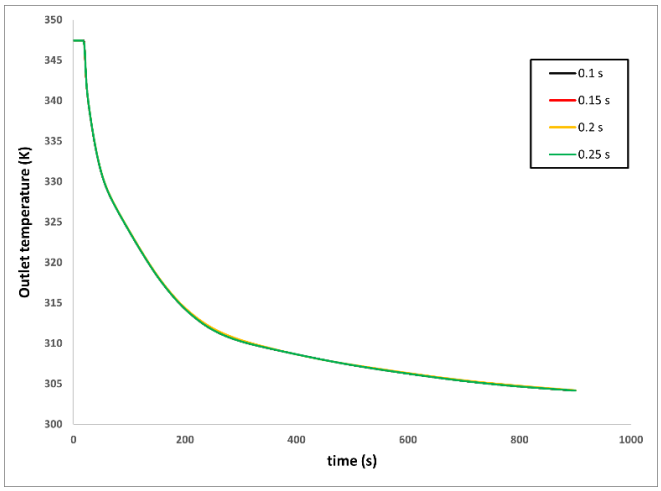

Figure 83 – Time step size independence check

4.12 Model validation

To validate the CFD model, it is used to replicate the results of He et al. work [198]. The design proposed by He et al. is slightly different from the one developed in this thesis: while in the He et al. work water flows inside a metallic serpentine tube wrapped by PCM, in the present thesis water runs inside a serpentine rectangular-section channel drilled into a metallic plate. In order to make a comparison under the same conditions of Reynolds number, the rectangular section of the channel is then modified so that its hydraulic diameter is equal to that of the tube.

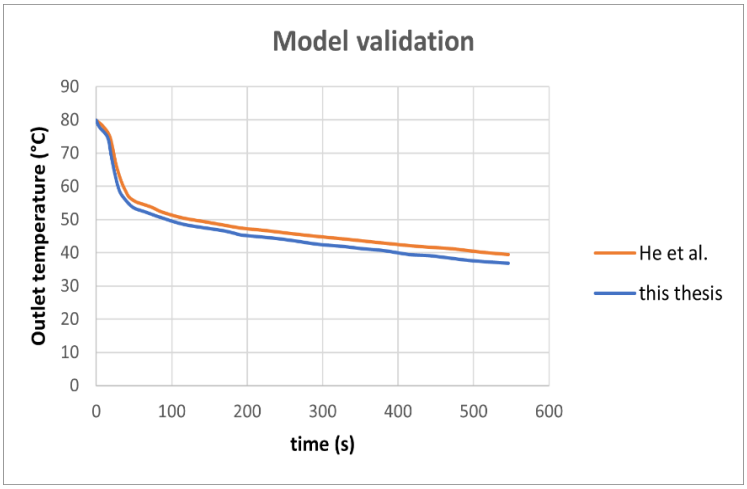

Figure 84 – Model validation

Figure 84 shows a good agreement between the two models, with a maximum temperature difference of 2.54°C. The discrepancy may depend on the different proportion between mass of metal and mass of PCM characterising the two designs. Since the structure of the simulated model in this thesis closely resembles He et al.'s model, it is indirectly proved that the numerical model here developed is sufficiently accurate.

4.13 Default case results: the Derby – BNS route

In this section the results of the CFD analysis for the default case are presented. For each of the studied routes, particular attention is devoted to the estimation of:

- The amount of energy that trains' TES systems can store per day, compared to the heat generated by PEMFC modules in the same time frame
- How much of the energy stored on board of the trains can be actually discharged at the station on a daily basis

For the sake of convenience, the details of calculations are given just for the Derby – BNS route. As regards the other routes, only the main results will be provided.

Based on Eq. (101), it results that approximately 6.81 kg per second of water flow through the cooling circuit, absorbing the waste heat generated by the 150 kW fuel cell module. From Table 74, it is known that $9.46 \cdot 10^{-3}$ kg/s and $1.274 \cdot 10^{-2}$ kg/s are the two mass flow rates per channel chosen for charging process. Since the two default designs include 10 and 17 channels, the total mass flow rates $\dot{m}_{w,ch,TOT}$ entering module 1 and module 2 are respectively $9.46 \cdot 10^{-2}$ kg/s and $2.17 \cdot 10^{-1}$ kg/s.

Module	Number of channels	$\dot{m}_{w,ch,TOT}$ (kg/s)
1	10	$9.46 \cdot 10^{-2}$
2	17	$2.17 \cdot 10^{-1}$

Table 75 – Total charging mass flow rates for module 1 and 2

TES modules are arranged on the carriage roof as Figure 74 describes. Each row of the TES system is formed by two module 1 and two module 2 and therefore requires $6.23 \cdot 10^{-1}$ kg/s of water to be charged. In view of the above, the maximum number of TES rows that can be installed on the roof of each coach is equal to:

$$n_{TES\ max\ rows} = \frac{\dot{m}_{coolant}}{\dot{m}_{w,ch,row}} = \frac{6.81}{6.23 \cdot 10^{-1}} \cong 11 \tag{133}$$

where $\dot{m}_{coolant}$ was calculated in Eq. (101).

Since each row is as long as Module 2 (i.e. 60 cm), the 11 rows can be easily allocated on the 23.5 m-long roof of the coach.

As mentioned in '*CFD analysis of TES modules: initial and boundary conditions*' section, the entire computational domain is initialised with a temperature of 15°C if the first charging of the trains' working day is analysed. Below, the main results of the simulations are introduced. Figure 85 and Figure 86 display the ANSYS Fluent temperature contours for Module 1 and Module 2 at different times. Figure 87 highlights instead how liquid fraction varies throughout the charging process. While a complete charging (i.e. $\beta_L = 1$) of Module 1 is achieved after 3910 s, Module 2 needs 5140 s.

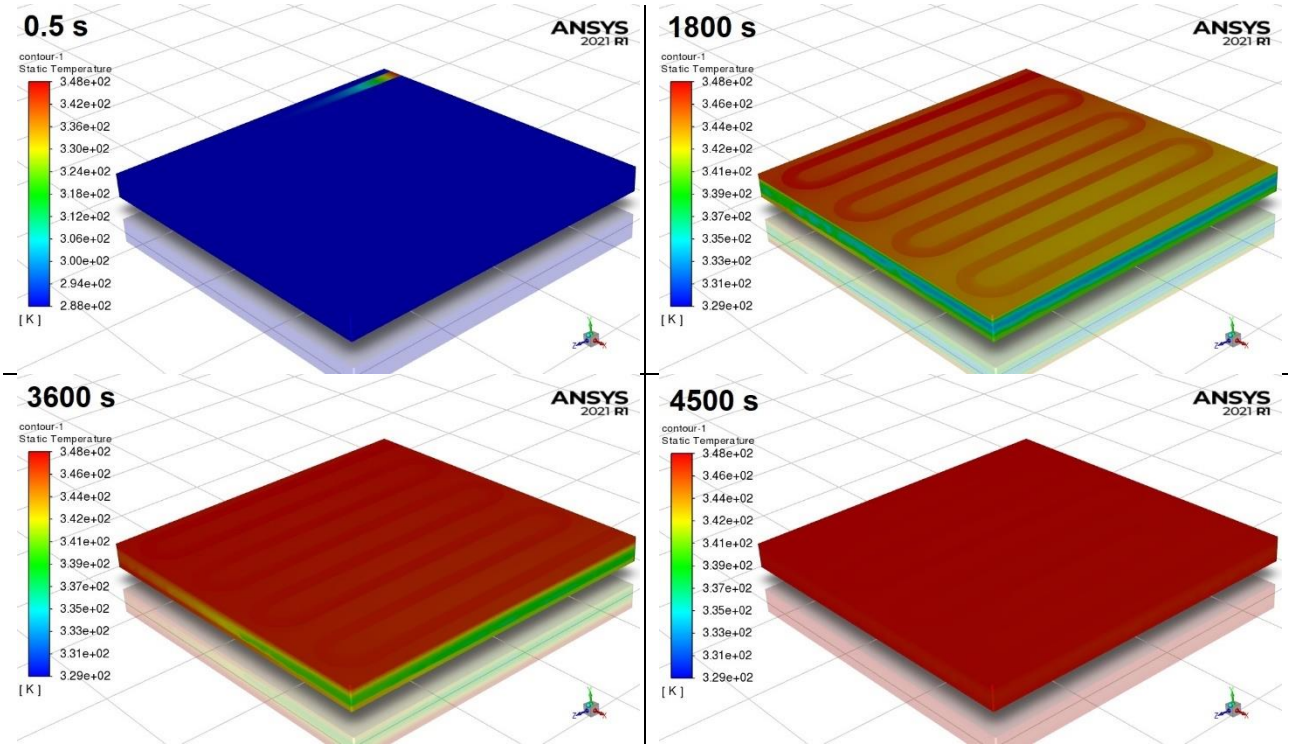

Figure 85 – Temperature contours from t = 0s to t = 4500s (Module 1 charging)

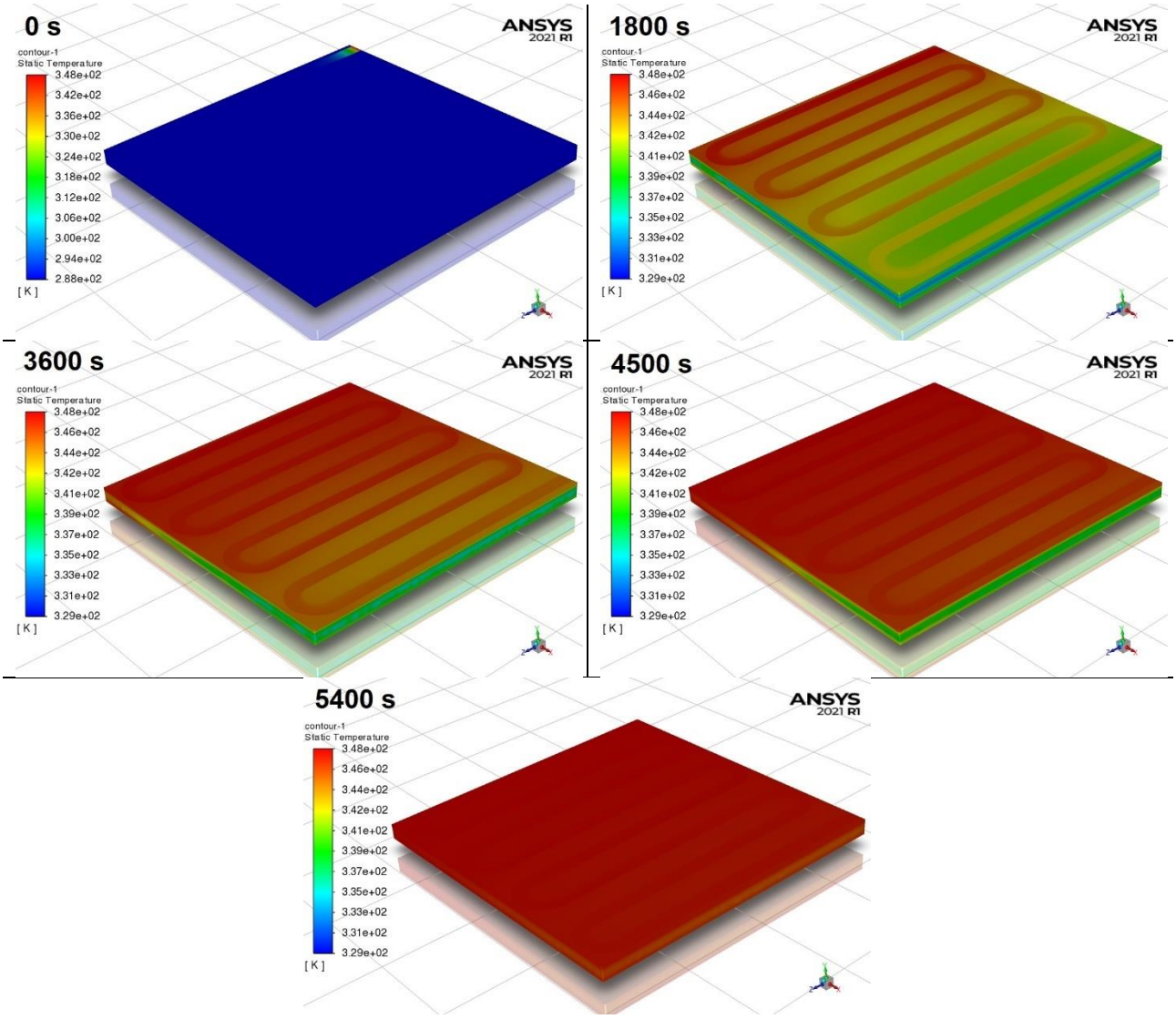

Figure 86 – Temperature contours from t = 0s to t = 5400s (Module 2 charging)

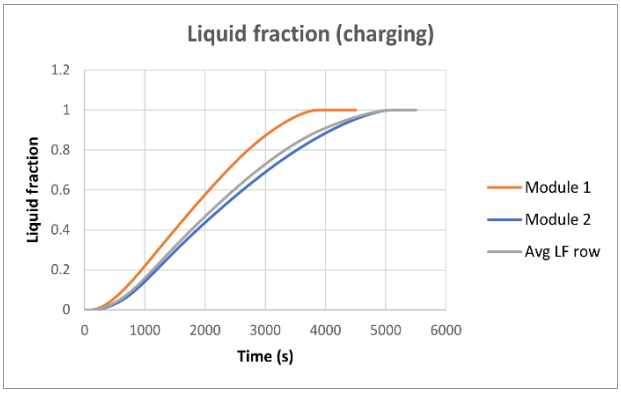

Figure 87 – Liquid fraction variation over time

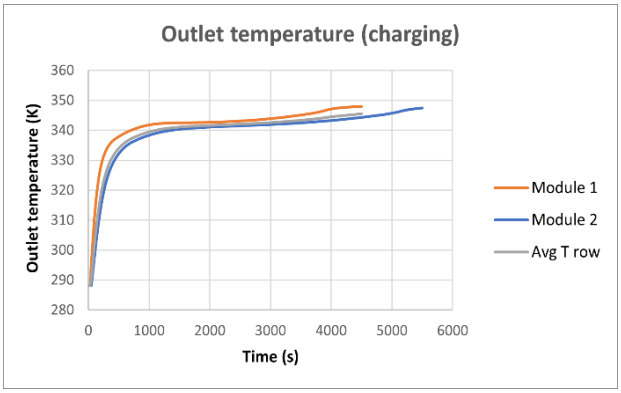

Figure 88 – Outlet temperature trend over time

Finally, Figure 88 shows the trend over time of the water outlet temperature as PCM melts. It is important to note that, during the first 1500 s of charging, the temperature of the water exiting TES modules does not match the operating range of the fuel cell cooling system (i.e. $70 \leq T_{coolant} \leq 75°C$). This issue makes the integration of the TES system into the cooling loop more challenging. A possible solution consists in installing a system of valves to make sure that the water temperature at fuel cell module's inlet is never lower than 70°C. The logic behind how charging progresses is explained with the help of the following simplified PID diagram.

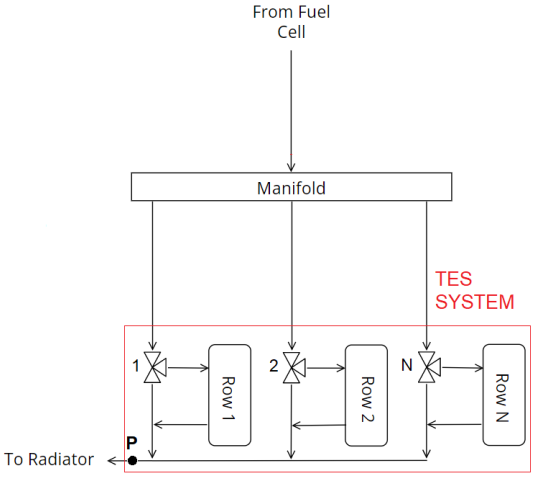

Figure 89 – TES system's PID diagram

At the beginning of charging, while valve 1 lets water enter row 1 and charge TES modules, the remaining N valves are positioned so that the only option for the other N water flows is to continue their paths to radiator. The condition to be met before starting the charging of the first half of row 2 is expressed below:

$$\frac{\dot{m}_{w,ch,ro}\bar{T}_{out,ch,row}(t) + 0.5 \cdot \dot{m}_{w,ch,row}\bar{T}_{out,ch,row}(0s) + \left(\dot{m}_{coolant} - 1.5 \cdot \dot{m}_{w,ch,row}\right) \cdot 348.15}{\dot{m}_{coolant}} = 343.15 \quad (134)$$

where $\bar{T}_{out,ch,row}(t)$ and $\bar{T}_{out,ch,row}(0\ s)$ are the mass weighted average temperatures at time t and t = 0 of the water exiting a TES system row (calculated from Figure 88),

$\left(\dot{m}_{coolant} - 1.5 \cdot \dot{m}_{w,ch,row}\right)$ is the mass flow rate not involved in the charging process and 348.15 K is the temperature of water whenever it bypasses TES modules.

In order to retrieve the time $t_{0.5\,row\,2}$ at which the charging of the first half of row 2 can start, Eq. (134) is implemented in an Excel spreadsheet. The value for $t_{0.5\,row\,2}$ is 240 s, as Figure 90 displays.

	A	B	C	D	E	G
1	$t(s)$	$\bar{T}_{out,ch,row}(t)$	$\bar{T}_{out,ch,row}(0\,s)$	$\dot{m}_{w,ch,row}$	$\dot{m}_{coolant}$	$Eq\ 103$
2	5	288.15	288.15	0.623	6.81	339.91652
3	10	288.15	288.15	0.623	6.81	339.91652
4	15	288.15	288.15	0.623	6.81	339.91652
5	20	288.150001	288.15	0.623	6.81	339.91652
6	25	288.150841	288.15	0.623	6.81	339.916597
7	30	288.231763	288.15	0.623	6.81	339.924
8	35	289.102864	288.15	0.623	6.81	340.003691
9	40	290.157379	288.15	0.623	6.81	340.100161
10	45	290.894227	288.15	0.623	6.81	340.16757
11	50	291.743876	288.15	0.623	6.81	340.245299
12	55	293.067034	288.15	0.623	6.81	340.366345
13	60	294.355631	288.15	0.623	6.81	340.48423
14	65	295.56924	288.15	0.623	6.81	340.595255
15	70	296.752156	288.15	0.623	6.81	340.703472
16	75	297.917358	288.15	0.623	6.81	340.810068
17	80	299.067105	288.15	0.623	6.81	340.915251
18	85	300.200248	288.15	0.623	6.81	341.018914
19	90	301.314837	288.15	0.623	6.81	341.12088
20	95	302.409006	288.15	0.623	6.81	341.220978
21	100	303.481198	288.15	0.623	6.81	341.319066
22	105	304.530054	288.15	0.623	6.81	341.415018
23	110	305.554518	288.15	0.623	6.81	341.508739
24	115	306.553801	288.15	0.623	6.81	341.600157
25	120	307.527334	288.15	0.623	6.81	341.689219

	A	B	C	D	E	G
26	125	308.47472	288.15	0.623	6.81	341.775888
27	130	309.395731	288.15	0.623	6.81	341.860145
28	135	310.290307	288.15	0.623	6.81	341.941984
29	140	311.158513	288.15	0.623	6.81	342.02141
30	145	312.000525	288.15	0.623	6.81	342.09844
31	150	312.816545	288.15	0.623	6.81	342.173092
32	155	313.606848	288.15	0.623	6.81	342.245391
33	160	314.371821	288.15	0.623	6.81	342.315374
34	165	315.111926	288.15	0.623	6.81	342.383081
35	170	315.827661	288.15	0.623	6.81	342.448558
36	175	316.519537	288.15	0.623	6.81	342.511853
37	180	317.188064	288.15	0.623	6.81	342.573012
38	185	317.833791	288.15	0.623	6.81	342.632085
39	190	318.457274	288.15	0.623	6.81	342.689124
40	195	319.059134	288.15	0.623	6.81	342.744184
41	200	319.640004	288.15	0.623	6.81	342.797323
42	205	320.200508	288.15	0.623	6.81	342.8486
43	210	320.741351	288.15	0.623	6.81	342.898078
44	215	321.263247	288.15	0.623	6.81	342.945823
45	220	321.766886	288.15	0.623	6.81	342.991897
46	225	322.252924	288.15	0.623	6.81	343.036361
47	230	322.721956	288.15	0.623	6.81	343.07927
48	235	323.174609	288.15	0.623	6.81	343.12068
49	240	323.611536	288.15	0.623	6.81	343.160651

Figure 90 – Portion of Excel spreadsheet to find $t_{0.5\,row\,2}$

By extending the calculation to more and more TES rows, Figure 91 is obtained for the particular case of the Derby – BNS route.

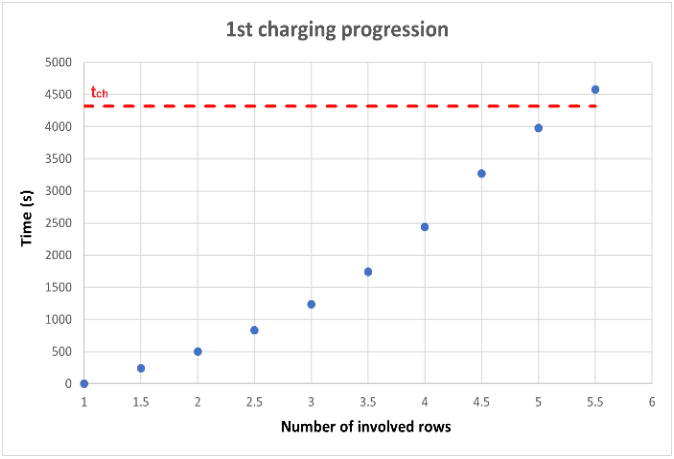

Figure 91 – First charging progression

As Table 76 proves, the Derby – BNS route has to be served by three trains to meet the timetable. This implies that three first charging processes have to be simulated, one for each train. Table 77 provides the liquid fraction's values achieved at the end of the first charging for all the involved modules. The energy E_{ch} accumulated in each train at the end of the first charging is calculated by applying Eq. (128) to the 18 TES modules experiencing melting.

train 1	train 2	train 3							
Der - Birm				10.53 - 11.27	12.53 - 13.27			20.53 - 21.30	22.50 - 23.27
Birm - Der	6.03 - 6.35	6.30 - 7.06	7.03 - 7.40			13.30 - 14.05	14.28 - 14.58		

Table 76 – Derby-BNS timetable

$Train$	$t_{ch}(hr)$	$n_{inv\ rows}$	$\beta_{L_{row\ 1}}$		$\beta_{L_{0.5\ row\ 2}}$		$\beta_{L_{row\ 2}}$		$\beta_{L_{0.5\ row\ 3}}$		$\beta_{L_{row\ 3}}$		$\beta_{L_{0.5\ row\ 4}}$		$\beta_{L_{row\ 4}}$		$\beta_{L_{0.5\ row\ 5}}$		$\beta_{L_{row\ 5}}$		$E_{ch}(MWh)$
			Mod 1	Mod 2	Mod 1	Mod 2	Mod 1	Mod 2	Mod 1	Mod 2	Mod 1	Mod 2	Mod 1	Mod 2	Mod 1	Mod 2	Mod 1	Mod 2	Mod 1	Mod 2	Mod 1	Mod 2	
train 1	1.2	4.5	1	0.93	1	0.93	1	0.9	0.99	0.85	0.96	0.79	0.89	0.71	0.76	0.59	0.54	0.40	0.24	0.16	0.02	0.01	0.0830
train 2	1.2	4.5	1	0.93	1	0.93	1	0.9	0.99	0.85	0.96	0.79	0.89	0.71	0.76	0.59	0.54	0.40	0.24	0.16	0.02	0.01	0.0830
train 3	1.2	4.5	1	0.93	1	0.93	1	0.9	0.99	0.85	0.96	0.79	0.89	0.71	0.76	0.59	0.54	0.40	0.24	0.16	0.02	0.01	0.0830

Table 77 – First charging results for a single coach

Starting from the β_L values in Table 77, the CFD analysis of the first discharging process for the three trains can now be performed. Temperature contours and how liquid fraction and outlet temperature vary over time for a discharging starting from β_L = 1 are shown below.

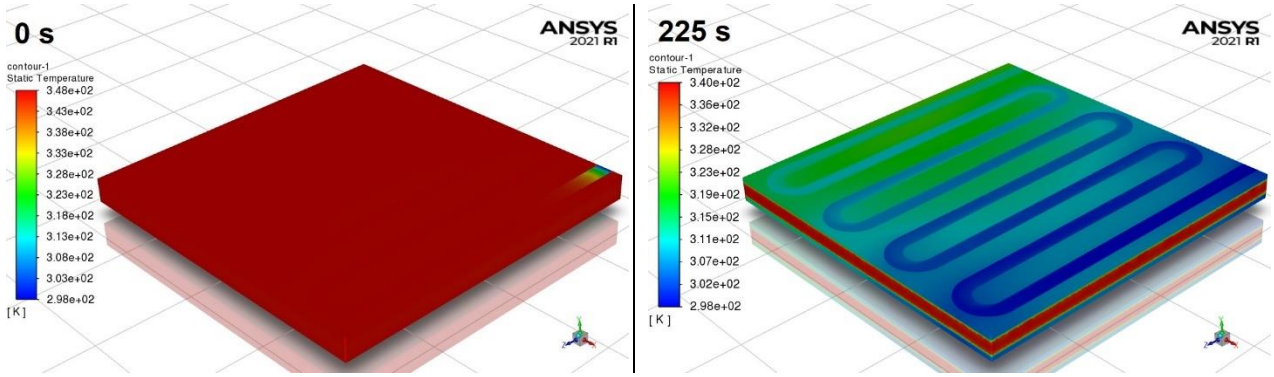

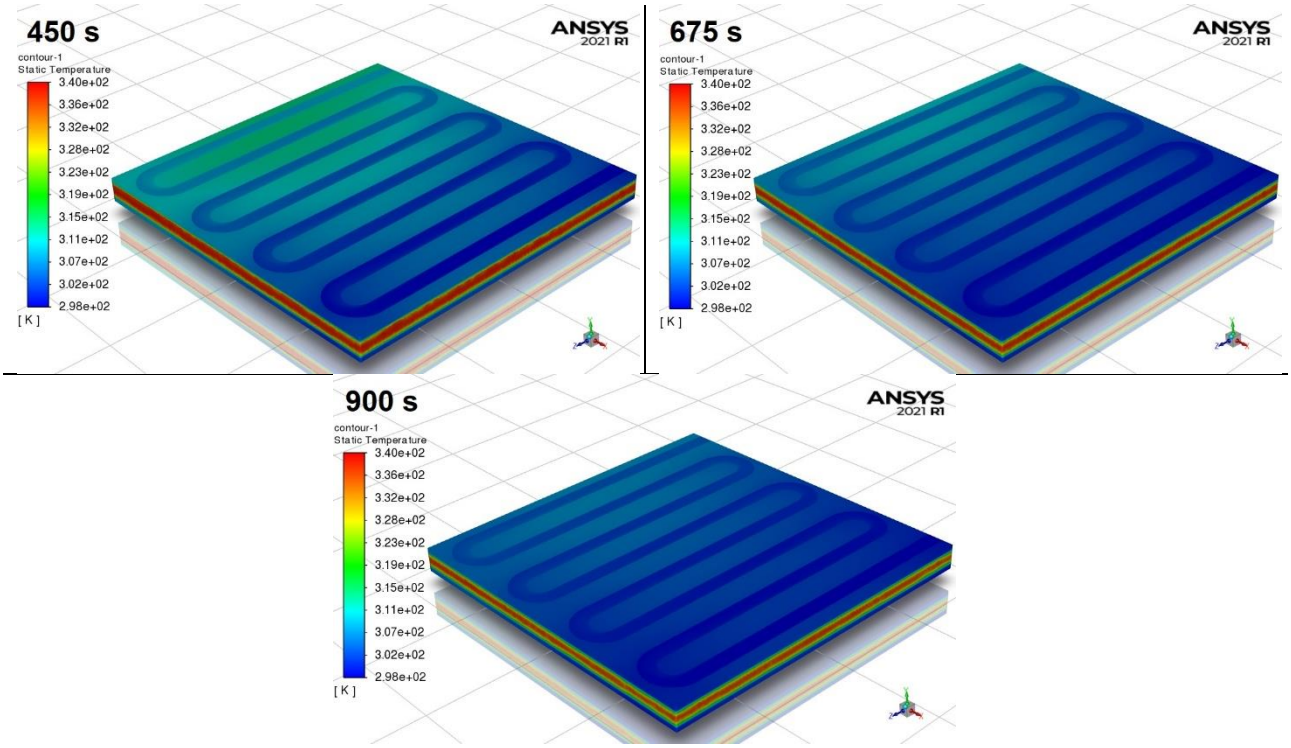

Figure 92 – Temperature contours from t = 0s to t = 900s (Module 1 discharging)

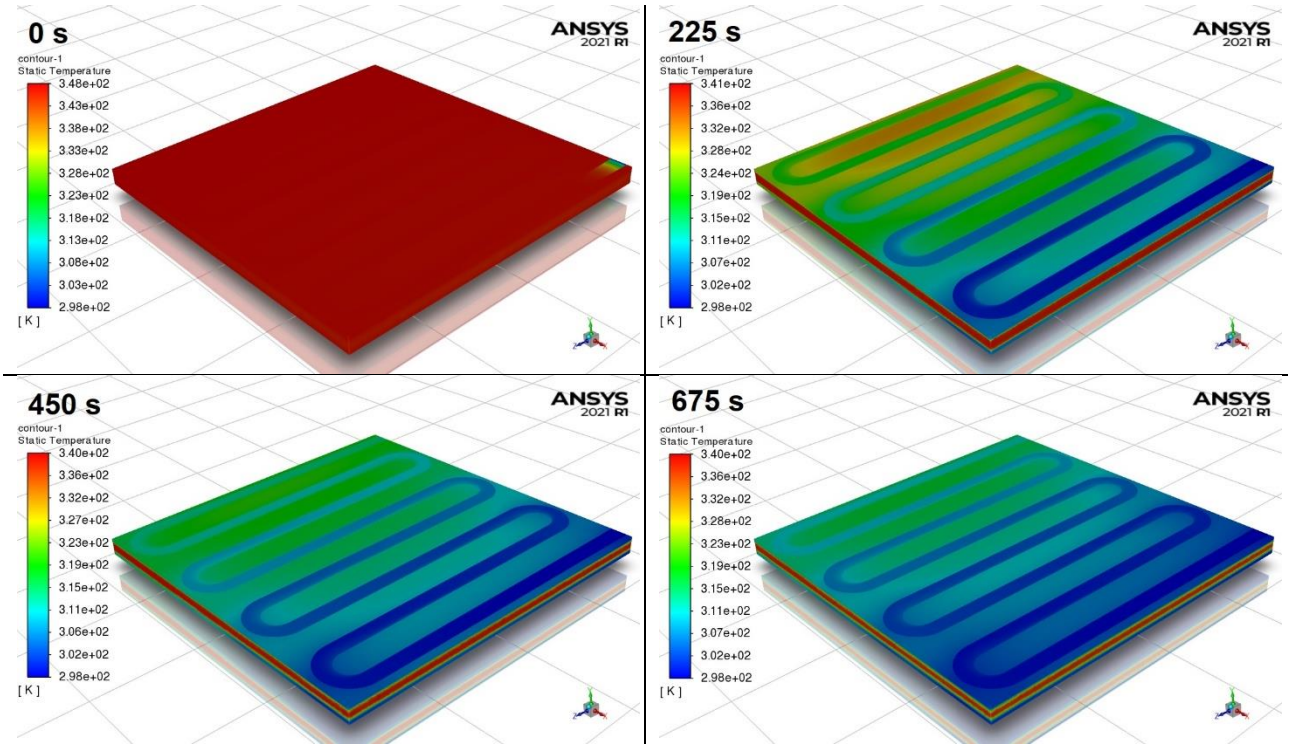

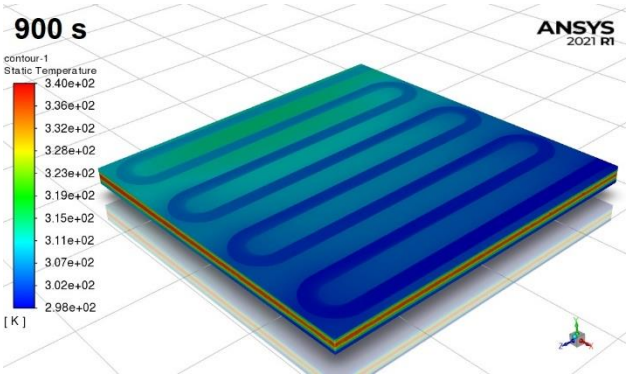

Figure 93 - Temperature contours from t = 0s to t = 900s (Module 2 discharging)

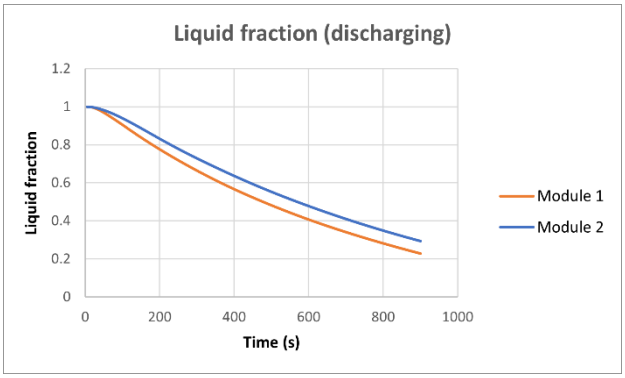

Figure 94 – Liquid fraction variation over time

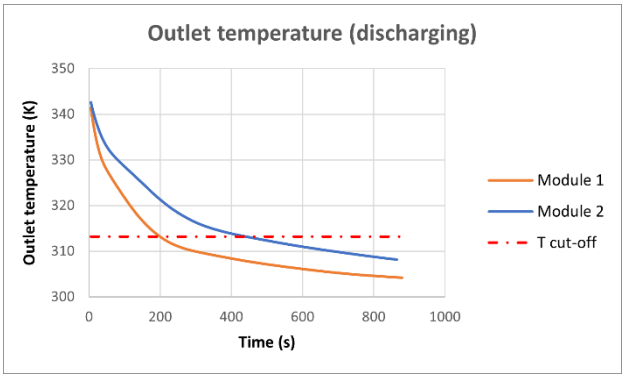

Figure 95 – Outlet temperature trend over time

A table similar to Table 77 but gathering the CFD simulations' outcomes for the first discharging is now presented.

Train	$t_{disch}(hr)$	$\beta_{L_{row\ 1}}$				$\beta_{L_{0.5\ row\ 2}}$		$\beta_{L_{row\ 2}}$		$\beta_{L_{0.5\ row\ 3}}$		$\beta_{L_{row\ 3}}$		$\beta_{L_{0.5\ row\ 4}}$		$\beta_{L_{row\ 4}}$		$\beta_{L_{0.5\ row\ 5}}$		$\beta_{L_{row\ 5}}$		$E_{disch}(MWh)$
		Mod 1	Mod 2	Mod 1	Mod 2	Mod 1	Mod 2	Mod 1	Mod 2	Mod 1	Mod 2	Mod 1	Mod 2	Mod 1	Mod 2	Mod 1	Mod 2	Mod 1	Mod 2	Mod 1	Mod 2	
train 1	0.25	0.75	0.57	0.75	0.57	0.75	0.55	0.75	0.52	0.75	0.5	0.68	0.41	0.59	0.35	0.35	0.16	0.08	0.03	0.00	0.00	0.0352
train 2	0.25	0.75	0.57	0.75	0.57	0.75	0.55	0.75	0.52	0.75	0.5	0.68	0.41	0.59	0.35	0.35	0.16	0.08	0.03	0.00	0.00	0.0352
train 3	0.25	0.75	0.57	0.75	0.57	0.75	0.55	0.75	0.52	0.75	0.5	0.68	0.41	0.59	0.35	0.35	0.16	0.08	0.03	0.00	0.00	0.0352

Table 78 – First discharging results for one coach

As evident from Figure 95, $t_{cut-off}$ is significantly lower than $t_{disch,max}$ for both the module types. Thus, the liquid fraction's values in Table 78 are those obtained at the end of $t_{cut-off}$. The energy $E_{disch,train}$ discharged at the station throughout t_{disch} by each of the three trains is assessed by using Eq. (129), where the parameter $T_{w,out}(t)$ in the formula is one of the main output of CFD investigation.

Once the time profiles $T_{w,out}(t)$ of all the involved TES modules are known, they are averaged to obtain a single temperature trend $\bar{T}_{w,out,train}(t)$ for the whole train's TES system.

According to the Derby – BNS timetable (Table 76), train 1 and train 2's TES systems undergo a second charging process. However, as train 2 does not have the chance to discharge the stored heat at BNS, only train 1's second charging will be included in the calculation. The outcomes of the second charging are given in Table 79. It is worth noting that the number of involved rows has changed. In fact, TES modules are already partially melted when the second charging begins, affecting the trend over time of $\bar{T}_{out,ch,row}$. The number of rows involved as the second charging progresses is shown in Figure 96. The change of the curve's slope after approximately 1000 s is because row 6 and 7 experience melting for the first time and then their β_L starts from zero.

$Train$	$t_{ch}(hr)$	$n_{inv\ rows}$	$\beta_{L_{row\ 1}}$				$\beta_{L_{0.5\ row\ 2}}$		$\beta_{L_{row\ 2}}$		$\beta_{L_{0.5\ row\ 3}}$		$\beta_{L_{row\ 3}}$		$\beta_{L_{0.5\ row\ 4}}$		$\beta_{L_{row\ 4}}$		$\beta_{L_{0.5\ row\ 5}}$		$\beta_{L_{row\ 5}}$	
			Mod 1	Mod 2	Mod 1	Mod 2	Mod 1	Mod 2	Mod 1	Mod 2	Mod 1	Mod 2	Mod 1	Mod 2	Mod 1	Mod 2	Mod 1	Mod 2	Mod 1	Mod 2	Mod 1	Mod 2
train 1	1.2	7.5	1	1	1	1	1	1	1	1	1	1	1	1	1	1	1.00	0.95	1	0.87	0.95	0.78

$\beta_{L_{0.5\ row\ 6}}$		$\beta_{L_{row\ 6}}$		$\beta_{L_{0.5\ row\ 7}}$		$\beta_{L_{row\ 7}}$		$\beta_{L_{0.5\ row\ 8}}$		$E_{ch}(MWh)$
Mod 1	Mod 2	Mod 1	Mod 2	Mod 1	Mod 2	Mod 1	Mod 2	Mod 1	Mod 2	
0.72	0.56	0.52	0.39	0.33	0.23	0.13	0.07	7E-05	6.E-05	0.1342

Table 79 – Second charging outcomes for single carriage

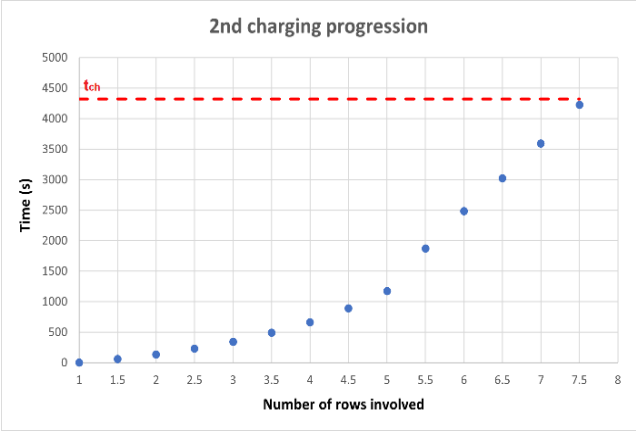

Figure 96 – Second charging progression

Finally, liquid fractions and E_{disch} for the second discharging process are evaluated and collected in Table 80.

Train	$t_{disch}(hr)$	$\beta_{L_{row\ 1}}$		$\beta_{L_{0.5\ row\ 2}}$		$\beta_{L_{row\ 2}}$		$\beta_{L_{0.5\ row\ 3}}$		$\beta_{L_{row\ 3}}$		$\beta_{L_{0.5\ row\ 4}}$		$\beta_{L_{row\ 4}}$		$\beta_{L_{0.5\ row\ 5}}$		$\beta_{L_{row\ 5}}$	
		Mod 1	Mod 2	Mod 1	Mod 2	Mod 1	Mod 2	Mod 1	Mod 2	Mod 1	Mod 2	Mod 1	Mod 2	Mod 1	Mod 2	Mod 1	Mod 2	Mod 1	Mod 2	Mod 1	Mod 2
train 1	0.25	0.75	0.57	0.75	0.57	0.75	0.57	0.75	0.57	0.75	0.57	0.75	0.57	0.75	0.57	0.75	0.56	0.75	0.54	0.72	0.48

$\beta_{L_{0.5\ row\ 6}}$		$\beta_{L_{row\ 6}}$		$\beta_{L_{0.5\ row\ 7}}$		$\beta_{L_{row\ 7}}$		$\beta_{L_{0.5\ row\ 8}}$		$E_{disch}(MWh)$
Mod 1	Mod 2	Mod 1	Mod 2	Mod 1	Mod 2	Mod 1	Mod 2	Mod 1	Mod 2	
0.72	0.3	0.33	0.17	0.15	0.07	0.02	0.004	0.01	0	0.0609

Table 80 – Second discharging results for one carriage

The overall energy discharged daily at the station by the three trains running on the Derby – BNS line is then equal to:

$$E_{disch\ Derby-BNS} = (0.0352 \cdot 3 + 0.0609) \cdot 3.8 = 0.63\ MWh \tag{135}$$

where 3.8 is the average number of carriages forming Derby – BNS trains from Table 63.

Besides, by means of Eq. (132), the round-trip efficiencies of the trains' TES systems can be now estimated:

$$\eta_{round-trip\ train\ 1} = \frac{E_{disch,train}}{E_{ch,train}} = \frac{0.0352 + 0.0609}{0.0830 + 0.1342} = 0.44 \tag{136}$$

$$\eta_{round-trip\ train\ 2,train\ 3} = \frac{E_{disch,train}}{E_{ch,train}} = \frac{0.0352}{0.0830} = 0.42 \tag{137}$$

4.14 Default case results: all routes

	2030			2040		
Route	E_{ch} **(MWh)**	E_{disch} **(MWh)**	$\eta_{round-trip}$	E_{ch} **(MWh)**	E_{disch} **(MWh)**	$\eta_{round-trip}$
Leicester - BNS	0.71	0.33	46.7%	9.63	4.50	46.8%
Nottingham - BNS	0.88	0.40	45.2%	12.03	5.44	45.3%
Stansted - BNS	0.68	0.32	47.3%	9.33	4.41	47.2%
Cambridge - BNS	0.29	0.13	46.1%	3.95	1.82	46.1%
Derby - BNS	0.06	0.03	45.8%	0.83	0.38	46%

Shrewsbury - BNS	0.81	0.37	45.4%	11.06	5.02	45.4%
Worcester - BNS	0.04	0.02	47.5%	0.61	0.29	46.5%
Hereford - BNS	0.63	0.27	42.5%	8.54	3.63	46.2%
G. Malvern - BNS	0.07	0.03	45.8%	0.96	0.44	46.3%
TOT	**4.18**	**1.9**	**45.5%**	**56.25**	**25.94**	**46.2%**

Table 81 – E_{ch} and E_{disch} for all the studied routes

Table 81 collects the values of E_{ch} and E_{disch} for all the examined routes. The table also highlights how the heat stored and then discharged at the station is going to increase over the years due to the growth of the fuel cell train fleet (see Table 10). Every day, the trains running on the selected lines can store 4.18 MWh of heat in 2030, which becomes 56.25 MWh in 2040. Approximately 1.9 MWh and 26 MWh of the stored heat is then discharged daily at the station in 2030 and 2040, with an average round-trip efficiency of 46%. By comparing these results with those provided in Table 65, it follows that around half of the waste heat generated per day by all the fuel cell powertrains can be stored in on-board TES systems. Therefore, the heat discharged at the station is about 1.7% of the overall BNS waste heat potential in 2030, reaching 23% in 2040.

The average temperature of waste heat is approximately 51.3 °C.

4.15 Parametric study: optimisation

The results obtained so far are exclusively valid for the default design, whose main dimensions and features have been summarised in Table 72 and Table 74.

In the present section, the effect of PCM and plate thickness and number of serpentine's turns on the magnitude of energy that can be discharged at the station is investigated. The

goal of this parametric analysis is to determine which configuration allows to achieve the better performance in terms of E_{disch} (Eq. (129)).

4.15.1 PCM thickness effect

Among the selected parameters, the influence of PCM thickness is the first to be studied. Through repeated Fluent simulations of discharging process, PCM slab thickness is increased from 0.01 m to 0.05 m. All the other parameters remain instead constant and equal to the default values, which are listed below.

Module	PCM thickness	Plate thickness	Channel cross-section	Reynolds number	Number of turns
1	0.02 m	0.01 m	0.02x0.006 m	1800	8
2			0.029x0.006 m		

Table 82 – Default values

The default designs of Module 1 and Module 2 are made of 10 and 17 PCM slabs, respectively, and as many metallic plates. The upper and the lower bounds for PCM thickness variation are such that the number of PCM slabs ranges between -50% and +50% of the default value.

Figure 97 highlights how the PCM thickness affects the amount of energy that a single module can discharge throughout every discharging process (i.e. E_{disch}). All the simulations start with the PCM domain completely melted ($\beta_L = 1$).

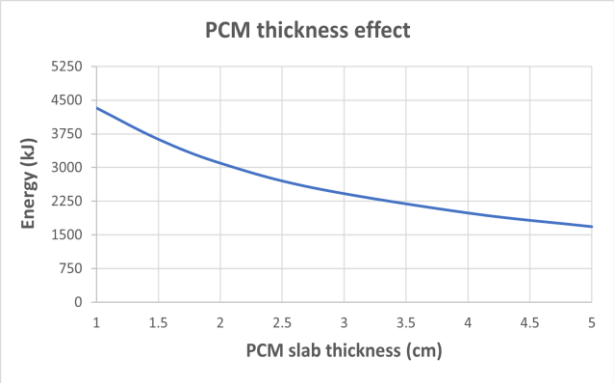

Figure 97 – PCM thickness effect (Module 1)

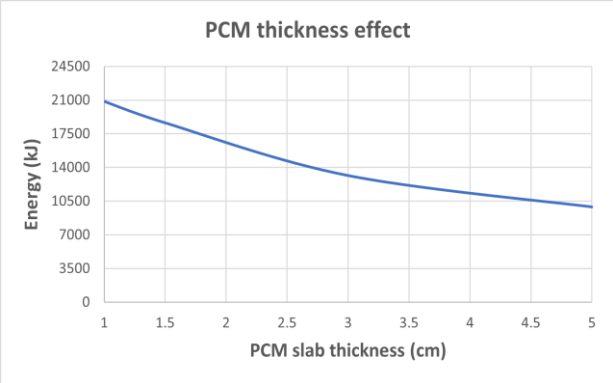

Figure 98 – PCM thickness effect (Module 2)

As the PCM thickness decreases and the number of PCM slabs increases, the E_{disch} becomes higher and higher. A further reduction (below 0.01 m) of PCM thickness is not considered to avoid an excessive reduction of TES module's energy capacity. The PCM with a thickness of 0.01 m represents then the optimal choice, allowing to discharge 40% (Module 1) and 32% (Module 2) more energy than the default cases.

4.15.2 Impact of metallic plate thickness

The impact of the metallic plate thickness is now studied. It is varied between 0.01 m and 0.05 m. Changing the plate thickness has also an effect on the height of the channel, while width is kept constant. The relationship between plate thickness and height of the channel is expressed by the following formula:

$$H_c = H_{plate} - 0.04 \tag{138}$$

where H_c and H_{plate} are measured in meters. Besides, in order to maintain constant the Reynolds number at 1800, the water mass flow rate entering the channel has to be adjusted according to Eq. (126). Two sets of Fluent simulations, one for each module type, is run to assess the effect of plate thickness. The values adopted for the main parameters are summarised in

Table **83** and Table 84.

Plate thickness	PCM thickness	Channel cross section	$\dot{m}_{w,disch}$	Number of turns
0.01 m	0.01 m	0.02x0.006 m	0.0152 kg/s	8
0.02 m		0.02x0.016 m	0.0211 kg/s	
0.03 m		0.02x0.026 m	0.0269 kg/s	
0.04 m		0.02x0.036 m	0.0328 kg/s	
0.05 m		0.02x0.046 m	0.0386 kg/s	

Table 83 – Setting for the 'plate thickness effect' simulations (Module 1)

Plate thickness	PCM thickness	Channel cross section	$\dot{m}_{w,disch}$	Number of turns
0.01 m	0.01 m	0.029x0.006 m	0.0205 kg/s	8
0.02 m		0.029x0.016 m	0.0263 kg/s	
0.03 m		0.029x0.026 m	0.0322 kg/s	
0.04 m		0.029x0.036 m	0.0380 kg/s	
0.05 m		0.029x0.046 m	0.0439 kg/s	

Table 84 – Setting for the 'plate thickness effect' simulations (Module 2)

Figure show the profile of E_{disch} under different plate thicknesses for Module 1 and 2. It is evident that the thinnest plate considered (i.e. 0.01 m) is the best option for both the module types. Therefore, the optimal plate thickness corresponds to the default one.

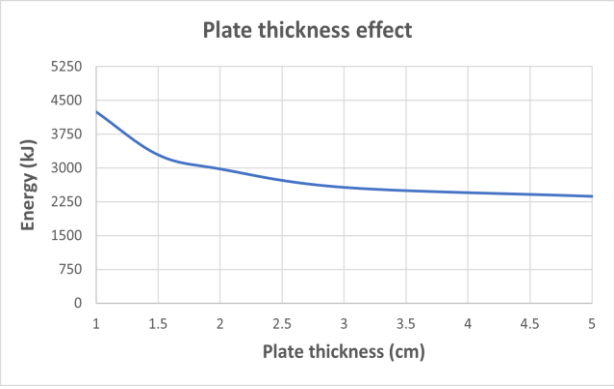

Figure 99 – Plate thickness effect (Module 1)

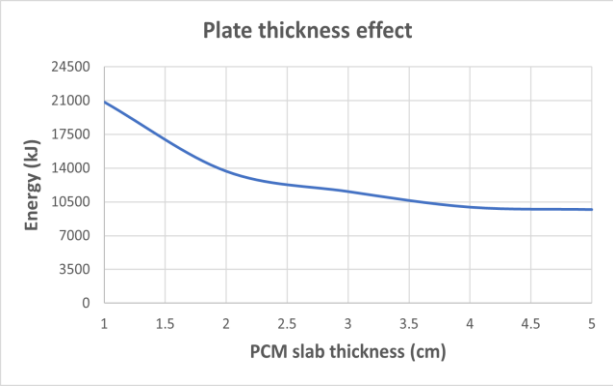

Figure 100 – Plate thickness effect (Module 2)

Based on the outcomes displayed in Figure 97 – Figure 100, it results that the optimised designs of TES modules must have the following dimensions (in bold text the changes compared to the default design):

Module	PCM slab dimensions (WxDxH)	Plate dimensions (WxDxH)	Number of PCM slabs	Number of plates	Module dimensions (WxDxH)
1	0.41x0.41x**0.01**m	0.41x0.41x0.01m	**15**	**15**	0.41x0.41x0.3m
2	0.595x0.595x**0.01**m	0.595x0.595x0.01m	**26**	**26**	0.595x0.595x0.52m

Table 85 – Optimised designs dimensions

4.15.3 Influence of number of serpentine turns

Once the plate and PCM slab thicknesses are fixed, the impact of the number of serpentine turns on discharging performance can be analysed. To accommodate a different number of turns than 8 (i.e. default value), the channel width needs to be varied as specified in Table 86 and Table 87. Moreover, the same tables clarify how $\dot{m}_{w,disch}$ has to be modified to study the heat transfer problem under the same Reynolds number.

Number of turns	Plate thickness	PCM thickness	Channel width	Channel height	$\dot{m}_{w,disch}$
6	0.01 m	0.01 m	0.0275 m	0.006 m	0.0196 kg/s
8			0.02 m		0.0152 kg/s
10			0.016 m		0.0129 kg/s
12			0.013 m		0.0112 kg/s
14			0.011 m		0.00995 kg/s

Table 86 – Setting for the 'number of serpentine turns effect' simulations (Module 1)

Number of turns	Plate thickness	PCM thickness	Channel width	Channel height	$\dot{m}_{w,disch}$
6	0.01 m	0.01 m	0.04 m	0.006 m	0.0269 kg/s
8			0.029 m		0.0205 kg/s
10			0.023 m		0.017 kg/s

12			0.0188 m		0.0145 kg/s
14			0.016 m		0.0129 kg/s

Table 87 – Setting for the 'number of serpentine turns effect' simulations (Module 2)

The trend of E_{disch} at different number of turns can be seen in Figure 101 and Figure 102

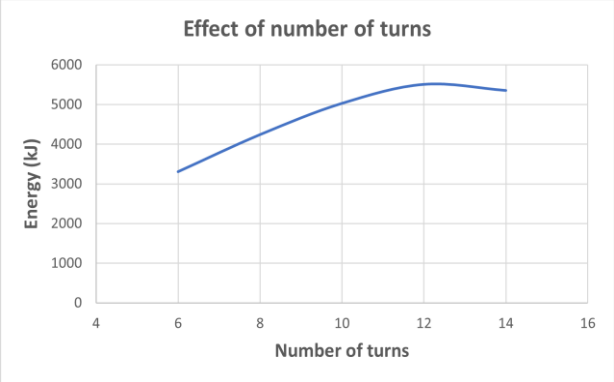

Figure 101 – Effect of number of turns (Module 1)

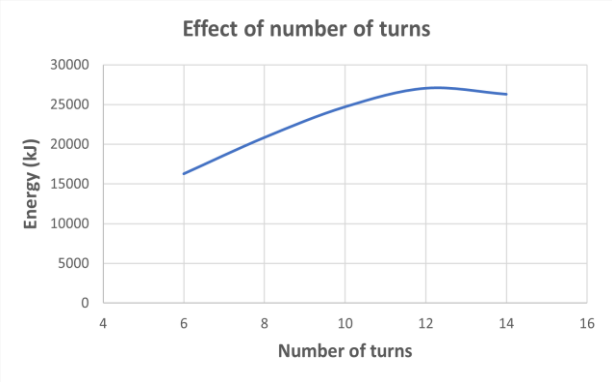

Figure 102 – Effect of number of turns (Module 2)

Plate design with 12 serpentine turns allows to maximise the value of E_{disch} in both the module types.

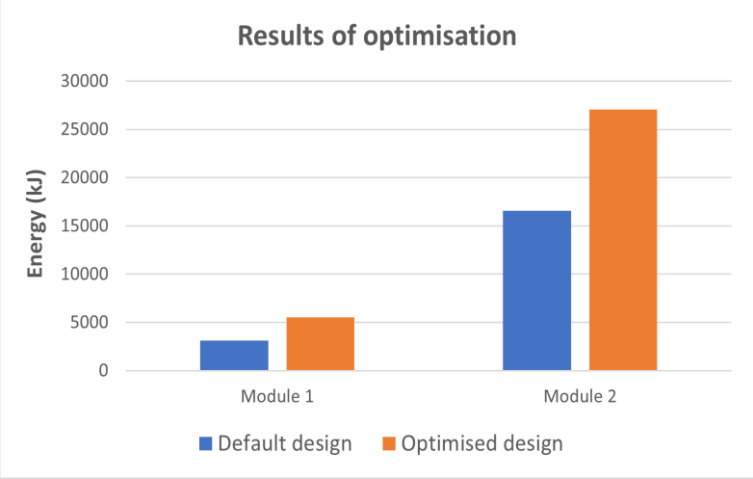

Figure 103 – Effect of optimisation on energy discharged

Figure 103 shows how optimisation affects the E_{disch} parameter. The optimised designs of Module 1 and 2 can discharge 77% and 63% more energy than the default ones, respectively.

4.15.4 Optimised case results: all routes

In view of the above, the amount of heat that can be discharged daily at the station is expected to increase. The new values of E_{ch} and E_{disch} for all the analysed routes are:

	2030		2040		
Route	E_{ch} (MWh)	E_{disch} (MWh)	E_{ch} (MWh)	E_{disch} (MWh)	$\eta_{round-trip}$
Leicester - BNS	0.65	0.43	8.86	5.85	66.1%
Nottingham - BNS	0.81	0.52	11.07	7.08	63.9%
Stansted - BNS	0.63	0.42	8.58	5.73	66.7%
Cambridge - BNS	0.27	0.17	3.63	2.37	65.1%
Derby - BNS	0.06	0.04	0.76	0.49	65%
Shrewsbury - BNS	0.75	0.48	10.17	6.53	64.2%
Worcester - BNS	0.04	0.03	0.56	0.37	65.7%
Hereford - BNS	0.53	0.35	7.24	4.72	65.3%
G. Malvern - BNS	0.07	0.04	0.88	0.57	65.4%
TOT	**3.80**	**2.47**	**51.75**	**33.72**	**65.3%**

Table 88 – E_{ch} and E_{disch} for optimised designs

After TES design optimisation, 30% more energy can be discharged daily at the station, for a total of 2.47 (2030) and 33.72 MWh (2040).

4.16 Examples of waste heat utilisation

In the next two sections, two potential uses of the waste heat discharged at the station are briefly described. While the first one can help to reduce carbon emissions, the second tries to address one of the main issues related to FCH technology, namely the need of large radiators. Scenario 2040 is considered, that is when the replacement of diesel trains with hydrogen hybrid ones has been completed

4.16.1 Waste heat integration into district heating

One of the possible utilisation of the waste heat discharged at the station is its integration into nearby energy system.

In 2016, Birmingham New Street station has been connected to the Broad Street heating network[70], which is one of the three schemes forming the Birmingham District Energy Scheme (BDES). Therefore, thermal energy from trains could be supplied to BDES, taking advantage of the existing infrastructures.

Currently, BDES heat suppliers are CHP plants. Assuming a thermal efficiency of 65% [199], it follows that each CHP plants requires 154 m^3 of natural gas to produce 1 MWh of heat. Considering an emission factor of 1.94 kg CO_2 per m^3 of natural gas[71], 10.1 tons of CO_2 emissions could be avoided daily by integrating into the district heating the 33.72 MWh from trains instead of using CHP plant to produce them.

4.16.2 Effect of waste heat on radiator size

According to [200], heat lost by radiator throughout a journey can be calculated as:

$$Q_{radiator} = A_{radiator} \cdot U_{radiator} \cdot (T_{out,coolant} - T_{amb}) \cdot t_{journey} \quad (139)$$

As part of the heat removed by coolant circuit is stored in TES systems, less energy needs to be rejected through radiator. To estimate the reduction in radiator area thanks to the integration of TES system, E_{ch} values from Table 81 and waste heat potential in Table 69 are combined into a single table.

[70] https://www.theade.co.uk/case-studies/utility/birmingham-district-energy-scheme
[71] https://www.epa.gov/energy/greenhouse-gases-equivalencies-calculator-calculations-and-references#:~:text=The%20average%20carbon%20dioxide%20coefficient,cubic%20foot%20(EIA%202022).

Route	Q_{route} (MWh)	E_{ch} (MWh)	E_{disch} (MWh)
Leicester - BNS	15.85	8.86	5.85
Nottingham - BNS	19.91	11.07	7.08
Stansted - BNS	29.69	8.58	5.73
Cambridge - BNS	12.89	3.63	2.37
Derby - BNS	2.55	0.76	0.49
Shrewsbury - BNS	15.39	10.17	6.53
Worcester - BNS	0.85	0.56	0.37
Hereford - BNS	13.30	7.24	4.72
G. Malvern - BNS	1.51	0.88	0.57
TOT	**111.94**	**51.75**	**33.72**

Table 89 – Waste heat potentials and amount of heat stored and discharged for all the examined routes

For instance, it can be noted that trains running on Leicester – BNS route store daily 8.86 MWh out of 15.85 MWh. Thus, a train serving that line can store around 56% of the excess heat available, reducing the energy that its radiator has to discharge by 56%. In theory, radiators 56% smaller could be used.

5. Chapter five

Conclusions and future research

5.1 Conclusions and future research: well-to-wheel analysis of fuel cell hybrid train operating in the Birmingham area

Fourteen different WTW pathways, regarded as the most likely for the Birmingham area, have been selected. As UK hydrogen sector is a fast-changing field, two different scenarios are chosen: 2030 and 2040. The aim is to show how technological advancement may positively affect hydrogen pathways' efficiencies.

The following conclusions, grouped according to the stage of WTW analysis to which they refer, can be drawn:

Well-to-tank step

1. *Efficiency of Production Methods:*

- SMR+CCS storage proves to be more efficient than wind-powered electrolysis, offering a primary energy efficiency of 61%. This advantage stems from well-optimized industrial processes that minimize losses. Energy requirements for NG extraction and processing contribute significantly to the energy losses in the SMR process. The production of hydrogen through PEM electrolyzers is instead heavily penalized by the inherently energy-intensive nature of the electrolysis process.
- Wind-powered electrolysis is 52% efficient in 2030 and 58% in 2040. The main efficiency losses originate from the electrolysis process itself, electricity transmission,

hydrogen compression, minor leakage losses, and, where applicable, seawater desalination. The increase in efficiency is driven by the expected improvement in PEM electrolysis technology over the years.

2. *Transport and Storage:*

- Until an all-H2 network is established, transporting compressed gaseous hydrogen via 700 bar-tube trailers remains the most efficient method. Liquid hydrogen transport is less efficient due to high liquefaction energy requirements.
- While pipelines become the dominant transport method after the abandonment of blending, the prior investment in both compressed hydrogen tube trailers and liquid hydrogen tankers creates a form of technology lock-in. The sunk costs associated with high-pressure compression, liquefaction facilities, specialized storage, and dedicated tanker fleets could slow down the transition to pipelines or introduce economic resistance.
- Hydrogen storage has a negligible effect on WTT efficiency compared to production and transport.

3. *Best WTT Routes:*

- In the 2030 scenario, SMR+CCS for production, 700 bar-tube trailers for transport, and dispensing with HRS using overflow filling are identified as the best WTT route (pathway 11). The most efficient WTT pathways are predominantly of the blue hydrogen type.
- By 2040, improvements in electrolysis efficiency and primary energy factor reduce the gap between green and blue hydrogen WTT routes. After the abandonment of

blending, the most efficient WTT paths adopt pipeline transport, emphasizing the importance of an all-H2 network. One of the green H_2 paths manages to reach the podium.

Tank-to-wheel step

- WTW efficiency of diesel train is higher than that of fuel cell hybrid train, for all the pathways and scenarios considered
- If the results of WTW analysis are expressed in terms of kWh_P per km travelled, then fuel cell hybrid train is a better option than diesel train. The reason is the high performance of the fuel cell based powertrain which leads to a better fuel economy

Uncertainty analysis step

- Pathways 1 to 6 and 13 to 14 have higher standard deviations (i.e. average $\sigma = 0.037$) due to the complexities of technologies like electrolysis. In contrast, pathways 7 to 12, using mature technologies like natural gas reforming, have low standard deviations (i.e. average $\sigma = 3.9 \cdot 10^{-4}$) and less uncertainty in WTW efficiencies.

The main conclusion that can be drawn is that fuel cell hybrid trains, despite the more energy needed for the hydrogen WTT step, may already offer lower primary energy consumption than diesel ones. The main reason is their superior fuel economy and efficiency in converting energy to traction power. Specifically, FCH trains utilize hydrogen more efficiently in their fuel cells, converting a higher percentage of the energy content of hydrogen into useful work (electricity for traction) compared to the internal combustion engines in diesel trains, which are less efficient and lose more energy as waste heat.

However, to be comprehensive, the comparison between two competing technologies must include an economic analysis. In the specific case of hydrogen fuelled trains, levelized cost of hydrogen, vehicle's CAPEX and OPEX should be determined.

Moreover, to increase the accuracy of the evaluation, it would be also important to consider the real-life driving profile of the train and the route's characteristics.

5.2 Conclusions and future research: Waste heat from fuel cell hybrid trains: the Birmingham New Street station scenario

The main conclusions that can be drawn from Chapter 4 are summarised below:

- Based on the assumptions made and Birmingham New Street timetables, a waste heat potential for BNS equal to 114 MWh per day has been estimated. This is the heat that would be available at the station if all the thermal energy generated by fuel cells is first stored in the on-board TES and then discharged with a 100% round-trip efficiency
- A dynamic model of the cabin air temperature is developed in Simulink to assess how much energy is required to maintain thermal comfort in the carriage throughout the year. It emerged that only 3.9% of the BNS daily waste heat potential has to be spent in winter for cabin heating.
- In 2040, TES systems can store 56 MWh of heat per day. 916 tons of PCM will need to be distributed across 735 trains, about 1.25 tons per train. Approximately 26 MWh of the stored heat is then discharged daily at the station, with an average round-trip efficiency of 46%. The heat discharged at the station is about 23% of the overall BNS winter waste heat potential. The average temperature of the heat is 51.3°C.

- Compared to the default design, whose performance is detailed in Table 81, 30% more energy can be discharged daily at the station thanks to design optimisation.
- Heat from trains can be integrated into the Broad Street heating network. Approximately 10.1 tons of CO_2 emissions could be saved daily by heat integration into the district heating.
- As part of the excess heat from fuel cell powertrains is stored in TES systems, surface area of radiator can be smaller. For instance, the developed TES design allows to reduce by 56% the radiator area of the trains running between Leicester and BNS.

This chapter highlights the remarkable quantity of heat that could be available at the station for later use. The contributions of Chapter 4 to research are:

- to have proven the feasibility of the integration of PCM-based TES into the FCH train layout, addressing issues such as sizing and positioning of the proposed TES modules
- to have assessed, using a CFD model of the storage modules, the amount of heat that could be stored and then actually discharged at the BNS station.

In a further study, the possibility to install TES storage also inside the train cabin to increase the amount of heat stored may be evaluated. Moreover, it would be important to know the duty cycle and speed profile of the trains involved to assess, with a higher level of accuracy, the waste heat generated during the train's journey. An analysis aiming to determine the effect of weight increase due to PCM on train performance is also advisable.

The proposed thermal integration between fuel cell modules and PCM-based TES could be even more effective for a fuel cell train implementing solid oxide fuel cells. The higher temperature of the heat stored would open up the field to a more opportunities of integration.

References

[1] HM Government, “Net Zero Strategy: Build Back Greener,” 2021. [Online]. Available: https://assets.publishing.service.gov.uk/government/uploads/system/uploads/attachment_data/file/1033990/net-zero-strategy-beis.pdf.

[2] D. for Transport, “Decarbonising Transport: A Better, Greener Britain,” 2021. [Online]. Available: https://assets.publishing.service.gov.uk/government/uploads/system/uploads/attachment_data/file/1009448/decarbonising-transport-a-better-greener-britain.pdf.

[3] Y. Ruf, T. Zorn, P. A. De Neve, P. Andrae, S. Erofeeva, and F. Garrison, “Overcoming technological and non-technological barriers to widespread use of FCH in rail applications – Recommendations on future R&I,” 2019. [Online]. Available: https://rail-research.europa.eu/wp-content/uploads/2019/04/Report-3.pdf.

[4] L. Silvestri, S. Di Micco, A. Forcina, M. Minutillo, and A. Perna, “Power-to-hydrogen pathway in the transport sector: How to assure the economic sustainability of solar powered refueling stations,” *Energy Convers. Manag.*, vol. 252, 2022.

[5] A. K. Ankur, S. Kraus, T. Grube, R. Castro, and D. Stolten, “A Versatile Model for Estimating the Fuel Consumption of a Wide Range of Transport Modes,” *Energies*, vol. 15, no. 6, 2022, doi: 10.3390/en15062232.

[6] A. Huss *et al.*, *JEC Tank-To-Wheels report v5: Passenger cars*. 2020.

[7] M. Muron, G. Pawelec, and D. Fraile, “Clean Hydrogen Production Pathways,” 2024. [Online]. Available: https://hydrogeneurope.eu/wp-content/uploads/2024/06/2024_H2E_CleanH2ProductionPathwaysReport.pdf.

[8] R. . El-Emam and H. Ozcan, “Comprehensive review on the techno-economics of sustainable large-scale clean hydrogen production,” *J. Clean. Prod.*, vol. 220, pp. 593–609, 2019.

[9] J.-J. Hwang, “Sustainability study of hydrogen pathways for fuel cell vehicle applications,” *Renew. Sustain. Energy Rev.*, vol. 19, pp. 220–229, 2013.

[10] Z. Du *et al.*, “A Review of Hydrogen Purification Technologies for Fuel Cell Vehicles,” *Catalysts*, vol. 11, no. 3, 2021.

[11] P. Sun *et al.*, “Criteria Air Pollutants and Greenhouse Gas Emissions from Hydrogen Production in U.S. Steam Methane Reforming Facilities,” *Environ. Sci. Technol.*, vol. 53, no. 12, pp. 7103–7113, 2019.

[12] T. Longden, F. J. Beck, F. Jotzo, R. Andrews, and M. Prasad, “‘Clean’ hydrogen? – Comparing the emissions and costs of fossil fuel versus renewable electricity based hydrogen,” *Appl. Energy*, vol. 306, 2022.

[13] E. M. Washing and S. S. Pulugurtha, “Well-to-Wheel Analysis of Electric and Hydrogen Light Rail,” *J. Public Transp.*, vol. 18, no. 2, 2015.

[14] Q. Wang, M. Xue, B.-L. Lin, Z. Lei, and Z. Zhang, “Well-to-wheel analysis of energy

consumption, greenhouse gas and air pollutants emissions of hydrogen fuel cell vehicle in China," *J. Clean. Prod.*, vol. 275, 2020.

[15] A. Martinez-Rodriguez and A. Abanades, "Comparative Analysis of Energy and Exergy Performance of Hydrogen Production Methods," *Entropy*, vol. 22, 2020.

[16] M. Younas, S. Shafique, A. Hafeez, F. Javed, and F. Rehman, "An Overview of Hydrogen Production: Current Status, Potential, and Challenges," *Fuel*, vol. 316, 2022.

[17] S. Campanari, G. Manzolini, and F. G. de la Iglesia, "Energy analysis of electric vehicles using batteries or fuel cells through well-to-wheel driving cycle simulations," *J. Power Sources*, vol. 186, no. 2, pp. 464–477, 2009.

[18] P. Burmistrz, T. Chmielniak, L. Czepirski, and M. Gazda-Grzywacz, "Carbon footprint of the hydrogen production process utilizing subbituminous coal and lignite gasification," *J. Clean. Prod.*, vol. 139, pp. 858–865, 2016.

[19] A. Midilli, H. Kucuk, M. E. Topal, U. Akbulut, and I. Dincer, "A comprehensive review on hydrogen production from coal gasification: Challenges and Opportunities," *Int. J. Hydrogen Energy*, vol. 46, no. 50, pp. 25385–25412, 2021.

[20] C.-C. Cormos, F. Starr, E. Tzimas, and S. Peteves, "Innovative concepts for hydrogen production processes based on coal gasification with CO2 capture," *Int. J. Hydrogen Energy*, vol. 33, no. 4, pp. 1286–1294, 2008.

[21] N. V. Gnanapragasam, B. V. Reddy, and M. A. Rosen, "Hydrogen production from coal gasification for effective downstream CO2 capture," *Int. J. Hydrogen Energy*, vol. 35, no. 10, 2010.

[22] H. Ishaq, I. Dincer, and C. Crawford, "A review on hydrogen production and utilization: Challenges and opportunities," *Int. J. Hydrogen Energy*, vol. 47, no. 62, pp. 26238–26264, 2022.

[23] IEA, "The Future of Hydrogen," 2019. [Online]. Available: https://iea.blob.core.windows.net/assets/9e3a3493-b9a6-4b7d-b499-7ca48e357561/The_Future_of_Hydrogen.pdf.

[24] M. David, C. Ocampo-Martinez, and R. Sanchez-Pena, "Advances in alkaline water electrolyzers: A review," *J. Energy Storage*, vol. 23, pp. 392–403, 2019.

[25] Y. Guo, G. Li, J. Zhou, and Y. Liu, "Comparison between hydrogen production by alkaline water electrolysis and hydrogen production by PEM electrolysis," *IOP Conf. Ser. Earth Environ. Sci.*, vol. 371, no. 4, 2019.

[26] S. S. Kumar and H. Lim, "An overview of water electrolysis technologies for green hydrogen production," *Energy Reports*, vol. 8, pp. 13793–13813, 2022.

[27] T. Wang, X. Cao, and L. Jiao, "PEM water electrolysis for hydrogen production: fundamentals, advances, and prospects," *Carbon Neutrality*, vol. 1, 2022.

[28] S. S. Kumar and V. Himabindu, "Hydrogen production by PEM water electrolysis – A review," *Mater. Sci. Energy Technol.*, vol. 2, no. 3, pp. 442–454, 2019.

[29] S. Kiemel, T. Smolinka, F. Lehner, J. Full, A. Sauer, and R. Miehe, "Critical materials

for water electrolysers at the example of the energy transition in Germany," *Int. J. Energy Res.*, vol. 45, no. 7, 2021.

[30] A. Hauch *et al.*, "Recent advances in solid oxide cell technology for electrolysis," *Science (80-.).*, vol. 370, no. 6513, 2020.

[31] A. Nechache and S. Hody, "Alternative and innovative solid oxide electrolysis cell materials: A short review," *Renew. Sustain. Energy Rev.*, vol. 149, 2021.

[32] G. Min, S. Choi, and J. Hong, "A review of solid oxide steam-electrolysis cell systems: Thermodynamics and thermal integration," *Appl. Energy*, vol. 328, 2022.

[33] L. Vidas and R. Castro, "Recent Developments on Hydrogen Production Technologies: State-of-the-Art Review with a Focus on Green-Electrolysis," *Appl. Sci.*, vol. 11, no. 23, 2021.

[34] IRENA, "Green Hydrogen Cost Reduction: Scaling up Electrolysers to Meet the 1.5^0C Climate Goal," 2020.

[35] T. Bui, D. Lee, K. Y. Ahn, and Y. S. Kim, "Techno-economic analysis of high-power solid oxide electrolysis cell system," *Energy Convers. Manag.*, vol. 278, no. September 2022, p. 116704, 2023, doi: 10.1016/j.enconman.2023.116704.

[36] S. Krishnan *et al.*, "Present and future cost of alkaline and PEM electrolyser stacks," *Int. J. Hydrogen Energy*, vol. 48, no. 83, pp. 32313–32330, 2023, doi: 10.1016/j.ijhydene.2023.05.031.

[37] A. Franco and C. Giovannini, "Recent and Future Advances in Water Electrolysis for Green Hydrogen Generation: Critical Analysis and Perspectives," *Sustainability*, vol. 15, no. 24, p. 16917, 2023, doi: 10.3390/su152416917.

[38] H. Kojima, K. Nagasawa, N. Todoroki, Y. Ito, T. Matsui, and R. Nakajima, "Influence of renewable energy power fluctuations on water electrolysis for green hydrogen production," *Int. J. Hydrogen Energy*, vol. 48, no. 12, pp. 4572–4593, 2023, doi: 10.1016/j.ijhydene.2022.11.018.

[39] E. Ghirardi, G. Brumana, G. Franchini, and A. Perdichizzi, "H2 contribution to power grid stability in high renewable penetration scenarios," *Int. J. Hydrogen Energy*, vol. 48, no. 32, pp. 11956–11969, 2023.

[40] Y. Ruf, T. Zorn, P. A. De Neve, P. Andrae, S. Erofeeva, and F. Garrison, "STUDY ON THE USE OF FUEL CELLS & HYDROGEN IN THE RAILWAY ENVIRONMENT - Overcoming technological and non-technological barriers to widespread use of FCH in rail applications Recommendations on future R & I," 2019, [Online]. Available: https://rail-research.europa.eu/wp-content/uploads/2019/04/Report-3.pdf.

[41] I. A. Hassan, H. S. Ramadan, M. A. Saleh, and D. Hissel, "Hydrogen storage technologies for stationary and mobile applications: Review, analysis and perspectives," *Renew. Sustain. Energy Rev.*, vol. 149, 2021.

[42] R. Moradi and K. M. Groth, "Hydrogen storage and delivery: Review of the state of the art technologies and risk and reliability analysis," *Int. J. Hydrogen Energy*, vol. 44, no. 23, pp. 12254–12269, 2019.

[43] J. O. Abe, A. P. I. Popoola, E. Ajenifuja, and O. M. Popoola, “Hydrogen energy, economy and storage: Review and recommendation,” *Int. J. Hydrogen Energy*, vol. 44, no. 29, pp. 15072–15086, 2019.

[44] M. Li *et al.*, “Review on the research of hydrogen storage system fast refueling in fuel cell vehicle,” *Int. J. Hydrogen Energy*, vol. 44, no. 21, pp. 10677–10693, 2019.

[45] M. R. Usman, “Hydrogen storage methods: Review and current status,” *Renew. Sustain. Energy Rev.*, vol. 167, 2022.

[46] H. W. Langmi, N. Engelbrecht, P. M. Modisha, and D. Bessarabov, “Chapter 13 - Hydrogen storage,” in *Electrochemical Power Sources: Fundamentals, Systems, and Applications*, T. Smolinka and J. Garche, Eds. Elsevier, 2022, pp. 455–486.

[47] H. Barthelemy, M. Weber, and F. Barbier, “Hydrogen storage:Recent improvements and industrial perspectives,” *Int. J. Hydrogen Energy*, vol. 42, pp. 7254–7262, 2017.

[48] R. Tarkowski, “Underground hydrogen storage:Characteristics and prospects,” *Renew. Sustain. Energy Rev.*, vol. 105, pp. 86–94, 2019.

[49] N. S. Muhammed, B. Haq, D. Al Shehri, A. Al-Ahmed, M. M. Rahman, and E. Zaman, “A review on underground hydrogen storage: Insight into geological sites, influencing factors and future outlook,” *Energy Reports*, vol. 8, pp. 461–499, 2022.

[50] H. Dagdougui, R. Sacile, C. Bersani, and A. Ouammi, “Chapter 4 - Hydrogen Storage and Distribution: Implementation Scenarios,” in *Hydrogen Infrastructure for Energy Applications*, H. Dagdougui, R. Sacile, C. Bersani, and A. Ouammi, Eds. Academic Press, 2018, pp. 37–52.

[51] Z. Yanxing, G. Maoqiong, Z. Yuan, D. Xueqiang, and S. Jun, “Thermodynamics analysis of hydrogen storage based on compressed gaseous hydrogen, liquid hydrogen and cryo-compressed hydrogen,” *Int. J. Hydrogen Energy*, vol. 44, no. 31, pp. 16833–16840, 2019.

[52] S. Z. S. Al Ghafri *et al.*, “Modelling of Liquid Hydrogen Boil-Off,” *Energies*, vol. 15, no. 3, 2022.

[53] D. Berstad, S. Gardarsdottir, S. Roussanaly, M. Voldsund, Y. Ishimoto, and P. Neksa, “Liquid hydrogen as prospective energy carrier: A brief review and discussion of underlying assumptions applied in value chain analysis,” *Renew. Sustain. Energy Rev.*, vol. 154, 2022.

[54] R. K. Ahluwalia, J.-K. Peng, and T. Q. Hua, “5 - Cryo-compressed hydrogen storage,” in *Compendium of Hydrogen Energy*, R. B. Gupta, A. Basile, and T. N. Veziroglu, Eds. Woodhead Publishing, 2016, pp. 119–145.

[55] K. Kunze, “Performance of a cryo-compressed hydrogen storage,” in *World hydrogen energy conference – WHEC (2012)*, 2012.

[56] A. M. Abdalla, S. Hossain, O. Nisfindy, A. T. Azad, M. Dawood, and A. K. Azad, “Hydrogen production, storage, transportation and key challenges with applications: A review,” *Energy Convers. Manag.*, vol. 165, pp. 602–627, 2018.

[57] W. Alsaba, S. A. Al-Sobhi, and M. A. Qyyum, “Recent advancements in the

hydrogen value chain: Opportunities, challenges, and the way Forward–Middle East perspectives," *Int. J. Hydrogen Energy*, 2023.

[58] M. Ball and M. Weeda, "11 - The hydrogen economy—Vision or reality?," in *Compendium of Hydrogen Energy*, M. Ball, A. Basile, and T. N. Veziroglu, Eds. Woodhead Publishing, 2016, pp. 237–266.

[59] O. Faye, J. Szpunar, and U. Eduok, "A critical review on the current technologies for the generation, storage, and transportation of hydrogen," *Int. J. Hydrogen Energy*, vol. 47, no. 29, pp. 13771–13802, 2022.

[60] K. Reddi, A. Elgowainy, N. Rustagi, and E. Gupta, "Techno-economic analysis of conventional and advanced high-pressure tube trailer configurations for compressed hydrogen gas transportation and refueling," *Int. J. Hydrogen Energy*, vol. 43, no. 9, pp. 4428–4438, 2018.

[61] F. Parolin, P. Colbertaldo, and S. Campanari, "Development of a multi-modality hydrogen delivery infrastructure: An optimization model for design and operation," *Energy Convers. Manag.*, vol. 266, 2022.

[62] F. Ustolin, N. Paltrinieri, and F. Berto, "Loss of integrity of hydrogen technologies: A critical review," *Int. J. Hydrogen Energy*, vol. 45, no. 43, pp. 23809–23840, 2020.

[63] B. C. Tashie-Lewis and S. G. Nnabuife, "Hydrogen Production, Distribution, Storage and Power Conversion in a Hydrogen Economy - A Technology Review," *Chem. Eng. J. Adv.*, vol. 8, 2021.

[64] T. Capurso, M. Stefanizzi, M. Torresi, and S. M. Camporeale, "Perspective of the role of hydrogen in the 21st century energy transition," *Energy Convers. Manag.*, vol. 251, 2022.

[65] M. E. Demir and I. Dincer, "Cost assessment and evaluation of various hydrogen delivery scenarios," *Int. J. Hydrogen Energy*, vol. 43, no. 22, pp. 10420–10430, 2018.

[66] A. Witkowski, A. Rusin, M. Majkut, and K. Stolecka, "Comprehensive analysis of hydrogen compression and pipeline transportation from thermodynamics and safety aspects," *Energy*, vol. 141, pp. 2508–2518, 2017.

[67] I. A. Gondal, "12 - Hydrogen transportation by pipelines," in *Compendium of Hydrogen Energy*, R. B. Gupta, A. Basile, and T. N. Veziroglu, Eds. Woodhead Publishing, 2016, pp. 301–322.

[68] R. Gerboni, "11 - Introduction to hydrogen transportation," in *Compendium of Hydrogen Energy*, R. B. Gupta, A. Basile, and T. N. Veziroglu, Eds. Woodhead Publishing, 2016, pp. 283–299.

[69] S. Singh *et al.*, "Hydrogen: A sustainable fuel for future of the transport sector," *Renew. Sustain. Energy Rev.*, vol. 51, pp. 623–633, 2015.

[70] U. S. DRIVE, "Hydrogen Delivery Technical Team Roadmap," 2017. [Online]. Available: https://www.energy.gov/eere/vehicles/articles/us-drive-hydrogen-delivery-technical-team-roadmap.

[71] M. Minutillo, A. Perna, A. Forcina, S. Di Micco, and E. Jannelli, “Analyzing the levelized cost of hydrogen in refueling stations with on-site hydrogen production via water electrolysis in the Italian scenario,” *Int. J. Hydrogen Energy*, vol. 46, no. 26, pp. 13667–13677, 2021.

[72] N. Chrysochoidis-Antsos, M. R. Escudé, and A. J. M. van Wijk, “Technical potential of on-site wind powered hydrogen producing refuelling stations in the Netherlands,” *Int. J. Hydrogen Energy*, vol. 45, no. 46, pp. 25096–25108, 2020.

[73] D. Apostolou and G. Xydis, “A literature review on hydrogen refuelling stations and infrastructure. Current status and future prospects,” *Renew. Sustain. Energy Rev.*, vol. 113, 2019.

[74] Z. Tian, H. Lv, W. Zhou, C. Zhang, and P. He, “Review on equipment configuration and operation process optimization of hydrogen refueling station,” *Int. J. Hydrogen Energy*, vol. 47, no. 5, pp. 3033–3053, 2022.

[75] A. Bauer, T. Mayer, M. Semmel, M. A. Guerrero Morales, and J. Wind, “Energetic evaluation of hydrogen refueling stations with liquid or gaseous stored hydrogen,” *Int. J. Hydrogen Energy*, vol. 44, no. 13, pp. 6795–6812, 2019.

[76] M. Genovese and P. Fragiacomo, “Hydrogen refueling station: Overview of the technological status and research enhancement,” *J. Energy Storage*, vol. 61, 2023.

[77] C. F. Guerra, L. Reyes-Bozo, E. Vyhmeister, J. L. Salazar, M. J. Caparros, and C. Clemente-Jul, “Sustainability of hydrogen refuelling stations for trains using electrolysers,” *Int. J. Hydrogen Energy*, vol. 46, no. 26, pp. 13748–13759, 2021.

[78] A. Elgowainy, K. Reddi, D.-Y. Lee, N. Rustagi, and E. Gupta, “Techno-economic and thermodynamic analysis of pre-cooling systems at gaseous hydrogen refueling stations,” *Int. J. Hydrogen Energy*, vol. 42, no. 49, pp. 29067–29079, 2017.

[79] T. Mayer, M. Semmel, M. A. Guerrero Morales, K. M. Schmidt, A. Bauer, and J. Wind, “Techno-economic evaluation of hydrogen refueling stations with liquid or gaseous stored hydrogen,” *Int. J. Hydrogen Energy*, vol. 44, no. 47, pp. 25809–25833, 2019.

[80] G. Correa, P. Munoz, T. Falaguerra, and C. R. Rodriguez, “Performance comparison of conventional, hybrid, hydrogen and electric urban buses using well to wheel analysis,” *Energy*, vol. 141, pp. 537–549, 2017.

[81] M. Torchio and M. G. Santarelli, “Energy, environmental and economic comparison of different powertrain/fuel options using well-to-wheels assessment, energy and external costs – European market analysis,” *Energy*, vol. 35, no. 10, pp. 4156–4171, 2010.

[82] Q. Lu, B. Zhang, S. Yang, and Z. Peng, “Life cycle assessment on energy efficiency of hydrogen fuel cell vehicle in China,” *Energy*, vol. 257, 2022.

[83] S. Lombardi, L. Tribioli, G. Guandalini, and P. Iora, “Energy performance and well-to-wheel analysis of different powertrain solutions for freight transportation,” *Int. J. Hydrogen Energy*, vol. 45, no. 22, 2020.

[84] M. S. Sheng, A. V. Sreenivasan, B. Sharp, and B. Du, “Well-to-wheel analysis of

greenhouse gas emissions and energy consumption for electric vehicles: A comparative study in Oceania," *Energy Policy*, vol. 158, 2021.

[85] A. Hoffrichter, A. R. Miller, S. Hillmansen, and C. Roberts, "Well-to-wheel analysis for electric, diesel and hydrogen traction for railways," *Transp. Res. Part D Transp. Environ.*, vol. 17, no. 1, pp. 28–34, 2012.

[86] M. Yazdanie, F. Noembrini, S. Heinen, A. Espinel, and K. Boulouchos, "Well-to-wheel costs, primary energy demand, and greenhouse gas emissions for the production and operation of conventional and alternative vehicles," *Transp. Res. Part D Transp. Environ.*, vol. 48, pp. 63–84, 2016.

[87] M. Li, X. Zhang, and G. Li, "A comparative assessment of battery and fuel cell electric vehicles using a well-to-wheel analysis," *Energy*, vol. 94, 2016.

[88] P. Keen and R. Phillpotts, "Low Cost Electrification for Branch Lines," 2010. [Online]. Available: https://assets.publishing.service.gov.uk/government/uploads/system/uploads/attachment_data/file/3872/low-cost-electrification-report.pdf.

[89] Y. Ruf, T. Zorn, P. A. De Neve, P. Andrae, S. Erofeeva, and F. Garrison, "STUDY ON THE USE OF FUEL CELLS & HYDROGEN IN THE RAILWAY ENVIRONMENT - State of the art & business case and market potential," 2019. [Online]. Available: https://rail-research.europa.eu/wp-content/uploads/2019/04/Report-1.pdf.

[90] E. Fedele, D. Iannuzzi, and A. Del Pizzo, "Onboard energy storage in rail transport: Review of real applications and techno-economic assessments," *IET Electr. Syst. Transp*, vol. 11, no. 4, pp. 279–309, 2021.

[91] H. J. Kaleybar, M. Brenna, H. Li, and D. Zaninelli, "Fuel Cell Hybrid Locomotive with Modified Fuzzy Logic Based Energy Management System," *Sustainability*, vol. 14, 2022.

[92] R. Thorne, A. H. Amundsen, and I. Sundvor, "Battery Electric and Fuel Cell Trains: Maturity of Technology and Market Status," 2020. [Online]. Available: https://www.toi.no/getfile.php?mmfileid=52027.

[93] C. Calvert, J. Allan, P. Amor, S. Hillmansen, C. Roberts, and P. Weston, "Concept development and testing of the UK's first hydrogen-hybrid train (HydroFLEX)," *Railw. Eng. Sci.*, vol. 29, pp. 248–257, 2021.

[94] J. Ling-Chin *et al.*, "Technology roadmap for hydrogen-fuelled transportation in the UK," *Int. J. Hydrogen Energy*, 2023.

[95] F. Bouyssou, "D5.1.- FCHPP Implementation and Integration in Demonstrator Train," 2022. [Online]. Available: https://verkehrsforschung.dlr.de/public/documents/2023/FCH2RAIL_D5.1_FCHPP Implementation and Integration in Demonstrator_submitted.pdf.

[96] X. Yu, N. S. Sandhu, Z. Yang, and M. Zheng, "Suitability of energy sources for automotive application – A review," *Appl. Energy*, vol. 271, 2020.

[97] G. Trencher, A. Taeihagh, and M. Yarime, "Overcoming barriers to developing and diffusing fuel-cell vehicles: Governance strategies and experiences in Japan,"

Energy Policy, vol. 142, 2020.

[98] M. Inci, M. Buyuk, M. H. Demir, and G. Ilbey, “A review and research on fuel cell electric vehicles: Topologies, power electronic converters, energy management methods, technical challenges, marketing and future aspects,” *Renew. Sustain. Energy Rev.*, vol. 137, 2021.

[99] W. A. N. W. Mohamed, B. Singh, M. F. Mohamed, A. M. Aizuwan, and A. B. . Zubair, “Effects of fuel cell vehicle waste heat temperatures and cruising speeds on the outputs of a thermoelectric generator energy recovery module,” *Int. J. Hydrogen Energy*, vol. 46, no. 50, pp. 25634–25649, 2021.

[100] C. Q., G. Zhang, X. Zhang, C. Sun, K. Jiao, and Y. Wang, “Thermal management of polymer electrolyte membrane fuel cells: A review of cooling methods, material properties, and durability,” *Appl. Energy*, vol. 286, 2021.

[101] A. Farsi and M. A. Rosen, “Thermal management of polymer electrolyte membrane fuel cells: comparative assessment of cooling systems,” *e-Prime - Adv. Electr. Eng. Electron. Energy*, vol. 4, 2023.

[102] S. G. Kandlikar and Z. Lu, “Thermal management issues in a PEMFC stack – A brief review of current status,” *Appl. Therm. Eng.*, vol. 29, no. 7, 2009.

[103] H. Q. Nguyen and B. Shabani, “Proton exchange membrane fuel cells heat recovery opportunities for combined heating/cooling and power applications,” *Energy Convers. Manag.*, vol. 204, 2020.

[104] S. Rashidi, N. Karimi, B. Sunden, K. C. Kim, A. G. Olabi, and O. Mahian, “Progress and challenges on the thermal management of electrochemical energy conversion and storage technologies: Fuel cells, electrolysers, and supercapacitors,” *Prog. Energy Combust. Sci.*, vol. 88, 2022.

[105] A. Baroutaji *et al.*, “Advancements and prospects of thermal management and waste heat recovery of PEMFC,” *Int. J. Thermofluids*, vol. 9, 2021.

[106] Q. Li, Z. Liu, Y. Sun, S. Yang, and C. Deng, “A Review on Temperature Control of Proton Exchange Membrane Fuel Cells,” *Processes*, vol. 9, no. 2, 2021.

[107] R. Singh, A. S. Oberoi, and T. Singh, “Factors influencing the performance of PEM fuel cells: Areview on performance parameters, water management,and cooling techniques,” *Int. J. Energy Res.*, vol. 46, no. 4, pp. 3820–3842, 2022.

[108] M. H. . Bargal, M. A. Abdelkareem, Q. Tao, J. Li, J. Shi, and Y. Wang, “Liquid cooling techniques in proton exchange membrane fuel cell stacks: A detailed survey,” *Alexandria Eng. J.*, vol. 59, pp. 635–655, 2020.

[109] R. Singh, A. S. Oberoi, and T. Singh, “Heat pipes for PEM fuel cell cooling: State of the art review,” *Mater. Today Proc.*, 2023.

[110] S. Shahsavari, A. Desouza, M. Bahrami, and E. Kjeang, “Thermal analysis of air-cooled PEM fuel cells,” *Int. J. Hydrogen Energy*, vol. 37, no. 23, pp. 18261–18271, 2012.

[111] M. V. Oro and E. Bazzo, “Flat heat pipes for potential application in fuel cell cooling,”

Appl. Therm. Eng., vol. 90, pp. 848–857, 2015.

[112] M. H. . Bargal, M. A. Abdelkareem, Q. Tao, J. Li, J. Shi, and Y. Wang, “Liquid cooling techniques in proton exchange membrane fuel cell stacks: A detailed survey,” *Alexandria Eng. J.*, vol. 59, no. 2, pp. 635–655, 2020.

[113] M. R. Islam, B. Shabani, and G. Rosengarten, “Nanofluids to improve the performance of PEM fuel cell cooling systems: A theoretical approach,” *Appl. Energy*, vol. 178, pp. 660–671, 2016.

[114] I. Zakaria, W. A. N. W. Mohamed, W. H. Azmi, A. M. I. Mamat, R. Mamat, and W. R. W. Daud, “Thermo-electrical performance of PEM fuel cell using Al2O3 nanofluids,” *Int. J. Heat Mass Transf.*, vol. 119, pp. 460–471, 2018.

[115] Y. Yu, M. Chen, S. Zaman, S. Xing, M. Wang, and H. Wang, “Thermal management system for liquid-cooling PEMFC stack: From primary configuration to system control strategy,” *eTransportation*, vol. 12, 2022.

[116] T. Wilberforce *et al.*, “Recovery of waste heat from proton exchange membrane fuel cells – A review,” *Int. J. Hydrogen Energy*, 2022.

[117] A. Colmenar-Santos, L. Alberdi-Jimenez, L. Nasarre-Cortes, and J. Mora-Larramona, “Residual heat use generated by a 12 kW fuel cell in an electric vehicle heating system,” *Energy*, vol. 68, pp. 182–190, 2014.

[118] M. Nasri, I. Burger, S. Michael, and E. Friedrich, “Waste heat recovery for fuel cell electric vehicle with thermochemical energy storage,” in *2016 Eleventh International Conference on Ecological Vehicles and Renewable Energies (EVER)*, 2016, pp. 1–6.

[119] P. Royo, L. Acevedo, V. J. Ferreira, T. Garcia-Armingol, A. M. Lopez-Sabiron, and G. Ferreira, “High-temperature PCM-based thermal energy storage for industrial furnaces installed in energy-intensive industries,” *Energy*, vol. 173, pp. 1030–1040, 2019.

[120] S. Kahwaji, M. B. Johnson, A. C. Kheirabadi, D. Groulx, and M. A. White, “A comprehensive study of properties of paraffin phase change materials for solar thermal energy storage and thermal management applications,” *Energy*, vol. 162, pp. 1169–1182, 2018.

[121] HM Government, “UK Hydrogen Strategy,” 2021. [Online]. Available: https://assets.publishing.service.gov.uk/government/uploads/system/uploads/attachment_data/file/1011283/UK-Hydrogen-Strategy_web.pdf.

[122] BEIS, “UK Low Carbon Hydrogen Standard - Guidance on the greenhouse gas emissions and sustainability criteria,” 2022. [Online]. Available: https://assets.publishing.service.gov.uk/government/uploads/system/uploads/attachment_data/file/1092809/low-carbon-hydrogen-standard-guidance-v2.1.pdf.

[123] BEIS, “Hydrogen Sector Development Action Plan,” 2022. [Online]. Available: https://assets.publishing.service.gov.uk/government/uploads/system/uploads/attachment_data/file/1092353/hydrogen-sector-development-action-plan.pdf.

[124] E. B. Agyekum, C. Nukator, A. M. Agwa, and S. Kamel, “A Critical Review of

Renewable Hydrogen Production Methods: Factors Affecting Their Scale-Up and Its Role in Future Energy Generation," *Membr.*, vol. 12, no. 2, 2022.

[125] HM Government, "ENERGY WHITE PAPER - Powering our Net Zero Future," 2020. [Online]. Available: https://assets.publishing.service.gov.uk/government/uploads/system/uploads/attachment_data/file/945899/201216_BEIS_EWP_Command_Paper_Accessible.pdf.

[126] "HyNet Low Carbon Hydrogen Plant - Phase 1 Report for BEIS," 2019. [Online]. Available: https://assets.publishing.service.gov.uk/government/uploads/system/uploads/attachment_data/file/866401/HS384_-_Progressive_Energy_-_HyNet_hydrogen.pdf.

[127] BEIS, "Hydrogen Strategy update to the market: July 2022," 2022. [Online]. Available: https://assets.publishing.service.gov.uk/government/uploads/system/uploads/attachment_data/file/1092555/hydrogen-strategy-update-to-the-market-july-2022.pdf.

[128] HM Government, "The Ten Point Plan for a Green Industrial Revolution," 2020. [Online]. Available: https://assets.publishing.service.gov.uk/government/uploads/system/uploads/attachment_data/file/936567/10_POINT_PLAN_BOOKLET.pdf.

[129] Department for International Trade, "Hydrogen Investor Roadmap," 2022. [Online]. Available: https://assets.publishing.service.gov.uk/government/uploads/system/uploads/attachment_data/file/1114758/hydrogen-investor-roadmap.pdf.

[130] J. Williams, P. Williamson, D. Parkes, K. Kirk, M. Akhurst, and J. Pearce, "Theoretical capacity for underground hydrogen storage in UK salt caverns," 2020. [Online]. Available: https://ukccsrc.ac.uk/wp-content/uploads/2020/05/John-Williams_CCS-and-Hydrogen.pdf.

[131] C. Jackson, G. Smith, and A. R. Kucernak, "Deblending and purification of hydrogen from natural gas mixtures using the electrochemical hydrogen pump," *Int. J. Hydrogen Energy*, vol. 52, pp. 816–826, 2024, doi: 10.1016/j.ijhydene.2023.05.065.

[132] Element Energy Ltd, "Hydrogen supply chain evidence base," 2018. [Online]. Available: https://assets.publishing.service.gov.uk/government/uploads/system/uploads/attachment_data/file/760479/H2_supply_chain_evidence_-_publication_version.pdf.

[133] S. D.-L. Almaraz and C. Azzarro-Pantel, "Chapter 4 - Design and Optimization of Hydrogen Supply Chains for a Sustainable Future," in *Hydrogen Economy*, A. Scipioni, A. Manzardo, and J. Ren, Eds. Academic Press, 2017, pp. 85–120.

[134] H. Nazir *et al.*, "Is the H2 economy realizable in the foreseeable future? Part II: H2 storage, transportation, and distribution," *Int. J. Hydrogen Energy*, vol. 45, no. 41, pp. 20693–20708, 2020.

[135] M. Spiryagin, C. Cole, Y. Q. Sun, M. McClanachan, V. Spiryagin, and T. McSweeney, *Design and Simulation of Rail Vehicles*, 1st ed. CRC Press, 2014.

[136] D. S. Armstrong and P. Swift, “Lower energy technology. Part A, identification of energy use in multiple units. Report MR VS 077,” Derby, 1990.

[137] Building Research Establishment Ltd, “SAP 10 Technical Paper S10TP-15,” 2020. [Online]. Available: https://files.bregroup.com/sap/S10TP-15_-_CO2_and_Primary_Energy_factors_for_SAP_v1_1_10_1.pdf?_its=JTdCJTIydmlkJTIyJTNBJTIyMzIyYTdlY2YtZmZiYS00ODZkLWJlOWEtN2FhODQyNmFlNjU4JTIyJTJDJTIyc3RhdGUlMjIlM0ElMjJybHR%2BMTY2ODYwNTQxNX5sYW5kfjJfNzc4NzlfZGlyZWN0X2UwM.

[138] M. Prussi, M. Yugo, L. De Prada, M. Padella, R. Edwards, and L. Lonza, “JEC Well-to-Tank report v5,” 2020. doi: 10.2760/959137.

[139] “HyNet Low Carbon Hydrogen Plant - Phase 2 Report for BEIS,” 2021. [Online]. Available: https://assets.publishing.service.gov.uk/government/uploads/system/uploads/attachment_data/file/1056041/Phase_2_Report_-_Progressive_Energy_-_HyNet_Low_Carbon_Hydrogen__3_.pdf.

[140] Johnson-Matthey, “Clean hydrogen. Hydrogen from natural gas through cost effective CO2 capture,” 2021, [Online]. Available: https://matthey.com/documents/161599/440415/Reprint+-+Hydrogen+from+Natural+Gas+Through+Cost+Effective+CO2+Capture+%28c2021%29.pdf/a4e2aead-46c9-1a45-7fcf-cf6987262944?t=1653488219254.

[141] “Offshore Wind Report,” 2021. [Online]. Available: https://www.thecrownestate.co.uk/media/4095/2021-offshore-wind-report.pdf.

[142] Y. J. Lim, K. Goh, M. Kurihara, and R. Wang, “Seawater desalination by reverse osmosis: Current development and future challenges in membrane fabrication – A review,” *J. Memb. Sci.*, vol. 629, 2021.

[143] M. A. Khan *et al.*, “Seawater electrolysis for hydrogen production: a solution looking for a problem?,” *Energy Environ. Sci.*, no. 9, 2021.

[144] A. Hoffrichter, “Hydrogen as an energy carrier for railway traction,” University of Birmingham, 2013.

[145] Frazer-Nash Consultancy, “Fugitive Hydrogen Emissions in a Future Hydrogen Economy,” 2022. [Online]. Available: https://assets.publishing.service.gov.uk/government/uploads/system/uploads/attachment_data/file/1067137/fugitive-hydrogen-emissions-future-hydrogen-economy.pdf.

[146] J. Larsson, “Transmission Systems for Grid Connection of Offshore Wind Farms,” Uppsala University, 2021.

[147] E. Apostolaki-Iosifidou, R. McCormack, W. Kempton, P. McCoy, and D. Ozkan, “Transmission Design and Analysis for Large-Scale Offshore Wind Energy Development,” *IEEE Power Energy Technol. Syst. J.*, vol. 6, no. 1, pp. 22–31, 2019.

[148] M. Barton, L. Soriano, J. Stahley, and A. Talakar, “Under Pressure: The Challenge of Hydrogen Compression,” 2021. [Online]. Available: https://assets.siemens-energy.com/siemens/assets/api/uuid:d985fced-fb7e-4881-a1b9-87cd6d7eac63/se-

he-august2021-challenges-hydrogencompression-article.pdf.

[149] M. A. Khan, C. Young, C. MacKinnon, and D. B. Layzell, “The Techno-Economics of Hydrogen Compression. Transition Accelerator Technical Briefs,” vol. 1, no. 1, pp. 1–36, 2021, [Online]. Available: https://transitionaccelerator.ca/wp-content/uploads/2021/10/TA-Briefs-1.2-The-Techno-Economics-of-Hydrogen-Compression-FINALPDF.pdf.

[150] D. . Ratnayaka, M. J. Brandt, and K. M. Johnson, “CHAPTER 13 - System Design and Analysis,” in *Water Supply (Sixth Edition)*, D. D. Ratnayaka, M. J. Brandt, and K. M. Johnson, Eds. Butterworth-Heinemann, 2009, pp. 499–530.

[151] “HyNet CCUS Pre-FEED KKD WP1 - Basis of Design,” 2019, [Online]. Available: https://assets.publishing.service.gov.uk/government/uploads/system/uploads/attachment_data/file/1079831/HyNet_CCUS_Pre-FEED_KKD_WP1_-_Full_Chain_Basis_of_Design.pdf.

[152] “HyNet CCUS Pre-FEED KKD WP5 - Flow Assurance Report,” 2019. [Online]. Available: https://assets.publishing.service.gov.uk/government/uploads/system/uploads/attachment_data/file/1079837/HyNet_CCUS_Pre-FEED_KKD_WP5_HYN01-03_Rev_03_Flow_Assurance_Report.pdf.

[153] “HyNet CCUS Pre-FEED Key Knowledge Deliverable WP1: Final Report,” 2020. [Online]. Available: https://assets.publishing.service.gov.uk/government/uploads/system/uploads/attachment_data/file/1079830/HyNet_CCUS_Pre-FEED_KKD_WP1_-_Final_Report-with-sig.pdf.

[154] BEIS, “Drax BECCS Project – CO2 Compression and Dehydration Unit Report,” 2021, [Online]. Available: https://assets.publishing.service.gov.uk/government/uploads/system/uploads/attachment_data/file/1057604/KKD_CO2_Compression_and_Dehydration_Unit_Report.pdf.

[155] D. A. Simpson, “Chapter Eight - Gas Compression,” in *Practical Onshore Gas Field Engineering*, D. A. Simpson, Ed. 2017, pp. 513–571.

[156] BEIS, “PROJECT HYSECURE PHASE 1 SUMMARY SEPT 2019,” 2019. [Online]. Available: https://assets.publishing.service.gov.uk/government/uploads/system/uploads/attachment_data/file/866376/Phase_1_-_Inovyn_-_HySecure.pdf.

[157] N. Gonzalez Diez, S. van der Meer, J. Bonetto, and A. Herwijn, “Technical assessment of Hydrogen transport, compression, processing offshore,” 2020. [Online]. Available: https://north-sea-energy.eu/static/7ffd23ec69b9d82a7a982b828be04c50/FINAL-NSE3-D3.1-Final-report-technical-assessment-of-Hydrogen-transport-compression-processing-offshore.pdf.

[158] D. D. Ratnayaka, M. J. Brandt, and K. M. Johnson, “CHAPTER 12 - Hydraulics,” in *Water Supply (Sixth Edition)*, Butterworth-Heinemann, Ed. 2009, pp. 463–498.

[159] M.-R. Tahan, “Recent advances in hydrogen compressors for use in large-scale renewable energy integration,” *Int. J. Hydrogen Energy*, vol. 47, no. 83, pp. 35275–35292, 2022.

[160] H. W. Langmi, N. Engelbrecht, P. M. Modisha, and D. Bessarabov, “Chapter 13 - Hydrogen storage,” in *Electrochemical Power Sources: Fundamentals, Systems, and Applications,* T. Smolinka and J. Garche, Eds. 2022, pp. 455–486.

[161] E. Rivard, M. Trudeau, and K. Zaghib, “Hydrogen Storage for Mobility: A Review,” *Mater.*, vol. 12, no. 12, 2019.

[162] Element Energy, “Low Carbon Hydrogen Well-to-Tank Pathways Study - Full Report,” 2021. [Online]. Available: http://www.element-energy.co.uk/wordpress/wp-content/uploads/2021/08/Zemo-Low-Carbon-Hydrogen-WTT-Pathways-full-report.pdf.

[163] S. Z. Al Ghafri *et al.*, “Hydrogen liquefaction: a review of the fundamental physics, engineering practice and future opportunities,” *Energy Environ. Sci.*, vol. 15, no. 7, pp. 2690–2731, 2022, doi: 10.1039/d2ee00099g.

[164] M. Aasadnia and M. Mehrpooya, “Large-scale liquid hydrogen production methods and approaches: A review,” *Appl. Energy*, vol. 212, pp. 57–83, 2018.

[165] “Transmission Planning Code,” 2012. [Online]. Available: https://www.nationalgrid.com/gas-transmission/document/63741/download.

[166] NationalgridESO, “Transmission Losses,” 2019. [Online]. Available: https://www.nationalgrideso.com/electricity-transmission/document/144711/download.

[167] B. Reuter, M. Faltenbacher, O. Schuller, N. Whitehouse, and S. Whitehouse, “New Bus ReFuelling for European Hydrogen Bus Depots,” 2017. [Online]. Available: www.fuelcellbuses.eu/sites/default/files/documents/NewBusFuel_D4.3_Guidance-document-for-large-scale-hydrogen-refuelling_final.pdf.

[168] J.-Q. Li, J.-C. Li Li, K. Park, and J.-T. Kwon, “Investigation on the changes of pressure and temperature in high pressure filling of hydrogen storage tank,” *Case Stud. Therm. Eng.*, vol. 37, 2022.

[169] S. Tamhankar, “Terminal Operations for Tube Trailer and Liquid Tanker Filling: Status, Challenges and R&D Needs,” 2014. [Online]. Available: https://www.energy.gov/sites/default/files/2014/07/f17/fcto_2014_h2_trans_dist_wkshp_tamhankar.pdf.

[170] H. A. Nasution, H. Ambarita, H. V. Sihombing, E. Y. Setiawan, and H. Kawai, “The effect of stage number on the performance of a vapor compression refrigeration cycle using refrigerant R32,” *IOP Conf. Ser. Mater. Sci. Eng.*, vol. 851, 2020.

[171] S. Rubio, B. Nieto, and J. Martin, “D1.5 – Hydrogen refuelling and storage requirements for rail vehicles,” 2021. [Online]. Available: https://ec.europa.eu/research/participants/documents/downloadPublic?documentIds=080166e5e284e9d6&appId=PPGMS.

[172] J. Li *et al.*, “Liquid pump-enabled hydrogen refueling system for heavy duty fuel cell

vehicles: Pump performance and J2601-compliant fills with precooling," *Int. J. Hydrogen Energy*, vol. 46, no. 42, pp. 22018–22029, 2021.

[173] W. Liu, T. Placke, and K. T. Chau, "Overview of batteries and battery management for electric vehicles," *Energy Reports*, vol. 8, pp. 4058–4084, 2022.

[174] M. Kapetanovic, M. Vajihi, and R. M. P. Goverde, "Analysis of Hybrid and Plug-In Hybrid Alternative Propulsion Systems for Regional Diesel-Electric Multiple Unit Trains," *Energies*, vol. 14, 2021.

[175] H. S. Das, M. F. Chowdhury, S. Li, and C. W. Tan, "9 - Fuel cell and hydrogen power plants," in *Hybrid Renewable Energy Systems and Microgrids*, E. Kabalci, Ed. Academic Press, 2021, pp. 313–349.

[176] P. Sharma and O. P. Pandey, "Chapter 1 - Proton exchange membrane fuel cells: fundamentals, advanced technologies, and practical applications," in *PEM Fuel Cells*, G. Kaur, Ed. Elsevier, 2022, pp. 1–24.

[177] D. Lu, F. Yi, and J. Li, "Optimization of the Adaptability of the Fuel Cell Vehicle Waste Heat Utilization Subsystem to Extreme Cold Environments," *Sustainability*, vol. 14, no. 18, p. 11570, 2022.

[178] A. Fly and R. H. Thring, "A comparison of evaporative and liquid cooling methods for fuel cell vehicles," *Int. J. Hydrogen Energy*, vol. 41, no. 32, pp. 14217–14229, 2016.

[179] X. Chen *et al.*, "Temperature and voltage dynamic control of PEMFC Stack using MPC method," *Energy Reports*, vol. 8, pp. 798–808, 2022.

[180] A. Hoffrichter, S. Hillmansen, and C. Roberts, "Conceptual propulsion system design for a hydrogen-powered regional train," *IET Electr. Syst. Transp.*, vol. 6, no. 2, pp. 1–11, 2015.

[181] S. Kent, "FCEMU Project - Phase 1 Report - Issue 1 University of Birmingham, Hitachi Rail, Fuel Cell Systems Limited," 2016. [Online]. Available: https://www.birmingham.ac.uk/Documents/college-eps/railway/1-Class-156-Fuel-Cell-Electric-Multiple-Unit-Feasibility-Study-Issue-1.pdf.

[182] G. Barone, A. Buonomano, C. Forzano, G. F. Giuzio, and A. Palombo, "Energy, economic, and environmental impacts of enhanced ventilation strategies on railway coaches to reduce Covid-19 contagion risks," *Energy*, vol. 256, no. 124466, 2022.

[183] G. Barone, A. Buonomano, C. Forzano, and A. Palombo, "Enhancing trains envelope – heating, ventilation, and air conditioning systems: A new dynamic simulation approach for energy, economic, environmental impact and thermal comfort analyses," *Energy*, vol. 204, no. 117833, 2020.

[184] M. A. Fayazbakhsh and M. Bahrami, "Comprehensive Modeling of Vehicle Air Conditioning Loads Using Heat Balance Method," *SAE Int.*, 2013, [Online]. Available: https://saemobilus.sae.org/content/2013-01-1507/.

[185] W. Liu, Q. Deng, W. Huang, and R. Liu, "Variation in cooling load of a moving air-conditioned train compartment under the effects of ambient conditions and body thermal storage," *Appl. Therm. Eng.*, vol. 31, no. 6–7, pp. 1150–1162, 2011.

[186] D. Suszanowicz, “Internal heat gain from different light sources in the building lighting systems,” *E3S Web Conf.*, vol. 19, 2017.

[187] P. M. Pattison, M. Hansen, and J. Y. Tsao, “LED lighting efficacy: Status and directions,” *Comptes Rendus Phys.*, vol. 19, no. 3, pp. 134–145, 2018.

[188] M. Liu, W. Saman, and F. Bruno, “Validation of a mathematical model for encapsulated phase change material flat slabs for cooling applications,” *Appl. Therm. Eng.*, vol. 31, no. 14–15, pp. 2340–2347, 2011.

[189] W. Villasmil, L. J. Fischer, and J. Worlitschek, “A review and evaluation of thermal insulation materials and methods for thermal energy storage systems,” *Renew. Sustain. Energy Rev.*, vol. 103, pp. 71–84, 2019.

[190] M. Kirincic, A. Trp, and K. Lenic, “Influence of natural convection during melting and solidification of paraffin in a longitudinally finned shell-and-tube latent thermal energy storage on the applicability of developed numerical models,” *Renew. Energy*, vol. 179, pp. 1329–1344, 2021.

[191] V. R. Voller, M. Cross, and N. C. Markatos, “An enthalpy method for convection/diffusion phase change,” *Int. J. Numer. Methods Eng.*, vol. 24, no. 1, pp. 271–284, 1987.

[192] W. Youssef, Y. T. Ge, and S. A. Tassou, “CFD modelling development and experimental validation of a phase change material (PCM) heat exchanger with spiral-wired tubes,” *Energy Convers. Manag.*, vol. 157, pp. 498–510, 2018.

[193] C. Reichl, S. Both, P. Mascherbauer, and J. Emhofer, “Comparison of Two CFD Approaches Using Constant and Temperature Dependent Heat Capacities during the Phase Transition in PCMs with Experimental and Analytical Results,” *Processes*, vol. 10, no. 2, 2022.

[194] Z. Li and E. Gariboldi, “Review on the temperature-dependent thermophysical properties of liquid paraffins and composite phase change materials with metallic porous structures,” *Mater. Today Energy*, vol. 20, no. 100642, 2021.

[195] M. Sosnowski, J. Krzywanski, K. Grabowska, and R. Gnatowska, “Polyhedral meshing in numerical analysis of conjugate heat transfer,” *EPJ Web Conf.*, vol. 180, 2018.

[196] T. Deng, G. Zhang, and Y. Ran, “Study on thermal management of rectangular Li-ion battery with serpentine-channel cold plate,” *Int. J. Heat Mass Transf.*, vol. 125, pp. 143–152, 2018.

[197] Ansys, “ANSYS Meshing User’s Guide.” pp. 724–746, 2013.

[198] Y. He, W. Yuan, J. Cao, L. Li, and Z. Ling, “Compact latent heat exchanger for the fast supply of hot water with serpentine tubes in shape-stabilized composite phase change material and auxiliary electric heating,” *Appl. Therm. Eng.*, vol. 211, 2022.

[199] “Combined Heat and Power – Technologies A detailed guide for CHP developers – Part 2,” 2021. [Online]. Available: https://assets.publishing.service.gov.uk/government/uploads/system/uploads/attachment_data/file/961492/Part_2_CHP_Technologies_BEIS_v03.pdf.

[200] Y. Saygili, I. Eroglu, and S. Kincal, “Model based temperature controller development for water cooled PEM fuel cell systems,” *Int. J. Hydrogen Energy*, vol. 40, no. 1, pp. 615–622, 2015.